MID-INFRARED INTERFEROMETRY OF YOUNG STELLAR OBJECTS:

Detection of a hot component inside the circumbinary cavity of V892 Tau

INAUGURAL-DISSERTATION

zur
Erlangung des Doktorgrades (Dr. rer. nat.)
der
Mathematisch-Naturwissenschaftlichen Fakultät
der
Universität zu Köln

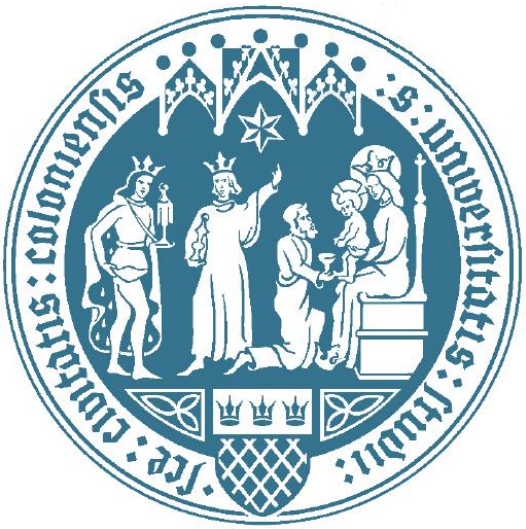

vorgelegt von
Juan Andrés Cahuasquí Llerena
aus
Ambato, Ecuador

Köln 2019

Berichterstatter/in:	Prof. Dr. Lucas Labadie
	Prof. Dr. Astrid Kiendler-Scharr
Tag der mündlichen Prüfung:	25. Oktober 2018

Abstract

Stars are the essential elements of the universe that govern the evolution of galaxies and the interstellar medium. The star formation process carries two ubiquitous byproducts that dispose the excess of angular momentum: binary or higher-order stellar systems, and the formation of circumstellar disks surrounding most – if not all – stars. Although these two outputs embrace a wide field of astronomy by their own, the link between them seems to be a natural consequence. Namely, stellar and substellar companions forming multiple systems dynamically perturb primordial circumstellar disks and settle the conditions for planets to grow in such scenario.

Due to their young age ($<$10 Myr) and observability after dispersing part of their gaseous and dusty envelope, the low-mass T Tauri ($<$2 $M_\odot$) and the intermediate-mass Herbig Ae/Be (2–10 $M_\odot$) stellar objects in the pre-main sequence phase are ideal laboratories to characterize protoplanetary disks. At this stage, observations with different techniques and at different wavelengths allow to investigate the star-disk environment through strong emission lines indicative of accretion of gas onto the central star, excess emission at infrared and longer wavelengths, and resolved thermal and scattered light. Additionally, a more advanced evolutionary stage in the so-called transition disks may be identified via dust-depleted cavities as consequence of forming planets, photoevaporation, self-shadowing or a dead zone inside the disk.

Numerical simulations and dedicated surveys of T Tauri binary systems have revealed that the influence of the stellar companions depends on the orbital parameters and masses of the components. The evolution of disks in close binary ($<$1 AU) and large-separation systems ($>$100 AU) seems well understood. Whereas for the first case both stars would be surrounded by a common circumbinary disk, the large-separated stars may host independent circumstellar disks whose evolution is indistinct to disks around single objects. On the contrary, the understanding of intermediate-separation systems is poorer, and the disk lifetime seems to be reduced to $\sim$10% of the typical life expectancy because of tidal truncation effects. Nonetheless, as evidenced by some multiple objects (e.g. GG Tau A), circumbinary plus circumstellar components may coexist, and the feeding from one to another through streamers may extend the disk lifetime for planets to assemble.

For Herbig stars, the bigger masses and gravitational forces at play can apparently cause a faster disk disruption. Still, observational evidence and statistical surveys to understand the spatial distribution of dust and gas, and the possibility of their survival in the inner environment are scarcer, with even only few known objects that harbour circumbinary disks.

In particular, the Herbig Ae/Be object V892 Tau, also known as Elias 1, is a near-equal brightness binary system located in the Taurus-Auriga star-forming region, located at 140 pc, known to be surrounded by a large circumbinary disk. The stellar pair has a separation of $\sim$7 AU, and the circumbinary component has an inner radius of $\sim$18 AU.

This doctoral thesis aims at contributing in the understanding of the central circumstellar environment of Herbig binary systems by taking advantage of the high-angular (milliarcsec-

ond) resolution provided by long-baseline interferometry, and offers the first mid-infrared multi-epoch interferometric study of V892 Tau. Due to its sensitivity to thermal emission of dust with temperatures of the order $\sim$100–1000 K, the MID-infrared Interferometric instrument (MIDI) at the Very Large Telescope Interferometer (VLTI) allows to resolve dusty structures within the circumbinary cavity of this particular object.

The mid-IR (8–13 μm) interferometric data consisting of visibilities and differential phases, in conjunction with photometric measurements, is modelled with a temperature-gradient approach and χ^2-minimization algorithms. This method allows to scrutinize the geometry of the system and discuss the possibility of dust survival within an environment affected by tidal interaction and strong gravitational forces that settle the conditions for planetary growth.

By investigating different possible morphologies capable of achieving a satisfactory fit to the mid-IR observations of V892 Tau, I conclude that a disk-like dusty source in the central vicinity of the stars is the most plausible origin of near-IR flux. This newly proposed component reproduces well the photometric measurements and causes a brightness asymmetry which influences the MIDI visibilities and differential phases. Moreover, the profit of this multi-epoch study reveals that this detected source is presumably unattached to any of the stars and possesses signs of variability over the five observing runs covering a 9-year period. Nevertheless, the application of semi-physical models to reproduce interferometric signals and the detection of this near-IR floating component based on N-band data suggest caution with the interpretation of this finding. Although the outcomes clearly expose the existence of a dusty structure, a follow-up investigation with the newest second generation of interferometers and high-resolution direct imaging techniques is required to certainly determine its morphology. Granted K-band observations in forthcoming periods of V892 Tau with both astronomical techniques will complement this project and offer a wider insight into the field of planet formation and disk evolution in intermediate-separation binary Herbig objects.

Zusammenfassung

Sterne sind die wesentlichen Elemente des Universums, die die Entwicklung der Galaxien und des interstellaren Mediums bestimmen. Der Sternentstehungsprozess trägt zwei allgegenwärtige Nebenprodukte, die den Überschuss an Drehimpuls abgeben: binäre oder höherwertige Sternensysteme und die Bildung von zirkumstellaren Scheiben, von denen die meisten - wenn nicht alle - Sterne umgeben. Obwohl diese beiden Ergebnisse ein weites Feld der Astronomie umfassen, scheint die Verbindung zwischen ihnen eine natürliche Konsequenz zu sein. Stellare und (sub)stellare Begleiter, die mehrere Systeme bilden, stören dynamisch primordiale zirkumstellare Scheiben und regeln die Bedingungen für das Wachstum von Planeten in einem solchen Szenario.

Dank ihres jungen Alters ($<$10 Myr) und ihrer guten Möglichkeit zur Beobachtung, nachdem sie einen Teil ihrer gasförmigen und staubigen Hülle verteilt haben, sind die massearmen T Tauri ($<$2 $M_\odot$) und die Zwischenmassen Herbig Ae/Be (2–10 $M_\odot$) stellare Objekte in der Phase vor der Hauptsequenz ideale Laboratorien, um protoplanetare Scheiben zu charakterisieren. In diesem Stadium erlauben Beobachtungen mit verschiedenen Techniken und bei verschiedenen Wellenlängen die Untersuchung der Stern-Scheibe-Umgebung durch starke Emissionslinien, die eine Anreicherung von Gas auf den Zentralstern, überschüssige Emission bei Infrarot- und längeren Wellenlängen und aufgelöstes thermisches und gestreutes Licht anzeigen. Zusätzlich kann über staubarme Hohlräume als Folge von Planetenbildung, Photoverdampfung, Selbstbeschattung oder einer Totzone innerhalb der Scheibe ein weiter fortgeschrittenes Entwicklungsstadium in den sogenannten Übergangsscheiben identifiziert werden.

Numerische Simulationen und spezielle Untersuchungen von T Tauri-Binärsystemen haben gezeigt, dass der Einfluss der stellaren Begleiter von den Bahnparametern und Massen der Komponenten abhängt. Die Entwicklung von Scheiben in engen binären ($<$1 AU) und Systemen mit großer Separation ($>$100 AU) scheint gut verstanden. Während im ersten Fall die Sterne nur von einer umlaufenden Scheibe umgeben sind, können die großseparierten Sterne unabhängige zirkumstellare Scheiben beherbergen, deren Entwicklung ähnlich zu Scheiben um einzelne Objekte ist. Im Gegenteil, das Verständnis von Systemen mit mittlerer Separation ist schlechter, und die Lebensdauer der Scheiben scheint aufgrund von Gezeitenabschneidungseffekten auf $\sim$10% der typischen Skalen reduziert zu sein. Nichtsdestotrotz können, wie einige Mehrfachobjekte (z.B. GG Tau A) zeigen, zircumbinäre plus zirkumstellare Komponenten koexistieren und die Zuführung von einem zum anderen durch Streamer kann die Lebensdauer der Scheibe verlängern, damit sich Planeten zusammensetzen können.

Für Herbig-Sterne können die größeren Massen und Gravitationskräfte offenbar eine schnellere Disruption der Scheibe verursachen. Dennoch sind Beobachtungsdaten und statistische Erhebungen zum Verständnis der räumlichen Verteilung von Staub und Gas und der Möglichkeit ihres Überlebens in der inneren Umgebung seltener, mit nur wenigen bekannten Objekten, die umlaufende Scheiben beherbergen.

Insbesondere das Herbig Ae/Be-Objekt V892 Tau, auch bekannt als Elias 1, ist ein nahezu

gleich-helles binäres System, das sich in der Taurus-Auriga-Sternbildungsregion befindet, die bei 140 pc liegt und bekanntermaßen von einer großen zirkumbinären Scheibe umgeben ist. Das stellare Paar hat eine Trennung von $\sim$7 AU, und die Umfangskomponente einen inneren Radius von $\sim$18 AU.

Diese Dissertation zielt darauf ab, einen Beitrag zum Verständnis der zentralen zirkumstellaren Umgebung von Herbig-Binärsystemen zu leisten, indem sie die Vorteile der hochwinkligen (Milliarcsekunden) Auflösung nutzt, die durch die Interferometrie mit langer Baseline bereitgestellt wird, und bietet die erste interferometrische Multi-Epochenstudie im mittleren Infrarotbereich von V892 Tau. Das MID-Infrarot-Interferometer (MIDI) am Very Large Telescope Interferometer (VLTI) ermöglicht dank seiner Empfindlichkeit gegenüber thermischer Staubemission bei Temperaturen in der Größenordnung von $\sim$100–1000 K die Auflösung von staubigen Strukturen im umlaufenden Hohlraum dieses speziellen Objekts.

Die interferometrischen Daten im mittleren IR-Bereich (8–13 μm), die aus Visibilities und Differentialphasen bestehen, werden in Verbindung mit photometrischen Messungen mit einem Temperaturgradientenansatz und χ^2-Minimierungsalgorithmen modelliert, um die Geometrie des Systems zu untersuchen und die Möglichkeit des Staubüberlebens in einer Umgebung zu diskutieren, die durch Gezeitenwechselwirkung und starke Gravitationskräfte beeinflusst wird, die die Bedingungen für das planetare Wachstum festlegen.

Die Untersuchung verschiedener möglicher Morphologien, die in der Lage sind, eine zufriedenstellende Anpassung an die Mittel-IR-Beobachtungen von V892 Tau kommt zu dem Schluss, dass eine scheibenförmige staubige Quelle in der zentralen Umgebung der Sterne der plausibelste Ursprung des Nah-IR-Flusses ist, der den photometrischen Messungen entspricht, und eine Helligkeitsasymmetrie erzeugt, die die MIDI-Sichtbarkeiten und Differenzphasen beeinflusst. Darüber hinaus zeigt diese Multi-Epochen-Studie, dass diese neu entdeckte Komponente vermutlich nicht an einen der Sterne gebunden ist und Anzeichen von Variabilität über die 5 Beobachtungsläufe über einen Zeitraum von 9 Jahren aufweist.

Die Anwendung von semi-physikalischen Modellen zur Reproduktion interferometrischer Signale und die Detektion dieser near-IR Floating-Komponente auf Basis von N-Band-Daten lassen Vorsicht bei der Interpretation dieses Befundes zu. Die Ergebnisse zeigen jedoch deutlich die Existenz einer staubigen Struktur, deren Untersuchung mit der neuesten zweiten Generation von Interferometern und hochauflösenden Direktabbildungstechniken fortgesetzt werden muss. Bewilligte K-Band-Beobachtungen in den kommenden Perioden von V892 Tau mit beiden astronomischen Techniken werden dieses Projekt ergänzen und einen breiteren Einblick in das Feld der Planetenbildung und Scheibenentwicklung in binären Herbig-Objekten mit Zwischentrennung bieten.

Contents

CHAPTER 1

Scientific Motivation

In November 2014 ESA astronaut Alexander Gerst, crew member of the Expedition 40/41, landed back on Earth after 166 days at the International Space Station. His mission included experiments with the purpose of improving life on Earth and preparing further exploration of the Solar System. Interestingly, the mission was called "Blue Dot" after the American astronomer Carl Sagan described our planet as "a pale blue dot", as seen on a photograph taken by NASA's Voyager at a distance of six billion kilometres.
Sagan's statement made reference to everything what happens and happened on our planet, including, for example, people, philosophers and astronomers that for centuries have wondered about the origin and uniqueness of our planet and our system in the vast universe.

Nowadays we know that the fundamental blocks of luminous matter in the universe – stars – form from the gravitational collapse and fragmentation of clumpy and filamentary molecular clouds into smaller cores. As an aftermath of this process, first, most of stars are part of a binary or small multiple system, and second, the newborn stars are surrounded by gaseous and dusty material forming circumstellar disks.

Theory suggests that the leading mechanism that results in binary formation is the fragmentation of a prestellar core [Bonnell and Bate, 1994]. Other theories, such as the catastrophic evolution of a gravitationally unstable circumstellar disks [Bonnell, 1994] or the capture of objects into a bound system, may also serve to explain the different separation scales between stellar components of binary systems. Either way, observational surveys evidence the high degree of multiplicity in solar-type ($\sim$50%) and pre-main sequence stars ($\sim$70%) [e.g. Raghavan et al., 2010, Bouvier and Corporon, 2001, Kraus et al., 2011]. On the other hand, circumstellar disks assemble because the progenitor molecular clouds are turbulent [e.g. Larson, 1981, McKee and Ostriker, 2007] and any collapsing region with nonzero angular momentum leads to their formation. Whereas these disks inherit their initial mass, size and chemical composition from the broader star formation environment, their evolution may be influenced by external effects such as the impact of a stellar companion. The pre-main sequence phase of young stellar systems amalgamates both an established high degree of multiplicity and the assets of disks around the stars, creating an ideal scenario to study and understand the impact of binarity/multiplicity on the evolution of primordial circumstellar disks and the subsequent formation of planets.

In the case of isolated pre-main sequence low-mass stars objects – T Tauri (TTS) – and intermediate-mass objects – Herbig Ae/Be (HAeBe) –, protoplanetary disks showing excess emission at infrared and longer wavelengths, strong emission lines indicative of accretion of gas onto the central star and resolved thermal and scattered light, have been assessed. These physical processes take place in a timescale of $\sim$10 million years before the gas is dispersed by the formation of planets [e.g. Sicilia-Aguilar et al., 2006]. Additionally, during this period of time, the primordial disk transforms from full gas-rich to debris cold disk, undergoing also a transitional phase with dust-depleted cavities in the disk as consequence of forming planets [e.g. Papaloizou et al., 2007], photoevaporation [e.g. Hollenbach et al., 1994], self-shadowing [e.g. Dong, 2015] or a dead zone inside the disk [e.g. Pinilla et al., 2016].

On the contrary, in binary systems the lifetime of protoplanetary disks is shorten due to the dynamical perturbations between the stars, hazarding not only a normal evolution of the disk, but also the potential for planets to grow. The consequences depend essentially on three factors: the stellar masses, their separation and the eccentricity. Models suggest that for very close systems – less than 1 AU – planets can form and survive in circumbinary orbits around both members [Quintana and Lissauer, 2006], whereas in wide binaries – more than 100 AU – planet formation seems indistinct of the one seen for single stars [e.g. Kraus et al., 2016, Bonavita and Desidera, 2007]. The dynamics of disk evolution and planet formation in systems with intermediate separations – less than 100 AU – is more difficult to predict.

Numerical simulations find that circumstellar disks around individual components and circumbinary disks can coexist in intermediate-separation systems. For eccentricities less than 0.25, the inner edge of a circumbinary disk is tidally truncated to within 1.8–2.6 times the semimajor axis of the binary orbit, and the outer edge of the circumstellar disks are truncated at half this length [e.g. Artymowicz and Lubow, 1994, Papaloizou and Pringle, 1977]. Moreover, statistical studies targeting low-mass T Tauri binary systems located in some of the nearest and most active star forming regions, such as Taurus, Ophiuchus or Chamaeleon I, have demonstrated that, in comparison to disks that evolve around single stars, the lifetime and accretion activity of circumstellar disks in systems with physical separations less than 100 AU is reduced [e.g. Cieza et al., 2009, Daemgen et al., 2013]. Considering a stellar pair with a separation of 30 AU – the statistical peak-separation expected for a population of T Tauri [Duquennoy and Mayor, 1991] – the lifetime of the disks around the individual components should be $\sim$10% of the one around single components with a typical radius of 100 AU [Vicente and Alves, 2005, Andrews and Williams, 2007b], or in other words, just a fraction of a million year. An accelerated disk dissipation subsequently disrupts the timescale needed to form terrestrial and giant planets through core accretion [Duchêne, 2010]. In spite of these statistical and numerical expectations, observations from hot to cold regimes of the T Tauri system GG Tau A have traced a significant reservoir of dust and gas accreting onto the stars and surrounding the stellar components separated 35 AU [Dutrey et al., 2014]. The triple system GG Tau A has an age of $\sim$2 Myr, and as it possesses circumstellar and circumbinary disks, it is a preeminent laboratory to study the sustainability of planet formation. Indeed, the lifetime of circumstellar disks may be prolonged as long as they are replenished by an external factor – a circumbinary disk –, leaving time for planets to grow.

It is clear that most of what we know about disk evolution in young multiple systems derives from the studies of T Tauri objects. Assessing the more massive and luminous Herbig Ae/Be objects is considerably more challenging. Although their binary frequency is expected to be similar to the one of the low-mass counterparts, the amount of them imposed by the stellar initial mass function is scarce. Also, the majority of them are located

at least 300 pc away, and the large mass and contrast ratios for unequal systems make an accurate characterization of the systemic properties difficult [Duchêne, 2015]. While at intermediate separations no dedicated multiplicity survey has been conducted, few multiple HAeBe objects have been resolved with circumstellar and/or circumbinary emission. For instance, the quadruple system TY CrA, whose close triple system is separated from the fourth component by about 40 AU, is surrounded by dusty emission [e.g. Chauvin et al., 2003, Boersma et al., 2009]. HD142527 having a low-mass companion at 12 AU shows flows of gas through a dust-depleted gap of $\sim$30 AU [e.g. Biller et al., 2012, Casassus et al., 2013, Lacour et al., 2016]. The nearly identical binary system AK Sco is surrounded by a circumbinary disk and shows spectral features indicating outflow and infall activities in the system [e.g. Alencar et al., 2003, Anthonioz et al., 2015, Gómez de Castro et al., 2016]. This work enriches the sample of HAeBes in the context of intermediate-separation binary systems that host circumstellar emission by investigating the source V892 Tau.

V892 Tau – also known as Elias 3-1 or Elias 1 – is a HAeBe system with a spectral type B8.5V–A0Ve [Mooley et al., 2013], located at 140 pc in the Taurus-Auriga star-forming region. It consists of a near-equal stellar pair with a separation of $\sim$7 AU [Smith et al., 2005] and a circumbinary disk with an inner radius of $\sim$18 AU [Monnier et al., 2008]. Submillimetre interferometric observations have resolved also the colder extension of the disk up to $\sim$100 AU [Hamidouche, 2010]. The presence of hydrogen emission lines and infrared excess in the spectrum of V892 Tau point to accretion activity and thermal emission in a region closer to the stars.

Through this first ever study of Elias 1 based on multi-epoch mid-infared interferometric data acquired with the Very Large Telescope Interferometer, I aim at characterizing the central environment of the circumbinary cavity and the spatial distribution of dust, whose dissipation may be accelerated by the presence of the more massive stars at play.

Spectroscopic techniques can only probe the environment of stellar companions out to $\sim$1 AU. On the contrary, by combining several apertures, the long-baseline interferometry technique that I use in this work allows to explore with high-angular resolution the innermost regions – less than 100 AU – of single and multiple systems, where the evolution of protoplanetary disks and planet formation occur. Since the warm dust directly exposed to the stellar emission has temperatures of 100–1000 K, the N-band in the mid-infrared window is ideal to study the dust distribution around young stellar objects [Dullemond and Monnier, 2010]. Therefore, in this investigation, observations acquired with the Unit Telescopes (UTs) and the MID-infrared Interferometric instrument (MIDI) in the wavelength range 8–13 μm enable to characterize the cavity and the inner region of the large circumbinary disk in V892 Tau, achieving a maximum spatial resolution of $\sim$3 AU for a typical baseline of 100 m.

Besides this motivational Chapter 1, this doctoral thesis is organized in five chapters. Chapter 2 introduces the picture of star formation and subsequent evolution to form planetary systems. Chapter 3 presents the theoretical and practical principles on which interferometry is grounded and how its high-angular resolution capability allows to assess the inner scales of circumstellar disks around single and binary stellar systems. This chapter announces also the numerical modelling of interferometric data implemented for this work. Chapter 4 develops the main purpose of this investigation, the Herbig Ae/Be star V892 Tau, including information on its nature collected from the literature and the analysis performed based on the mid-infrared spectro-interferometric measurements. Chapter 5 discusses the results of this research and delineates prospects for further investigation of V892 Tau with state-of-the-art facilities.

CHAPTER 2

Introduction

2.1 The big picture of star formation

The nebular hypothesis, first published by Immanuel Kant in his "Allgemeine Naturgeschichte und Theorie des Himmels" back in 1755, states that the Solar System formed from nebulous material. Although in general words it is true and applies throughout the whole Universe, star formation is a more complicated process. The material from which stars form is located mainly in spiral arms or near the center of galactic nuclei, forming massive and dense molecular clouds whose main constituents are molecular hydrogen, atomic helium and CO (Fig. 2.1). These molecular complexes have sizes up to a kiloparsec and masses up to $10^7\,M_\odot$ [e.g. Solomon and Sanders, 1985, Elmegreen, 1993]. They may contain several giant molecular clouds (GMCs) with sizes up to 100 pc and masses up to $10^6\,M_\odot$, and these GMCs, in turn, contain smaller scale structures that may be filamentary or clumpy on a wide range of scales [e.g. Blitz and Williams, 1999, Williams et al., 2000]. The substructures seen in GMCs range from massive clumps with several parsecs in size and masses of thousands of solar masses, where entire clusters of stars may form, to small dense cloud cores with sizes of the order of 0.1 pc and masses of the order of $1\,M_\odot$, which may form individual stars or small multiple systems [e.g. Lada et al., 1993, Williams et al., 2000, Visser et al., 2002]. Table 2.1 illustrates some properties and spatial scales of the different structures forming molecular clouds. Molecular clouds are the densest regions of the interstellar medium, surrounded by less dense envelopes of atomic gas. Hydrogen molecules form on the surface of dust grains, and the rate of this process increases with increasing density. A sufficient opacity due to dust enables the survival of the molecules, protecting them from dissociation due to ultraviolet radiation. This protection is effective if the molecular clouds have a column density – the number of molecules along the line of sight through, for instance, a clump, divided by the projected area of the clump – of at least $20\,M_\odot\,pc^{-2}$, although most of them have column densities much higher than that [e.g. Elmegreen, 1993]. Because of the lack of external radiation to which molecular clouds are exposed, and the high cooling efficiency by collisions of excited atoms and molecules, these clouds are very cold and have typical temperatures of only about 10–20 K. Higher temperatures up to 100 K can be reached only in regions heated by luminous newly formed stars. However, in the densest collapsing cloud cores gas becomes thermally coupled to dust and, in turn, dust keeps a low and constant temperature of about 10 K over a wide range of densities due to its strong temperature-dependent thermal emission

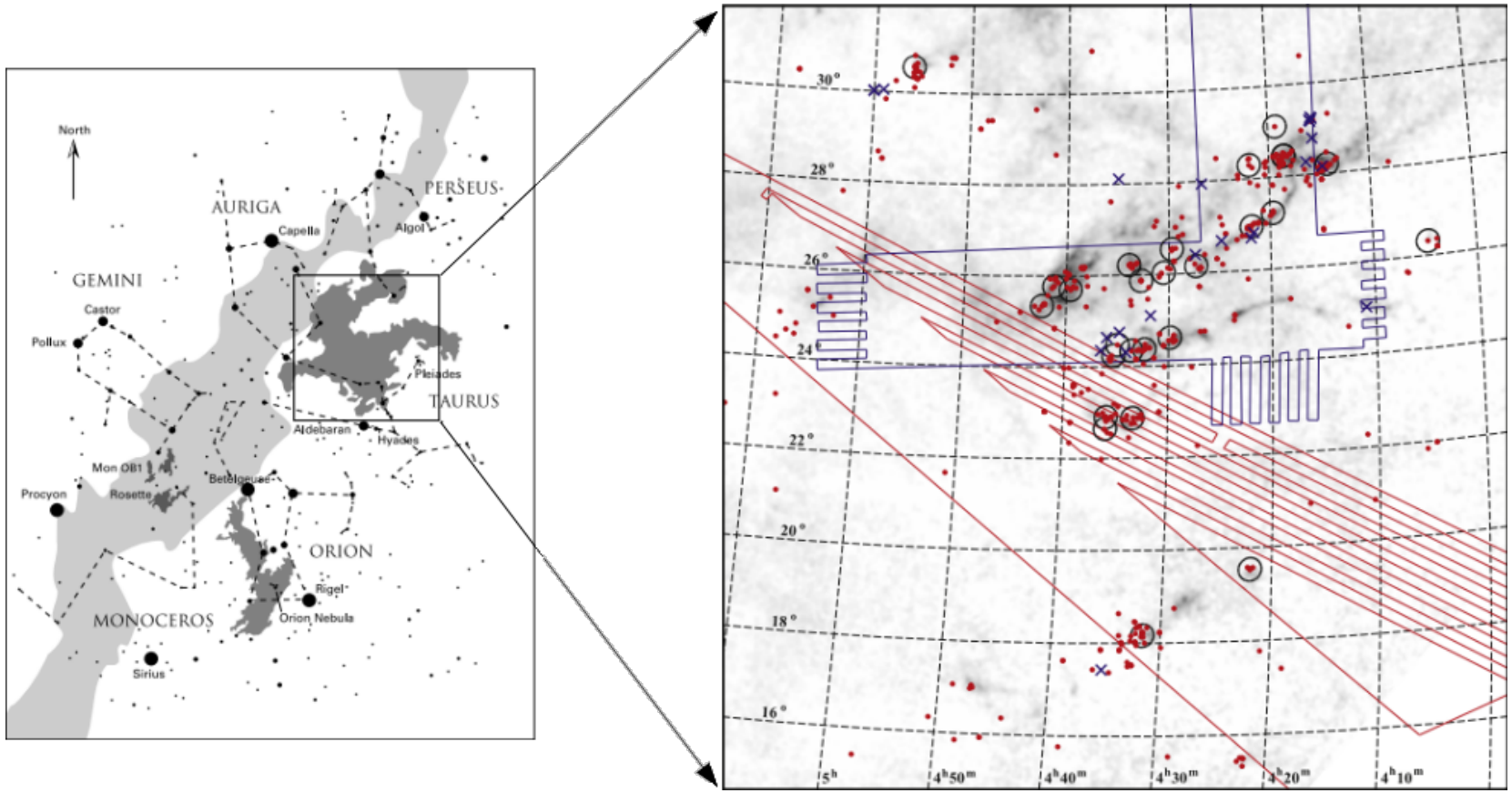

Figure 2.1: *Left*: Map of a portion of the northern sky of the Milky Way (grey), including the Orion and Taurus GMCs. The brightest stars and prominent constellations are also labelled. *Right*: Spatial distribution of known members (>400) of the Taurus star forming region (crosses and filled circles) as observed by different runs of the Sloan Digital Sky Survey. The large circles correspond to regions observed in X-ray ranges with the mission XMM-Newton. The darker regions in this gray-scale map denote higher densities. [Credit: Luhman et al. [2017]. Reproduced with permission ©AAS.]

Table 2.1: Typical values for some properties of molecular clouds at different scales [e.g. Larson, 2003]. The density is traced in molecules of H_2 per cubic centimetre.

	Molecular complex	GMC	Molecular clump	Molecular core
Size [pc]	1000	100	$\sim$10	$\sim$1
Mass [$M_\odot$]	10^7	10^6	10^3	$\sim$10
Density n(H_2) [cm^{-3}]	$\sim$10	10^2	10^3	10^5

[e.g. Hayashi and Nakano, 1965, Larson, 1985, Masunaga and Inutsuka, 2000]. The low and constant temperature is fundamental for the star formation process because it makes possible the collapse of prestellar cloud cores with masses comparable or less than one solar mass. Due to the low temperatures and high densities in molecular clouds, self-gravity largely dominates over thermal pressure. Therefore, molecular clouds would be expected to collapse effectively and rapidly into stars. However, only a few percent of their mass turn into stars before being dispersed, suggesting that, in addition to thermal pressure, other factors such as magnetic fields [e.g. Chandrasekhar and Fermi, 1953, Basu and Mouschovias, 1994, Adams and Shu, 2007], rotation [e.g. Field, 1978, Evans, 1999] and turbulence [e.g. Norman and Silk, 1980, Mac Low and Klessen, 2004, Ballesteros-Paredes et al., 2007] support the clouds in near-equilibrium against gravity and prevent a rapid collapse.

2.1.1 Gravitational instability, free-fall phase and cloud fragmentation

To understand the conditions that lead to the collapse of a molecular cloud substructure into stars, the Jeans instability (James Jean, 1902) considers only gravitation and thermodynamics. Nevertheless, it provides a good insight into the development of protostars. Out of the several ways to derive such a criterion, as follows I review the one based on the virial theorem, according to which the condition for equilibrium of a stable, gravitationally bound system is given by

$$2K + U = 0 \tag{2.1}$$

where K is the kinetic energy and U is the potential energy. If $2K > |U|$, the force due to gas pressure will dominate the force of gravity and the cloud will expand. On the contrary, if $2K < |U|$, the cloud will collapse under the force of gravity. The gravitational potential energy is defined as

$$U = -\frac{3}{5}\frac{GM_\mathrm{c}^2}{R_\mathrm{c}} \tag{2.2}$$

where M_c and R_c are the mass and the radius of the considered cloud, and G is the gravitational constant[1]. In turn, the kinetic energy per particle is defined as

$$K = \frac{3}{2}kT \tag{2.3}$$

where k is the Boltzmann constant[2]. Thus, the total internal kinetic energy of the cloud is

$$K = \frac{3}{2}NkT \tag{2.4}$$

[1] $G = 6.674 \times 10^{-8} \mathrm{cm}^3\ \mathrm{g}^{-1}\ \mathrm{s}^{-2}$
[2] $k = 1.38064852 \times 10^{-16} \mathrm{erg}\ \mathrm{K}^{-1}$

where N is the total number of particles, and it can be written in terms of the mass of the cloud and the mean molecular weight in units of hydrogen atom mass $m_{\rm H}$

$$N = \frac{M_{\rm c}}{\mu m_{\rm H}}. \tag{2.5}$$

Then, the condition for gravitational collapse $2K < |U|$ takes the form

$$\frac{3M_{\rm c}kT}{\mu m_{\rm H}} < \frac{3}{5}\frac{GM_{\rm c}^2}{R_{\rm c}}. \tag{2.6}$$

From this equation the radius $R_{\rm c}$ can be eliminated assuming that the cloud is a sphere of constant density ρ_0 prior to collapse according to

$$R_{\rm c} = \left(\frac{3}{4}\frac{M_{\rm c}}{\pi\rho_0}\right)^{1/3}. \tag{2.7}$$

Finally, the concept of Jeans mass is obtained from the substitution of the previous equation

$$M_J \simeq \left(\frac{5kT}{G\mu m_{\rm H}}\right)^{3/2}\left(\frac{3}{4\pi\rho_0}\right)^{1/2}. \tag{2.8}$$

If the mass of a cloud is greater than Eq. 2.8, the cloud will be unstable against gravitational collapse. Also, for a given μ, the Jeans mass depends only on the density and temperature. The higher the density and the lower the temperature, the smaller the cloud mass needs to be to gravitationally collapse. Other magnitudes related to the Jeans mass are the Jeans length and the Jeans density

$$R_J \simeq \left(\frac{15kT}{4\pi G\mu m_{\rm H}\rho_0}\right)^{1/2} \tag{2.9}$$

$$\rho_J \simeq \frac{3}{4\pi M_{\rm c}^2}\left(\frac{5kT}{G\mu m_{\rm H}}\right)^3 \tag{2.10}$$

where the conditions for gravitational collapse are $R_{\rm c} > R_J$ and $\rho_{\rm c} > \rho_J$ for Eqs. 2.9 and 2.10, respectively.

For example, one can consider a dense core in a molecular cloud with typical values of $T \sim 10$ K and $n_{\rm H_2} \sim 10^5$ cm^{-3}. The density is thus $\rho_0 \sim 2n_{\rm H_2}m_{\rm H} \sim 2(10^5)(1.7 \times 10^{-24}) \sim 3.4 \times 10^{-19}$g cm^{-3}. Then, by replacing these values in Eq. 2.8 and taking $\mu = 2$, it results in a Jeans mass of $\sim 5 \times 10^{33}$g, or $\sim 3\,{\rm M}_\odot$[3]. This value demonstrates that, indeed, dense cores of GMCs in the order of few solar masses are unstable to gravitational collapse.

The early stages of the collapse are isothermal and the cloud is basically in free-fall collapse under its own gravitational attraction. This free-fall timescale [Spitzer, 1978] of a cloud collapsing from an initial radius r_0 to a smaller one $r_{\rm final}$ can be estimated according to the expression[4]

$$t_{\rm ff} = \left(\frac{3\pi}{32}\frac{1}{G\rho_0}\right)^{1/2}. \tag{2.11}$$

This means that the free-fall timescale depends only on the initial density ρ_0. For models of

[3]The mass of a hydrogen atom is $\sim 1.7 \times 10^{-24}$ g, and $1{\rm M}_\odot \sim 2 \times 10^{33}$ g.

[4]More detailed information about the theory of star formation can be appreciated from publicly available resources [e.g. Larson, 2003, Stahler and Palla, 2005, Kippenhahn et al., 2012]. More complex models and theory that consider the role of magnetic fields, turbulence and rotation in the star formation process are also developed. However, they are beyond the scope of this investigation, and only the most relevant principles are here recalled.

spherical molecular clouds of uniform density, all parts of the cloud take the same length of time to collapse and the density increases at the same rate everywhere, in what is called homologous collapse.

As a consequence of the free-fall collapse, the density within the cloud increases by many orders of magnitude. Assuming that the temperature remains more or less constant, then the Jeans mass of Eq. 2.8 supposes that the mass limit for instability drastically decreases. It follows that any density inhomogeneities within the cloud may cause individual regions to collapse locally (Fig. 2.2,a)). This process is called fragmentation, and given the inefficient rates of converting the total gas mass of the parent cloud into stars (about only 1%), there is a minimum limit at which the fragmentation process stops. Indeed, the increasing density causes also heating and increase in gas pressure within each fragment, turning an isothermal scenario into adiabatic and forming a thermally supported inner core which collapses into the protostar [Fig. 2.2,b); e.g. Larson, 1969, Machida et al., 2006, 2007]. The minimum obtainable Jeans mass corresponding to when adiabatic effects become important and limit fragmentation is

$$M_{J_{\min}} = 0.03 \left(\frac{T^{1/4}}{e^{1/2}\mu^{9/4}} \right) \mathrm{M}_{\odot} \tag{2.12}$$

where T is the temperature at the time when adiabatic effects are significant, and e is an adiabatic efficiency factor between 0 and 1. For instance, for a hydrogen cloud with $\mu = 1$, $e \sim 0.1$ and $T \sim 1000$ K, the minimum obtainable mass is $M_{J_{\min}} \sim 0.5\ \mathrm{M}_{\odot}$. That is, fragmentation ceases when individual fragments are of the order of a solar mass, being, indeed, the most common mass-type of stars in the galaxy.

2.1.2 Protostar and pre-main sequence phase

The formation of a protostar is established when the density of a collapsing fragment increases enough for the gas to become opaque to infrared photons. The radiation contained in the central part of the cloud leads to heat and increase in gas pressure, and the cloud core adopts a nearly hydrostatic equilibrium. Most of the final mass of a star is acquired through free-fall accretion from the surrounding material, preferentially funnelled along the magnetic field lines. The accretion of gas generates gravitational energy, part of which goes into heating of the core and part of which is radiated away, providing the luminosity of the protostar

$$L \sim L_{\mathrm{acc}} = \frac{1}{2} \frac{G M_{\star} \dot{M}}{R_{\star}} \tag{2.13}$$

where $\dot{M}$ is the rate of mass accretion onto the star, and $M_{\star}$ and $R_{\star}$ are the mass and radius of the newborn star. The accretion rate is very high during the earliest and most heavily obscured phases of protostellar evolution and declines strongly with time during the later stages [e.g. Hartmann, 1998, André et al., 1999, Andre et al., 2000]. Evidence of already visible stars continuing infall, whose accretion rate is several orders of magnitude smaller than those at the main accretion phase, shows fiducial values in the order of 10^{-7} or $10^{-8}\ \mathrm{M}_{\odot}\mathrm{yr}^{-1}$ [e.g. Hartmann, 1998]. Because the accretion timescale t_{ff} is much smaller than the thermal timescale t_{KH}, the core heats up practically adiabatically. The thermal timescale is defined by the Kelvin-Helmholtz time [e.g. Kippenhahn et al., 2012]

$$t_{\mathrm{KH}} = \frac{G M_{\star}^2}{2 R_{\star} L_{\star}}. \tag{2.14}$$

Accretion onto the star is not a spherical process. Even a slowly rotating prestellar cloud

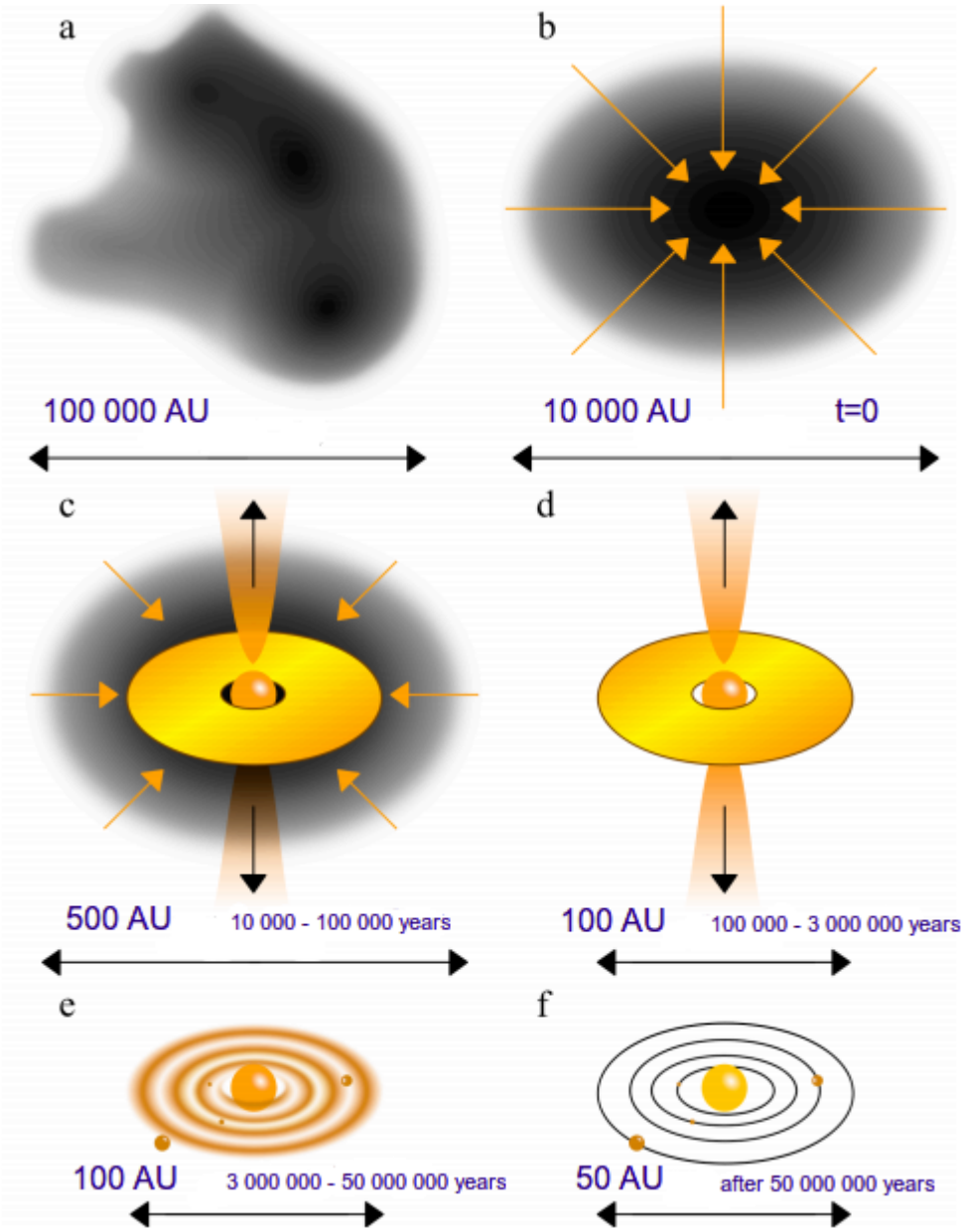

Figure 2.2: Schematic view of the stages of star formation. In the lower part of each panel the referential spatial and time scales of each stage are indicated. a) Density inhomogeneities in a molecular cloud fragment and gravitationally collapse to smaller clumps and cores. b) Each core becomes unstable and self-gravitationally collapses into a protostar. c) A protostar and disk form from the collapsing envelope when centrifugal forces balance gravitational forces, causing also winds or jets. d) The envelope settles into an accreting disk and is dispersed by winds and outflows. The protostar becomes visible at optical wavelengths with associated outflows and a protoplanetary disk. e) The protoplanetary disk goes through a transitional phase with the formation of dust-free gaps due to planet formation. During this pre-main sequence phase accretion and contraction still may occur. f) A planetary system is finally formed and the star joins the main sequence when nuclear fusion in its core begins. [Credit: adapted from Shu et al. [1987], Greene [2001], Braiding [2011]]

has a significant amount of angular momentum for the mass to fall directly into the core, and some of the material will form a circumstellar disk [e.g. Hartmann, 1998, Bate, 2000]. At this accretion stage, as the dynamically-infalling gas collides with the protostar also jet-like bipolar outflows are expected (Fig. 2.2,c)). The outflows eventually disperses the infalling envelope, and their early presence during the first 10^4 years of evolution, when a protostar is still heavily obscured, is the first sign that an accreting protostar has formed [e.g. Reipurth, 1991, Fukui et al., 1993]. The energy source of these outflows is believed to be the gravitational energy of the accreted matter, and their collimation is caused by a helical magnetic field coupled to the inner part of the circumstellar disk or to the central protostar [e.g. Konigl and Pudritz, 2000, Shu et al., 2000, Tomisaka, 2002].

Once the temperature of the core reaches a temperature of about 2000 K, the average particle energy is comparable to the dissociation energy of molecular hydrogen. Therefore, the core experiences another dynamical instability, a second collapse occurs, in which the released gravitational energy is absorbed by the dissociating molecules without a significant rise in temperature. The core comes back to hydrostatic equilibrium and temperature rises again when molecular hydrogen is completely dissociated into atomic hydrogen. Later, when the newly formed star comes out from the dynamical collapse, it makes its first visible appearance after emerging from their birth clouds. In the Hertzsprung-Russell diagram of star evolution, the star appears along a locus of nearly constant radius, denominated by Stahler [1983] as the 'birthline'. From this moment on the young stellar object enters the pre-main sequence (PMS) and evolves along the Hayashi evolutionary tracks for a determined mass [Hayashi et al., 1962].

The Hayashi track (Fig. 2.3) is a luminosity-temperature dependence with a practically vertical line for fully convective stars with masses less than 3 $\mathrm{M}_\odot$, it means with a constant effective temperature $T_{\rm eff}$. The region to the right of the Hayashi line in the H-R diagram – at lower $T_{\rm eff}$ – is a forbidden region for stars in hydrostatic equilibrium. On the contrary, stars to the left of the Hayashi line – at higher $T_{\rm eff}$ – cannot be fully convective, but most have some portion of their interior in radiative equilibrium[5]. During the PMS phase the star is still cool for nuclear burning, and its energy source for its luminosity is gravitational contraction. Based on the virial theorem, this causes an increase of its internal temperature. After that, the luminosity of the star decreases as long as the opacity remains high and the young object is fully convective. An approximated track for this evolution is given by the expression

$$\log L_\star = 10 \log M_\star - 7.24 \log T_{\rm eff} + C. \tag{2.15}$$

The evolutionary track steeply descends, and shifts upward with increasing initial mass. The point of minimum luminosity of the track corresponds to the moment a radiative core develops, containing more and more of the stellar mass. Due to the shrinking star, the effective temperature continues increasing and evolves left from the Hayashi line. When the central temperature is sufficiently high to ignite nuclear fusion, the star stops contracting and settles on the zero age main sequence (ZAMS). The time it takes a PMS star to do so is given by the Kelvin-Helmholtz contraction of Eq. 2.14. The smaller $R_\star$ and $L_\star$, the longer this time is. In conclusion, massive protostars reach the ZAMS much earlier than the lower-mass. For stars with $M_\star > 1\ \mathrm{M}_\odot$, this time is approximately

[5]Convection and radiative transfer are mechanisms of transport of heat in the interior of stars determined by the opacity of the region. The stability against convection is given by the Schwarzschild criterion, according to which low-mass stars, like the Sun, have convective envelopes. In contrast, higher-mass stars have radiative envelopes and convective cores. The details that involve stellar physics and convection are a big field of astronomy and are not reviewed in this investigation.

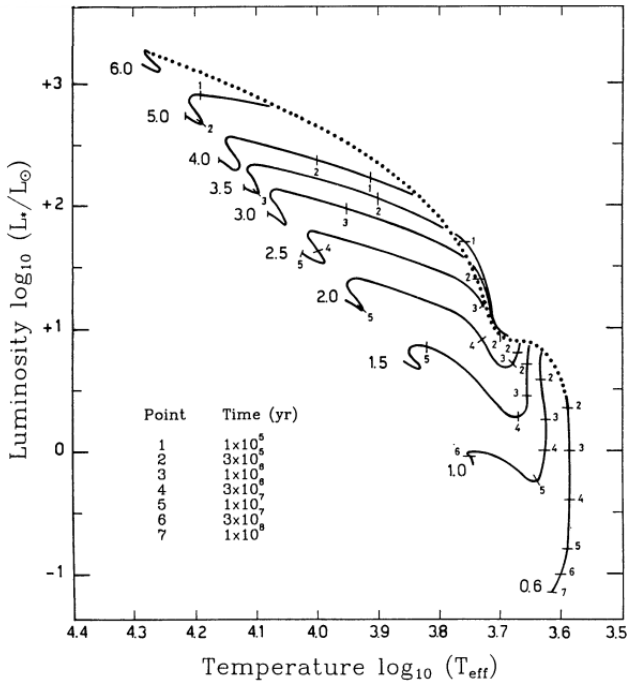

Figure 2.3: Evolutionary tracks, also known as Hayashi tracks, in the Hertzsprung-Russell diagram computed for stellar masses up to $6\,\mathrm{M}_\odot$. The Hayashi line is the vertical locus with near-constant temperature more evident for lower masses. The corresponding mass in solar units is labelled for each track and the tick marks indicate evolutionary times. The dotted curve from which the tracks start is the 'birthline', and their left extreme enters the ZAMS. [Credit: Palla and Stahler [1993]. Reproduced with permission ©AAS.]

$$t_{\mathrm{KH}} \approx 5 \times 10^7 \left(\frac{M_\star}{\mathrm{M}_\odot}\right)^{-2.5} \text{years.}$$

As seen from Fig. 2.3, stars with masses $\gtrsim 5\,\mathrm{M}_\odot$ become stable against convection very quickly, and spend shorter time moving horizontally on their Hayashi tracks. This trajectory is called also the Henyey track of fully radiative stars. Contrarily, stars with masses circa $0.5\,\mathrm{M}_\odot$ do not become stable against convection, and evolve vertically onto the ZAMS as fully convective stars.

2.1.3 Young stellar objects

The evolutionary stage and primordial properties (e.g. luminosity, temperature, level of embeddedness in circumstellar material) of newborn stars is derived using unresolved information from the spectral energy distribution (SED), which measures the distribution of flux as function of frequency or wavelength. Young stellar objects (YSOs) are conventionally classified based on the slope of the SED according to the parameter

$$\alpha_{\mathrm{IR}} = \frac{\Delta \log(\lambda F_\lambda)}{\Delta \log \lambda} \tag{2.16}$$

with typical measurements that span a wavelength range between the near-IR and the mid-IR (often 5 μm or 25 μm). Based on the magnitude of α_{IR} [e.g. Andre et al., 1993, Andre and Montmerle, 1994] the classification consists of four groups of objects (Fig. 2.4):

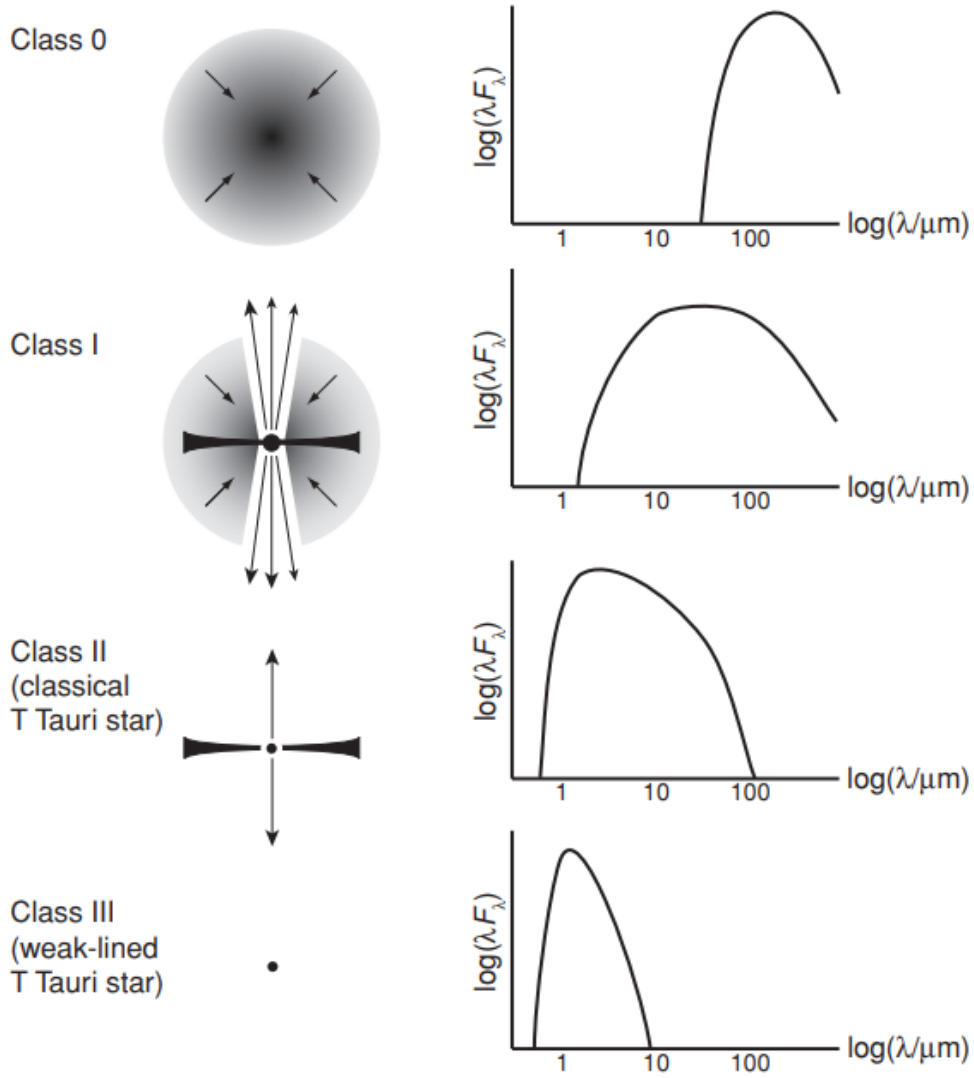

Figure 2.4: Classification scheme for young stellar objects according to the magnitude of the parameter $\alpha_{\rm IR}$. [Credit: Armitage [2010]]

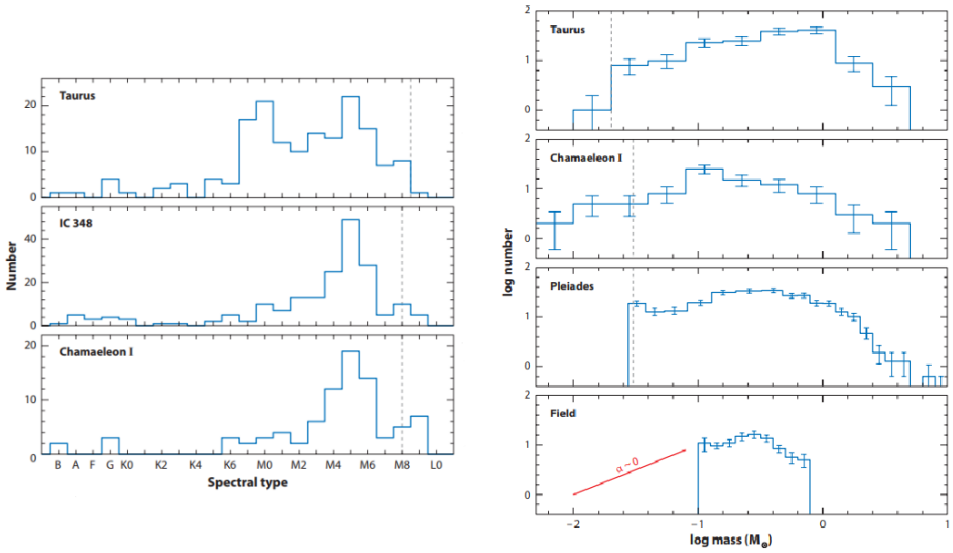

Figure 2.5: Statistical analysis of stellar distributions in different star forming clusters. *Left*: Distribution of spectral types for samples of Taurus, IC348 and Chamaeleon I, showing that the majority of members are of solar-mass ranges or less (peak at M5). *Right*: Initial mass functions for Taurus, Chamaeleon I, the Pleiades, and the field, supporting also the larger population of low-mass stars. The dashed lines in both panels show the level of completeness of the studies. [Credit: Luhman [2012] and references therein]

- Class 0: ($\alpha_{\rm IR}$ undetectable in the near-IR) Objects just after collapse that are characterized by a deeply embedded central core in a large accreting envelope. The flux peaks in the far-IR or mm regime.
- Class I: ($\alpha_{\rm IR} \geq -0.3$) Objects with a flat or rising SED between near- and mid-IR ranges. Sources with $\alpha_{\rm IR} \simeq 0$ are usually refereed as "flat-spectrum" and true "class I" are sources with $\alpha_{\rm IR} > 0.3$.
- Class II: ($-1.6 \leq \alpha_{\rm IR} < -0.3$) Objects with most of the circumstellar material found in a disk of gas and dust, thus the SED falls noticeably between near- and mid-IR wavelengths.
- Class III: ($\alpha_{\rm IR} < -1.6$) Objects with almost pure stellar photosphere and little contribution from the disk.

However, it is necessary to emphasize that YSOs seen edge-on can be misinterpreted under this classification due to high obscuration caused by their surrounding material.

The process of star formation after the fragmentation and gravitational collapse into smaller cores leads to the formation of stars with a wide range of masses. This distribution of stellar masses that form in one star formation event in a given volume of space is called the initial mass function (IMF). The study of the IMF is important not only to answer questions of how molecular clouds fragment into stars, but also to understand the evolution of the Galaxy dictated by the relative initial numbers of brown dwarfs ($< 0.08\,{\rm M}_\odot$) that do not fuse hydrogen to helium, very-low mass stars (0.08 to $0.5\,{\rm M}_\odot$), low-mass stars (0.5 to $2\,{\rm M}_\odot$), intermediate-mass stars (2 to $8\,{\rm M}_\odot$), and massive stars ($>8\,{\rm M}_\odot$). On the one hand, since several decades it has been thought that the star formation process is a bimodal process [e.g. Larson, 1986], leading to the formation of high-mass stars (OB associations) or low-mass stars (T associations), but rarely forming the same amount of them in the same place and

at the same time because these groups form by different physical mechanisms [e.g. Shu and Lizano, 1988]. On the other hand, estimates for different stellar populations – from small and dense to giant and metal-poor molecular clouds – have revealed that the IMF is rather universal [e.g. Kroupa, 2002]. Reliable constancy or variations between the IMF of different populations requires uniformity in the application of evolutionary models, spectral classification, temperature scale and completeness to avoid effects of mass segregation [e.g. Luhman, 2012].

Nevertheless, the fact that the majority of young objects in the Ophiuchus, Taurus-Auriga and Chamaeleon I star-forming regions are solar-mass stars surrounded by thick circumstellar disks seems well established [e.g. Furlan et al., 2009], as depicted also by the initial mass functions for different clusters in Fig. 2.5. Especially the Taurus-Auriga dark cloud complex, with a distribution of ages between 1 and several Myr [e.g. Kenyon and Hartmann, 1995, Hartmann, 2001, Luhman et al., 2003], exhibits a surplus of PMS solar-mass stars and only a handful of more massive A and B stars relative to the mass functions of clusters like the Orion Nebular Cluster, IC348 and Chamaeleon I [e.g. Luhman, 2000, Mooley et al., 2013, Luhman et al., 2017]. Indeed, for the slightly more than 400 members identified in Taurus to date (Fig. 2.1), the distribution of spectral types peaks alike the clusters IC348 and Chamaeleon I at M5, but this star forming region also has an additional surplus of K7–M1 stars with masses $\lesssim$1 $M_\odot$ (Fig. 2.5).

Considering the classification of YSOs according to the shape of their SED, and the broad range of stellar masses that can be found in star forming regions, constraining the properties of two subgroups of PMS objects is of especial relevance for our understanding of the planet formation phenomenon:

1. **T Tauri stars (TTS):** This group of objects was first characterized by Joy [1945]. They posses low stellar masses ($<$2 $M_\odot$) and circumstellar disks in their surroundings. Their spectral classification corresponds to spectral types later than F (most of the young stellar population). When the circumstellar disk is still in an accretion phase onto the star and causes an excess at infrared wavelengths (Class II objects), which decreases over time as the disk material is dissipated, the objects are referred to as classical T Tauri stars (CTTSs). At later stages, when the disk has stopped accreting and thus has little or no circumstellar material left, the object is known as weak-lined T Tauri stars (WTTSs)[6].

2. **Herbig Ae/Be stars (HAeBe):** These intermediate-mass counterparts have masses between 2 and 10 $M_\odot$. This group was first defined by Herbig [1960] (and therefore named after him) as objects of spectral type A and B located in an obscured region that present emission lines of hydrogen in their spectra and are associated with nebulosity in its immediate region. Later definitions of this group [e.g. van den Ancker et al., 1998, Waters and Waelkens, 1998] included stars of spectral type F to close the gap between the upper limits of TTS. Similarly to TTS, HAeBe also present infrared excess in their SED due to circumstellar material and spectral signatures of accretion activity. As stated previously, this group has radiative interiors and evolve more rapidly than TTS. PMS objects with intermediate masses are referred to as UX Ori when they show strong photometric and polarimetric variability due to fluctuating extinction by circumstellar dust [e.g. Natta et al., 1997].

[6]The accretion activity that determines whether the object is CTTS or WTTS is defined by the equivalent width of the hydrogen emission line Hα, being respectively either $>$10 Å or $<$10 Å for each group.

2.2 Byproducts of star formation

The amount of angular momentum in a typical star-forming cloud core is several orders of magnitude larger than the one contained in a single star. For instance, the angular momentum of a $\sim$0.1 pc small core is in the order of $\sim 10^{54}\mathrm{g\ cm^2\ s^{-1}}$ in comparison to magnitudes of $\sim 10^{48} - 10^{50}\mathrm{g\ cm^2\ s^{-1}}$ in Solar System scales. This significant difference and its dispersion is known as the 'angular momentum problem' of star formation. Over the last decades this problem has been explained in terms of magnetic braking and decoupling by ambipolar diffusion during the early low-density phases of cloud evolution, but it solves the excess only partially [e.g. Bodenheimer, 1995, Mouschovias and Ciolek, 1999, Myers et al., 2000, Belloche et al., 2002].

In addition, there are two ways to dispose of the excess of angular momentum:

1. much of the initial angular momentum could go into the orbital motions of the stars in a binary or multiple system, or

2. it could be transported to outlying diffuse material, for example by viscous transport processes in a protostellar accretion disk, thus allowing most of the mass to be accreted by a central star.

2.2.1 Stellar multiplicity

The first way treated in this section, indeed, states that binary formation takes place during the fragmentation of a prestellar core, either before – prompt core fragmentation – or shortly after the free-fall collapse phase. Fragmentation could lead to binary systems on two distinct spatial scales, a wide one during the initial collapse when the cloud becomes Jeans unstable, and a narrower occurring after the dissociation of molecular hydrogen [Bonnell and Bate, 1994]. The characteristics and conditions of fragmentation are set by the balance of pressure and forces in the collapsing core, including rotation and turbulence that generally enable the formation of multiple seeds in the core. The role of magnetic fields and radiative feedback are supposed to be more inhibitive [e.g. Offner et al., 2009, Commerçon et al., 2010], although it has been also suggested that these factors can significantly alter the collapse [e.g. Bate, 2012, Myers et al., 2013]. The gravitational instability of a massive circumstellar disk can also give birth to a binary system on the scale of the disk radius [e.g. Bonnell, 1994]. Moreover, some of the most detailed and realistic numerical simulations show that the formation of a binary or a multiple system is more likely to occur if collapse begins with initial configurations far from being axisymmetric, for example if the initial configuration is filamentary, or if a collapsing core is perturbed by interactions with other cloud cores in a forming group or cluster [e.g. Bodenheimer et al., 2000, Bate et al., 2002a,b, 2003].

It seems that most of stars form in stellar associations and clusters, and that the formation of single stars occurs only in special cases [e.g. Lada and Lada, 2003, Bressert et al., 2010], with a large dispersion in the properties of binary or multiple systems. The broad dispersion and no preferred values for parameters such as separation and eccentricity suggests that the formation process is very dynamic and chaotic [Larson, 2001]. Nevertheless, some estimations are known based on different surveys of given stellar populations.

A quantification for different evolutionary stages and/or in different regions can be determined through the fraction of multiple systems in a population – the multiplicity frequency – of the form

$$MF = 1 - f_1 = f_2 + f_3 + f_4 + ... \tag{2.17}$$

where f_n is the fraction of systems containing n stars [Batten, 1973]. This value is also expressed as

$$MF = \frac{B + T + Q}{S + B + T + Q} \tag{2.18}$$

where S, B, T, Q are the number of single, binary, triple, and quadruple systems [Reipurth and Zinnecker, 1993]. In the same manner, another common comparative value is given by the companion frequency[7]

$$CF = f_2 + 2f_3 + 3f_4 + ... \tag{2.19}$$

which gives the average number of stellar companions per target and can be greater than 100%

$$CF = \frac{B + 2T + 3Q}{S + B + T + Q}. \tag{2.20}$$

With these two magnitudes some of the most complete and less biased surveys have determined that solar-type main sequence (MS) stars have $CF^{\rm MS}_{0.7-1.3{\rm M}_\odot} = 62 \pm 3\%$ and $MF^{\rm MS}_{0.7-1.3{\rm M}_\odot} = 44 \pm 2\%$, meaning that a slightly majority of them are actually single, just as the Sun [Raghavan et al., 2010]. For low-mass stars these quantities have been established as $CF^{\rm MS}_{0.1-0.5{\rm M}_\odot} = 33 \pm 5\%$ and $MF^{\rm MS}_{0.1-0.5{\rm M}_\odot} = 26 \pm 3\%$ [Fischer and Marcy, 1992]. On the other hand, for high-mass populations an interpolation between spectroscopic and visual stars has suggested values of $CF_{M_\star \gtrsim 16{\rm M}_\odot} \approx 130 \pm 20\%$ and $CF_{8-16{\rm M}_\odot} \approx 100 \pm 20\%$.

Concerning the multiplicity of PMS objects, surveys targeting T associations like the star forming regions Taurus-Auriga or Chamaeleon have determined companion frequencies of around twice the value of solar-type MS stars [Duchêne, 1999]. Namely, one of the largest studies to date of Taurus by Kraus et al. [2011] measures values of $CF^{\rm Class\,II/III}_{0.7-2.5{\rm M}_\odot} = 64^{+11}_{-9}\%$ and $CF^{\rm Class\,II/III}_{0.25-0.7{\rm M}_\odot} = 79^{+12}_{-11}\%$ over a separation range of 3–5000 AU. Similarly, for HAeBe stars Bouvier and Corporon [2001] have suggested a binary fraction of roughly 60%, with a possible binary frequency higher for the more massive Herbig Be stars than for the Herbig Ae stars [Baines et al., 2006]. Studies of PMS binary systems show that they do not only have a higher companion frequency, but also appear much more coeval than random pairs within a given star-forming region, strongly suggesting that they do indeed form simultaneously from a common core [e.g. Kraus and Hillenbrand, 2009, Baraffe and Chabrier, 2010].

Surveys with different techniques and sensitivity addressing the characterization of multiplicity at different mass ranges [e.g. Allen, 2007, Raghavan et al., 2010, Kraus and Hillenbrand, 2012, Chini et al., 2012, De Rosa et al., 2014] have concluded that binarity is a strongly decreasing function with decreasing stellar mass. The left panel of Fig. 2.6 shows the frequency of visual companions for separations ranging from few tens to a couple of thousands AU among a variety of stellar populations as a function of their age and stellar mass. One can notice that the PMS HAeBe stars have statistically a companion frequency similar to the one of non-disk-bearing intermediate-mass stars in the Scorpius–Centaurus OB association, but higher than that of intermediate-mass field stars. HAeBe objects show also a higher companion frequency than lower-mass stars in the regions Taurus-Auriga, Chameleon and Upper Scorpius, whose main components are TTS. The mass-multiplicity dependence is also seen from the right panel of Fig. 2.6. The dependency of companion frequency (CF) and multiplicity frequency (MF) with primary mass for MS stars and very-low-mass (VLM) objects traces a steep function of stellar mass.

Also separations over an enormous range can be deduced for binaries, from contact binaries to tenuously bound ultrawide binaries and proper motions with separations up to a

[7]The frequency of companions CF refers to the average number of companions per target. For example, if all the sources were single, the CF would be 0, and if all the sources were binary stars, the CF would be 100%.

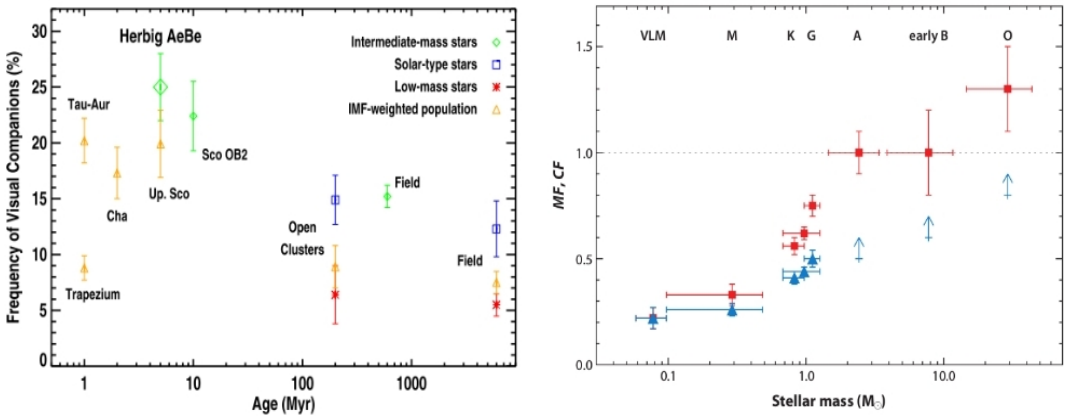

Figure 2.6: *Left*: Frequency of visual companions per decade of separation as a function of stellar mass and age. The plot covers separations wider than ∼10 AU, over a 1- to 2-decade-wide separation range depending on the sensitivity of existing surveys. *Right*: CF (red symbols) and MF (blue symbols) with primary mass for main-sequence and very-low-mass objects showing a steep mass-multiplicity dependence. [Credit: Duchêne and Kraus [2013], Duchêne [2015] and references therein]

parsec. The separation distribution of binaries provides information about the mechanisms of formation and the dynamical evolution. For convenience, the projected separations are commonly used in the literature. This distribution is determined as linear combinations of log-normal and power-law functions [Duchêne and Kraus, 2013]. In regions of massive star formation, such as the Orion Nebula Cluster, wide binaries are lacking [e.g. Reipurth et al., 2007]. Solar-type binaries show a distribution peaking at ∼30–50 AU [Duquennoy and Mayor, 1991, Raghavan et al., 2010]. Among less densely populated low-mass star-forming regions such as Taurus, the study of stars with a mass range between 0.7 and 2.5 $M_\odot$ has a log-flat distribution over a wide separation range of 3–5000 AU [Kraus et al., 2011]. For VLM objects, it has been found that young stars and brown dwarfs with masses between 0.02 and 0.5 $M_\odot$ have a mean separation and separation range of binaries that smoothly declines with mass [Kraus and Hillenbrand, 2012]. On the other hand, the intermediate-mas PMS stars have a companion frequency with short periods just as the one for field star, and an excess for wide and visual binaries. Separations proved with interferometry – between ∼1 and 100 AU – reveal a deficit of these objects, possibly because of interferometric sensitivity or the lack of them in comparison to field stars [Duchêne, 2015]. A graphic summary of these statistics is shown in Fig. 2.7.

Another key parameter in the characterization of the properties of binary systems is the mass ratio between components

$$q = \frac{M_2}{M_1}. \tag{2.21}$$

As observed in young stars, the mass ratio is defined during the protobinary accretion phase, having the later circumbinary disk accretion phase only a limited effect on it. Estimates of this parameter in YSOs is especially biased since they are based on individual photometry with significant caveats coming from accretion luminosity, distinct extintion of the components, and high-luminosity contrasts between the stars. The mass ratio distribution can be fitted with a declining function for rising mass ratios of the form

$$f(q) \sim q^{-n} \tag{2.22}$$

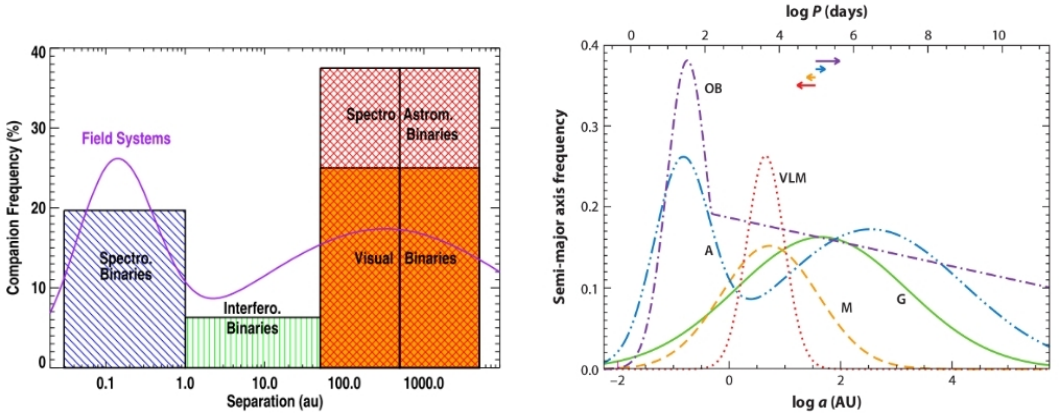

Figure 2.7: *Left*: Distribution of separation for multiple HAeBe systems. The companion frequency is expressed in terms of decade of separation, as in Fig. 2.6. The purple curve, also plotted on the right panel, is a distribution built for field A-type stars. The separation technique that proved each separation range is also indicated. *Right*: Using the notation of Fig. 2.6, the orbital period distribution of each stellar population is traced. [Credit: Duchêne and Kraus [2013], Duchêne [2015] and references therein]

being $n = 0.33$ determined for young intermediate-mass stars in the Scorpius OB2 association [Kouwenhoven et al., 2005]. In contrast, low-mass YSOs have a rising distribution for rising mass ratios, which becomes increasingly steep for VLM objects, showing tendency for $q \sim 1$ binaries [Kraus et al., 2011, 2012]. At the intermediate-mass range, HAeBe objects with $q \lesssim 0.1$ are challenged to characterize because of the large contrast ratios and circumstellar material associated to each component [Duchêne, 2015].

2.2.2 Circumstellar disks

As previously mentioned, disks form because angular momentum during protostellar collapse is conserved, and the rotational velocities of molecular cores imply that young stars should be surrounded by centrifugally supported disks with extensions of tens to hundreds of AUs. The terminology defining circumstellar disks is a matter of discussion [e.g. Evans et al., 2009], although depending of the stages of evolution the following definitions are used:

- **protoplanetary disks** are primordial disks containing the reservoir enough to form planets
- **transition disks** are more evolved disks, in the stage between protoplanetary and debris disks, usually harbouring gas- or dust-depleted cavities, signatures of possible planet formation
- **debris disks** are disks with little or no gas, whose dusty material has overcome some reprocessing and collisions

This research focuses mainly on the two first phases, which enable the physical understanding of how disks evolve and impact the formation and evolution of plnaetary systems.

In addition to be the sites of planet formation, circumstellar disks contain the material reservoir from which newborn stars accrete their mass (also recalled in subsection 2.1.2). Indeed, the accreting mass in the disk must be transported inward to be accreted by the star, meaning that its angular momentum must somehow be removed or transported outward through the disk. The outward transport of angular momentum occurs if the disk is viscous

or if some mechanism creates an effective viscosity in the disk. Long decades of working on understanding the problem have not brought to clear conclusions. Some mechanisms such as hydrodynamic, gravitational, or magnetic forces [e.g. Quataert and Chiang, 2000, Stone et al., 2000], weak gravitational instabilities in a marginally stable disk [e.g. Stone et al., 2000, Gammie, 2001], or magnetorotational instability of magnetized disks [e.g. Balbus and Hawley, 1998, Stone et al., 2000], can each play a role in some regions of the disk or given circumstances, and at different scales. Even 'external' effects such as the tidal effect of a companion star or the formation of a massive planet can generate spiral disturbances and tidal waves in a circumstellar disk capable of transporting angular momentum and driving an inflow [e.g. Blondin, 2000, Boffin, 2001, Bate et al., 2002c].

As seen from Fig. 2.4, the circumstellar structure becomes optically visible during the PMS phase, making Class II T Tauri and Herbig objects an ideal scenario to study the disks by which they are surrounded. These protoplanetary disks are detected or observed through a number of complementary techniques [Armitage, 2010], including:

- Detection of near- or mid-IR excess over the stellar photospheric flux that indicates the presence of warm dust close to the star on the order of an AU or closer.
- Detection of accretion an outflow signatures indicating that gas is accreted onto the star or winds are outflowing from it. The observational indicators include ultraviolet excess, hydrogen lines (e.g. Hα, Hβ) in emission with a large equivalent width, and several other emission lines in the infrared (e.g. the Ca II triplet, Br γ, Pa γ, He I).
- Observation of mm or sub-mm flux arising from cool dust in the outer disk.
- Imaging of the disk in scattered visible light from the central star, or in silhouette against a bright background nebula.
- Detection of line emission from molecular species such as CO or NH_3, either as an unresolved source or as a spatially resolved image.

2.2.2.1 Physical parameters of circumstellar disks

Missions such as the Infrared Space Observatory (ISO)[8], Spitzer[9] or Herschel[10] have successfully discovered and characterized protoplanetary disks through the infrared and (sub)millimetre thermal dust emission presented as an excess to the radiation of stellar photospheres in their SED, allowing us to discriminate some of their physical properties here recalled.

Disk opacity

A canonical assumption indicates a gas-to-dust mass ratio close to 100. However, dust is the dominant opacity source of protoplanetary disks beyond the innermost regions of the disk, where the high temperatures ($T \sim 1500$ K) destroy dust silicate grains and leave only

[8]ISO was a space telescope covering wavelengths between 2.5 and 240 μm operated by a consortium between the European Space Agency (ESA), ISAS and National Aeronautics and Space Administration (NASA). Website: `irsa.ipac.caltech.edu/applications/ISO/`

[9]The Spitzer Space Telescope is an infrared telescope operating between 3 and 180 μm launched in 2003 as part of NASA's Great Observatories program. Website: `irsa.ipac.caltech.edu/Missions/spitzer.html`

[10]ESA's Herschel Space Observatory was the largest infrared telescope ever launched that actively operated between 2009 and 2013. It was sensitive to far-IR and submillimetre wavebands (55-672 μm). Website: `sci.esa.int/herschel/`

molecular opacity. At a given location within the disk, the total opacity due to the dust depends mainly on the temperature, chemical composition and geometry of the dust particles. As a beam of light of intensity I_λ travels through the conglomerate, some of the photon will be removed via scattering off and absorption. Then, one can write

$$\mathrm{d}I_\lambda = -\kappa_\lambda \rho I_\lambda \mathrm{d}s \tag{2.23}$$

where $\mathrm{d}s$ is the distance travelled, ρ is the density of the medium and κ_λ is the absorption coefficient, or opacity, expressed in [cm^2 g^{-1}]. The integral of the dust opacity times the density is known as the optical depth τ_λ

$$\tau_\lambda = \int_0^s \rho \kappa_\lambda \mathrm{d}s = \kappa_\lambda \Sigma \tag{2.24}$$

where Σ is the projected surface density of the disk. Since the units of the surface density are given in [g cm^{-2}], τ_λ is a unitless magnitude. By integrating Eq. 2.23 with the definition of Eq. 2.24, one obtains

$$I_\lambda = I_{\lambda,0} e^{-\tau_\lambda} \tag{2.25}$$

where $I_{\lambda,0}$ is the intensity as a function of wavelength measured in the absence of absorption and scattering. Environments with $\tau_\lambda \gg 1$ are said to be optically thick, whereas $\tau_\lambda \ll 1$ are referred to as optically thin. The calculation of opacities, which depend on the chemical composition, pressure and temperature of the gas, as well as the wavelength of the incident light, can be simplified by using a mean opacity averaged over all wavelengths. The most commonly used opacity is the Rosseland mean defined as

$$\frac{1}{\kappa_\mathrm{R}} = \frac{\int_0^\infty \frac{1}{\kappa_\lambda} \frac{\partial B_\lambda(T)}{\partial T} \mathrm{d}\lambda}{\int_0^\infty \frac{\partial B_\lambda(T)}{\partial T} \mathrm{d}\lambda} \tag{2.26}$$

where B_λ is the Planck function. Fig. 2.8 shows the temperature dependence of the Rosseland mean opacity for dusty gas with density scales as $10^{-19} \times T^3 \mathrm{g\ cm^{-3}}$ calculated by Semenov et al. [2003] and compared to other works therein. The plot shows that at temperatures $\lesssim$150 K, or snowline zone, the opacity is dominated as T^2 by water ice and volatile organic materials. On the other hand, after a flat pattern shown until the destruction temperature for silicates (1500 K), the opacity decays by some two orders of magnitude.

Disk mass

Whereas the dust of circumstellar disks dominates the opacity, the thermal and geometrical structure, and their emission properties, the gas dominates the mass and the dynamics of the disk. Although the inner 10 AU constitute a substantial fraction of the planet-forming region of the disk, protoplanetary disks are generally much larger than this. The total disk mass is better determined from (sub)millimetre observations of the flux F_λ up to the thin outer regions of the disk, according to the expression

$$M_\mathrm{d} = \frac{F_\lambda d^2}{\kappa_\lambda B_\lambda(T)} \tag{2.27}$$

where d is the distance to the object. The disk mass is fundamental in the context of planet formation. Therefore, the distribution of disk masses, $f(M_\mathrm{d})$, is a key characteristic in determining the demographic properties of exoplanets [e.g. Alibert et al., 2005, Mordasini et al., 2009].

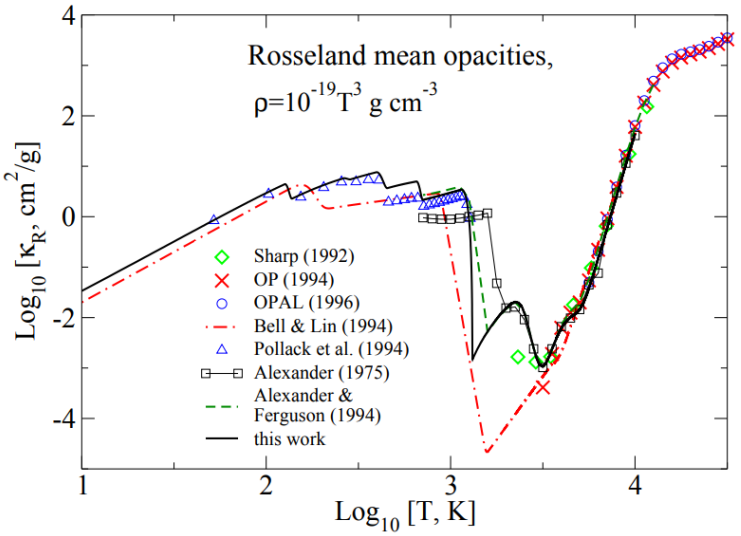

Figure 2.8: Rosseland mean opacity determined for a dusty gas with density scales as $10^{-19} \times T^3 \mathrm{g\ cm^{-3}}$. This opacity is calculated by Semenov et al. [2003] and compared to other works. [Credit: Semenov et al. [2003] and references therein. Reproduced with permission ©ESO.]

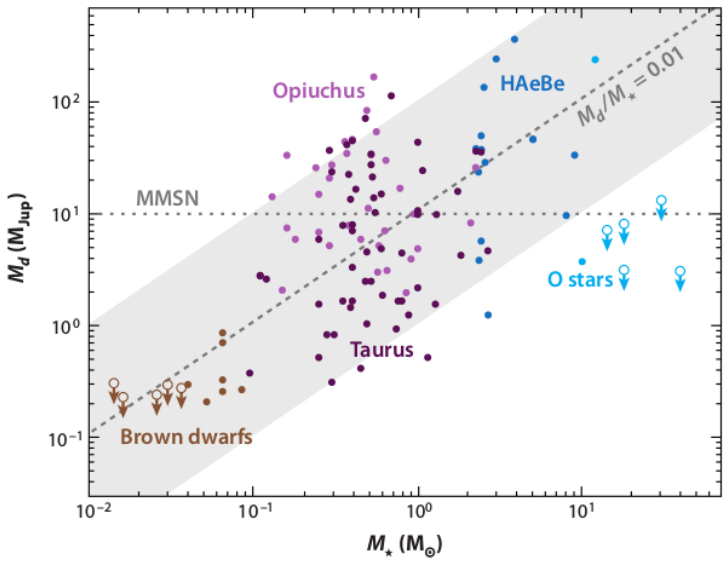

Figure 2.9: Dependence of protoplanetary disk mass on the mass of the central star as determined for different populations. The dashed diagonal line traces a mass ratio of 1%, close to the median value of the detections. O stars lay out of the range due to the non-detection of disks at (sub)millimetre wavelengths, indicating a probably short disk lifetime. [Credit: Williams and Cieza [2011] and references therein]

Submillimetre surveys have shown that the median mass of disks around Class II YSOs is $5\,\mathrm{M_{Jup}}$ (or $5\times10^{-3}\,\mathrm{M_\odot}$), and the average disk-to-star mass ratio is 0.2–0.6% in the star-forming regions Taururs-Auriga and ρ Ophiuchi [Andrews and Williams, 2005, 2007a,b, Andrews et al., 2013]. The results obtained using Eq. 2.27 have been demonstrated to be in agreement with observations of CO (with a characteristic temperature of $T = 20$ K). Fig. 2.9 shows (sub)millimetre measurements of Class II YSOs disks for different stellar populations available in the literature. Although for low-mass and intermediate-mass stars their disks remain well within the found $M_\mathrm{d}/M_\star$ values, the relationship for most massive stars break down, possibly due to very high photoevaporation rates so that disks are not detectable by the time O stars become visible [Zinnecker and Yorke, 2007].

Disk size or radius

The disk radii are difficult to determine due to the vanishing emission at their cold and low-density outer edges. Moreover, imaging disks at millimetre regimes demands high-resolution observations with (sub)millimetre interferometers on account of the small angular scales in even the closest star-forming regions. Such studies have confirmed that circumstellar dust disks are geometrically thin with radii between 10 and thousands of AU, but with a typical value of 100 AU [e.g. Dutrey et al., 1996, Kitamura et al., 2002]. The largest gaseous molecular components of disks are H_2 and CO. However, since H_2 is a homonuclear molecule without allowed electric dipole transitions it is more convenient to use the polar asymmetric carbon monoxide molecule (CO) as a tracer of their masses and sizes. The rotational lines of CO have shown that the gas portion in disks significantly exceed the extension of the dust continuum [e.g. Isella et al., 2007].

Radial surface density distribution

The study of the vertical structure of a circumstellar disk is simplified by assuming that the disk is isothermal (a vertical temperature profile $T(z) = \mathrm{const.}$) and thin (the height above the midplane z is much smaller than the radial distance r to the star). Therefore the vertical component of the stellar gravity is in balance with the vertical pressure gradient

$$c_\mathrm{s}^2 \frac{\mathrm{d}\rho}{\mathrm{d}z} = -\rho z \frac{GM_\star}{r^3} \tag{2.28}$$

where c_s is the isothermal sound speed, G the gravity constant, ρ the disk density, and $M_\star$ the mass of the central star. Then, by integration of this formula, it is obtained a Gaussian density profile of the form

$$\rho = \rho_0 \exp\left(-\frac{z^2}{2h_\mathrm{p}^2}\right) \tag{2.29}$$

where the midplane density is denoted as ρ_0, and the pressure scale height is h_p. The vertically integrated column density, or surface density, provides a measure of the radial evolution of the disk. Namely,

$$\Sigma_r = \int_{-\infty}^{\infty} \rho(r, z)\mathrm{d}z. \tag{2.30}$$

This expression is generally used to investigate the dust radial distribution of circumstellar disks from two different approaches [e.g. Isella et al., 2010, Pinilla et al., 2018]. First, a more complex one in which viscous accretion disks are used [e.g. Lynden-Bell and Pringle,

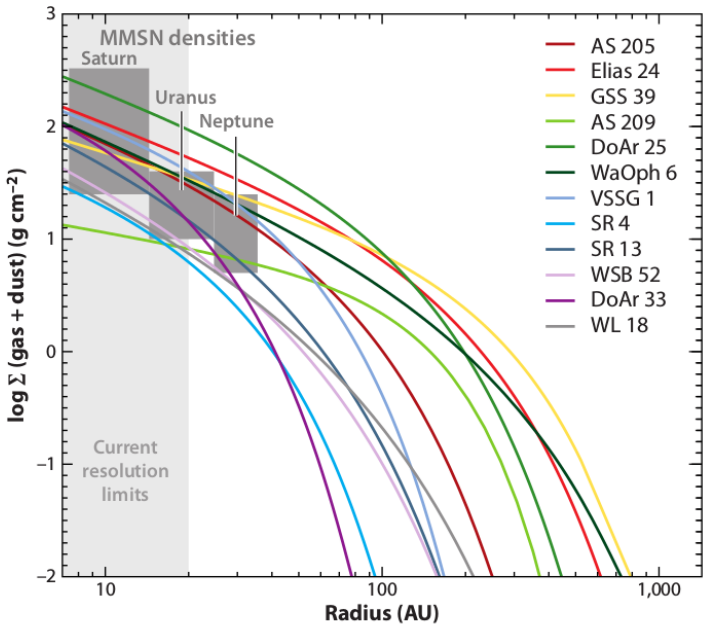

Figure 2.10: Radial surface density for a sample of Class II YSOs in Ophiuchus as observed at 880 μm and infrared wavelengths. The rectangular regions denote the surface densities determined for Saturn, Uranus, and Neptun in the MMSN. [Credit: Williams and Cieza [2011] and references therein]

1974, Hartmann, 1998, Williams and McPartland, 2016], and whose solution is given by

$$\Sigma_r = (2-\gamma)\frac{M_\mathrm{d}}{2\pi R_c^2}\left(\frac{r}{R_c}\right)^{-\gamma}\exp\left[-\left(\frac{r}{R_c}\right)^{2-\gamma}\right] \tag{2.31}$$

where M_d is the disk mass, R_c is a characteristic radius, and γ specifies the radial dependence of the viscosity. And second, a more simplistic one consisting of a classical power-law parametrization

$$\Sigma_r = \Sigma_{R_c}\left(\frac{r}{R_c}\right)^{-p}, \quad \text{for } R_\mathrm{in} < r < R_\mathrm{out} \tag{2.32}$$

where R_in and R_out are the inner and outer disk radii, respectively. Surface densities between 10 and 100 g cm^{-2} at 20 AU in a sample of Ophiuchus disks have been shown to be in agreement with the density determined for the minimum mass solar nebula (MMSN) with a power-law exponent of $p = 1.5$ [Fig. 2.10; Andrews et al., 2009, 2010]. Obtained values of p close to 1 indicate a relatively flat distribution [Guilloteau et al., 2011]. The determination of the surface densities is more problematic closer to the star due to the so far limited spatial resolution, and because the emission becomes optically thick.

Radial temperature profile

The temperature profile of circumstellar disks is set by the balance between cooling and heating originating from two factors:

- intercepted stellar radiation by dust which is then reradiated at longer wavelengths, and

- accretional heating caused by the dissipation of gravitational potential energy as matter

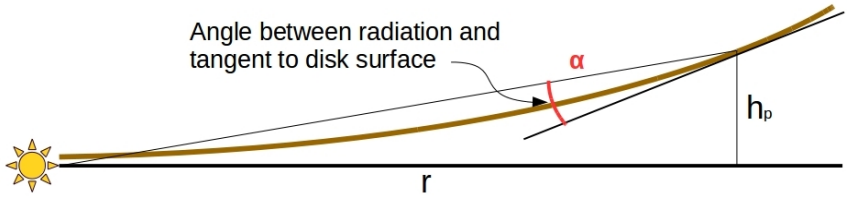

Figure 2.11: Sketch of a flared circumstellar disk whose surface is directly exposed to stellar radiation. [Credit: reproduced from Armitage [2010]]

flows towards the star.

Both of these sources decrease with increasing distance from the star. At early epochs, when accretion onto the star is the strongest, internal heating dominates over reprocessing of stellar radiation. One reduces the analysis to the case of protoplanetary disks where stellar radiation strongly dominates over accretion – also known as passive disks –. In this case the temperature profile and SED are determined by the mechanism responsible for absorbing and reemiting stellar radiation and by the shape of the disk, whether the disk is flat, flared, or warped. The disk is considered flared if the ratio $h_{\rm p}/r$ is an increasing function of radius. Since in the representation of a flared disk all points of the surface are exposed to stellar radiation, these disks absorb a higher fraction of the stellar radiation and produce stronger infrared excesses than flat disks.

The temperature profile of a flared disk can be calculated by measuring the stellar flux from a point source intercepted by the disk surface at a radius r, as seen from Fig. 2.11. One assumes that $r \gg R_\star$, and that the disk about the midplane has height $h_{\rm p}$. Then, the total stellar energy output per second, or luminosity, is given by the amount of flux (Stefan-Boltzmann law) over the whole surface area according to

$$L_\star = 4\pi R_\star^2 \sigma T_\star^4. \tag{2.33}$$

In addition, one has to consider the angle between the incident radiation and the local disk surface given by

$$\alpha = \frac{{\rm d}h_{\rm p}}{{\rm d}r} - \frac{h_{\rm p}}{r}. \tag{2.34}$$

As light leaves the source, the photons spread out in a spherical pattern. Therefore, the rate of heating per unit disk area at distance r is

$$Q_+ = 2\alpha \left(\frac{L_\star}{4\pi r^2}\right) \tag{2.35}$$

where the factor 2 derives from the fact that the disk has symmetrically two sides. On the other hand, the cooling rate at which the disk portion at distance r emits as a blackbody is given by

$$Q_- = 2\sigma T_r^4. \tag{2.36}$$

Equating 2.35 and 2.36, the temperature profile becomes

$$\begin{aligned} Q_+ &= Q_- \\ 2\alpha \left(\frac{L_\star}{4\pi r^2}\right) &= 2\sigma T_r^4 \\ T_r &= \left(\frac{\alpha L_\star}{4\pi r^2 \sigma}\right)^{1/4} \end{aligned}$$

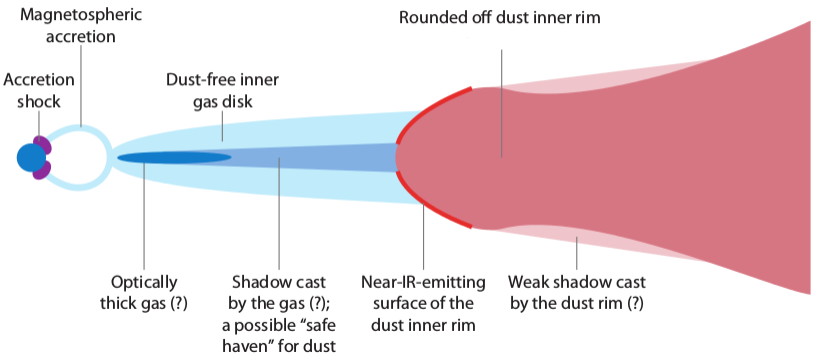

Figure 2.12: Schematic view of the inner region of circumstellar disks around PMS objects, whose structure to date is basis of debate. [Credit: Dullemond and Monnier [2010]]

and introducing Eq. 2.33, the resulting temperature radial profile becomes

$$T_r = \alpha^{1/4} T_\star \left(\frac{r}{R_\star} \right)^{-1/2}. \tag{2.37}$$

At large radii, Kenyon and Hartmann [1987] found that the surface temperature approaches

$$T_r \propto r^{-1/2}.$$

A more general expression for calculating the temperature radial profile of a circumstellar disk, in analogy with the surface density profile of Eq. 2.32, is given by the relation

$$T_r = T_{R_c} \left(\frac{r}{R_c} \right)^{-q} \tag{2.38}$$

where R_c is characteristic radius for which the temperature T_{R_c} is known, and q is an exponent that characterizes the flaring geometry of the disk. Values of q between 0.4 and 0.7, which are in agreement with SED modelling [Andrews and Williams, 2005], have been determined for TTS and HAeBe [Guilloteau and Dutrey, 1998, Piétu et al., 2007].

In reality, instead of reradiating as a single temperature blackbody as considered above, the disk radiation is governed by the dust opacity, which absorbs short wavelength starlight (at around 1 μm) more efficiently than it emits longer wavelength thermal radiation. Once the radiative properties of the dust are known, the temperature of the dust in the disk surface layer can be determined, for which it is necessary to define the emissivity ϵ. The emissivity is the ratio of the efficiency with which the dust emits or absorbs radiation relative to a blackbody surface. For instance, a perfect absorber and emitter has $\epsilon = 1$. The emissivity factor is given by the expression

$$\epsilon_{\tau_\lambda} = 1 - e^{\tau_\lambda} \tag{2.39}$$

where τ_λ is the dust opacity given by Eq. 2.24. Dust is a good absorber of radiation at wavelengths that are smaller in comparison with the particle size, with the emissivity dropping at longer wavelengths.

2.2.2.2 The inner region of circumstellar disks

The large spatial and dynamic scales of protoplanetary disks mean also that different observational techniques and spectral regimes have to be used to probe the different regions of these disks. The inner region of circumstellar disks, in the order of few AUs from the central star, is the place where temperatures are high enough to even evaporate the dust of the disk. This region contains a large amount of energy in the form of ultraviolet, optical, and near-IR radiation, whose role is crucial in the overall energy balance of the disk.

Beyond the stellar borders, the temperature in the range of several thousands degrees creates an optically thin dust-free region which extends up to an optically thick "wall" of dust at the evaporation temperature ($\sim$1500 K). Since the dust wall is much hotter than the disk behind, it has a "puffed up" shape and a larger vertical scale height [Dullemond et al., 2001]. Such structure has been consistently found and studied in the PMS low-mass TTS and intermediate-mass HAeBe objects, [e.g. McClure et al., 2013, Kraus, 2015, Lazareff et al., 2017]. Moreover, size measurements of the near-IR bump of circumstellar disks with high-angular resolution techniques have established a size-luminosity dependence between the ring radius and the host star consistent of $R_{\rm d} \propto L_{\star}^{1/2}$ with a dust evaporation temperature between 1000 and 1500 K (Fig. 2.13). Only the Herbig Be objects show disk radii smaller than the trend of the rest.

In addition to the signs of magnetospheric accretion that can be produced close to the star, 2D and 3D models to characterize the shape of the inner rim have revealed that the disk adopts a round-off profile built by the complexity of the dust composition, a backwarming effect where heat is reabsorbed by neighbour grains, and efficiency between evaporation and condensation [e.g. Isella and Natta, 2005, Tannirkulam et al., 2007, Dullemond and Monnier, 2010]. Observations have also shown disk emission inside the "dust evaporation" region, presumably arising from a gaseous or refractory hot component contributing at near-IR wavelengths [e.g. Eisner et al., 2007a]. The debate on the structure of the inner rim is further extended through predictions of self-shadowed or partly self-shadowed disks, in which context some observations and variability of HAeBe in the far-IR could be explained [e.g. Dullemond and Dominik, 2004a, Juhász et al., 2007, Muzerolle et al., 2009]. Fig. 2.12 shows a schematic view of the magnetospheric accretion region near the star, the dust-free gas disk in the middle, and the dust rim.

2.3 Disk evolution and planet formation

2.3.1 Dispersal time vs. transition time

From the classification of YSOs one reminds that circumstellar disks, although being different evolutionary stages, are present in Class II and Class III objects. The disk lifetime – or the time it takes a Class II disk to completely disperse – and the dust clearing time – or time for the transition from Class II to Class III – is the basis that sets the formation conditions of a planetary system.

Measurements of the fraction of young stars with infrared excesses in young stellar clusters, where many relatively coeval stars are located within a small area, have shown that the disk frequency is close to 100% for clusters whose mean stellar age is less than $\sim$1 Myr (Fig. 2.14). Later on the disk frequency drops steadily, reaching around 50% at 3 Myr, and with at least one third of all stars – or even close to 50% – having a disk when they reach an age of 10 Myr [Pfalzner et al., 2014].

Observational surveys at infrared ranges, e.g. Spitzer, that probe the dusty constituent of circumstellar disks, have revealed that dust at larger distances and wavelengths (22–

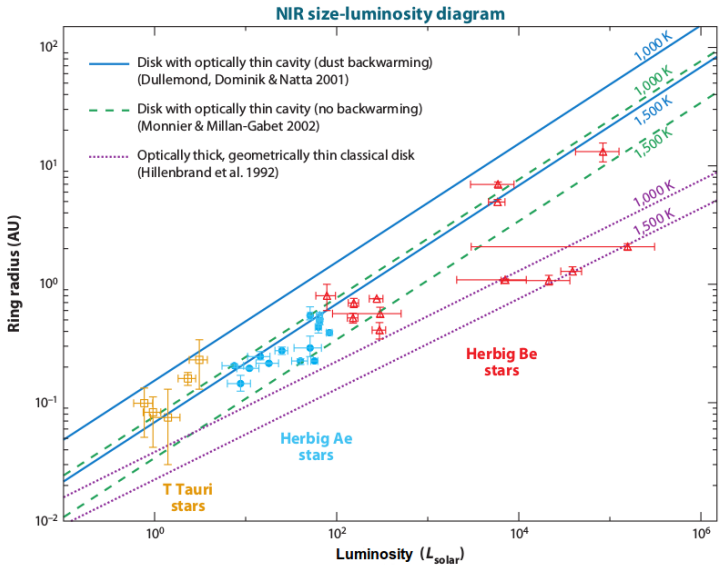

Figure 2.13: Size-luminosity dependence between disk radii and stellar luminosities measured in T Tauri and Herbig stars via interferometric high-angular techniques. The different line type denote different models applied to measure the disk size. Temperatures of the inner "wall" show values between 1000–1500 K. [Credit: Dullemond and Monnier [2010] and references therein]

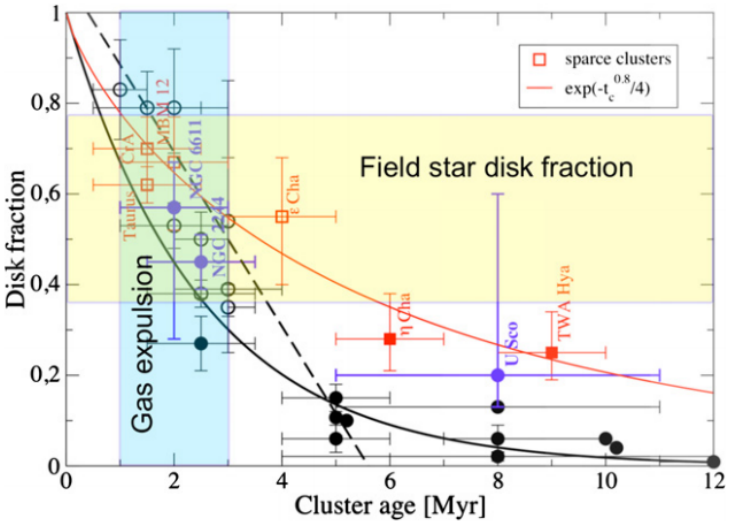

Figure 2.14: Disk fraction as a function of cluster age for different stellar populations. The dashed line traces a linear approximation by Haisch et al. [2001], whereas the solid line corresponds to an exponential approximation by Mamajek [2009]. Full symbols indicate massive extended clusters, and open symbols indicate still embedded lower-mass compact clusters. The red squares are data added by Fang et al. [2013], and by considering unbiased selection effects their approximation shows a larger survival time of disks. [Credit: Pfalzner et al. [2014] and references therein. Reproduced with permission ©AAS.]

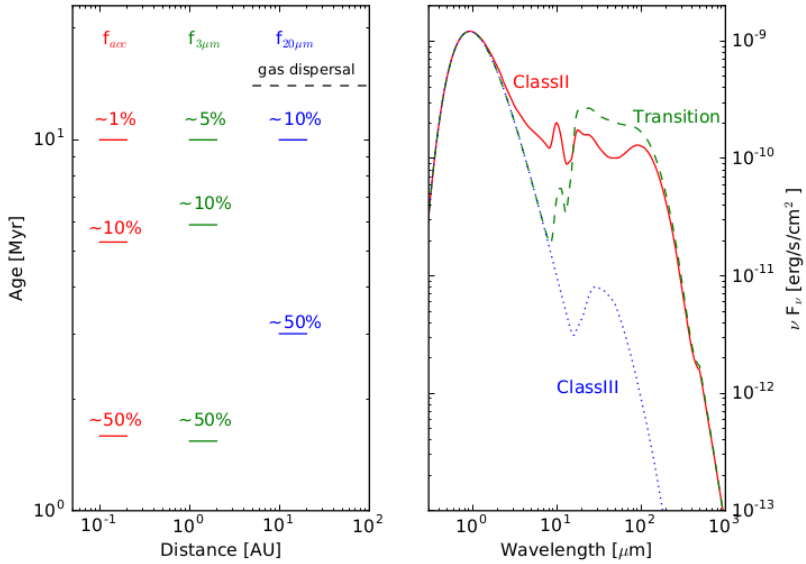

Figure 2.15: *Left*: Illustration of the dispersal time of circumstellar disks traced through their gaseous and dusty constituents. *Right*: SED shapes adopted by a Class II disk, a transition disk with a dust gap at 2 AU, and a Class III debris disk. [Credit: Ercolano and Pascucci [2017] and references therein]

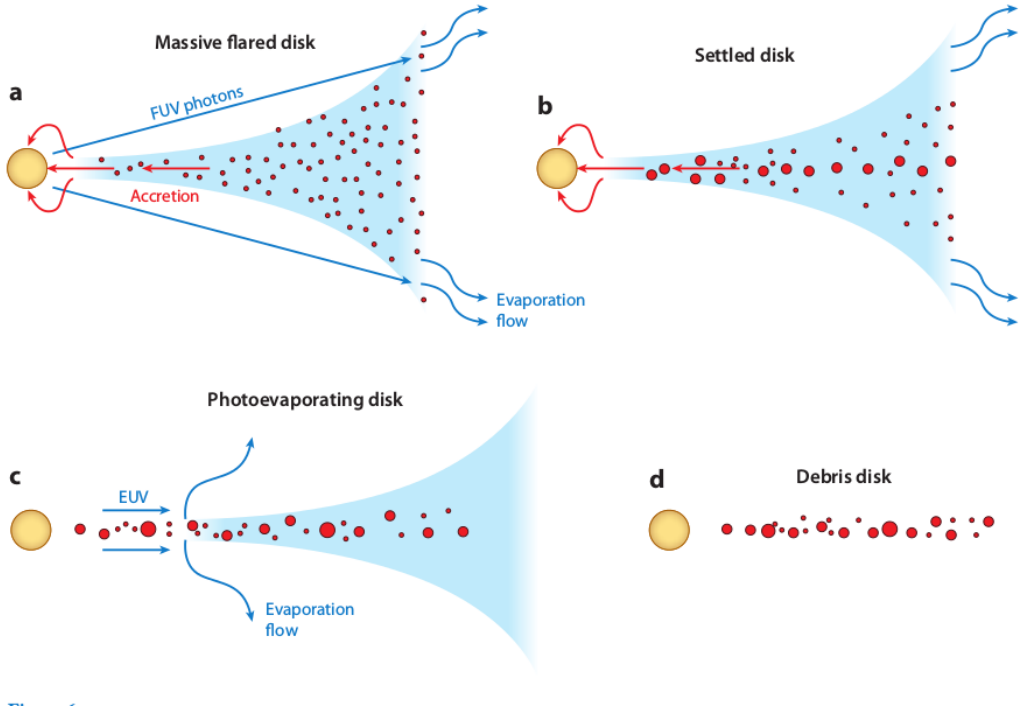

Figure 2.16: Schematic view of the evolution of a typical circumstellar disk. a) Initially the disk loses mass through accretion onto the star and photoevaporation induced by stellar radiation. b) At the same time, micron-sized grains grow into larer bodies and settle to the midplane of the disk. c) When photoevaporation becomes dominant the inner disk drains on a viscous timescale, and an inner hole is formed. d) Once the remaining gas evaporates, the small grains are removed and only the larger, planetesimal-sized bodies, remain. [Credit: Williams and Cieza [2011] and references therein]

24 μm) survives longer than material at shorter ones (3–12 μm), suggesting that disks evolve inside-out [e.g. Currie et al., 2008, McCabe et al., 2006]. In this inside-out perspective, the diagnostic of accretion rates close to the star through optical/UV excess emission from shocked gas at the stellar surface has shown that the fraction of accreting stars declines with cluster age approaching zero at $\sim$10 Myr. This exponential decay has an e-folding time[11] of 2–3 Myr, in agreement also with the e-folding time of the dusty material at $\sim$1 AU probed with observations in the range 3–12 μm. SED analyses at this wavelengths display that the frequency of transition disks, i.e. disks with little or no near-IR excess but large mid- to far-IR excess emission, is only about 10% of the total Class II disks [e.g. Furlan et al., 2009], implying a dust clearing time of a few 10^5 years, much shorter than the disk lifetime. On the other hand, although still limited in sample size, surveys at infrared and (sub)millimetre wavelengths probing gas at tens or hundreds of AU determine a gas lifetime of $\sim$10–20 Myr. Fig. 2.15 belonging to an updated review on the dispersal of planet-forming disks by Ercolano and Pascucci [2017] summarizes well the dispersal time of the dusty and gaseous components as a function of distance from the star. The right panel illustrates the SED shape adopted by a full Class II disk, a transition disk with a dust gap at 2 AU, and a Class III debris disk.

2.3.2 Dispersal mechanisms

The evolution of primordial protoplanetary disks, from optically thick to optically thin (Fig. 2.16), is established by various processes, including viscous accretion, photoevaporation by UV and X-ray radiation, dust settling and coagulation, forming planets, and external effects such as the dynamical interaction with (sub)stellar companions. Two of them, accretion and phtoevaporation, are believed to be responsible for the abrupt disk dispersal lasting about 10 times faster than the disk lifetime.

As previously mentioned, accretion is managed by viscosity, although the source of viscosity is still a matter of debate [e.g. Ercolano and Pascucci, 2017]. The initial evolution of primordial disks is generated by viscous transport during which material from the inner disk is accreted onto the star, and the outer disk plays the role of supplier of the inner disk and dissipator of angular momentum. According to the standard model of circumstellar disk accretion, turbulence is generated by magneto-rotational instabilities (MRI). Its conditions are: a sufficiently ionised gas, a disk weakly but non-negligibly magnetised, and an angular frequency that decreases with radius. However, MRI might be absent in regions of the disk lying under large column densities of material in the inner disc, which for their neutral status are known as "dead zones". Magnetocentrifugal winds as a result of magneto-hydrodynamical (MHD) simulations can be also responsible for driving accretion and removing angular momentum [e.g. Bai and Stone, 2013]. Nevertheless, global models for the evolution of disks rely on a number of important assumptions with no clear consensus [e.g. Bai, 2016].

However, viscosity is only dominant during the accretion phase onto the star and just a first-order approximation of a much more complex evolution that includes other physical processes. Indeed, when the accretion rate decreases to photoevaporation rates ($\sim 10^{-10}$–10^{-9} $M_\odot$ yr^{-1}), and the remnant inner disk is removed on a viscous timescale ($\lesssim 10^5$ yr), an inner hole is formed and photoevaporation governs the disk evolution [McCabe et al., 2006, Williams and Cieza, 2011]. Radiation from the central star penetrates the disk atmosphere and heats the gas. Then, thermal wind are created if the gas temperature at a given location

[11] The e-folding time is the time interval in which an exponentially growing quantity increases by a factor of e.

is higher than the local escape temperature, driving evaporation in the far-UV (FUV: 6 eV$<$ $h\nu$ $<$13.6 eV), extreme-UV (EUV: 13.6 eV$<$ $h\nu$ $<$0.1 keV), and X-ray ($h\nu$ $>$0.1 eV) energy ranges. Each process influencing differently in the disk. It is believed that whereas EUV radiation induces higher evaporation rates in the inner regions of the disk, X-rays and FUV drive photoevaporation at larger distances due to their capacity to penetrate larger columns of neutral gas and heat gas located deeper and further away from the central star. Although photoevaporation models including these three energetic regimes [e.g. Gorti et al., 2009, Owen et al., 2010] have predicted rates of the order of $10^{-8}\,\mathrm{M}_{\odot}\,\mathrm{yr}^{-1}$, a significant amount of PMS stars with large inner holes, massive disks ($\gtrsim$10 $\mathrm{M}_{\mathrm{Jup}}$) and no, or little accretion, observations of WTTS [e.g. Andrews and Williams, 2005, 2007a, Cieza et al., 2010] suggest that these objects have disks with lower masses ($\lesssim$1–2 $\mathrm{M}_{\mathrm{Jup}}$). The incongruence between models and observations thus suggest discretion with interpretations.

2.3.3 From dust to protoplanets

Dusty material accounts for only $\sim$1% of the initial mass of the disk. However, its influence dominating the disk opacity and material forming terrestrial planets and the cores of giant planets is immense. First, since gas orbits the central star at velocities slightly different from Keplerian due to pressure, dust grains (size of $\sim$0.1 μm) that have a large surface-to-mass ratio are swept along with the gas. These grains collide and stick together, decreasing their surface-to-mass ratio and decoupling from the gas motion. Subsequently, grains suffer a strong drag force and settle toward the midplane. As a result, the density of the dust in the interior of the disk increases, accelerating grain growth and forming larger grains in the interior. Because circumstellar disks are a turbulent environment, some vertical stirring and mixing of grains impede a perfectly stratified disk [e.g. Dullemond and Dominik, 2005]. Another evidence of dust settling is found in the SED slopes of TTS [e.g. D'Alessio et al., 2006], showing reduced mid-IR emission in most of them since this process reduces the scale height and the flaring angle of the disk [Dullemond and Dominik, 2004a].

The way dust grains grow is controlled by a balance between coagulation (sticking) and fragmentation. Silicate grains surveyed in hundreds of circumstellar disks in nearby star-forming regions [e.g. Oliveira et al., 2010, McClure et al., 2010] have shown that micron-sized particles are present, and that submicron grains are absent, meaning that grain growth is more efficient that fragmentation or that submicron grains are efficiently removed from the upper layers of the disk by stellar winds. In the surface layers of the disk, the balance between grain growth and destruction is also influenced by crystallization via thermal annealing and amorphization (e.g. through X-ray irradiation) [e.g. Furlan et al., 2009, Oliveira et al., 2010].

The posterior growth of particles to millimetre scales is probed by SED slopes at (sub)millimetre wavelengths. Surveys of Taurus disks at 3 mm [Rodmann et al., 2006] and 7 mm [Ricci et al., 2010] demonstrated that a shallow SED slope generally extends to the observing wavelength, and have inferred opacity indices of $\beta = 0.6$ and 1. The implication that centimetre-sized particles are common in circumstellar disks has been also demonstrated by resolving the disks of TW Hydra and WW Cha reaching sizes of up to 10 cm [Wilner et al., 2005, Lommen et al., 2009].

It is believed that classical coagulation makes possible bodies to grow up to kilometre sizes by two-body collisions. However, two problems arise at what is called the "meter-sized barrier". On the one hand, objects that grow up to meter size drift extremely quickly towards the central star, and there they are destroyed by the high temperatures. The drift time is then shorter than the time needed to form such bodies, making growth extremely ineffective [Klahr and Bodenheimer, 2006]. On the other hand, meter sized boulders do not stick well together, but rather demolish at typical collision speeds. Although it is also a topic of

debate, a gravoturbulent method has been developed, according to which turbulence and streaming stability make the formation of planetesimals possible [Youdin and Goodman, 2005, Johansen et al., 2006].

In the subsequent phase, when planetesimals adopt a kilometre size, gravity is the dominant force. The growth from planetesimals to protoplanets is, however, harassed by different factors. First, the initial conditions since the formation mechanism and thus the distributin of the first bodies is poorly known. Second, N-body simulations with planetesimals in the order of some millions and time scales of million years represent high computational costs. Third, the dynamical mechanisms such as collisions, shock waves, or fracturing play an important role and more knowledge is lacking.

Since the scope of this investigation is not focused on the planet formation itself, but instead on the characterization of disk at the earliest stages, one may refer to wide and specialized reviews in the literature [e.g. Armitage, 2010, Williams and Cieza, 2011, Wolf et al., 2012]. Fig. 2.16 summarizes what it has been exposed in this subsection, from the earliest stages dominated by viscous accretion, photoevaporation induced by the stellar emission, dust settling to the midplane of the disk, and formation of larger bodies up to planetesimal scales.

2.4 Influence of (sub)stellar companions

In previous sections it has been established that two ubiquitous byproducts of star formation which dispose the excess of angular momentum are the creation of stars forming multiple systems and the association of circumstellar disks around most – if not all – of them. Although, as seen from the descriptions above they represent, in a way, individual scenarios, they are also tenuously linked to each other. Namely, because stellar and substellar companions forming multiple systems may influence the evolution of their disks, and thus the possibility of planet formation. Nevertheless, according to up-to-date exoplanet catalogues [Schneider et al., 2011, Rein, 2012][12], the fact that to date of this writing out of the 3741 exoplanets forming 2816 planetary systems, 134 are planets in binary or higher-order multiple systems manifests that planet growth under the companions influence is not an inconceivable task.

2.4.1 External photoevaporation

Given the fact that most stars form in large clusters and they highly likely contain luminous and massive O stars, one of the scenarios in which companions externally influence the evolution of circumstellar disks is when these massive companions generate strong UV-radiation fields enough to truncate by photoevaporation other disk outer edges. This scenario is plausible, especially, in systems where the disk is sufficiently large that weakly gravitationally bound material at the disk outer edge can be efficiently photoevaporated.

Numerical simulations have even demonstrated that in binary systems the dispersal of circumstellar disks surrounding primary and secondary stars is accelerated from outside-in if the maximum of X-ray photoevaporation is close to the tidal truncation (see next subsection). Consequently fewer transition disks – at least, of the type created by photoevaporation – are expected in binary systems with few tens of AU of separation [Rosotti and Clarke, 2018].

On the observational side, ALMA observations have evidenced that the protoplanetary disk around the young object IM Lup is expected to shrink rapidly due to mass-loss induced by external UV-fields of 8–16 G_0 down to about 400 AU [Haworth et al., 2017]. Also, external photoevaporation is discussed as the cause of finding more massive disks farther

[12]Websites: `www.exoplanet.eu`; `www.openexoplanetcatalogue.com`

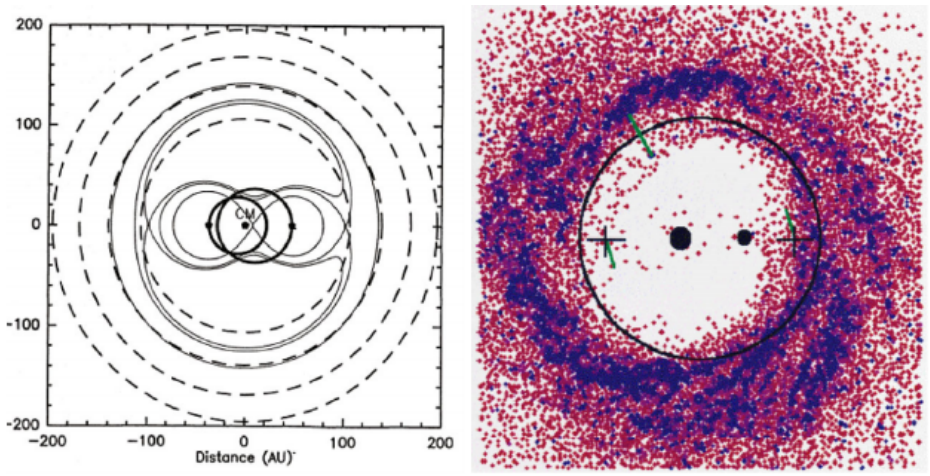

Figure 2.17: *Left*: Diagram of the Roche equipotentials (thin lines) for a stellar pair with masses of 0.65 $M_\odot$ and 0.5 $M_\odot$ orbiting with respect to their mass centre (CM). The thick lines are the stellar orbits and the dashed ones the 2:1, 3:1, 4:1 and 5:1 resonances. The CB disk is truncated beyond the 3:1 orbital resonance. *Right*: Smoothed-particle hydrodynamics (SPH) simulation of a binary system with denser regions denoted in blue. The black circle is the 2:1 Lindblad resonance, and the black crosses the saddle points of the potential. The green streaks point to areas where accretion onto the binary occurs. [Credit: Dutrey et al. [2016] and references therein]

away from the center of clusters compared to the less massive disks found in their dense center [e.g. Olczak et al., 2006, Pfalzner et al., 2014].

2.4.2 Tidal truncation

If each young star forming binary systems harbours its own circumstellar disk, then the tidal perturbing effect of the companion star on each disk can produce a gravitational torque that extracts angular momentum from the disk and transfers it to the binary orbit [Bate, 2000, Lubow and Artymowicz, 2000]. These tidal interactions tend to be self-regulating, meaning that if too little angular momentum is removed from a circumstellar disk, the disk will expand towards the companion as it gains matter, subsequently increasing the strength of the interaction; on the contrary, if too much angular momentum is removed, the disk will shrink and the tidal effect will be reduced. The architecture of the binary system, which includes individual circumstellar (CS) (or also known as circumprimary) and/or circumbinary (CB) disks, depends essentially on three parameters: the orbital eccentricity, the stellar masses, and the separation between companions.

In cases where the orbit of a binary system is eccentric, the tidal effect is time dependent and causes strong disturbances at each periastron passage, causing episodes of rapid accretion onto one or both stars, and being a possible cause of the FU Orionis phenomenon[13] [Bonnell and Bastien, 1992]. In some cases the disturbances can be that strong that circumstellar disks can be severely disturbed or even disrupted [e.g. Bate et al., 2003]. For eccentricities between 0 and 0.25, theoretical models of tidal truncation determine that the CB disk has an inner hole of approximately 1.8–2.6a, where a is the semi-major axis of the binary system [Artymowicz and Lubow, 1994]. The CB inner edge depends on the binary eccentricity and

[13]FU Orionis variables are PMS objects which undergo a rapid increase in luminosity of up to 5 magnitudes in a period of years with decay times of tens of years to greater than a hundred years [Hartmann, 1991].

increases with it [Lubow and Artymowicz, 1997]. On the other side, the outer edge of the CS disks are truncated at $\sim$0.3–0.5a [Papaloizou and Pringle, 1977].

The mass ratio between the companions is relevant to define the inner edge of the CS disks, although it has been demonstrated that the eccentricity plays a more important role in shaping the environment [Pierens and Nelson, 2013].

As result of orbital resonances in binary systems, theory predicts the possibility of survival of material forming CS disks around each of the components, inside the Roche lobes[14], and an outer CB disk in Keplerian rotation beyond the L2 and L3 Lagrangian points (Fig. 2.17). These configurations are imposed by the binary separation, distinguishing three different categories:

- Very close or spectroscopic binaries ($\lesssim$1 AU)
- Intermediate separation binaries (1–100 AU)
- Wide binaries ($>$100 AU)

For binaries with large separations and for spectroscopic binaries the mm-flux is similar to the field value. This means that in the case of wide binaries the two stars are individually surrounded by circumstellar disks behaving just as disks around unperturbed single stars. On the other hand, very close stars are surrounded by a circumbinary disk which resembles a disk around a single star [Kley and Burkert, 2000]. In support, also models of planet formation in very close systems state that planets can form and survive in circumbinary orbits around both members [Quintana and Lissauer, 2006], whereas in wide binaries planet formation seems indistinct of the one seen for single stars [e.g. Kraus et al., 2016, Bonavita and Desidera, 2007].

The case of intermediate separation binaries is more complex because CS and CB disks can coexist. Moreover, models show that the circumbinary cavity with low surface density is not totally empty (see Fig. 2.17). Accretion streams that feed the CS disks with material to make possible their survival are also predicted [Artymowicz and Lubow, 1996]. The accretion arms are variable, being modulated by the torque of the stellar pair and showing a period similar to the one of the stars [Artymowicz et al., 1991].

2.4.3 Observational evidence in T Tauri and Herbig Ae/Be binary systems

It is still unclear how the presence of a companion at intermediate separations affects the evolution of disks and the conditions to grow planets. Statistical observational studies targeting low-mass T Tauri binary systems located in some of the nearest and most active star-forming regions such as Taurus, Ophiuchus or Chamaeleon I, have demonstrated that, in comparison to disks that evolve around single stars, the lifetime and accretion activity of circumstellar disks in systems with physical separations less than 100 AU is reduced [e.g. Cieza et al., 2009, Daemgen et al., 2013]. For instance, considering a stellar pair with a separation of 30 AU – the separation peak expected for a population of T Tauri [Duquennoy and Mayor, 1991] – the lifetime of the disks around the individual components should be $\sim$10% of the one around single components with a typical radius of 100 AU [Andrews and Williams, 2007b], or in other words, just a fraction of a million year. An accelerated disk dissipation subsequently disrupts the timescale needed to form terrestrial and giant planets through core accretion [Duchêne, 2010].

[14]The Roche lobe is the tear-drop-shaped region bounded by a critical gravitational potential. The point at which the two Roche lobe apexes around two stars forming a binary system intersect is known as L1 Lagrangian point.

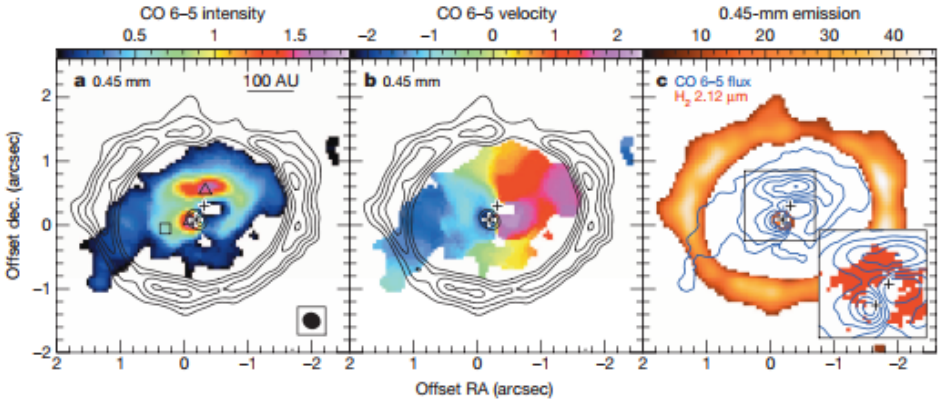

Figure 2.18: ALMA observations of the triple system GG Tau A. *Left*: 0.45-mm emission (black countours) and CO 6-5 flux (color). *Middle*: Addition of the CO velocity field (color) to the previous contours. *Right*: 0.45-mm emission, CO 6-5 flux and H_2 intensity in red. [Credit: Dutrey et al. [2014]]

In spite of these statistical and numerical expectations several samples in the group of T Tauri stars have been reported. The most prominent of them is undoubtedly GG Tau, first detected by Cohen and Kuhi [1979]. This objects is actually a quintuple system divided in a triple one, GG Tau A [Dutrey et al., 2014], and a binary one, GG Tau B. The projected separation between A and B components is some 1400 AU. Long-baseline near-IR interferometry PIONIER and direct imaging NACO resolved in the A triplet a close binary with a 4.5 AU separation at 30° and an orbital period of 16 years [Di Folco et al., 2014]. The third component is located 36 AU to the south of the pair. The total mass of GG Tau A is estimated in 1.3 $M_\odot$ [Guilloteau et al., 1999]. Observations from infrared to submillimetre bands have provided a complete overview of such a complex system. Spectroscopy and photometric studies have detected accretion signatures and silicate features originating from the Aa and Ab circumstellar disks. In addition, an outer disk with a radius of 180 AU has been spotted by several groups (see the black contours of Fig. 2.18). Inside the cavity, scattered light emission of the dust ring in the near-IR, and more interestingly the velocity maps of CO 6-5 within the cavity stream from the outer ring have been depicted (Fig. 2.18). In the same way, H_2 lines associated to material infalling onto the inner CS disks have been mapped. Other multiple TTS with spatially resolved CB or CS at intermediate separations are [Dutrey et al., 2016], for instance: HH30, SR24N, FS Tau, UZ Tau W or L1551 NE.

It is clear that most of what we know about disk evolution in young multiple systems derives from the studies of T Tauri objects. The case of Herbig Ae/Be objects is particularly intriguing because, for instance, they are more massive and suppose a stronger gravitational interplay with the companions and the inner environment of the disks. However, assessing them is considerably more challenging because although their binary frequency is expected to be similar to the one of the low-mass counterparts, the amount of them imposed by the stellar initial mass function is scarce (section 2.1.3). Also, the majority of them are located at least at 300 pc away from the Sun, and the large mass and contrast ratios for unequal systems makes difficult an accurate characterization of the systemic properties [Duchêne, 2015]. While at intermediate separations no dedicated multiplicity survey has been conducted, few multiple HAeBe objects have been resolved with circumstellar and/or circumbinary emission. For instance, the quadruple system TY CrA, whose close triple system is separated from the fourth component some 40 AU, is surrounded by dusty emission [e.g. Chauvin et al., 2003, Boersma et al., 2009]; HD142527 with a low-mass companion at 12 AU shows flows of gas

through a dust-depleted gap of $\sim$30 AU [e.g. Biller et al., 2012, Casassus et al., 2013, Lacour et al., 2016]; the nearly identical binary system AK Sco is surrounded by a circumbinary disk and shows spectral features indicating outflow and infall activities in the system [e.g. Alencar et al., 2003, Anthonioz et al., 2015, Gómez de Castro et al., 2016]; or the source of this investigation V892 Tau.

CHAPTER 3

Modelling of Interferometric Data

3.1 High-angular resolution studies of circumstellar disks

The characterization of the dusty material in circumstellar disks is possible thanks to observational techniques profiting from, for instance, scattered light and thermal emission.

Because circumstellar disks are not emitters, but instead their temperature is limited to the one of dust sublimation ($\sim$1500 K for silicate grains), at optical wavelengths they can be only imaged in scattered light, i.e. photons that reach the observer after being scattered off by dust grains. The implications of scattered light can be determined up to mid-IR ranges, however, depending on the star/s and dust properties, the contribution of thermal emission by hot dust in the innermost regions may dominate at redder wavelengths [Pinte et al., 2008]. Through this technique it is possible to determine the geometry of the disk (e.g. inclination, outer radius, vertical scale height of dust component, flaring) and surface density profiles which reveal the presence of planets through gaps and asymmetries. Also, scattering images in the optical and near-IR probe the grain properties (e.g. grain size distribution, porosity) due to photons that are highly linearly polarized.

On the other hand, thermal emission of dust grains that are heated by the central stars and reemit as gray bodies is detected at near-, mid-IR and longer wavelengths. The inner few AUs of a disk are particularly identified in near- and mid-IR ranges, making possible to resolve details of the inner radius and immediate environment of the central stars.

An additional approach to spatially resolve protoplanetary disks around PMS objects is observations of Polycyclic Aromatic Hydrocarbons (PAHs) grains in the near- and mid-IR. These are grains stochastically heated by UV radiation that emit in bands between 3 and 12 μm. Because PAHs grains are excited up to large distances in the surface layers of flared disks, they give information about the global structure of disks (e.g. vertical height, flaring). Another method to gain spatial information of disks – especially in the innermost regions – is through multi-epoch photometry that reveals variability due to inhomogeneities and/or asymmetries within the disk.

Of course, these techniques are only fruitful if astronomical instrumentation is capable of achieving the required spatial resolution that disks demand. Spectroscopic analysis probes the accretion rates and the star-disk interaction in the closest regions to the star [e.g. Fairlamb et al., 2015, Schöller et al., 2016]. Protoplanetary disks are too distant to be imaged with ground-based facilities at optical or infrared wavelengths. The angular scale that is probed

by a telescope equals λ/D radians, where λ is the wavelength at which the observation is acquired and D is the main-mirror diameter. Even diffraction-limited techniques, such as adaptive optics (AO) on large ground-based telescopes or the Hubble Space Telescope (HST), reach only resolutions of $\sim$10 AU, unsatisfactory to probe the closest environment of disks. State-of-the-art instruments mounted on single- and multiple-aperture facilities, however, in recent years have enhanced our understanding of the innermost regions of protoplanetary disks in single and binary systems.

Representative instruments implemented on single-dish telescopes are, for instance:

- The Spectro-Polarimetric High-contrast Exoplanet REsearch instrument (SPHERE) at the 8 m-class Very Large Telescope (VLT) is dedicated to directly obtain images of exoplanets and dusty/debris disks around stars, where planets may be forming [Beuzit et al., 2008]. Because directly imaging these structures is especially difficult due to the high light-contrast between them and the stars, SPHERE exploits the advantages of adaptive optics and coronagraphy, that blocks out the central region of the star to reduce its contribution. Starlight in unpolarised, but when it is reflected by the surface of a planet or disk the reflected waves become partially polarised. This polarised signal is identified by SPHERE through polarimetric differential imaging (PDI) to get a sharp view of the disk or planet. For this purpose SPHERE is equipped with three subsystems: ZIMPOL[1] (600–900 nm), IRDIS[2] (900 nm–2.3 μm) and IFS[3]. Therefore, depending on the wavelength, the diffraction-limited spatial resolution is 20–80 mas, although the utilization of a coronagraph may obscure the central $\sim$100 mas. Preeminent results in the optical and near-IR have revealed the dusty disks in a sample of single and multiple T Tauri [Fig. 3.1; Avenhaus et al., 2018, Csépány et al., 2017] and Herbig objects [e.g. Bertrang et al., 2018, Wagner et al., 2018]. These results have allowed to determine a wide variety in disk sizes, geometry and polarised fluxes, as well as define specific trends in the morphology of TTS and HAeBe. Whereas disks around T Tauri form ring-shaped substructures, disks around Herbigs display spirals [e.g. HD142527 or HD100453A; Avenhaus et al., 2014, Wagner et al., 2018]. This difference can be attributed to different scenarios of interaction between protoplanetary disks and growing planets, which can shape the disks into vast rings, spiral arms or shadowed voids.

- Another outstanding instrument in a 10.4 m-class ground based telescope is CanariCam at the Gran Telescopio de Canarias (GTC), a mid-IR (8–25 μm) imager with spectroscopic, coronagraphic and polarimetric capabilities [Telesco et al., 2003]. This multimode instrument addresses a broad range of scientific problems. This instrument addresses projects to characterize protoplanetary systems and circumstellar disks around YSOs thanks to its sensitivity to dust temperatures between 100–1000 K. More specifically, its imaging and polarimetry modes are used to determine the disks' structure, magnetic field configurations and the role of these disks in shaping their immediate environment in a sample of Herbig Ae/Be and T Tauri stars. CanariCam achieves a mid-IR diffraction-limited resolution of 200 mas at 10 μm and 400 mas at 20 μm. Recently, in this context, new insight into the magnetic field activity of eight HAeBe and one TTS has been achieved by detecting linear polarization at 8.7,10.3

[1] ZIMPOL is a camera that makes sharp images and measures polarisation in visible and near-IR light. It can detect reflected polarised light of gaseous planets, very close to the stars, and scattered light from the dusty disks around YSOs.

[2] IRDIS is a camera whose main goal is to image young self-luminous giant planets due to PDI.

[3] IFS is a near-IR spectrograph that can simultaneously work with IRDIS to build a spectral map over the entire field-of-view.

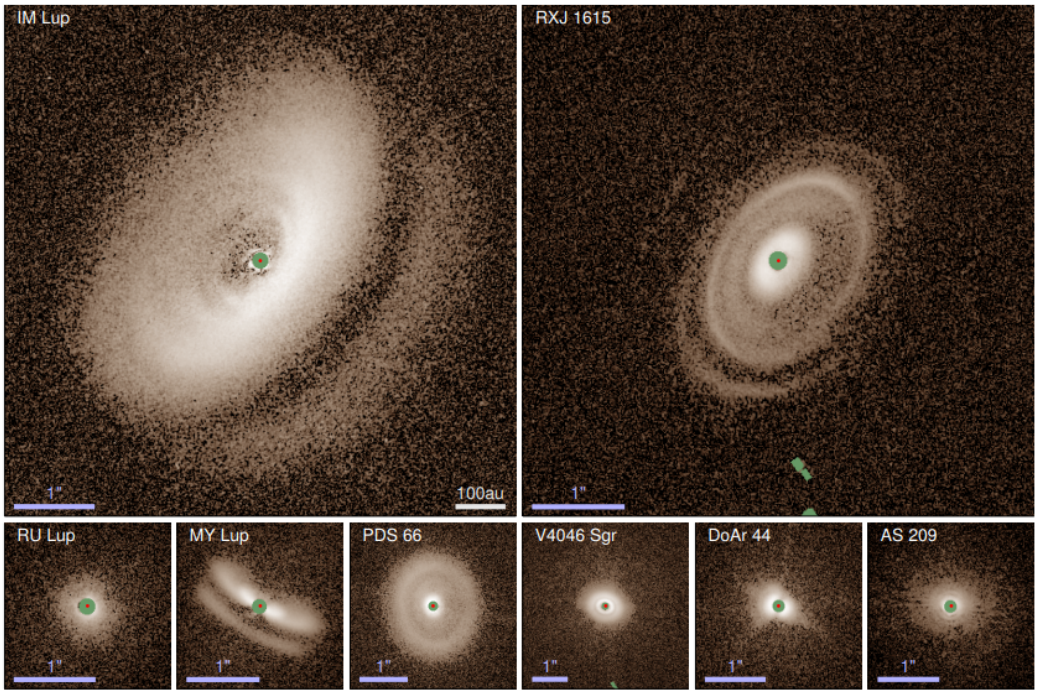

Figure 3.1: Sample of circumstellar disks in TTS imaged in H-band with SPHERE. The different sizes can be noted from the 1" angular scale in the bar of each panel. All panels have been re-scaled by the authors to represent the same physical size, meaning that the 100 AU scale bar applies to all of them. It is clear, for instance, the very big size of the disk around IM Lup in comparison to small-scale disks such as the one around RU Lup. The green areas are obscured regions due to the coronagraph or bad pixels, and the red dot marks the position of the stars. Within this sample, the object V4046 Sgr is the only close binary. It has a 2.4-day orbit, a transition structure with a ∼10 AU central cavity and two concentric rings separated by a gap at ∼20 AU. [Credit: Avenhaus et al. [2018]. Reproduced with permission ©AAS.]

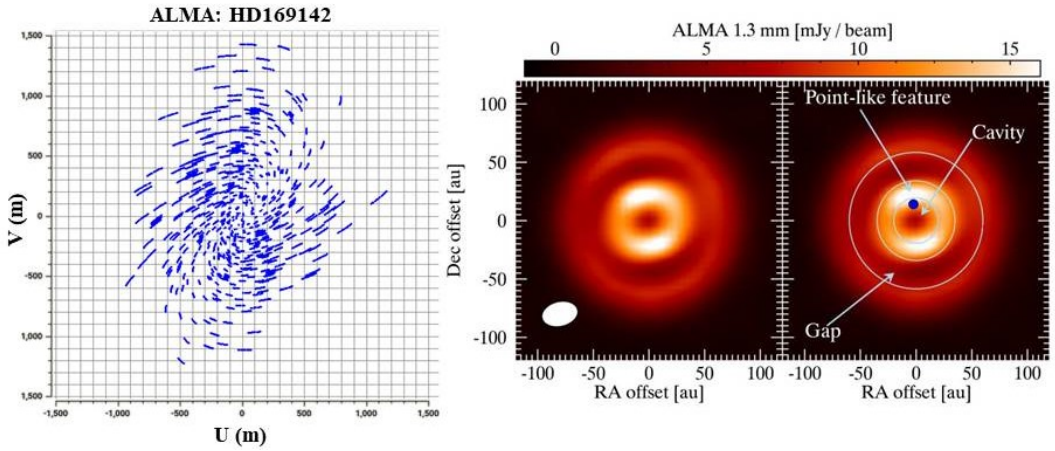

Figure 3.2: ALMA 1.3 mm observations of the Herbig Ae/Be star HD169142. The uv-plane completeness obtained with 35 antennas (left) produces a clear image of a double-ring structure in the dust distribution (center). The dust gap extends from ∼35 to 56 AU. In addition to the gap, an inner cavity (<20 AU) and a point-like feature detected in L'-band are overlaid (right). [Credit: Fedele et al. [2017]. Reproduced with permission ©ESO. uv-points provided by Dr. Álvaro Sánchez-Monge.]

and 12.5 μm from their disks. The detection of polarized mid-IR emission and/or absorption demonstrates that, commonly, magnetic fields make possible grain alignment in protoplanetary disks around PMS [Li et al., 2018]. Another area of research of this facility is the search at 10 μm of substellar companions harbouring circumstellar emission, therefore addressing the two tenuously related byproducts of star formation mentioned before [e.g. Béjar et al., 2015].

Nevertheless, although SPHERE and CanariCam join the advantages of the largest available apertures ($\sim$10 m) and diffraction-limited techniques, the spatial resolution at near- and mid-IR bands to assess the innermost regions and smallest structures of protoplanetary disks is still insufficient. The use of coronagraphs to block the light from the central star extends the resolution limit to only $\sim$100 mas, or some tens of AU from the central stars. Moreover, the characterization of binary systems and circumstellar emission with separations less than the resolution level (few AUs), representing, as previously stated, one of the modern astronomical areas to still bring to light, is unaffordable with these facilities.

On the other hand, long-baseline interferometry – the combination of two or more single apertures – enables high-resolution observations of circumstellar structures. Unlike the single-dish case, here the angular scale is given by λ/B, where λ is the wavelength and B is the baseline (distance) between a pair of telescopes. In order to investigate circumstellar disks, this technique is commonly applied to two distinctive spectral ranges: infrared and (sub)millimetre.

As follows, I highlight some main differences of the application of interferometry to these two spectral windows:

1. **Type of detection and beam combination:** The signal detection in (sub)millimetre interferometry is obtained at the antennae thanks to the heterodyne technique[4]. Then, each signal is coupled with a reference signal of high coherence, and the amplitude and phase of the coming electric field are recorded. The antennae signals are digitalized and combined in a correlator. After that, an electronic phase delay is applied to compenste the difference in path length between the arms. On the other hand, through single optical telescopes, infrared interferometry transmits light-beams to a central lab where the optical path is equalized, and they are combined to display interferometric fringes. The complexity of infrared interferometry has restricted number of telescopes that are simultaneously used in an observation to two, three or four baselines (second generation instruments). Therefore, in contrast to interferometry at radio wavelengths, it does not easily yield actual aperture-synthesized images [Dullemond and Monnier, 2010]. Infrared interferometry is thus only limited to measure sizes, brightness profiles and asymmetries of emitting regions in the plane of the sky. However, this information reveals a lot about the structure of the inner regions of protoplanetary disks and permits to build numerical models to reproduce the interferometric signals.

2. **Angular resolution determined by λ/B:** Due to constructive factors, millimetre antennae can be movable, and configure arrays of some hundred meters. For instance, for a 100 m baseline and observations at 1 mm, the achieved angular resolution is $\sim$2 arcseconds. On the contrary, monolithic optical telescopes at a similar baseline, generally unmovable, observing in the near- (e.g. K-band with central wavelength at 2.2 μm) and mid-IR (e.g. N-band with central wavelength at 10 μm) would achieve a diffraction-limited angular resolution of 4 and 20 mas, respectively. For an object

[4]The heterodyne technique is a non-linear signal processing method that creates new frequencies by combining or mixing other two frequencies with mixer devices such as vacuum tubes, transistors or diodes.

located at a distance of 140 pc, typical for some of the closest star-forming regions, this resolution leads to about $\sim$1 AU, which matches what is needed to probe the dust evaporation front. Additionally, the wavelengths at which each of them observe allow to probe different layers of the circumstellar disks: the outer and colder ones in the case of (sub)millimetre observations, and the hotter and closer to the stars in the infrared.

3. **Atmospheric influence:** The wavefront is deformed by the atmospheric turbulence at shorter wavelengths. The spatial Fried's parameter, r_0, which corresponds to the spatial scale of this turbulence, is smaller than the telescope size. Whereas this parameter adopts values in the near-IR of 0.5–1 m, in the (sub)millimetre its value is larger than the antennae sizes. Also the temporal Fried's parameter t_0, which corresponds to the temporal scale of the turbulence, is of the order of few hundred milliseconds in the infrared versus several minutes in the millimetre.

4. **Sources of noise:** The three type of noises at shorter wavelengths are: the photon noise, the read-out noise of the detectors and the background noise coming from either thermal emission or from the sky brightness. The main source of noise in millimetre interferometry is the thermal noise.

Two remarkable examples of interferometers operating at (sub)millimetre and infrared bands are, respectively, ALMA and the VLTI. The Atacama Large Millimetre/submillimetre Array (ALMA)[5] located in the Chilean desert, with its 66 movable antennae (54 twelve-meter diameter and 12 seven-meter diameter), is one of the most important interferometric facilities in the world. The simultaneous implementation of various antennae and baseline configurations ranging between few meters and 16 km provide a complete uv-coverage and, thus, reconstructed maps of continuum thermal emission and lines with information on the general structure and most minuscule details of astronomic sources in the millimetre band. At these (sub)millimetre wavelengths, the dust thermal emission in protoplanetary disks is mostly optically thin, excepting the innermost regions of the disk close to the star. Therefore, observations at this spectral range probe the bulk of solids in the disk midplane, where most of the material is found and where planet formation initiates. Some of the latest most outstanding discoveries in the field of circumstellar disk characterization and signatures of planet formation around young stars, such as GG Tau A (Fig. 2.18), HD169142 [Fig. 3.2; Fedele et al., 2017] or V1247 Orionis [Kraus et al., 2017b], have been achieved thanks to the ALMA capacities.

An independent section about the Very Large Telescope Interferometer (VLTI) is presented later as observational data acquired with this facility is the main purpose of this investigation.

As summary of this subsection, the milliarcsecond spatial scale and the temperature range at which the dusty structures of circumstellar disks are detected make infrared long-baseline interferometry the unique and optimal technique, in terms of angular resolution, to characterize them and gain information about their evolution and eventual process of planet formation. The applicability of infrared long-baseline interferometry is even enhanced when addressing the circumstellar environment of binary systems with separations inaccessible to the resolution provided by single-dish telescopes.

[5]Website: `www.almaobservatory.org`

3.2 Astronomical interferometry

The French physicist Hippolyte Fizeau first reported interference fringes in 1868. Later, in 1890, the American Albert Abraham Michelson experimented with small holes in a mask covering the larger aperture of a telescope to produce fringes. He introduced also for the first time the concept of fringe visibility and its application in the field of spatial interferometry. It remains as probably the most famous of his experiments the two 6-inch aperture Michelson stellar interferometer mounted in Mount Wilson, whose construction, although with some additional components, is nowadays still used in some of the most modern observatories. Interferometry found also its application in the middle of the XX century in radio astronomy, partially due to the technical developments that the Second World War forced. In the '70s, Antoine Labeyrie proposed a variation using only one aperture – the so-called speckle interferometry –, and for the first time the coherent combination of light using two separated telescopes was carried out, establishing the basis of modern long-baseline interferometry. Since then on it has become one of the most developed observational techniques that allows us to obtain higher resolution.

Long-baseline interferometry supposes the simultaneous observation with two or more single apertures separated a distance B – called baseline – to combine beams of light coming from an astronomical source. The angular resolution defined by λ/B enables to separate the telescopes large distances, much larger than the diameter of a single element. Besides the VLTI and ALMA, other facilities, such as the Laser Interferometer Gravitational-wave Observatory (LIGO)[6] located in the United States, also operate under interferometric principles. LIGO is composed of two identical interferometers – one in Hanford and one in Livingston – separated 3002 km with the purpose of noise calibration (Fig. 3.3). Each of them consists of two 4 km arms arranged in the shape of "L" with laser detectors, whose primary scientific mission is to detect gravitational waves. Although electromagnetic radiation is not detected, it accomplishes all basic principles of a Michelson interferometer.

3.2.1 Theoretical principles of interferometry

In this section I introduce the basic principles of stellar interferometry. This is based on vast and detailed information publicly available in online resources, as well as in books and publications [e.g. Lawson, 2000, Labeyrie et al., 2006, Haniff, 2007a, Millour, 2008, Glindemann, 2011].

Light from an astronomical source in the sky travels through the space and brings information on the shape and spectrum of the object. This information is received by an optical system and decoded to provide the insight on its spatial and spectral intensity distribution.

Monochromatic wave received by one optical detector

Let us consider the electric field vector $\vec{E}$ of an electromagnetic wave as a function of space and time. Under the assumption that the wave is plane monochromatic and propagates in vacuum along the z-direction (Fig. 3.4), the x-component of $\vec{E}$ can be written as

$$E_x = E_{x0} \cos(\omega t - kz) \tag{3.1}$$

[6] Website: `www.ligo.org`; `www.ligo.caltech.edu`

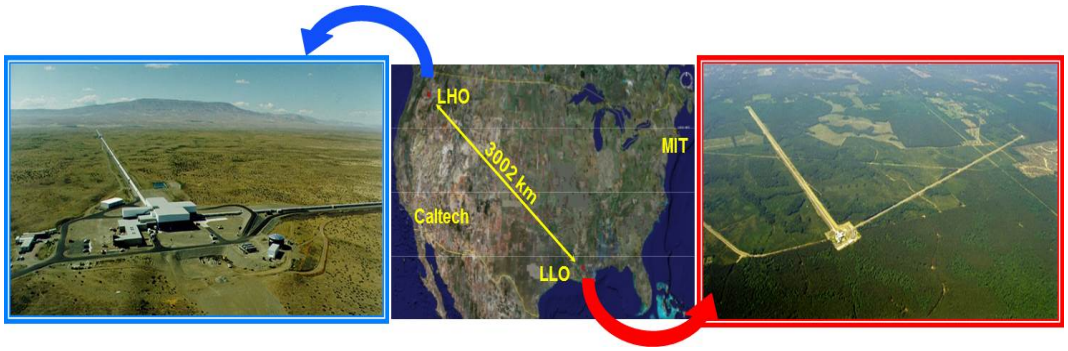

Figure 3.3: LIGO project consisting of two separated identical Michelson interferometers located in Hanford (left) and Livingston (right). Their laser arms are used as gravitational-wave detectors. [Credit: Caltech/MIT/LIGO Lab]

where $\omega = 2\pi\nu$, t is the time, $k = 2\pi/\lambda$ is the wave vector[7], ν is the frequency and λ is the wavelength of the monochromatic wave. The expression $\omega/k = \nu\lambda$ is the phase velocity. In the same manner also the y-component can be described. If the cosine functions of the x- and y-components are in phase, and thus the phase difference $\varphi = 0$, then the vector $\vec{E}$ oscillates in a plane (linear polarization). If the components are not in phase and $\varphi = \pi$, then the vector describes a circle (circular polarization). And, if the components are not in phase, but $\varphi \neq \pi$, then the vector describes an ellipse (elliptical polarization).

The electromagnetic wave contains also a magnetic field component $\vec{H}$. However, since hereafter only the propagation of a wave in isotropic media is described, it is not taken into account.

Optical detectors do not measure the electric field of an electromagnetic wave directly. The physical quantity that can be experimentally observed is the intensity related to the energy flow density given by the Poynting vector of the form

$$\vec{S} = \vec{E} \times \vec{H}. \tag{3.2}$$

The Poynting vector is orthogonal to the vectors $\vec{E}$ and $\vec{H}$, pointing to the direction of propagation along the z-axis if $\vec{E}$ is linearly polarized in the x-direction. Then, the component in the z-direction of the Poynting vector can be written as

$$S_z = c\,\varepsilon_0\,E_{x0}^2\cos^2(\omega t - kz). \tag{3.3}$$

Here, S_z has a dimension of W m^{-2}. c is the speed of the light in vacuum[8], and ε_0 is the permittivity of vacuum[9].

The Poynting vector oscillates with twice the frequency ν of the electromagnetic wave, i.e. some 10^{15} Hz in the optical range. Because the temporal resolution of the detectors is lower than 10^{-15} s, only an average time of the Poynting vector can be obtained according to

$$\langle S_z \rangle = \lim_{T\to\infty} \frac{1}{2T} c\,\varepsilon_0 \int_{-T}^{T} E_{x0}^2\cos^2(\omega t - kz)\mathrm{d}t = \frac{c\,\varepsilon_0}{2}E_{x0}^2. \tag{3.4}$$

[7] A general definition of the wave vector is $k = 2\pi n/\lambda = \omega n/c$, where n is the refractive index of the medium. $n = 1$ for the case of vacuum.

[8] $c = 2.998 \times 10^8 \mathrm{m\ s^{-1}}$. In a non-vacuum medium the speed of light is c/n.

[9] $\varepsilon_0 = 8.854 \times 10^{-12} \mathrm{F\ m^{-1}}$. In a non-vacuum medium the permittivity has to be multiplied also by ε, the dielectric constant of the material.

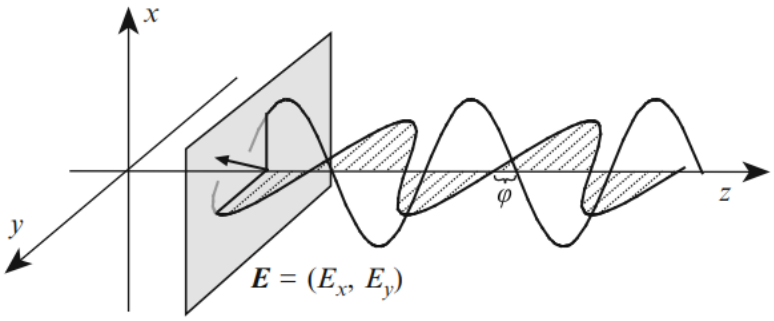

Figure 3.4: Propagation of an electromagnetic wave with electric field $\vec{E}$ along the z-direction. The projections on the x- and y-components describe the type of polarization according to the phase difference φ. [Credit: Glindemann [2011]]

This time-average of the Poynting vector is known as flux of the electromagnetic wave, and its units are W m^{-2}. In an optical detector, the measured quantity is the integral of the flux over the whole area of the detector, meaning the power in units of Watt.

To study the spatial flux distribution, it is convenient to introduce a dimensionless quantity known as the optical disturbance $v(\vec{r}, t)$, which is proportional to one component of the electric field (e.g. $v = CE_x$, where C is a constant to make v dimensionless)[10]. Also, for mathematical purposes, the optical disturbance of the electric component E_x propagating in the z-direction can be expressed as a complex quantity, as follows

$$v(z,t) = v_0 \cos(wt - kz) - \mathrm{i}\, v_0 \sin(wt - kz) = v_0\, e^{-\mathrm{i}(wt-kz)} \tag{3.5}$$

remarking that, besides this complex consideration, only the real part has physical significance representing the electromagnetic wave.

The purpose of achieving the intensity as a dimensionless quantity, but proportional to $\langle S_z \rangle$ and thus the signal measured with the detectors, is achieved by the time-average of the product $v\, v^*$, where * denotes the complex conjugate

$$I(z) := \lim_{T\to\infty} \frac{1}{2T} \int_{-T}^{T} v(z,t)\, v^*(z,t) \mathrm{d}t = v_0^2. \tag{3.6}$$

Another time-independent dimensionless quantity, the amplitude $V(\vec{r})$ at frequency ν, is conveniently introduced to describe the propagation of light in space. Consequently, the monochromatic optical disturbance can be written as

$$v(\vec{r}, t) = V(\vec{r}) e^{-\mathrm{i}2\pi\nu t}. \tag{3.7}$$

According to Eq. 3.6, it can be seen that

$$I(\vec{r}) = |V(\vec{r})|^2. \tag{3.8}$$

[10]The linear interaction of optical systems, e.g. astronomical telescopes, with the amplitude and phase of the incoming light can be also represented as a complex transfer function. After the interaction between light and optical system, the resulting wave is calculated as the product of both complex functions, the optical disturbance and the transfer function.

Polychromatic wave received by one optical detector

So far, only the monochromatic case has been considered. For the case of polychromatic light, the polychromatic optical disturbance is determined by the superposition of individual monochromatic waves, and the amplitude, instead, is replaced by the time-independent spectral amplitude $V(\vec{r},t)$. Subsequently

$$v(\vec{r},t) = \int_0^\infty V(\vec{r},t)e^{-\mathrm{i}2\pi\nu t}\mathrm{d}\nu. \tag{3.9}$$

Here, the units of $V(\vec{r},t)$ are expressed in Hz^{-1}. In practice, the imaginary part of the optical disturbance can be ignored only if the real part containing all the information is restricted to the positive frequencies. The spectral amplitude is zero for negative frequencies. Theoretically, one can extend the integration interval to $-\infty$, then the optical disturbance $v(\vec{r},t)$ can be determined through the Fourier transform of the spectral amplitude $V(\vec{r},t)$.

Analogously to the monochromatic intensity, the polychromatic spectral intensity takes the form

$$I(\vec{r}) = \int_0^\infty I(\vec{r},\nu)\mathrm{d}\nu. \tag{3.10}$$

The dimension of the spectral density $I(\vec{r},\nu)$ is Hz^{-1}, and it is proportional to the flux density in units[11] of Jansky or W $\mathrm{m}^{-2}\mathrm{Hz}^{-1}$.

Similarly to Eq. 3.8, the spectral intensity is also related to the spectral amplitude as

$$I(\vec{r},\nu) = |V(\vec{r},\nu)|^2. \tag{3.11}$$

The effects and propagation of light in space are generally described by $V(\vec{r})$ or $V(\vec{r},t)$, and $I(\vec{r})$. It is important to mention that the relative straightforward link between the monochromatic and the polychromatic case is valid because, as stated before, detectors measure only the time-average intensity.

Measurements with an interferometer

So far, only the detection by one optical detector has been deduced. However, interferometric detections consist of the combination of beams of light acquired simultaneously with two or more elements. The handling of such combination benefits also from the principle of superposition which establishes that the resulting intensity of a wave is determined by the sum of intensity of each individual component.

The experiment conducted by Thomas Young in 1802 is especially illustrative for the mathematical treatment of this phenomenon (Fig. 3.5). It consists of two pinholes separated a distance B that receive the light from a distant source (large enough to consider it as a plane wave). Once the light goes through these pinholes (considered as point sources), the light is diffracted and the spherical waves[12] outcoming from the pinholes interfere. A diffraction pattern – or fringe pattern – can be observed on a screen located at a distance z_1.

The shape of the fringe pattern acquired by an interferometer (or the Young's experiment) depends on whether the detection is monochromatic or along a spectral width, and on whether the emitting object is a point or extended source. For this reason, I present the following three cases:

a) Monochromatic observation of a point source

[11] 1 Jy = 10^{-26} W $\mathrm{m}^{-2}\mathrm{Hz}^{-1}$

[12] According to the Huygens-Fresnel principle of elementary waves that form the basis of diffraction theory.

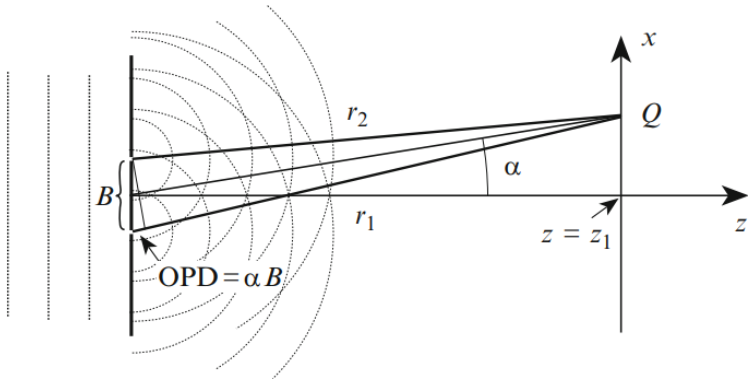

Figure 3.5: Scheme of Young's experiment. Two pinholes in the aperture plane with a separation B receive a plane wave. On a screen at distance z_1 the diffracted waves from the pinholes interfere to produce a fringe pattern. [Credit: Glindemann [2011]]

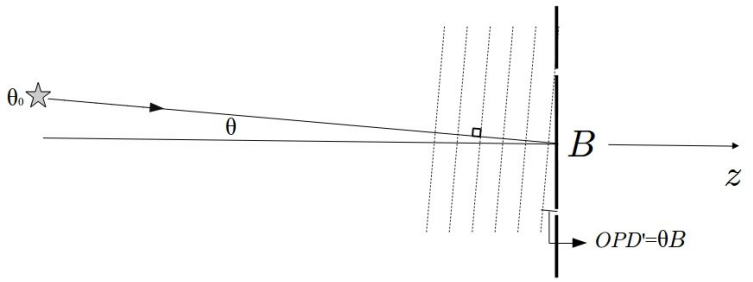

Figure 3.6: The scheme depicts an extended light source with angular diameter θ_0, whose position at an angle θ in the source plane influences the spatial coherence and introduces and additional OPD'. This effect causes a reduction in the contrast of the fringe pattern.

The spectral amplitude of a spherical wave at a distance $r = |\vec{r}|$ can be written as

$$V(\vec{r}, \nu) = \frac{V_0}{r} e^{\mathrm{i}kr} \tag{3.12}$$

and following Eq. 3.11, the spectral intensity as the squared modulus of the amplitude takes the form

$$I(\vec{r}, \nu) = \frac{V_0^2}{r^2}. \tag{3.13}$$

Now, considering the amplitude at a point Q with coordinates $(x, 0)$ on the screen, the sum of the two spherical waves coming from the pinholes is

$$\begin{aligned} V(x, \nu) &= \frac{V_0}{r_1} e^{\mathrm{i}kr_1} + \frac{V_0}{r_2} e^{\mathrm{i}kr_2} \\ &= \frac{V_0}{z_1} e^{\mathrm{i}\left(\frac{k(r_1 - r_2)}{2}\right)} 2\cos\left(\frac{k(r_1 - r_2)}{2}\right) \end{aligned} \tag{3.14}$$

where r_i are the distances from each pinhole to the point Q, and the approximation $r_1 = r_2 = z_1$ is implemented for the amplitudes V_0/r_i with $i = 1, 2$.

Subsequently, the spectral intensity of this last amplitude is defined as

$$I(x,\nu) = |V(x,\nu)|^2 = \left(\frac{V_0}{z_1}\right)^2 2\left(1+\cos(k(r_1-r_2))\right) = I_0\left(1+\cos(k(r_1-r_2))\right). \tag{3.15}$$

From Fig. 3.5 it can be deduced that for small diffraction angles α, the expression $\alpha = x/z_1$ and $r_1 - r_2 = \alpha B$ are valid. This last expression is known as optical path difference (OPD) between the optical paths from each pinhole to the point of observation. A difference in OPD from each pinhole supposes also a difference in arrival time, called time delay τ between the light from the two pinholes. The relation between time delay and optical path length is given by $\tau = \alpha B/c$, where c is the speed of light in vacuum.

By replacing the value of OPD in Eq. 3.15, I finally obtain the monochromatic distribution of the diffraction pattern as a function of the diffraction angle α

$$I(\alpha,\nu) = I_0\left(1+\cos(k\alpha B)\right). \tag{3.16}$$

This final intensity distribution is known as fringe pattern due to its cosinusoidal shape on the screen. Reminding that the wave vector in the vacuum is $k = 2\pi/\lambda$ and the properties of the cosine function, I can deduce that the first intensity minimum of this fringe pattern is found at $\alpha_{\min} = \lambda/(2B)$, and the OPD at this minimum is $r_1 - r_2 = \lambda/2$. Consequently, the time delay would equal $\tau = (\lambda/2)/c = 1/(2\nu)$. In the representation of the fringe patterns of Fig. 3.7, panel a) shows an individual monochromatic pattern obtained for a pinhole separation of 10 cm at $\lambda = 2.2\,\mu$m. Also, in panel b), for the same pinhole separation, it can be seen the independent monochromatic patterns at wavelengths 2, 2.2 and 2.4 μm, each showing a shifted first intensity minimum (blue, green and red lines, respectively). On the contrary, all of their intensity maximum coincide for a zero OPD, at $\alpha = 0$, known as the white-light fringe.

The monochromatic fringes have contrast values that oscillate between 0 and 1. Formally, this contrast, called fringe visibility, adopts the form

$$\mathcal{V} = \frac{I_{\max} - I_{\min}}{I_{\max} + I_{\min}}. \tag{3.17}$$

The measured dimension by stellar interferometry is the contrast of the fringes. A contrast of 1 in the fringe pattern, meaning perfect constructive and destructive interference in the maxima and minima, supposes that the light waves outcoming from the pinholes are perfectly coherent. This is the case of monochromatic plane waves. The word coherence describes the level of "good" or "bad" coherence between light waves. A perfect coherence results in a contrast of 1, and on the opposite, if there is no coherence, no fringe pattern will be formed, in which case the light is called incoherent.

b) Polychromatic observation of a point source

If instead of considering only monochromatic waves, one considers a finite spectral bandwidth $\Delta\nu$ of the light source, the resulting fringe pattern is obtained by adding up the individual interference patterns (following Eq. 3.16) to obtain the observed intensity distribution. This bandwidth dependence introduces what is known as temporal coherence, and reduces more the contrast of the fringe pattern the more the diffraction angle α, or in other words, the longer the time delay τ. The time delay related to the quasi loss of fringe contrast is called coherence time τ_c, which is proportional to the reciprocal of the spectral bandwidth $\Delta\nu$. From this definition, also the coherence length can be defined as $l_0 = c/\tau_0$.

Mathematically, this case can be deduced by integrating Eq. 3.16 over a wave vector (wavelength or frequency) with interval Δk and central value k_0, where $k_0 = 2\pi/\lambda_0$. Thus

$$\begin{aligned} I(\alpha, \Delta k) &= \int_{k_0-\frac{\Delta k}{2}}^{k_0+\frac{\Delta k}{2}} I_0 \left(1 + \cos(k\alpha B)\right) \mathrm{d}k \\ &= \int_{k_0-\frac{\Delta k}{2}}^{k_0+\frac{\Delta k}{2}} I_0 \mathrm{d}k + I_0 \int_{k_0-\frac{\Delta k}{2}}^{k_0+\frac{\Delta k}{2}} \cos(k\alpha B)\mathrm{d}k \\ &= I_0\Delta k + I_0 \left(\sin\left(\left(k_0 + \frac{\Delta k}{2}\right)\alpha B\right) - \sin\left(\left(k_0 - \frac{\Delta k}{2}\right)\alpha B\right)\right) \\ &= I_0\Delta k + I_0 \left(\sin\left(\alpha B k_0 + \alpha B\frac{\Delta k}{2}\right) - \sin\left(\alpha B k_0 - \alpha B\frac{\Delta k}{2}\right)\right). \end{aligned} \tag{3.18}$$

Then, by reminding the trigonometric identities $\sin(m+n) = \sin(m)\cos(n)+\cos(m)\sin(n)$ and $\sin(m-n) = \sin(m)\cos(n)-\cos(m)\sin(n)$, and applying them to the last expression, it results

$$I(\alpha, \Delta k) = I_0 \left(\Delta k + 2\cos\left(\alpha B k_0\right)\, \sin\left(\alpha B\frac{\Delta k}{2}\right)\right). \tag{3.19}$$

Eq. 3.19 produces a fringe pattern as the one shown with black line in panel b) of Fig. 3.7 for K-band (2.2±0.2 μm), where the sum of the monochromatic components determines the resulting pattern.

Another characteristic of the fringe pattern, namely the number of fringes observed in a pattern, can be deduced from the knowledge that the fringes are faded at an incident angle $\alpha = \pm\tau_c c/B = \pm 1/\Delta\nu\ \lambda\nu/B = \pm\nu/\Delta\nu\ \lambda/B$. Then, with a fringe spacing of λ/B, and the expression $\Delta\nu/\nu = \Delta\lambda/\lambda$, one obtains that the number of fringes is $2\lambda/\Delta\lambda$.

c) Observation of an extended source

Whereas a spectral bandwidth $\Delta\nu$ influences the temporal coherence, the size of the light source influences the fringe contrast and consequently the spatial coherence of the light. A spatial incoherent source, e.g. a star, is an object where each point on its surface radiates independently from its neighbour point. To determine the fringe pattern created in this case, it is considered that the distant source, whose monochromatic waves arrive at the pinholes of the Young's experiment in Fig. 3.5, has an angular size θ_0. If the incident angle θ of the wavefront is not perpendicular to the aperture plane (denoting the position of the distant light source), then an additional delay term $\mathrm{OPD}' = \theta B$ is added to the OPD (Fig. 3.6). Then, the monochromatic intensity distribution can be obtained by integrating the function $I(\alpha, \theta) = I_0(1 + \cos(k(\alpha + \theta)B)))$ (similar to Eq. 3.16 but dependent on both the diffraction angle α and the position of the source θ) over the angular diameter in the interval $[-\theta_0/2, \theta_0/2]$, which leads to

$$\begin{aligned} I(\alpha) &= \int_{-\frac{\theta_0}{2}}^{\frac{\theta_0}{2}} I(\alpha, \theta)\mathrm{d}\theta \\ &= \int_{-\frac{\theta_0}{2}}^{\frac{\theta_0}{2}} I_0 \left(1 + \cos(k(\alpha + \theta)B)\right) \mathrm{d}\theta \\ &= \int_{-\frac{\theta_0}{2}}^{\frac{\theta_0}{2}} I_0 \mathrm{d}\theta + \int_{-\frac{\theta_0}{2}}^{\frac{\theta_0}{2}} I_0 \cos(k(\alpha + \theta)B)\mathrm{d}\theta. \end{aligned} \tag{3.20}$$

The first term of this last expression is an integral over the source intensity. Now, the second

term can be further analysed. Namely, the cosine term can be expressed as

$$\begin{aligned}\cos(k(\alpha+\theta)B) &= \mathrm{Re}\left(e^{-\mathrm{i}k(\alpha+\theta)B}\right)\\ &= \mathrm{Re}\left(e^{-\mathrm{i}k\alpha B}e^{-\mathrm{i}k\theta B}\right)\end{aligned} \tag{3.21}$$

where the first factor depending on the diffraction angle α can be extracted, and only the second factor depends on θ. Consequently, this θ-depending factor can be written in terms of the Fourier transform of the function $I(B)$ as

$$\mathfrak{F}(I(B)) = \int I(\theta)e^{-\mathrm{i}k\theta B}\mathrm{d}\theta. \tag{3.22}$$

In this equation, the baseline B is the distance between the pinholes at Young's experiment – or between telescopes at an interferometer–. The Fourier transform can be explained as the relation between the coordinate spaces θ of the source plane and B of the aperture plane. In a two-dimensional system, these two planes can be given in vectorial form as $\vec{\theta}$ and $\vec{B}$, respectively. Therefore, turning back attention to Eq. 3.20, it can be rewritten as

$$\begin{aligned}I(\vec{\alpha}) &= I_0\left(1+\mathrm{Re}\left(\mu(\vec{B})e^{-\mathrm{i}k\vec{\theta}\vec{B}}\right)\right)\\ &= I_0\left(1+|\mu(\vec{B})|\cos(\phi(\vec{B})+k\,\vec{\theta}\,\vec{B})\right)\end{aligned} \tag{3.23}$$

where the integral over the source intensity $\int I_0\mathrm{d}\theta$ has been denoted as simply I_0, and the Fourier transform $\mathfrak{F}(I(B))$ as $\mu(\vec{B})$. The complex function $\mu(\vec{B})$ is known as visibility function, and $\phi(\vec{B})$ is its phase defining the position of the central white-light fringe. If $|\mu(\vec{B})| = 1$, then the fringe contrast is 1. On the contrary, no fringe pattern is observed if $|\mu(\vec{B})| = 0$. Formally, the visibility function can be expressed as

$$\mu(\vec{B}) = \frac{\int I(\vec{\theta})e^{-\mathrm{i}k\vec{\theta}\,\vec{B}}\mathrm{d}\vec{\theta}}{I_0} \tag{3.24}$$

and this definition relating through a Fourier transform the intensity distribution of the object $I(\vec{\theta})$ to the visibility fringe pattern is known as van-Cittert-Zernike theorem. This theorem is the cornerstone of spatial interferometry, and the quantities $|\mu(\vec{B})|$ and $\phi(\vec{B})$ are the measures obtained spatial interferometers.

A fringe pattern produced for a monochromatic extended source with a diameter of 2 arcsec is shown in panel c) of Fig. 3.7. The black curve resulting of adding up the monochromatic patterns with different incident angles demonstrates the reduction in contrast.

Similarly to the case of a point source, also an extended source along a bandwidth can be obtained by adding up the monochromatic patterns at different wavelengths. In this case the pattern will be both reduced in contrast and faded away from the central fringe for increasing diffraction angles. The panel d) of Fig. 3.7 displays an example of fringe pattern in the K-band (black curve) obtained for a source with a 2 arcsec angular size.

Optical Path Difference (OPD) correction

As seen from the Young's experiment, the coherent interference of the outcoming light from the pinholes demands a correction of the OPD. Moreover, since the relative position of the light source to the individual pinholes, or telescopes, may be also different, this introduces an additional "spatial delay". Three factors of OPD affects can de identified:

- *Internal (geometrical) effects*: Produced by the difference in optical path length (OPL)

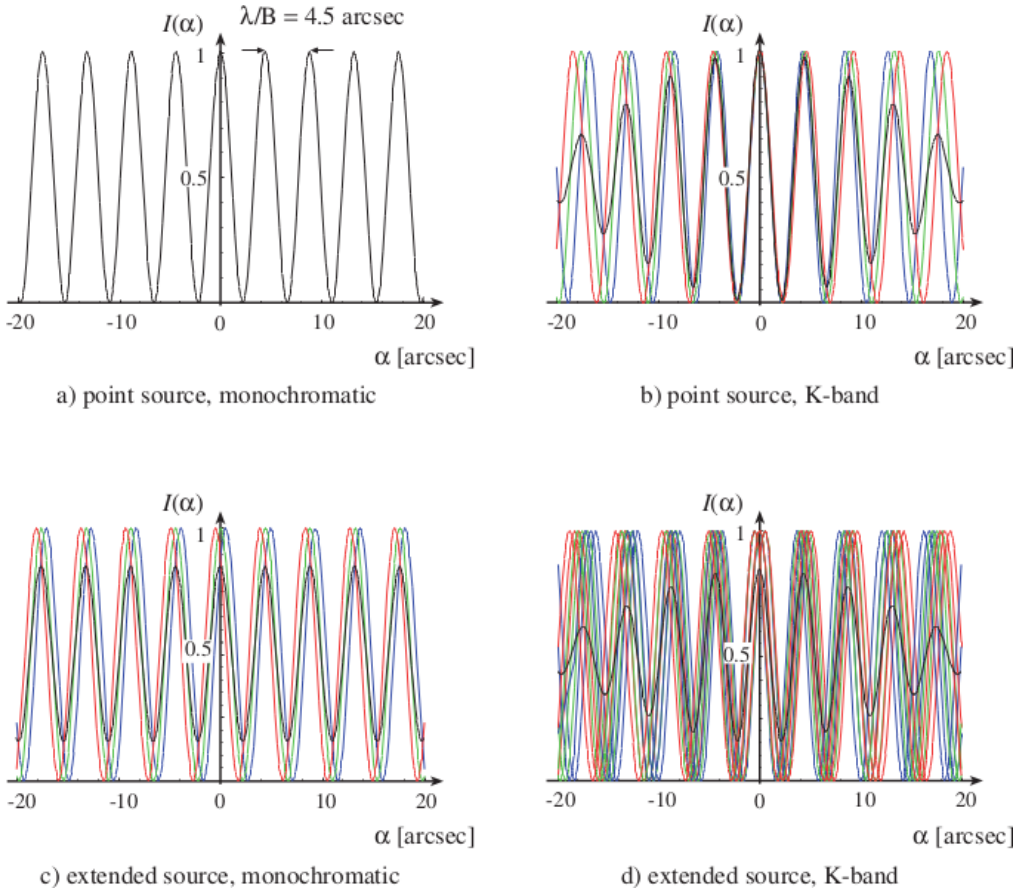

Figure 3.7: Fringe patterns produced by two pinholes separated 10 cm, where the intensity distribution is a function of the diffraction angel α. a) A monochromatic fringe pattern is illustrated. b) The sum of monochromatic patterns at 2 (blue lines), 2.2 (green lines) and 2.4 μm (red lines) create the black-curve pattern for a point source. c) A sample of monochromatic fringe patterns for an extended source of 2 arcsec in angular diameter is displayed. The resulting monochromatic fringe pattern traced with black lines is the sum of monochromatic fringe patterns with different incident angle, showing a reduction in contrast. d) A polychromatic pattern over the K-band is shown. In this case a spatial and temporal coherence influence the shape of the pattern, reducing it in contrast and fading it away from the central wavelength. [Credit: Glindemann [2011]]

of the telescopes, from their primary mirror to the point of beam combination.

- *External (sidereal) effects*: Caused by the diurnal motion of the source due to Earth's rotation and its position in relation to the baseline vector between the telescopes.

- *Rapid effects*: Originated from vibration in mechanical components and rapid atmospheric fluctuations.

For this reason, after the wavefront of a distant source arrives at the telescopes at different times, it goes through a complex optical system that compensates the OPD before the fringes are obtained in the interferometric laboratory. In the case of the VLTI described later, delay lines (DL) are used in an interferometric tunnel for corrections with nanometre accuracy (Fig. 3.10).

uv-plane coverage

The visibility function can be written in terms of the coordinates (α, β) of the intensity distribution $I(\vec{\theta})$ and in terms of the coordinates (u, v) of the baseline vector $\vec{B}$, where u and v are related to the baseline vector through its projection components on the two axes: $u = B_u/\lambda$ and $v = B_v/\lambda$, where λ is the wavelength. Therefore, the uv-plane is defined as the plane of the spatial frequencies u and v. Subsequently, Eq. 3.24 becomes

$$\mu(u, v) = \frac{\int\int I(\alpha, \beta) e^{-2\pi \mathrm{i}(\alpha u + \beta v)} \mathrm{d}\alpha \mathrm{d}\beta}{I_0} \tag{3.25}$$

where the value of the wave vector in the vacuum $k = 2\pi/\lambda$ has been taken into account.

Astronomical interferometers sample the visibility function, which is the Fourier transform of the angular brightness distribution of the observed object. Interferometers achieve unique angular resolution, however, it can be observed that one baseline configuration sample only one point in the frequency domain of Eq. 3.25, and therefore provides information along only one angular direction of the source plane. In order to gain more information about the observed object, it is indispensable to acquire as many uv-points as possible. The limitations of long-baseline interferometry to achieve a complete uv-coverage is known as the "uv-problem". There are three ways of dealing with such a problem [e.g. Ségransan, 2007, Millour, 2014]:

- *Supersynthesis*: It means that the rotation of Earth relative to the celestial sphere produces a baseline change with time, and elliptical uv-tracks are formed.

- *Adding more telescopes*: An increment of the number of telescopes increases the number of uv-points according to the relation $N_{\mathrm{baselines}} = N_{\mathrm{tel}}(N_{\mathrm{tel}} - 1)/2$.

- *Observations at different wavelengths*: Bandwidth observations improve the uv-plane thanks to the wavelength dependence of the spatial frequencies as $\propto 1/\lambda$.

Obtaining an extended uv-coverage with optical and infrared interferometers is still limited with current facilities due to the limited number of offered apertures and the big amount of observational time required to fill the uv-plane. On the contrary, as seen before, radio-telescopes as ALMA do take advantage of their capacities and construction (e.g. uv-plane in Fig. 3.2). Nevertheless, the interpretation of interferometric measurements in optical and infrared bands is possible thanks to the construction of numerical models to reproduce the interferometric signals. Furthermore, image reconstruction (Fig. 3.8) may be plausible with numerical algorithms for measurements of several spatial frequencies and differential phases [e.g. Baron, 2016, Thiébaut and Young, 2017].

3.2.2 The Very Large Telescope Interferometer

Previously, I had remarked the Very Large Telescope Interferometer (VLTI) as one the most – if not the most – advanced and modern interferometric facilities observing at infrared spectral ranges and allowing to characterize with high-angular resolution the circumstellar environment of YSOs. Here, I provide a deeper glance at the VLTI, and especially at the MIDI instrument used for this program, since the observational data used for my research was accomplished with this tool.

The VLTI[13] located on Paranal, Chile, is the facility of the European Southern Observatory (ESO) that combines the independent Unit Telescopes (UTs) of the VLT and the

[13]Website: `www.eso.org/sci/facilities/paranal/telescopes/vlti`

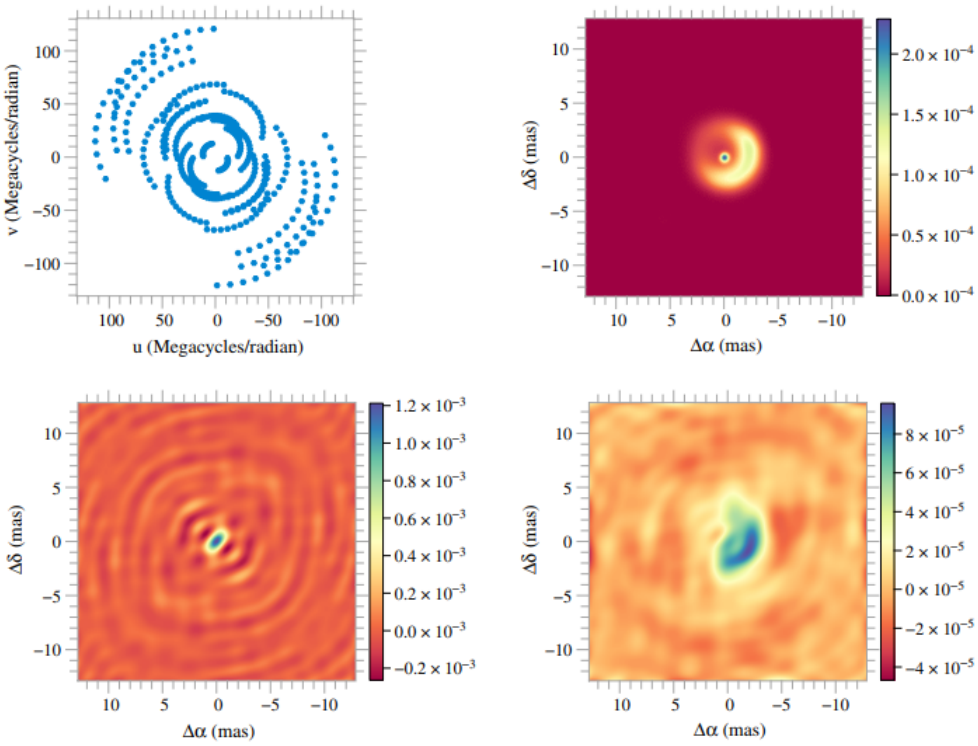

Figure 3.8: Interferometric observations with the Navy Prototype Optical Interferometer (NPOI) and reconstructed image of the Herbig Be star LkHa 101 and its circumstellar disk. *Top left*: Simulated uv-coverage sampled with a six-station. *Top right*: Model of the observed object. *Bottom left*: Dirty beam. *Bottom right*: Dirty image. [Credit: reprinted with permission from Thiébaut and Young [2017], Lawson et al. [2004], Journal of the Optical Society of America]

Auxiliary Telescopes (ATs) to work as a potent interferometer in near- and mid-IR bands (see Fig. 3.9). Each of the four UTs has a main mirror of 8.2 m, and their edge-to-edge maximum baseline reaches 130 m, which means a maximum spatial resolution λ/B of 16 mas at 10 μm or 3.2 mas at 2 μm. On the other hand, the four ATs that can be configured on 30 different stations have a main mirror of 1.8 m and a longest baseline of 200 m, providing a resolution of 10.3 mas at 10 μm or 2 mas at 2 μm. Unlike the UTs, the ATs are designed to exclusively work in interferometric mode. The VLTI is probably the best ground-based observatory of the world that combines all the advantages of interferometry with the ones of adaptive optics (Multi Application Curvature Adaptive Optics (MACAO) and Coudé Infrared Adaptive Optics (CIAO) for the UTs, System for Tip/tilt Removal with Avalanche Photodiodes (STRAP) and New Adaptive Optics Module for Interferometry (NAOMI) for the ATs) and stabilization devices (Fringe-tracking Instrument of NIce and TOrino (FINITO) and InfraRed Image Sensor (IRIS)).

3.2.2.1 First generation instruments

Two interferometric instruments working in the near-IR (PIONIER and AMBER), and one in the mid-IR (MIDI) are part of the first generation tools mounted on the VLTI.

The **Precision Integrated-Optics Near-infrared Imaging ExpeRiment (PIONIER)** is a 4-beam combiner instrument of the VLTI offered to the community from P96 onward [Le Bouquin et al., 2011]. The combination of 4 UTs or ATs in H-band provides, simultaneously,

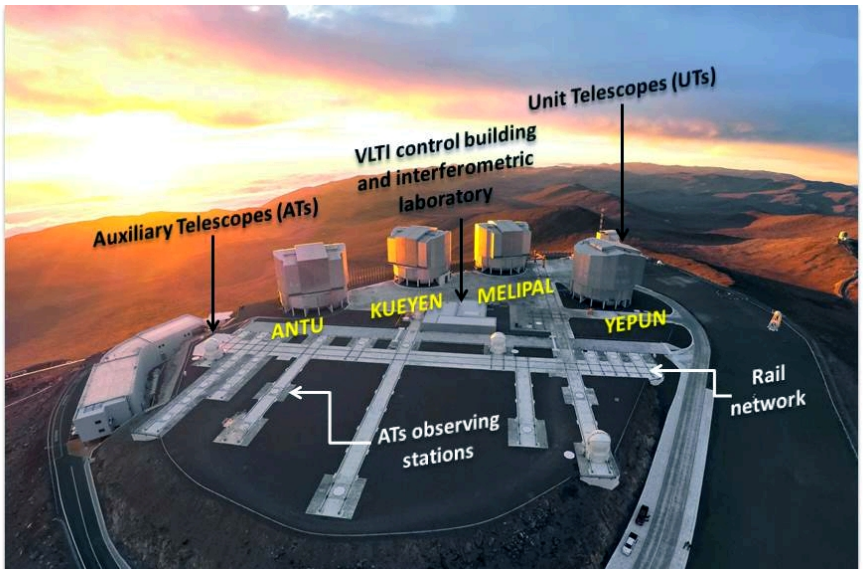

Figure 3.9: ESO's VLTI facility at 2635 m.a.s.l. on Cerro Paranal, Chile. The light collected by the UTs or ATs is combined in the interferometric laboratory. A rail network permits the ATs adopting 30 different stations depending on the needs of the observing project. [Credit: adapted from M. Struik (CERN)/ESO]

visibilities at six different baselines and four closure phase measurements. Its spectral capabilities are limited to one spectral channel ($\Delta\lambda/\lambda = 5$) or 6 spectral channels ($\Delta\lambda/\lambda = 30$). It is the first beam combiner using integrated optics (IO) technology, which brings significant advantages in terms of performance and instrumental design to face a new era of interferometric instruments.

The **Astronomical Multi-BEam combineR (AMBER)** combines interferometrically three UTs or ATs of the VLTI [Petrov et al., 2007]. It has been for the last time offered for observing period P101 (1 April – 30 September 2018) before decommissioning. It operates in H- and K-band, with spectral modes in low resolution ($\Delta\lambda/\lambda = 35$) for both bands (LR-K, LR-H), medium resolution ($\Delta\lambda/\lambda = 1500$) for both bands (MR-K, MR-H), and high resolution ($\Delta\lambda/\lambda = 12000$) in K-band (HR-K). AMBER can be used either as a self-coherencing fringe tracker or in conjunction with FINITO. The output set of an AMBER observation consists of visibilities, differential phases and one closure phase, which is the sum of the phases of the 3 baselines inside a triangle.

The **MID-infrared Interferometric instrument (MIDI)** was a two telescope beam combiner operating in the N-band (8–13 μm), either with the UTs or ATs [Leinert et al., 2003a, Chesneau, 2007]. It was decommissioned in March 2015 for preparing the upcoming second generation instruments. The observing mode of MIDI is the case of a coaxial beam combination, namely, it first modulates the internal delay and then detects the consequent temporal variations of the intensity.

Observation in the mid-IR spectral range are affected by atmospheric turbulence and transmission affected by molecular species such as O_3 (9.6 μm), CO_2 and H_2O (Fig. 3.11). Additionally, the thermal radiation of the atmosphere and telescope adds up additional complications, especially when observing faint targets. In the case of MIDI, the observations are particularly affected by 27 (UTs) or 24 (ATs) reflections that radiate like a blackbody. The chopping method helps in the discount of this effect, meaning high-frequency switching between the target and an empty sky region by moving the secondary mirror of the telescope for its subsequent background subtraction.

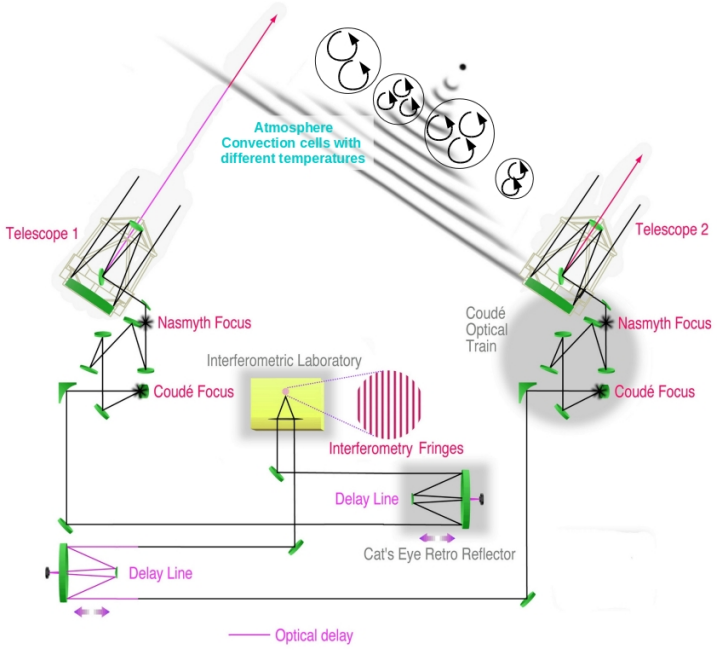

Figure 3.10: Optical layout of an interferometric observation with two telescopes at the VLTI. The scheme shows the hardware complexity of the process since the wavefront of a distant source arrives at the apertures until the detector measures the fringes in the interferometric laboratory. The atmosphere consists of convective cells that distort the wavefront and affect the OPD. The MACAO system is placed in the Coudé focii of the UTs. [Credit: adapted from Glindemann et al. [2003], ESO]

The optical setup of MIDI in the interferometric laboratory consists of warm optics, cold optics (contained in a cryostat), an infrared CO_2 laser used for calibration, and the electronic and cooling systems. As seen in Fig. 3.12, after the beams of the two telescopes are OPD-corrected by piezo-driven roof mirrors, they enter the cryostat. Then, the first stop pupil suppresses the outside thermal emission and the beams are directed to spatial filters that restrain other unwanted radiation. The two beams are recollimated and continue to be combined on the surface of a 50–50% beam splitter, close to the reimaged pupil plane. Spectral information can be obtained by dispersing the image with a PRISM (low spectral resolution, $\Delta\lambda/\lambda = 30$) or a GRISM (intermediate spectral resolution, $\Delta\lambda/\lambda = 230$). High precision flux measurements, SCI-PHOT, can be achieved by inserting 30:70 beam splitters (green in Fig. 3.12) in front of the beam combiner unit. Otherwise, in HIGH-SENS mode, the photometry is observed not simultaneously, but after the fringe tracking with no beam splitters inserted in the optical path before combination. Finally, the visibility measurements are imaged onto the detector.

The detector of MIDI elaborated by Raytheon is a 320×240-pixel Si:As Impurity Band Conduction (IBC) array. The pixel size is 50×50 μm with a peak quantum efficiency of 34%. Its operating temperature ranges 4–12 K.

3.2.2.2 Second generation instruments

Since March 2015 the VLTI operations have experienced stops with the purpose of upgrading its infrastructure in preparation for the second generation instruments GRAVITY and MATISSE. The upgrade of the interferometric laboratory began with the decommissioning

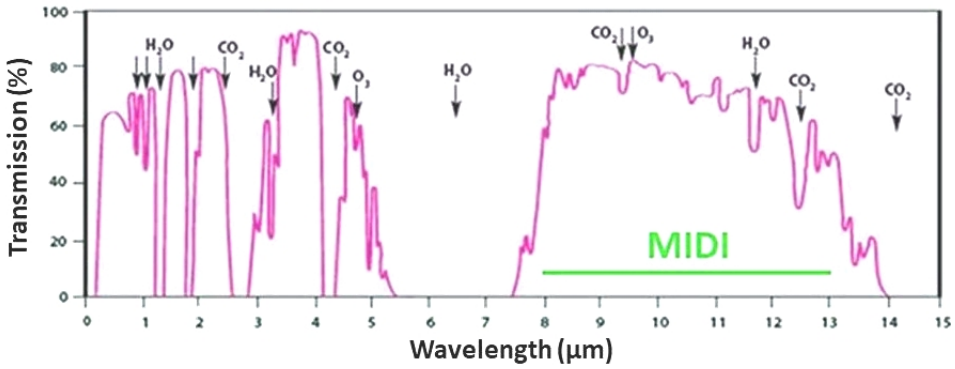

Figure 3.11: Atmospheric transmission as a function of wavelength affected by aerosol particles and other molecular species. The N-band of MIDI is especially affected by O_3 (9.6 μm), CO_2 and H_2O. The favourable astroclimate of Paranal and technical conditions of the VLTI, however, reduce the affects in observations.

of MIDI to give space to MATISSE. To make room for GRAVITY also PIONIER was moved to a new optical bench on the top of the fringe tracker FINITO. No only instruments, but also the four Coudé rooms of the UTs, the ATs, the VLTI and the Combined Coudé Laboratories, the VLTI computer room, the electrical, cryogenic, and cooling networks had to be modified and optimized.

GRAVITY [Gravity Collaboration et al., 2017a] is the first second generation instrument of the VLTI offered to the community since P98, although currently operating only in imaging mode. The high-precision astrometric mode remains under verification. It operates in the K-band (2–2.45 μm) and combines the light of four telescopes, either the UTs or ATs. GRAVITY produces in reality two sets of fringes, the science data and the fringe-tracking one. Its spectral capabilities are proposed in low resolution ($\Delta\lambda/\lambda = 20$), medium resolution ($\Delta\lambda/\lambda = 500$) and high resolution ($\Delta\lambda/\lambda = 4000$). CIAO, the infrared wavefront sensor at the Coudé focii of the UTs, has been specially implemented to operate in conjunction with this instrument. An innovative characteristic of GRAVITY is the ability to combine light from either one single source (single-field or on-axis) or from simultaneously two sources (dual-field mode or off-axis). Precisely this last one enables high-accuracy astrometric measurements and observations of faint targets with the tracking of a brighter star. The limiting magnitudes of observations for the last offered period (P101) with a seeing better than 0.6" were determined as faint as $8.5^{\mathrm{m}} + 3^{\mathrm{m}}$ for the ATs and $10.5^{\mathrm{m}} + 3^{\mathrm{m}}$ for the UTs, meaning that in dual-field mode one object has to be at most 3 magnitudes fainter than its fringe-tracking star.

The newest (since early 2018) instrument is the **Multi-AperTure mid-Infrared SpectroScopic Experiment (MATISSE)** that will cover L, M and N-band [Lopez et al., 2014]. This 4-beam combiner using the UTs or ATs will measure closure phase relations, thus favouring image reconstruction. Its spectral resolution is intended to be between 20 and 1000 in L-band, 20 and 550 in M-band, and 20 and 250 in N-band. Although AMBER and MIDI were able to study the brightest protoplanetary disks and few asteroids in our solar system, the performance of MATISSE will allow astronomers to characterize a wider sample of extrasolar systems and other minor bodies in our own. Another area of MATISSE implementation will be the study of active galactic nuclei.

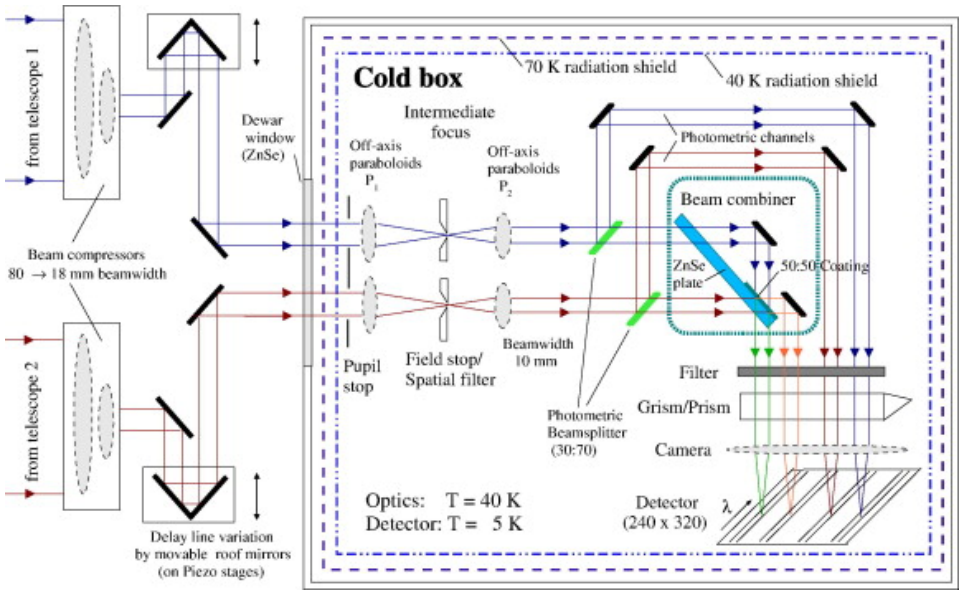

Figure 3.12: Optical schematic configuration of MIDI since the moment the beams are acquired by the two telescopes, move through the OPD corrector and enter the cold box (cryostat) to register the interferometric fringes on the detector. [Credit: Chesneau [2007], MPIA]

3.2.3 The impact of atmospheric turbulence

Ground-based optical and infrared interferometry are significantly affected by the Earth's atmosphere, and how to overcome the seeing[14] has been – and continues to be – the most important challenge for ground-based interferometers. Therefore, the exploitation of interferometric data demands the understanding and correction of spatio-temporal fluctuations produced by the atmosphere, which are typically described by a Kolmogorov model (Fig. 3.10). According to this model, the energy driving the turbulence form some "outer scales" with length L_0 (tens to a hundred of meters), within which some smaller and smaller scales eventually transform the kinetic energy of the flow into heat via viscous dissipation at the so-called "inner-scale" with length l_0. At this small spatial-scale fluctuations, the properties of the medium can be considered invariant and isotropic for observations.

The spatial fluctuations of the atmosphere are characterized by the Fried's parameter r_0 which varies with wavelength as $\lambda^{6/5}$. This parameter represents the maximum size of the diameter D of a telescope that for a given wavelength does not produce a distorted or speckled image. Table 3.1 summarizes some typical values for the seeing scale r_0 and the coherence time t_0 considered for VLTI observations at infrared wavelengths.

In interferometric observations, the visibility amplitude as a function of the ratio D/r_0 is used to estimate the impact of atmospheric fluctuations in the corrugation of the wavefront. The more problematic influence of the atmosphere in the infrared in comparison to radio interferometry can be deduced from this quantity, which is $D/r_0 \sim 10^{-3}$ for a $r_0 \sim 30$ km in the Very Long Baseline Array (VLBA), and $D/r_0 \sim 11$ for the 8 m-apertures of the UTs at the VLTI in K-band.

[14]The turbulent layers with varying refracting index n of the Earth's atmosphere produce two effects: twinkling and seeing, both with fluctuational frequencies of ∼100 Hz. Seeing implies that by observing one light source with a large optical telescope many images – speckles – are seen.

Table 3.1: Values for the Fried's parameter and the coherence time in infrared wavelengths valid for the VLTI. [Credit: Haniff [2007b]]

Wavelength λ [μm]	1.25	1.65	2.2	10.0	20.0
Fried's parameter r_0 [m]	0.39	0.55	0.77	4.7	10.9
Coherence time t_0 [s]	0.009	0.013	0.018	0.109	0.251

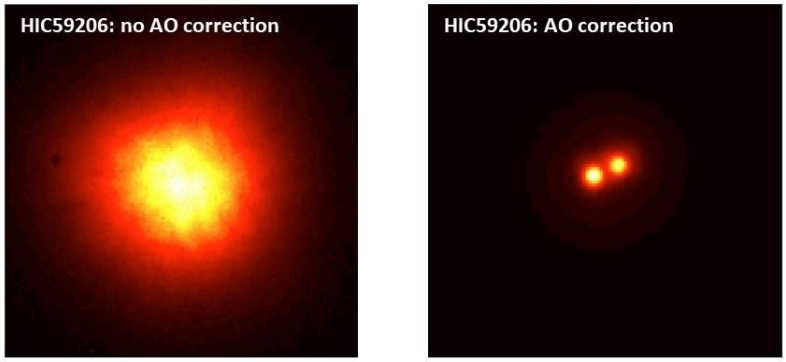

Figure 3.13: K-band image of the binary system HIC59206 without an AO system (left), and with a switched on AO correction (right). This is the first image acquired with the MACAO VLTI system that allowed to resolve the stellar pair with a separation of 120 mas. [Credit: ESO]

3.2.3.1 Adaptive optics

In order to correct the atmospheric spatial perturbations in the incoming wavefronts that cause a reduction in fringe visibility and signal-to-noise ratio, optical and interferometric ground-based interferometers implement adaptive optics (AO). This technology uses deformable mirrors controlled by computers to correct in real time the wavefront distortions caused by the atmosphere. Observations with AO demand a bright reference star within the field-of-view to measure the conditions of the local atmosphere and transmit it to the deformable mirror. In case there is no available reference star, then powerful laser beams can be used to create an artificial one. An outstanding example of such systems is the MACAO system implemented in each of the four UT Coudé focii of the VLTI (Fig. 3.10). MACAO uses a deformable mirror and a curvable wavefront sensor each with 60 elements, achieving images with diffraction-limited quality (Fig. 3.13). This corrector operates with reference stars of visible magnitude as faint as 17 mag, and at a maximum projected separation of 58" from the science target. At such on-axis conditions, a Strehl ratio of only $\sim$10% is achieved at 2.2 μm.

3.2.3.2 Fringe tracking

The temporal wavefront fluctuations induced by the atmosphere can be defined through the coherence time t_0, which measures the time over which the rms variation of the wavefront phase at a fixed point reaches one radian. Values of typical t_0 are, analogously to r_0, indicated in Table 3.1. The effect of these temporal fluctuations on interferometric observations originates from the variation in optical paths along the line of sight from the light collectors to the light source. Therefore, three distinct affects can be identified:

- Short-time fluctuations that reduce the fringes contrast, and thus the source visibility

amplitude. To eliminate this effects, exposure times less than t_0 are required.

- Long-time fluctuations causing offsets in the position of the center of the coherence envelope. These fluctuations are differently determined depending on the baseline length B. Assuming a Kolmogorov model and a baseline shorter than the outer scale, then the rms OPD is equal to $0.417\lambda(B/r_0)^{5/6}$. On the contrary, for baselines longer than the coherence length, a slow dynamic tracking of the white-light fringe motion is needed to obtain fringes.

- Phase-type fluctuations caused by the fringe motion, which results in the loss of information about the phase of the Fourier transform of the source brightness distribution.

To deal with these problems, fringe tracking techniques are applied during interferometric observations. Fringe tracking uses simultaneously the measurement of a bright star fringe position to compensate the OPD variations with a fast moving mirror, so that the fringe motion is stabilised. The bright guide star and the faint science object form what is called a dual-feed system. Instead of limiting observations to ∼millisecond exposure time, this tracking permits exposures of several seconds, improving the sensitivity by a factor of ∼100. In complement to this technique, extra equipment such as laser metrology allows to measure the OPD inside the interferometer and obtain reliable information on the visibiity function $\mu(\vec{B})$ and its phase $\phi(\vec{B})$.

In the case of the VLTI, the fringe tracking instrument is FINITO. This is a three-beam combiner operating in the H-band, whose function is measuring the relative phase difference between the light beams, identify the piston disturbances due to atmospheric turbulence, and the transmission of OPD correction values to the delay lines. The components of FINITO are mounted within the interferometric laboratory, allowing it to operate both with the UTs and ATs, and with collimated beams from either two or three telescopes at a time. For observations using the fringe tracker FINITO, the guide star must be within 13 arcsec from the science target and have a magnitude in H-band less than 8. However, in instruments such as AMBER and MIDI, also self-coherencing fringe tracking can be performed, in which case the fringe packet is centred on the detector[15].

3.3 Modelling methods

Unlike the possibility of producing images with radio-telescopes (e.g. Fig. 3.2 with ALMA) or second generation long-baseline interferometers that collect data more efficiently, increase the number of observables and offer dedicated image reconstruction algorithms in their data reduction packages [Kraus et al., 2018], interferometric data acquired with only a couple of optical or infrared apertures requires the development of analytic models to interpret the signals. Indeed, the received interferometric quantities include information about the spectro-photometric morphology of the source, its interferometric visibility and interferometric phase, which are then submitted to some of the following modelling methods:

3.3.1 Geometric models

A geometric or achromatic model of a circumstellar disks is a minimalist framework that allows to characterize an emission region with reduced number of free-parameters and

[15]The information provided in this subsection is referred to ESO's portal and documentation, as well as to literature resources such as Leinert et al. [2003b], Haniff [2007b], Glindemann [2011], Mérand et al. [2012], Müller et al. [2014].

a prescribed constant intensity distribution. A uniform disk, a Gaussian disk or a ring representing the puffed-up inner edge of the disk due to thermal emission, are the most simple geometric models to obtain a first impression of the properties (radius, inclination, position angle, flux contribution) of circumstellar disks. Afterwards, the disk size can be compared to the inferred central luminosity of the system, in what is known as size-luminosity relation [Fig. 2.13; Monnier and Millan-Gabet, 2002, Dullemond and Monnier, 2010].

Simple geometric models better constrain the properties of the disks at near-IR wavelengths because the disk emission comes from a compact region around the dust sublimation radius. On the contrary, the mid-IR intensity distribution corresponds to a more extended region over a wider range of temperatures. This discrepancy can be also seen in the disk size-luminosity relation. Whereas this dependence is well established for near-IR disk sizes [e.g. Monnier and Millan-Gabet, 2002, Eisner et al., 2007b], a weak correlation for the mid-IR has been found [e.g. Monnier et al., 2009, Menu et al., 2015]. Nevertheless, based on a continuous disk model, large interferometric studies in the mid-IR (MIDI/VLTI) have provided an atlas of disks around low- and intermediate-mass young stellar objects, and allowed establishing statistics for a wide population of pre-main sequence stars [Menu et al., 2015, Varga et al., 2018]. Other interferometric works have focused on measuring the disk properties in the near-IR (PIONIER/VLTI) by considering as a ring the puffed-up inner rim of the circumstellar disks [e.g. Anthonioz et al., 2015]. All these reports agree on presenting more elaborated models to refine the first findings by an achromatic simplistic approach.

3.3.2 Temperature-gradient models

The mid-IR emission generally coming from a large area is better represented by the sum of many rings that emit blackbody radiation with the temperature as a function of radius $T(r)$ [e.g. Vural et al., 2012, 2014, Matter et al., 2014, Varga et al., 2018]. The temperature distribution is assumed a power law of the form

$$T_r = T_0 \left(\frac{r}{r_0} \right)^{-q} \tag{3.26}$$

which represents well the temperature radial profile of Eq. 2.37. Here, T_0 and r_0 are respectively the effective temperature at a reference radius. The parameter q depends on the morphology of the disk and is predicted to vary between $\sim$0.4 and $\sim$0.75 for standard viscous disks or flat irradiated disks [Chiang and Goldreich, 1997]. Instead of determining exclusively the monochromatic size of circumstellar disks, this modelling allows to define a wavelength-dependent implication on the visibilities and fluxes, important to study the properties of the dust composition (e.g. spatial distribution, emissivity, mineralogy) and surface density distribution.

Because this modelling approach is developed in this investigation, later I tread this topic more extensively.

3.3.3 Radiative transfer models

Radiative transfer modelling is needed to derive more precise and physically realistic parameters about the structure and composition of inner regions of protoplanetary disks. The problem of radiative transfer in the rim has shown to be very complex [Dullemond and Monnier, 2010] because the numerical modelling has to take into account absorption, heating, backwarming, reemission and scattering processes of stellar photons by dust. Also dust growth and settling has to be considered because big grains, capable of surviving closer to the star thanks to their ability to cool more efficiently, are primarily found in the midplane, and

thereby round off the rim [Tannirkulam et al., 2007]. This implies that for a proper analysis the application of such modelling demands the input of high-angular resolution datasets probing a wide range of optical depths, over a wide range of temperatures and wavelengths.

Although the task of radiative transfer has been treated in 1-dimension [e.g. Dullemond et al., 2001, Isella and Natta, 2005], nowadays 2D and 3D radiative transfer modelling has shown progress in this field. 2D is actually meant to be 3D, in the sense that light disperses in all three directions, but the dust temperatures and other quantities axisymmetrically depend on two parameters: the radial coordinate r, and the height above the midplane z (subsection 2.2.2.1). Fig. 3.14 shows the results of a 2D radiative transfer study by Kama et al. [2009] aiming at describing the rounded-off rims of protoplanetary disks depending on the emissivity factor ϵ (Eq. 2.39) of their grains. The figure depicts that a sharply dust rim, both in temperature (red color map) and density structure (gray scale map), is better defined by a composition of only small 0.1-μm olivine grains (panel a) than by a sample of grains containing larger 10-μm olivine grains (1% in panel b, and 10% in panel c).

Two types of numerical radiative transfer algorithms are used to treat the problem of multidimensional radiative transfer: algorithms based on iterative integration of the formal transfer equation along predefined photon directions, known as grid-based or discrete ordinate codes because the angular directions are modelled as an angular grid, and algorithms based on a Monte Carlo type of simulation of photo movement [Dullemond and Monnier, 2010]. MCMax[16] [Min et al., 2009] and RADMC-3D[17] [Dullemond et al., 2012] are two widely-used and open sources that perform radiative transfer simulations based on the Monte Carlo method. These applications calculate the dust temperature for a given density self-consistently, and also calculate the vertical structure by directly integrating the equation of hydrostatic equilibrium. With these tools, the user specifies a Cartesian grid and the dust (or gas) density in each of these grid cells. Then, the characteristics of the energy sources, such as the location, luminosity and spectrum of the star, have to be introduced. Finally, the numerical code produces an image at some wavelength and zoom-factor, or produce an SED or spectrum, that can be compared to the user's expectations or observational data.

Because the analysis using these tools or radiative transfer methods are out of the scope of this investigation, these fields are not further exposed. However, several studies where radiative transfer modelling has been applied to describe the geometry and radiative properties of protoplanetary disks around young stellar objects can be referred. For instance, the gapped disk around the T Tauri-type star LkCa15 [Tannirkulam et al., 2007, Mulders et al., 2010], the disk around the classical TTS star DR Tau [Brunngräber et al., 2016], the disks around the components of the 2-arcsecond-separated T Tauri binary VV Corona Australis [Scicluna et al., 2016], the concentrical disks around the TTS object DG Tau [Varga et al., 2017], or a large sample of low- and intermediate-mass YSOs by Varga et al. [2018].

Indeed, as seen in the next chapter, the spectro-interferometric data used for this work is limited both in wavelength coverage to the N-band (8–13 μm) and in observing runs to only five epochs. Hence, instead of developing monochromatic models restricted to measure the disk sizes or a profound radiative transfer analysis which requires extended datasets, a temperature-gradient analysis is ideal to be applied to the high-resolution mid-IR data. As follows, I broad the numerical approach to simulate the interferometric observables: spectro-photometric measurements, interferometric visibilities and phases.

[16]Website: `http://www.hetisikke.nl/mcmax/`

[17]Website: `http://www.ita.uni-heidelberg.de/~dullemond/software/radmc-3d/`

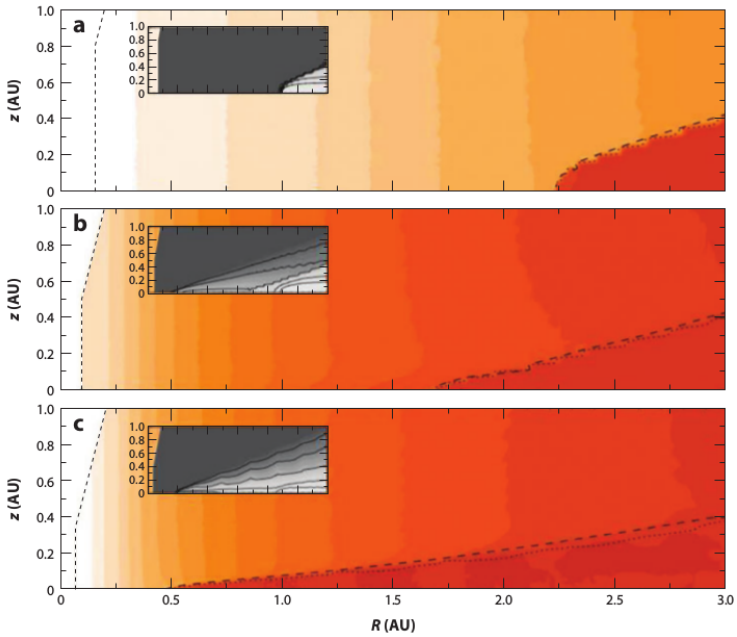

Figure 3.14: 2D modelled temperature (red color map) and density (gray scale map) of the inner rim of a disk around a star with a mass of 2.4 $M_\odot$, 2.4 $R_\odot$ of radius, an effective temperature of 10000 K, and a gas surface density of 100 g cm^{-2}. The rim temperature is 1300 K, and the contours are in steps of 100 K in the range 300–1600 K. The density contours are at factors of 2.7, 10, 10^4, 10^7 and 10^{10}, respectively. The inner rim is sharper for a dust composition of only small 0.1-μm olivine grains (a), than for a sample containing 1% of 10-μm olivine grains (b) and a sample containing 10% of 10-μm olivine grains (c). [Credit: Dullemond and Monnier [2010] and references therein]

3.4 Spectral energy distribution modelling

The SED modelling of an astronomical source permits to infer the photometric properties of each of its individual components, for instance a star and its circumstellar disk. In the particular case of YSOs, the SED permits to classify an astronomical source (subsection 2.1.3, Fig. 2.4) and determine its evolutionary sequence, whether it is deeply embedded or has a disk, whether the disk has been almost cleared or is at a transition phase with gaps.

Let us assume that a stellar object surrounded by a circumstellar disk is located at a distance d from the observer. The components of this object are observed with an inclination i with respect to the normal of the line of sight. Due to gaseous and dusty particles at the line of sight between the source and the observer, observations are affected by the absorption and scattering of electromagnetic radiation. This wavelength dependent magnitude is known as absolute visual extinction, and numerically it is expressed as

$$\frac{A(\lambda)}{A_V} = \frac{a(\lambda) + b(\lambda)}{R_V} \tag{3.27}$$

where the coefficients $a(\lambda)$ and $b(\lambda)$ are functions of wavelength and determined by extinction curves available in the literature [e.g. Cardelli et al., 1989, Gordon et al., 2003]. On the other side, the total extinction coefficient A_V is defined as the relation

$$A_V = R_V \, E(B - V) \tag{3.28}$$

with R_V being the parameter of relative visibility in the optical band and which differs along different lines of sight, and $E(B-V)$ is the selective extinction characterizing the color excess between B- and V-bands. Because the extinction linearly scales with the coefficient A_V, I consider this quantity for the posterior modelling. A value of $R_V = 6.5$ is also established for the implementation of Eq. 3.27, as measured for star-forming environments [e.g. Cardelli et al., 1989, Kandori et al., 2003]. Consequently, the flux transmission fraction as a function of wavelength which directly influences the flux calculation of the SED is defined as

$$A_V(\lambda) = 10^{-0.4\ A(\lambda)}. \tag{3.29}$$

Interstellar extinction is stronger at shorter wavelengths because dust absorbs and scatters blue light better than red light. For this reason, this effect manifests as a reduction of the optical to near-IR slope in the SED.

The amount of energy per unit area emitted by any of the systemic components is calculated through the Planck's law for a blackbody at a given temperature. For the case of a star with temperature $T_\star$, this quantity is expressed as

$$B(\lambda, T_\star) = \frac{2hc^2}{\lambda^5} \frac{1}{e^{\frac{hc}{\lambda k_{\rm B} T_\star}} - 1} \tag{3.30}$$

where h[18] is the Planck constant, $k_{\rm B}$[19] is the Boltzmann constant and c[20] is the speed of light the vacuum.

Consequently, the normalized per wavelength energy flux of the star – power per unit area radiated from the object –, with radius $R_\star$, is expressed as

$$\lambda F_\star(\lambda) = \frac{\lambda S_\star}{d^2} B(\lambda, T_\star) A_{\rm V}(\lambda) \tag{3.31}$$

where $S_\star$ is the area of the stellar disk ($S_\star = \pi R_\star^2$). Due to its point source nature, inclination effects are neglected for the stellar components. I use the magnitude of Eq. 3.31, expressed in W m^2, to graphically represent the SED of Fig. 3.15 and Fig. 4.14. Another inferential measure which is invoked often in this work is the stellar luminosity given by the Stefan-Boltzmann equation

$$L_\star = 4\pi R_\star^2 \sigma T_\star^4 \tag{3.32}$$

where σ is the Stefan-Boltzmann constant[21].

On the other hand, the temperature-gradient modelling that I implement in this research allows to numerically describe the flat circumstellar disk extending from an inner radius $R_{\rm in}$ to an outer radius $R_{\rm out}$ as the sum of many infinitesimal ringlets. The temperature and surface density radial profile, as given by Eq. 2.38 and Eq. 2.32, can be defined as

$$\begin{aligned} T_r &= T_{\rm in} \left(\frac{r}{R_{\rm in}} \right)^{-q} \\ \Sigma_r &= \Sigma_{\rm in} \left(\frac{r}{R_{\rm in}} \right)^{-p} \end{aligned} \tag{3.33}$$

where r is the distance of a given ringlet to the centre of the system, $T_{\rm in}$ and $\Sigma_{\rm in}$ are respectively the temperature and surface density at the inner radius of the disk $R_{\rm in}$. q is the

[18] $h = 6.62607004 \times 10^{-34}$ J s
[19] $k_{\rm B} = 1.38064852^{-23}$ J K^{-1}
[20] $c = 2.99792458 \times 10^8$ m s^{-1}
[21] $\sigma = 5.670367 \times 10^{-8}$W m^{-2} K^{-4}

temperature power-law exponent and p is the surface density power-law exponent. Unlike the star, the disk emission is affected by the inclination effects produced by the angle i. Moreover, the radiation transfer properties of the dust and gas shaping the disk are characterized by the emissivity factor

$$\epsilon_\tau(\lambda) = 1 - e^{\tau_{\lambda,r}/\cos i} \tag{3.34}$$

where the vertical optical depth $\tau_{\lambda,r}$ is a function of the dust opacity κ_λ according to the expression

$$\tau_{\lambda,r} = \kappa_\lambda \Sigma_r. \tag{3.35}$$

As a consequence, the total flux produced by the inclined disk is equal to the integral over r of the flux produced by each of its n inclined ringlets

$$F_{\mathrm{disk},i}(\lambda) = \frac{\cos i}{d^2} \int_{R_{\mathrm{in}}}^{R_{\mathrm{out}}} 2\pi r B(\lambda, T_r) \epsilon_\tau(\lambda) A_{\mathrm{V}}(\lambda) \mathrm{d}r. \tag{3.36}$$

The flux contribution of additional stellar or disk components are treated similarly to the mentioned above, and the total flux of the astronomical source is hence expressed as the sum of the individual contribution of its components $F_{\mathrm{total}}(\lambda) = \sum_{i=1}^{n} F_n(\lambda)$.

The impact of the dust opacity law κ_λ, which characterizes the dust mineralogy of protoplanetary disks, is crucial to model satisfactorily the spectral energy distribution from the near-IR to the sub-mm. Studying the properties (size, geometry, composition) of dust grains in the interstellar medium represents a broad astronomical field by its own, but the next simplified expression is commonly adopted [e.g. Beckwith et al., 1990, Li, 2005] to quantify the wavelength-dependent opacity

$$\kappa_\lambda = \begin{cases} \kappa_0, & \lambda < \lambda_0 \\ \kappa_0 \left(\frac{\lambda}{\lambda_0}\right)^{-\beta}, & \lambda \geq \lambda_0 \end{cases} \tag{3.37}$$

where κ_0 is a value defined by experimental measurements of cosmic dust analogues or models of interstellar dust at a reference wavelength λ_0. β is the wavelength-dependence exponent of the opacity. Observations of disks at $\lambda = 1.3$ mm have determined that for $\beta = 1$ the mass opacity is $\kappa_0 = 2.3 \times 10^{-3}$ m^2 kg^{-1} [e.g. Jørgensen et al., 2007]. Therefore, an achromatic wavelength dependence based on these measurements can be established as

$$\kappa_\lambda = 2.3 \times 10^{-3} \left(\frac{1.3 \times 10^{-3}}{\lambda} \right) \tag{3.38}$$

where λ is expressed in μm, and consequently κ_λ in m^2 kg^{-1}.

More complex dependences on the opacity properties of dust are publicly available online. For instance, the Astrophysical Laboratory of the University of Jena[22] offers an extended database [Henning et al., 1999] of dust optical properties that are applied to astrophysical modelling, including: silicates, metals, oxides, sulfides, carbonaceous and organic species. Based on some of these tables, in the top panel of Fig. 3.15 I present a comparison between the opacity distribution over wavelength for different conglomerates. The first distribution (blue line) corresponds to the achromatic case given by Eq. 3.38. The next dust composition (red line) represents a mix of olivine, orthopyroxene, organics, water ice, troilite and metallic iron grains as calculated by Pollack et al. [1994] and Semenov et al. [2003]. The law plotted with green line belongs to a mix of pure iron-free olivine (80%) and graphite (20%)

[22]Website: `https://www.astro.uni-jena.de/Laboratory/Database/databases.html`

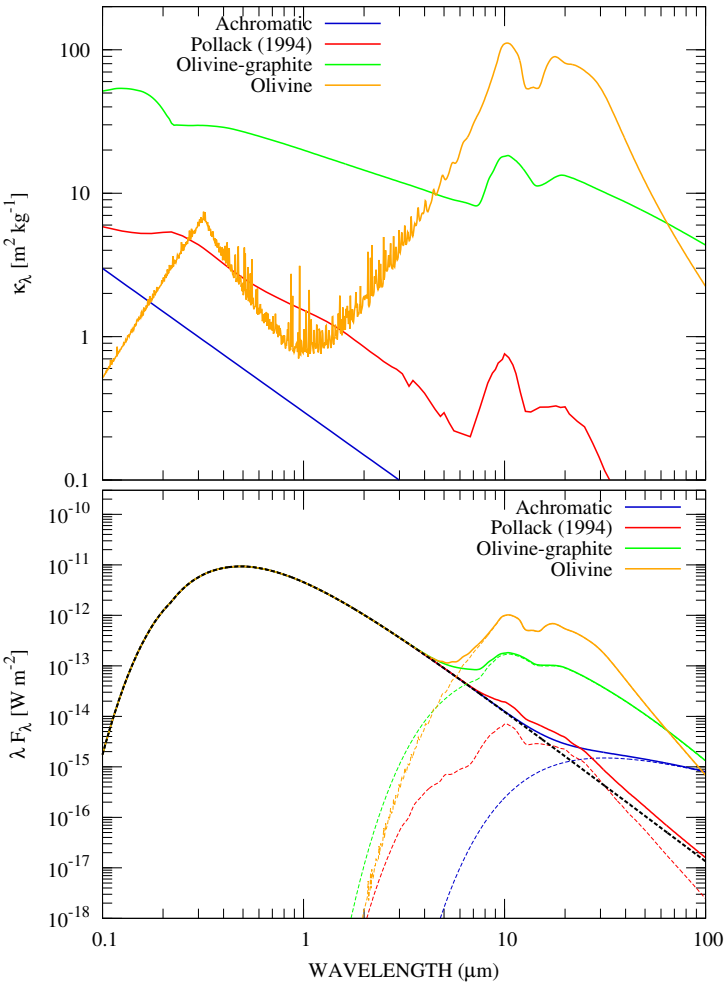

Figure 3.15: *Top*: Opacity distribution over wavelength for different dust compositions commonly implemented in the literature. *Bottom*: SED modelling by using the different dust conglomerates that differently impact on the infrared and (sub)millimetre flux. The total fluxes (solid lines) and the contribution of the circumstellar disk (dashed lines) are respectively coloured for each dust composition, whereas the common black dashed line traces the stellar contribution for a luminosity $L_\star = 8.7\ \mathrm{L}_\odot$. The stellar and disk parameters belong to the Herbig star HD139614 as reproduced with a one-component model by Matter et al. [2014]. The implemented opacity law used by these authors corresponds to a pure iron-free olivine composition (gold line).

which is a major constituent of interstellar grains, and such composition has been used to model observations of disks with featureless and refractory species [e.g. Meeus et al., 2002, Carmona et al., 2014, Matter et al., 2016]. Finally, the opacity law with gold line shows the dependence for a composition of pure iron-free olivine with a 60% fraction in mass of 2 μm-sized grains and 40% of 5 μm-sized grains, following the opacity implemented by Matter et al. [2014].

In the bottom part of Fig. 3.15 I illustrate the effect of the different κ_λ distributions on the modelling of the SED of young stellar objects. At near-IR wavelengths, when the stellar emission decays, the dust opacities become dominant and their composition shapes the SED at longer wavelengths. The ascribed stellar and disk parameters belong to the Herbig object

HD139614 as modelled by Matter et al. [2014] with a one-component method. The object is located at 140 pc and seen with a visual extinction coefficient $A_V = 0.09$. The stellar luminosity reaches 8.73 $L_\odot$, and the disk, inclined 20°, extends from $R_{\rm in} = 2.77$ AU to a typical $R_{\rm out} = 100$ AU. The temperature and density power-law exponents are respectively set to $q = 0.66$ and $p = 1.5$, with a high surface density of 10^{-3} kg m^{-2}. These authors simulated well the SED and interferometric data there presented by applying the opacity law defined by the pure iron-free olivine. However, as seen from the figure, I highlight that invoking distinctive dust aggregates may produce strong SED discrepancy.

3.5 Visibility modelling

Interferometers are sensitive only to the source brightness distribution projected onto the plane of the projected baseline, or in other words, to the plane containing the two telescopes and the astronomical source. The modelling of interferometric visibilities is carried out by applying "visibility building blocks" [e.g. Malbet et al., 2005, Berger and Segransan, 2007, Monnier, 2007] for the most common morphologies. For this purpose, I evoke the van Cittert-Zernike theorem of Eq. 3.25 which relates through a Fourier transform the brightness intensity distribution of the source $I(\vec{\theta})$ to the visibility function $\mu(\vec{B})$, where the coordinates in the sky plane of vector $\vec{\theta}$ are (α,β), and the coordinates of the baseline vector $\vec{B}$ are the spatial frequencies (u,v).

For simplicity and uniformity with the literature, let us introduce in the modelling the notation $V_\lambda(u,v) \equiv |\mu(u,v)|$ known as normalized visibility because the complex numerator of Eq. 3.25 is divided by the denominator I_0, which is the total flux of the source. Hence, $V_\lambda(u,v)$ is wavelength-dependent real number.

Point source

The simplest building block corresponds to a point source, which is used to describe unresolved objects with finite energy such stars. The intensity distribution for an object with coordinates (α,β) in the sky plane is given by a Dirac δ-function of the form

$$I(\alpha,\beta) = I_0\ \delta(\alpha-\alpha_0, \beta-\beta_0). \tag{3.39}$$

Consequently, the Fourier transform of the δ-function is a constant, and its normalized visibility is then

$$V_\lambda(u,v) = 1. \tag{3.40}$$

Therefore, the point source remains unresolved independently of the baseline and spatial frequency. The case a) of Fig. 3.16 shows the visibility function over wavelength for a point source, which is invariable over the wavelength domain.

Binary

A visibility building block consisting of several components can be defined as the sum of the brightness distributions of every object. Each of them has coordinates (α_j,β_j) in the plane of the sky, an intensity I_j and corresponding normalized visibilities $V_j(u,v)$, where the number of components is given by $j = 1...n$. Then, the total brightness distribution of the system can be expressed as

$$I(\alpha,\beta) = \sum_{j=1...n} I_j\ \delta(\alpha-\alpha_j, \beta-\beta_j). \tag{3.41}$$

Consequently, following the addition properties of the Fourier transform, the complex visibility function is written as

$$\mu(u,v) = \sum_{j=1...n} F_j(\lambda) V_j(u,v) e^{-2\pi \mathrm{i}(u\alpha_j + v\beta_j)} \tag{3.42}$$

and the total normalized visibility is defined as the total correlated flux divided by the total flux of the system, as follows

$$V_\lambda(u,v) = \frac{\sum_{j=1...n} F_j(\lambda) V_j(u,v) e^{-2\pi \mathrm{i}(u\alpha_j + v\beta_j)}}{\sum_{j=1...n} F_j(\lambda)}. \tag{3.43}$$

The simplest multicomponent model corresponds to a binary system with a brightness distribution defined as

$$I(\alpha,\beta) = I_1 \delta(\alpha - \alpha_{\mathrm{s1}}, \beta - \beta_{\mathrm{s1}}) + I_2 \delta(\alpha - \alpha_{\mathrm{s2}}, \beta - \beta_{\mathrm{s2}}) \tag{3.44}$$

where I and (α, β) are the intensity brightness distribution and the angular coordinates of star 1 and star 2 (subindexes $s1$ and $s2$). Consequently, the normalized visibility takes the form

$$V_\lambda(u,v) = \frac{F_{\mathrm{s1}}(\lambda) e^{-2\pi \mathrm{i}(u\alpha_{\mathrm{s1}} + v\beta_{\mathrm{s1}})} + F_{\mathrm{s2}}(\lambda) e^{-2\pi \mathrm{i}(u\alpha_{\mathrm{s2}} + v\beta_{\mathrm{s2}})}}{F_{\mathrm{s1}}(\lambda) + F_{\mathrm{s2}}(\lambda)}. \tag{3.45}$$

This same expression can be deduced for a known flux ratio between the components ($f = F_{\mathrm{s1}}/F_{\mathrm{s2}}$), becoming

$$V_\lambda(u,v) = \frac{f e^{-2\pi \mathrm{i}(u\alpha_{\mathrm{s1}} + v\beta_{\mathrm{s1}})} + e^{-2\pi \mathrm{i}(u\alpha_{\mathrm{s2}} + v\beta_{\mathrm{s2}})}}{1 + f}. \tag{3.46}$$

In the case b) of Fig. 3.16, I plot visibility curves for a binary system with different configurations, whose forms depend on the flux ratio of the components, their separation and the baseline configuration (length and position angle). Whereas the flux ratio determines the amplitude of the curves, reducing it for $f \neq 1$, the separation and the spatial frequency (baseline) at which the stars are observed determine the periodicity of the curve, unresolving the system when observing parallely to the position angle on the pair (blue line).

Ring

The analysis of a circular symmetric object is simplified by expressing the normalized complex visibility function expressed by the van-Cittert-Zernike theorem in Eq. 3.25 in polar coordinates. Thus, the coordinates of the object in the sky plane are given by $\rho = (\alpha^2 + \beta^2)^{1/2}$ and $\theta = \tan^{-1}(\alpha/\beta)$, and the coordinates in the uv-plane by $r = (u^2 + v^2)^{1/2}$ and $\phi = \tan^{-1}(u/v)$. Then, from the Fourier transform properties and by disregarding the normalizing factor in the denominator, the complex visibility function is expressed as

$$\mu(r,\phi) = \int_0^{2\pi} \int_0^{\infty} I(\rho,\theta) \rho \, e^{-2\pi \mathrm{i}(\rho r \cos(\theta - \phi))} \mathrm{d}\rho \mathrm{d}\theta. \tag{3.47}$$

Then, accounting for the symmetric properties of the intensity I and the function μ with respect to θ and ϕ, respectively, the equation becomes

$$\mu(r) = \int_0^{2\pi} \int_0^{\infty} I(\rho) \rho e^{-2\pi \mathrm{i} \rho r \cos\theta} \mathrm{d}\rho \mathrm{d}\theta. \tag{3.48}$$

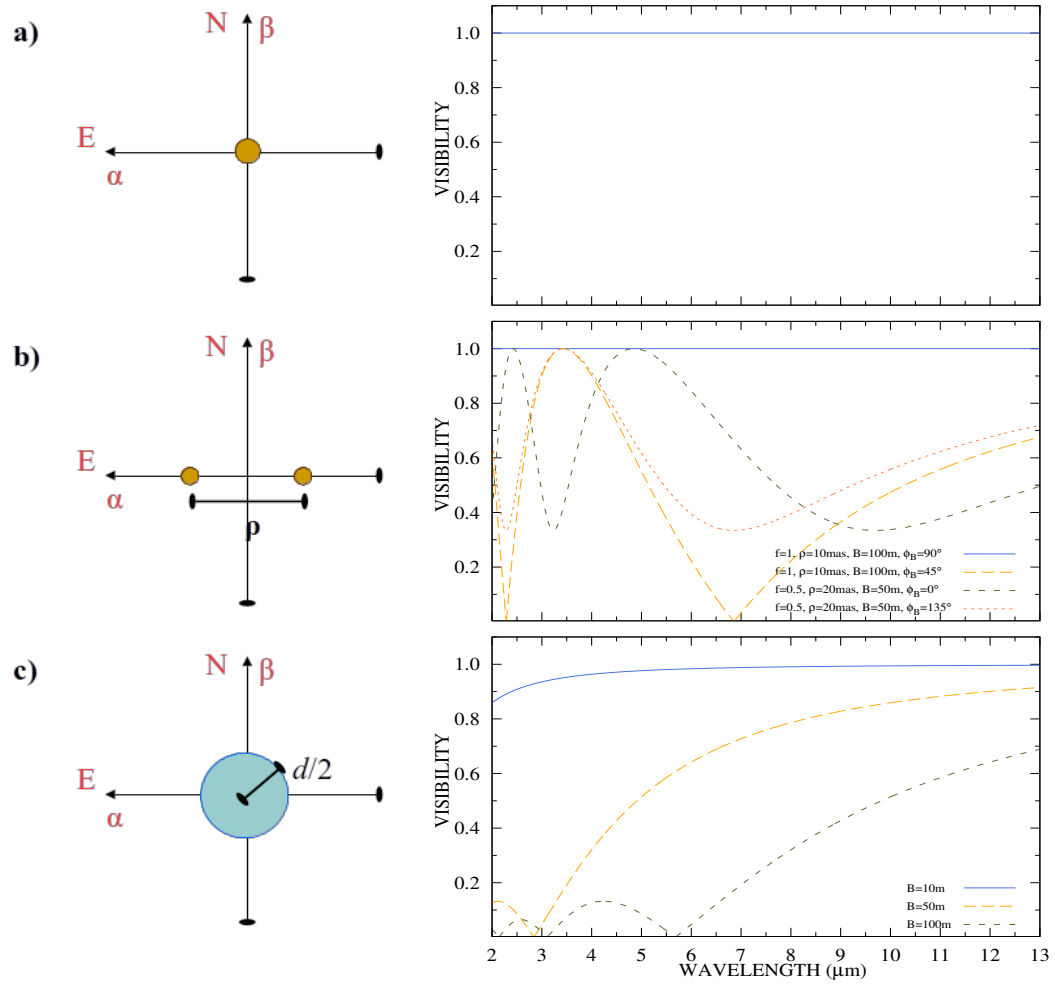

Figure 3.16: Example of visibility curves for (from top to bottom): a) an unresolved point source, b) a binary with separation ρ and flux ratio f, and c) a uniform disk with radius $d/2 = 1$ AU. The corresponding sketches are presented on the left side, whereas the visibility function over wavelength, from K- to N-band (2–13 μm), are displayed on the right side.

This equation can be quantified thanks to the zeroth-order Bessel function of the first kind with respect to θ

$$J_0(x) = \frac{1}{2\pi}\int_0^{2\pi} e^{-\mathrm{i}x\cos\theta}\mathrm{d}\theta \tag{3.49}$$

and subsequently the final expression for the unnormalized visibility function adopts the form

$$\mu(r) = 2\pi\int_0^{\infty} I(\rho)\rho J_0(2\pi\rho r)\mathrm{d}\rho. \tag{3.50}$$

Eq. 3.50 is the basis on which one can compute the visibility curves for a variety of centro-symmetric objects with a radial intensity dependence. For instance, a circular ring of infinitesimal thickness and radius ρ_0 possesses an intensity distribution given by the expression

$$I(\rho) = \frac{1}{2\pi\rho_0}\delta(\rho - \rho_0) \tag{3.51}$$

and its normalized visibility therefore is determined by the zeroth-Bessel function of the first

kind of the form

$$V_\lambda(u,v) = J_0(2\pi\rho_0 r). \tag{3.52}$$

Uniform disk

The uniform disk is commonly applied to model the visibility function of resolved stars thanks to its direct link to their diameter. The brightness distribution of a uniform disk with diameter d is defined as

$$I(\rho) = \begin{cases} \frac{4}{\pi d^2}, & \text{if } \rho \leq d/2 \\ 0, & \text{if } \rho > d/2 \end{cases} \tag{3.53}$$

and its respective normalized visibility is expressed by the equation

$$V_\lambda(u,v) = 2\frac{J_1(\pi d r)}{\pi d r} \tag{3.54}$$

where J_1 is the Bessel function of the first kind of order 1. The visibility curve of a uniform disk has several zeroes, indicating that the phase jumps by 2π. The case c) of Fig. 3.54 shows three visibility curves (for different baseline lengths) between 2–13 μm corresponding to a uniform disk with a radius of 1 AU. The longest baseline of 100 m better resolves the disk, and denotes three lobes.

3.6 Phase modelling

From the interferogram defined by Eq. 3.23, according to the expression

$$I(\vec{\alpha}) = I_0 \left(1 + |\mu(\vec{B})| \cos(\phi(\vec{B}) + k\,\vec{\theta}\,\vec{B})\right)$$

so far, only the amplitude given by the visibility function $|\mu(\vec{B})|$ has been treated. Whereas the scalar product between the vectors $\vec{\theta}$ and $\vec{B}$ shape the horizontal shrinking of the curve (period), the another observable quantity, the interferometric phase $\phi(\vec{B})$, contains information about the position of the fringes.

From the interferometric measurements that contain the fringe position, the displacement of the photocenter of a source is determined by the inverse relation to Eq. 3.22, which in vectorial form can be written as

$$\mathfrak{F}(I(\vec{\theta})) = \int I(\vec{B}) e^{\mathrm{i}k\vec{\theta}\vec{B}} \mathrm{d}\vec{B}. \tag{3.55}$$

Nevertheless, the interferometric visibility and phase measurements have to be provided by a sufficient number of baselines ($\vec{B}$) and spatial frequencies ($1/\lambda$).

A phase measurement per spectral channel $\phi(\lambda)$ is affected by a term linked to the instrumental piston $\phi_{\mathrm{ins}}(\lambda)$ and a term containing the atmospheric piston $\phi_{\mathrm{atm}}(\lambda)$ [e.g. Akeson et al., 2000, Petrov et al., 2007], being possible to express this dependence as

$$\phi(\lambda) = \phi_{\mathrm{s}}(\lambda) + \phi_{\mathrm{ins}}(\lambda) + \phi_{\mathrm{atm}}(\lambda) \tag{3.56}$$

where $\phi_{\mathrm{s}}(\lambda)$ is the intrinsic brightness distribution of the source.

The retrieval of the source phase is not an easy task. Whereas the instrumental effects are sustainably eliminated thanks to nanometre accuracy techniques and delay lines, the atmospheric inclusion leads to unknown variations in coherence time. To overcome this limitation, different techniques can be implemented:

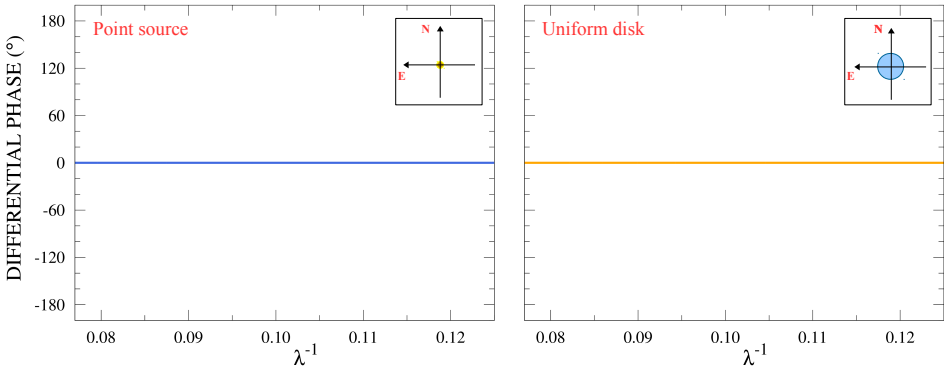

Figure 3.17: Modelled interferometric differential phases versus spatial frequencies over the N-band showing null-values for an unresolved point source (left) and a central-symmetric uniform disk (right). The sketches of each morphology are presented in the upper corners, with the position angle of the stars and the baseline configuration referred in the north-east direction.

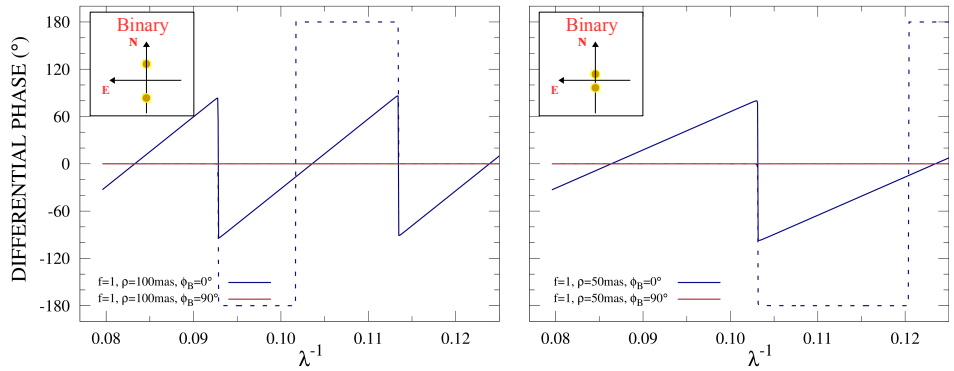

Figure 3.18: Samples of differential phases for a binary system with a flux ratio $f = 1$, and separations of 100 mas (left) and 50 mas (right). Because a perpendicular baseline to the disposition of the stars cancels their contribution, the red lines show zero-deviations.

- The so-called phase referencing method supposes to observe a second object nearby the science target whose phase $\phi_{\rm ref}$ is known (e.g. an unresolved star) to determine the atmospheric phase according to $\phi_{\rm atm} = \phi_{\rm obs} - \phi_{\rm ref}$.

- The so-called closure phase method is applicable to observations performed with at least three telescopes such as AMBER or new generation combiners. This technique implies to consider the phase delay introduced by the atmosphere above every pair of telescopes [e.g. Monnier, 2007]. For instance, in a 3-telescope array, the phase shift in the fringe between telescopes 1–2 is equal, but opposite, to the shift between telescopes 2–3. Thus, the sum of the three fringe phases, between 1–2, 2–3, and 3–1, is blind to the phase delay above telescope 2. The closure phase ϕ_{ijk} can subsequently be expressed in terms of the three telescopes i, j, k in the triangle

$$\phi_{ijk} = \phi_{ij} + \phi_{jk} + \phi_{ki}. \tag{3.57}$$

- The differential phase technique relies on simultaneous multiwavelength phase measurements – therefore known also as chromatic phase – to measure small phase variations as a function of wavelength, due to sources with wavelength-dependent and

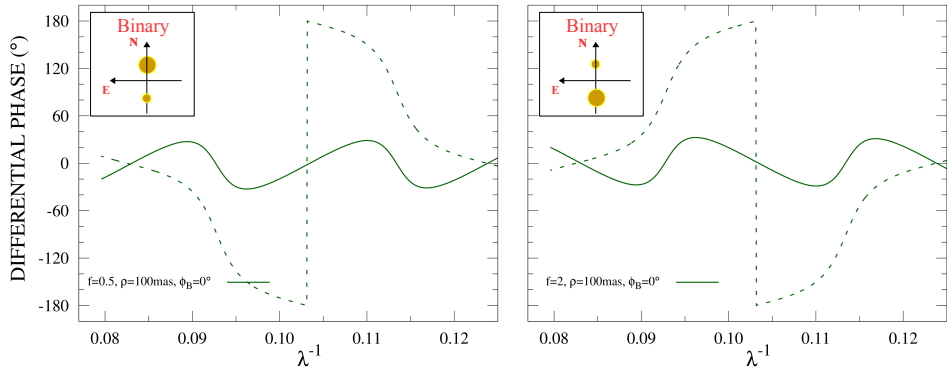

Figure 3.19: Modelled phases for an unequal binary system with a 100 mas separation. In the left panel the flux ratio equals 0.5, whereas in the right panel f is inversely 2.

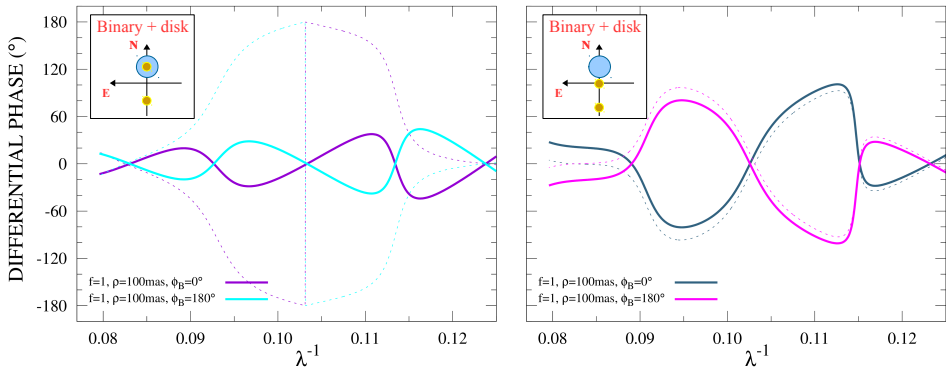

Figure 3.20: Differential phases for a system consisting of a 100 mas-separated pair and a uniform disk with a radius of 1 AU. The relation between the stellar flux and the disk flux is 50–50% at 10 μm. Whereas in the left panel the center of the disk and the center of one of the stars coincide, in the right panel the deviation to the south of the binary differently modulates the curves.

asymmetric structures [Schmitt et al., 2006]. Because the atmospheric influence is expected to be nearly constant across narrow spectral channels, this technique has been used to monitor the origin of spectral lines (e.g. Hα, Brγ, He I, NH_3, SiH_4) by comparing them to the continuum phase [e.g. Stee et al., 1995, Weigelt et al., 2006, Petrov et al., 2012, Gravity Collaboration et al., 2017a].

Because the broadband data that I exploit in this investigation is acquired with the 2-beam combiner MIDI, the differential phase method is optimal to be implemented in my modelling. By presuming that the atmospheric and instrumental disturbance in Eq. 3.56 remain constant across every spectral channel, and that they have been corrected trough fringe tracking methods, the source phase $\phi_s(\lambda)$ as a function of the wave number $k = 2\pi/\lambda$ can be written as

$$\phi_s(k) = \psi_0 + \psi_1 k + \psi_c(k). \tag{3.58}$$

The two first terms of this equation (of the form $y = a + bx + cx^n$) contain the linear atmospheric and instrumental residuals that can be well eliminated by subtracting a linear function [Petrov et al., 2007, Panić et al., 2014]. The intrinsic chromatic phase of the source is contained in the higher terms of the phase polynomial and can be finally retrieved from the interferometric measurements. The removal of the constant and first order phases means

that the measured complex correlated fluxes cannot be used directly in a Fourier transform reconstruction of the source structure – impeding image reconstruction techniques –, but the differential phases can be used to implement source modes, similarly to the use of closure phases in optical and radio interferometry [Panić et al., 2014].

In practice, each component of an astronomical source with a different spectral energy distribution induces a phase difference as a function of wavelength to the modelled correlated flux of Eq. 3.42

$$\mu(u,v) = \sum_{j=1...n} F_j(\lambda) V_j(u,v) e^{-2\pi \mathrm{i}(u\alpha_j + v\beta_j)}.$$

Since this expression is a complex quantity[23], the phase can be derived through the relation

$$\phi_{\mathrm{s}}(k) = \tan^{-1}\left(\frac{\mathrm{Im}(\mu(u,v))}{\mathrm{Re}(\mu(u,v))}\right). \tag{3.59}$$

Afterwards, following the analysis of Eq. 3.58, a linear function is subtracted from the resulting curve in order to remove the atmospheric and instrumental phase input, and the resulting phase belongs to the displacement of the photocenter of the observed source. Such method has been successfully applied to detect point asymmetry in the mid-IR brightness distribution of the circumstellar disk around the Herbig Be star HD100546 [Panić et al., 2014]. As revealed by MIDI observations of this object, the asymmetry arising from the disk wall is suggestive of dynamical perturbation by one or more unresolved objects. Also, interferometric differential phase has been discussed as one of the potential methods to detect exoplanets [e.g. Lopez and Petrov, 2000, Beuzit et al., 2007, Matter et al., 2010], sensitively diagnose circumstellar disks with high-spectral resolution [e.g. Faes et al., 2013] and detect faint (sub)stellar companions [e.g. Akeson et al., 2000].

The importance of the differential phase – although incapable of providing reconstructed images – lies in the capacity to portray the light geometry of an object. If the observations spatially resolve non-axisymmetrical sources of light, the differential phase exhibits a deviation from zero because the contribution from opposite sides of the system fails to cancel one another completely. However, most of models (such as the ones that I have previously exposed for modelling the visibilities) are used to interpret interferometric data from a conservatively symmetric morphology, resulting in zero phases.

In Figs. 3.17–3.20, I display samples of modelled differential phases as a function of spatial frequency over the N-band (0.08–0.13 λ^{-1}) for different morphologies, represented in their sketches. Fig. 3.17 shows zero-phase curves independently of their luminosity, baseline configuration or size, corresponding to the axisymmetrical point source and uniform disk. On the other hand, Fig. 3.18 traces differential phases for two binary systems with flux ratio $f = 1$, but for different separations of 100 mas (left) and 50 mas (right). The blue zigzag lines in both panels correspond to a baseline configuration of 100 m of length and which resolves the pair with a position angle across them. Unlike the blue lines, the zero-phase red lines show a null-phase signal for observations with a baseline perpendicular to the position of the objects since they cancel each other symmetrically. The dashed lines delineate the unwrapped phase signals before a linear function is applied to extract the piston. They present abrupt phase jumps between 0–180° attributed to the complex visibility amplitude traversing a null. Fig. 3.19 traces also the signals of a binary system with a 100 mas separation over a parallel baseline, but in the first case (left) the flux ratio equals $f = 0.5$, being brighter the northern component, and in the second case (right) the flux ratio inversely equals $f = 2$. In

[23] Eq. 3.43 is a direct consequence of the correlated flux, but with the total flux as a scalar normalizing factor. Therefore, the complex value of Eq. 3.43 can also be used analogously for the modelling of the differential phase.

Fig. 3.20, I introduce chromatic phase signals for a system consisting of an equal-brightness pair separated 100 mas and a uniform disk with a radius of 1 AU. Whereas in the left panel the position of the disk coincides with the one of the symmetrically disposed primary star, the right panel exhibits a case where the disk remains 50 mas separated north and the stars experience a shift of 50 mas south, locating one of the components at the origin of the coordinates frame. The phase curves are symmetrically different depending on whether the baseline position angle is 0° or 180°. Through these illustrative examples, I highlight the sensitivity of the interferometric differential phases to the baseline configuration, the flux ratio of the components, their location and size. Therefore, their exploitation in the infrared range is widely effective to reveal the light distribution and detect asymmetries originating from the different dusty substructures forming complex stellar systems.

CHAPTER 4

Mid-IR Interferometric Study of V892 Tau

4.1 V892 Tau in the context of binary Herbig Ae/Be objects

V892 Tau is a stellar object located in the north-west region of the Taurus-Auriga star-forming complex, located at 140 pc (Fig. 4.1). As seen from the Digitized Sky Survey (DSS) and Spitzer Infrared Array Camera (IRAC) images in the right panels of the same figure, this object appears as an isolated point source at shorter wavelengths (panels a) and b)). However, the 8 μm image of panel c) reflects a nebulous environment, proof of its youth and associated circumstellar material that extinguishes the light at the line of sight via absorption and scattering. Some of their closest and brightest neighbours are the pre-main sequence TTS objects: MHO 11 in the south-east direction (35" separation), Hubble 4 in north-east at 99" distance, and CZ Tau (separation 182") and DD Tau (separation 208") in the south-west direction. Additionally, V892 Tau has a low-mass companion at 4" – some 550 AU at the distance of the object – north-east from the Herbig star.

4.1.1 Spectral type

This object was first characterized by Elias [1978] in his study of the Taurus dark cloud complex. Interestingly, V892 Tau was the first in his list of objects, and since no name was associated to this member it is also known from then on as Elias 1 or Elias 3-1. He described this object as a star associated with a nebulosity, with strong Hα emission, and near-IR variability. The spectrum did not show evidence of the Brγ hydrogen line at 2.17 μm. The simplest explanation that this author had to explain the $\sim$50% flux excess at 2.2 μm was that V892 Tau is a Herbig Ae/Be star which is heating circumstellar dust. Although Elias [1978] reported a spectral type A0 for V892 Tau, other authors have later estimated its spectral class differently: A6 with a visual extinction coefficient $A_{\rm V} = 3.9$ and 38 $L_{\odot}$ luminosity [Berrilli et al., 1992], B9 [Strom and Strom, 1994], or B8V [Hernández et al., 2004].

The analysis of the SED of a group of HAeBe brought Hillenbrand et al. [1992] to classify Elias 1 as a type II HAeBe object because it shows a flat and rising infrared spectrum. The shape of such a SED is best interpreted within the context of intermediate-mass stars or star-disk systems which are surrounded by a gaseous and dusty envelope.

Recently, based on spectroscopy and atmosphere fitting, Mooley et al. [2013] assigned it as a spectral type B8.5V–A0Ve with an effective temperature of $T_{\rm eff} = 11000$ K. They

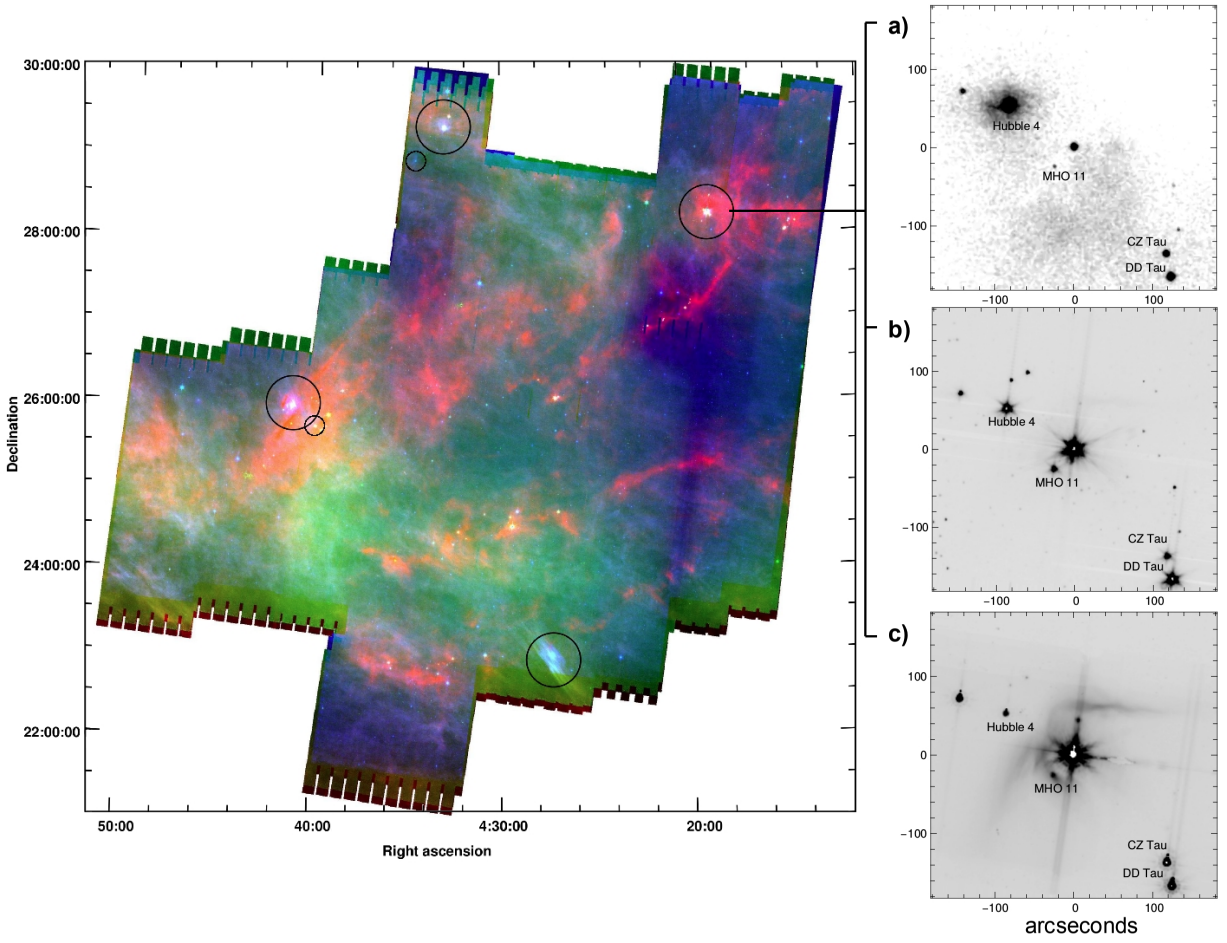

Figure 4.1: *Left*: Spitzer mosaic of the Taurus complex in colors blue (8 μm), green (24 μm) and red (160 μm). The top-right nebulosity is the target of this investigation V892 Tau (also known as Elias 1). *Right panels*: Maps of the stellar neighbourhood of V892 Tau as seen in the optical DSS (a) and infrared IRAC at 3.6 μm (b) and 8 μm (c). Elias 1, in the very center of the fields, is enclosed by the TTS objects MHO 11, Hubble 4, CZ Tau and DD Tau. The images show an inverse gray scale where dark regions represent high intensity. The field-of-view is ∼6'. In the images north points up, and east is left. [Credit: Spitzer mosaic from Mooley et al. [2013]. Reproduced with permission ©AAS.]

reported Balmer emission lines as evidence of its young stage and membership of the Taurus-Auriga molecular cloud.

4.1.2 X-ray emission

In addition to its relatively uncertain spectral classification and variability, also X-ray emission has been associated with this young object [Zinnecker and Preibisch, 1994]. Indeed, by analysing XMM-Newton and Chandra exposures, Giardino et al. [2004] concluded that the source of X-ray activity is the HAeBe V892 Tau object and not the north-east companion located at 4". They reported that the X-ray flux varies within a factor of 2 in less than 2 ks, being the first report for a Herbig star. A second exposure of the XMM-Newton, where a flare event takes place, showed a source luminosity increasing by a factor of 15 (from 1.6×10^{30} to 2.4×10^{31} erg s^{-1}) and a plasma temperature from $kT = 1.5$ keV to $kT = 8.1$ keV. These authors concluded that in order to confine the plasma pressure at the equilibrium point (peak of the flare), a magnetic field of 500 G with a dynamo system is required. In the case of Elias 1, a convective zone of at least 0.2% of the stellar radius would be needed. However, the presence of magnetic fields supported by convective zones – and consequently of X-ray emission – are rather a characteristic of low-mass stars. In low-mass stars and classical T Tauri stars the X-ray emission originates either in the stellar coronae, star-disk magnetospheres, winds or accretion shocks (subsection 2.1.3). For HAeBe stars, unbiased surveys of magnetic and X-ray activity are still necessary to make conclusions on the X-ray emission arising from these objects [Stelzer et al., 2006].

Another feature closely linked to the X-ray emission of V892 Tau is the detected Ne II line at 12.81 μm. This forbidden line has been widely identified and studied in many young

Table 4.1: Stellar parameters of V892 Tau as reported in the literature for the whole system.

Parameter	Value
Right ascension α [J2000]	04:18:40.62
Declination δ [J2000]	+28:19:15.5
Distance [pc]	140[a]
Spectral type	B8.5V–A0Ve[b]
Temperature T [K]	11000[b]
Luminosity L [L$_\odot$]	120[c]

References: a) Elias [1978], b) Mooley et al. [2013], c) Defined from evolutionary tracks.

Table 4.2: Orbital parameters of the binary system V892 Tau as determined by Monnier et al. [2008].

Parameter	Value
Reference epoch T_0 [MJD]	55480±900
Period P [yr]	13.8±1.5
Semimajor axis a [mas]	72.4±6.3
Eccentricity e	0.12±0.5
Inclination i [°]	60±3.8
Argument of periapsis ω [°]	233±42
Longitude of ascending node Ω [°]	28±5

planetary disks and the more evolved ones in their transition phase [e.g. Pascucci et al., 2007, Ratzka et al., 2007, Pascucci and Sterzik, 2009]. Because the Ne atoms have a large ionization potential (21.6 eV), the Ne II line is important to assess the role of extreme ultraviolet (EUV) and X-ray photons that cause irradiated disk atmospheres, photoevaporative disk winds, shocks and jets. Particularly in V892 Tau, Ne II is detected in a $\pm$50 AU region with a small blueshift, indicative of a photoevaporative disk induced by X-ray emission [Baldovin-Saavedra et al., 2012].

Skinner et al. [1993] reported V892 Tau also as a radio source, although its rising spectrum, though steep, can also be explained by thermal emission from a wind.

4.1.3 Binarity

Speckle interferograms recorded with the Special Astrophysical Observatory (SAO) 6-meter telescope in Russia in 1996 and 2003 allowed Smith et al. [2005] to determine that Elias 1 is a close binary with a separation of $\sim$50 mas ($\sim$7 AU) and a position angle of around 50°. The two observations pointed to a flux ratio between primary and secondary components $F_{\rm s}/F_{\rm p}$ between 0.7 and 1.

This binarity nature may be crucial to interpret the detected X-ray emission. The lack of a convective zone to drive a conventional dynamo in HAeBe is unnecessary if one of the companions is a low-mass source. The first reports on the systemic spectral type and a comparison with evolutionary tracks [Fig. 2.3; Palla and Stahler, 1993] suggested that the mass of the primary lies in a range between 2 and 2.5 $M_\odot$. Based on the flux ratio of the system, the companion has a mass between 1.5 and 2 $M_\odot$, which is just the boundary between fully radiative and partially convective stars. For this reason, it might be that the companion has a normal convection-generated magnetic field and a corona as the origin of the X-ray emission.

Later, by combining their single measurement and the two points previously obtained in K-band, Monnier et al. [2008] astrometrically estimated the orbital parameters of the stellar pair with a total mass of $\sim$5.5 $M_\odot$ and a spectral type B8V (Table 4.2).

In the table of Fig. 4.13 the epoch of these three observations, and the respective separation ρ and position angle θ of the pair, are reported. In the table I also declare the orbital configuration at the time of the observations with MIDI of this work.

4.1.4 PAHs, nanodiamonds and silicates

Different spectral features typical of low- and intermediate-mass PMS objects have been found in the spectrum of V892 Tau (Fig. 4.2).

Some of those infrared spectral features are attributed to polycyclic aromatic hydrocarbons (PAHs) which appear as broadband emission features at 3.3, 6.2, 7.7, 8.6, 11.3 and 12.7 μm. The detection rate of PAHs in TTS of less than 10% [e.g. Furlan et al., 2006, Geers et al., 2006], a higher one of 70% in HAeBe stars [Acke et al., 2010], and of almost none found in MS debris disks [e.g. Chen et al., 2006] indicates that they are dependent on the stellar properties and evolutionary phases of their protoplanetary disks.

PAHs have a strong influence in the thermal distribution and chemistry of protoplanetary disks, the planets birthplace. Their molecules in the surface layer of the disk are directly exposed to stellar radiation, can get efficiently photoionized, and provide photoelectrons for heating the ambient gas [e.g. Kamp and Dullemond, 2004, Seok and Li, 2016]. For these reasons, PAHs are a diagnostic tool of the physical conditions and structure of protoplanetary disks. Because of their stochastic nature, they can be detected far away from the central star,

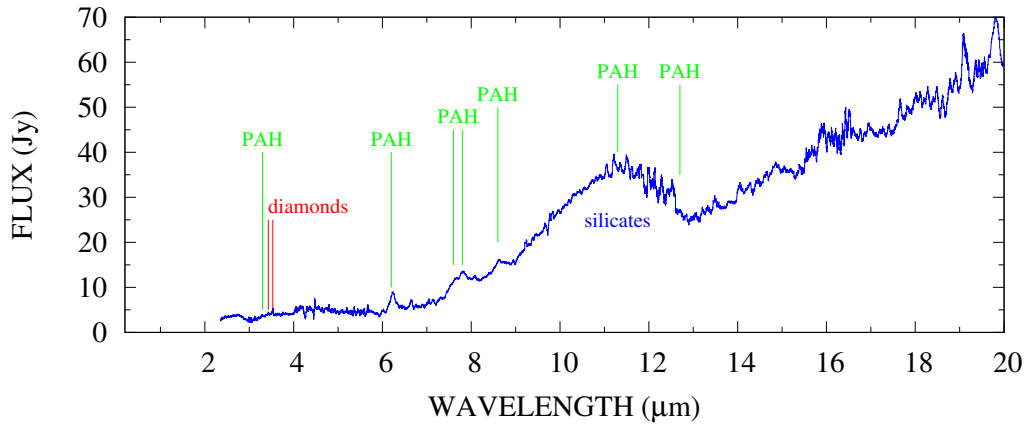

Figure 4.2: ISO SWS spectrum of V892 Tau between 2.5 and 20 μm, the spectral window studied in this work. The spectral features mentioned in subsection 4.1.4 are identified with green (PAHs), red (nanodiamonds) and blue at 10 μm (silicate band).

even in regions with larger extension than the emission of large grains in thermal equilibrium with the stellar radiation, and trace protoplanetary gaps [Maaskant et al., 2014].

In the particular case of Elias 1, mid-IR studies [e.g. Van Kerckhoven et al., 2002, Topalovic et al., 2006, Keller et al., 2008] found strong (up to 7 Jy) PAHs features at 6.2, 11.3, 12.7 and the 7.6–8.6 complex However, the 11.3 and 12.7 μm bands are hidden by the silicate emission. The 3.3 μm emission is rather small, exceeded by the 3.43 and 3.53 μm bands. The presence of PAHs emission suggests the presence of graphite because the PAHs molecules are physically and optically the low-mass end of graphite particles.

The 3.43 and 3.53 μm features of Elias 1 were convincingly correspondent with laboratory absorption spectra of the C-H stretching modes on hydrogen-terminated diamond nanocrystal films at $\sim$1000 K [Guillois et al., 1999]. Unlike the PAHs emission that arises from a more extended region ($\pm$100 AU) around the central objects, the 3.43 and 3.53 μm lines have a circular symmetric spatial distribution forming a Gaussian FWHM diameter of $\leq$48 AU according to Topalovic et al. [2006]. That is in agreement also with the radius of $<$22 AU found by Van Kerckhoven et al. [2002]. Later, however, Goto et al. [2009] reported that the PAHs molecules are much less abundant close to the star, within 30 AU from the center, and, on the contrary, diamond particles are more centrally concentrated at a peak near 30 AU, the place where the PAHs emission just starts to emerge.

Together with HD97048 and MWC 297, V892 Tau is one of the few Herbig stars known to have diamond signatures – or better called nanodiamonds since their size is smaller than 50 nm –. The formation of nanodiamonds is linked to carbonaceous structures under the radiation of high-energy particles, which probably originate in the X-ray and magnetic cycle found in Elias 1.

Also, V892 Tau shows a strong broadband silicate emission at 10 μm which originates from a circumstellar dusty disk [e.g. Van Kerckhoven et al., 2002, Keller et al., 2008]. Infrared surveys have revealed that many HAeBe objects have large abundances of crystalline silicate grains in their disks, indicating significant thermal dust processing as a consequence of the formation of the star-disk system. This emission band, indeed, is well seen in the N-band observations with the ISO short wavelength spectrometer (SWS) in Fig. 4.2, and with the MIDI low-resolution spectrum of this work.

4.1.5 Circumbinary disk

Based on mid-IR nulling interferometric observations with the Magellan I and the MMT 6.5 m telescopes, Liu et al. [2007] spatially resolved excess emission from V892 Tau along a position angle of 164° with a full width half maximum (FWHM) of 18–28 AU for a Gaussian disk model. Surprisingly, while near-IR coronagraphic observations could reveal in great detail the spatial properties of HAeBe disks such as AB Aur and HD142527 [e.g. Fukagawa et al., 2004, 2006], ground and space-based near-IR observations failed to image the disk around V892 Tau. One possible explanation is the low surface brightness in scattered light of this source [McCaughrean et al., 2000].

Later, Monnier et al. [2008] reported through infrared segment-tilting and aperture-masking experiments with the Keck I telescope the discovery of a circumbinary disk around the Herbig object V892 Tau. These authors used their near-IR measurement and the ones obtained by Smith et al. [2005] to confirm the binarity of the system and refine the orbit (subsection 4.1.3). The 10.7 μm mid-IR data showed elongated emission of approximately 320×180 mas along a position angle of 50°. The data was fitted with a "skewed asymmetric ring model" with an inner-hole diameter of 247×121 mas (35×17 AU) along 53°. These authors interpreted this model as a circumbinary disk that is in agreement with theoretical models of tidal truncation [Artymowicz and Lubow, 1994], where the inner hole of the CB disk is 1.8–2.6 times larger than the semi-major axis of the pair for eccentricities less than 0.25.

Monnier et al. [2008] also attempted to fit a "transitional" SED with this discovered disk and a combined stellar luminosity of 400 $L_\odot$ (two B8V stars with extinction coefficient $A_V = 10.95$). They modelled the warm inner wall of the disk as a blackbody with a temperature T∼450 K. An observational analysis of their SED in Fig. 4.3, however, allows me to deduce that a more detailed model – and probably the inclusion of an additional source of near-IR emission to compensate the photometric measurements – might be needed.

Through the exploitation of newer high-angular resolution interferometric data, I test the effort of Monnier et al. [2008] to reproduce the SED of V892 Tau with an enormous photometric flux under a high visual extinction. I believe that a more appropriate description of the SED of V892 Tau may be crucial to better understand the geometry and physical processes of this Herbig star.

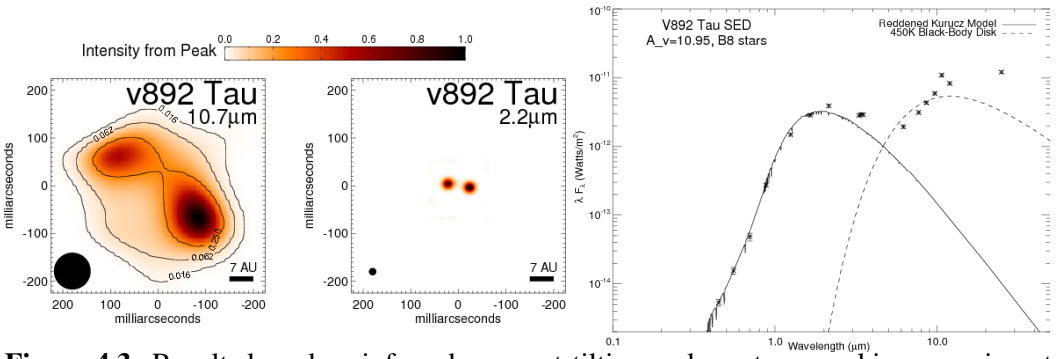

Figure 4.3: Results based on infrared segment-tilting and aperture-masking experiments presented in 2008. *Left*: The two panels show the reconstructed images at 10.7 and 2.2 μm. The resolution reached in each image are represented at the bottom left, 80 and 16 mas respectively. *Right*: SED fitted with photospheric flux of 400 $L_\odot$ and an inner wall of the CB disk with T=450 K. In spite of these two very bright components, my work remarks the still lack of near-IR flux in the SED. [Credit: Monnier et al. [2008]. Reproduced with permission ©AAS.]

4.1.6 Particularity of V892 Tau

Besides hosting an environment rich in spectral species (hydrogen, silicates, nanodiamonds, PAHs) as demonstrated in spectroscopic observations, the system V892 Tau peculiarly serves as a laboratory to characterize the spatial distribution of gas and dust provoked by the dynamical interactions between the near-equal brightness stellar pair and the large circumbinary disks.

In fact, although the abundance of intermediate-mass binary systems is expected to be similar to the frequency of the low-mass counterparts, the amount of them is diminished by the stellar initial mass function. Moreover, identifying cases of binary or higher-order multiple systems with circumstellar associated material among HAeBe – such as the scenario of V892 Tau – is observationally challenging because the companions may posses large contrast ratios if they have unequal masses, or because companions which host their own circumstellar disk significantly redden the systemic luminosity [Duchêne, 2015].

The relatively close location of V892 Tau – 117 AU according to new Gaia measurements – enables to constrain the innermost scales within the circumbinary disk by implementing infrared interferometry techniques [Kraus, 2015]. Even recent Gaia high-accuracy measurements of distances for a sample of 252 Herbig Ae/Be stars [Vioque et al., 2018] have identified few binary Herbig stars sited closer than V892 Tau. Most of such systems lie well beyond 300 pc. Furthermore, the sample of binary pre-main sequence stars with intermediate masses and separations between 1–100 AU is still poor to build a statistical and evolutionary comprehension of circumstellar disks affected by the dynamical interplay of more massive bodies, which presumably reduce the disks lifetime and perturb the process of planet formation.

In Table 4.3, I present a sample of multiple HAeBe systems located closer than 150 pc according to recent measurements with the high-precision astrometry mission Gaia [Vioque et al., 2018]. Out of the 9 sources fulfilling such condition, only 4 of them are closer than

Table 4.3: Sample of multiple close (< 150 pc) Herbig Ae/Be systems alike V892 Tau. Resolved circumstellar or circumbinary emission has been reported for some of them.

Object	Distance [pc]	Description
HD199603 (DV Aqr)	89.3	Eclipsing binary with a period of 1.575 days [Malkov et al., 2006].
HD100453 (MWC 758)	104.2	Binary system with a projected separation of 108 AU and a point-like source at 20 AU [Wagner et al., 2018, Reggiani et al., 2018].
HD104237 (DX Cha)	108.4	Spectroscopic binary with a period of 19.858 days [Cowley et al., 2013].
HD141569 A	110.6	Herbig star forming a triple system, separated 900 AU from the pair [Mawet et al., 2017].
V892 Tau (Elias 1)	140	The science target of this research. Although the distance used here is 140 pc, new Gaia measurements determine 117 pc.
HD53367 (MWC 166)	130.0	Visual binary system with a separation of 600 AU. The main companion may be forming an eccentric binary system with a separation of 1.7 AU [Pogodin et al., 2006].
HD135344 B	135.8	Herbig star hosting a transition disk and forming part of a visual binary with separation 21" ($\sim$3000 AU) [Stolker et al., 2016a].
TY CrA	136.5	Quadruple system with two components forming a spectroscopic binary system with a period of 3 days, and a third component in a wide orbit eclipsing the pair. The main Herbig-type star is separated some 40 AU from the triplet and is surrounded by dusty emission [Chauvin et al., 2003, Boersma et al., 2009, Vaňko et al., 2013].
HD152404 (AK Sco)	140.6	Spectroscopic binary with a separation of $\sim$0.15 AU surrounded by a circumbinary disk [Anthonioz et al., 2015].

V892 Tau (HD199603, HD100453, HD104237 and HD141569 A). In addition, information gathered from the literature exposes that 3 of them (HD199603, HD104237 and HD152404) are spectroscopic binaries and 4 (HD100453, HD141569 A, HD53367, HD135344 B) form large-separation systems. The system TY CrA is reported as a complex quadruple system, whose close triple system is separated from the fourth component some 40 AU. This last one, in turn, is surrounded by dusty emission [Chauvin et al., 2003, Boersma et al., 2009, Vaňko et al., 2013].

Although not included in this sample because of its larger distance (157.3 pc), only the Herbig binary system HD142527 with its low-mass companion at 12 AU and signatures of gas flowing through a dust-depleted gap of $\sim$30 AU [Biller et al., 2012, Casassus et al., 2013, Lacour et al., 2016] can be vaguely set side by side with the spatial configuration of Elias 1. Therefore, by exploiting the mid-IR long-baseline interferometric measurements of V892 Tau acquired for several epochs, my research offers new insight to understand the evolution and possibility of dust survival in such agitated scenario. This phenomenon may have consequences in a "normal" planet formation process. This study also sets the pace for the development of further radiative transfer modelling of V892 Tau and comparison to the context of analogous low-mass T Tauri stars.

4.2 MIDI observations

4.2.1 Observational sequence

Observations with MIDI begin with the definition of a set of parameters in what is called an observation block (OB). It contains information about the position of the target, the filter to be used, the mode, etc.. Once these OB parameters are set, the observation sequence is a rather automatized process.

The interferometric observations with MIDI consist of the following steps[1]:

- **Preset:** This 5–10 minute-phase begins with the pointing of the two telescopes in the direction of the source into the MIDI field-of-view of 2×2 arcsec, and the selection of a guide star within 10' from the science source. Once these two stars are in the observation field, an arm in the Nasmyth focus of each telescope receives the optical light from the guide (Fig. 3.10), and, by separating the beam through a beam splitter, the two beams are sent to two technical detectors (TCCDs). One of the detectors controls the tracking of the telescope, called acquisition guiding and field stabilisation (AGS), and the second performs the wavefront sensing for the active optics correction of the primary mirror. On the other hand, the light coming from the science target is fed into the Coudé focii and transmitted to the adaptive optics system, either MACAO or STRAP. This "Coudé" star is different from the "Nasmyth" star and has to be closer than 1' from the science target. Subsequently, also the delay line carriages in the tunnels are set to the expected $\mathrm{OPD} = 0$, with an accuracy better than 1 mm.

- **Acquisition:** The next step consists of the recording of some thousand (NDIT) acquisition images with typical detector integration times (DIT) of about 2 ms. These images are obtained through a chopping technique, meaning that images of the target and the sky are alternatively taken by tilting the secondary mirror. The background suppression is performed by subtracting the sky frames from the object frames, thus

[1]This subsection is based on the enlightening reviews and resources by Chesneau [2007] and Tristram [2007].

obtaining only the source flux. Depending on the brightness of the source, the number of individual exposures may vary in order to improve the signal-to-noise ratio.

- **Fringe search:** After the acquisition has guaranteed an overlapping of the two beams, a beam combiner and the PRISM ($\Delta\lambda/\lambda = 30$) or GRISM ($\Delta\lambda/\lambda = 230$) are implemented into the light path (Fig. 3.12). Then, two spectrally dispersed interferograms of opposite phase are recorded by the detector. It is important to note that since the background is uncorrelated and cancels out no chopping technique is used during the interferometric measurements. The dispersion of light suggests a longer integration time (DIT) than the acquisition. Usually, the DIT with PRISM has a length of 18 ms, and for GRISM 36 ms.

  The search of the fringes itself is performed by scanning the OPD over a few millimetres out of the expected position. To do so, the VLTI delay lines are moved and simultaneously the piezo-driven mirrors of MIDI scan a range in OPD of four to eight wavelengths ($\lambda \approx 10\,\mu$m) in steps of 2 μm. At each step an exposure is taken to record the interferometric signal in the N-band (8–13 μm), each with its corresponding OPD. After each scan of 40–80 μm the position of the fringe packet is defined and the delay lines recenter the packet for the next scan.

- **Fringe tracking:** Before the fringe tracking starts, the background noise is determined by scanning the optical delay shifted over few millimetres, but without fringe recording. Then, once the point of optical path equality is found, the tracking of the fringes is made in a similar manner to the method to search them. However, the signal-to-noise ratio of the searching measurements is low, and more frames recorded close to a zero optical path difference are needed. For this reason, 200 scans consisting each of 40 frames are obtained. For these new measurements, two different methods can be used: the first method implies keeping centred the white-light fringe (white-light tracking used by MIA for data reduction), and, on the contrary, the second method means that the tracking is performed next to the white-light fringe, enabling the evaluation of data with an incoherent method (data reduction performed with EWS).

  After each scan, a spectrally resolved temporal fringe pattern containing the information about the fringe amplitude – known as correlated flux – is obtained.

- **Photometry:** The spectro-photometric measurements are recorded independently for each telescope. This means that again a chopping procedure has to be carried out to suppress the background in the mid-IR. In the case of MIDI, SCI-PHOT mode – the synchronous measurement of the photometry – is needed if a higher precision is required, although 30% in the visibility measurement would be lost. As a consequence, the photometric measurements with MIDI contain large errors and restrain the accuracy of the visibility, especially for faint targets.

By definition, the visibility is obtained as the ratio of the correlated flux (from the interferometric measurement) to the total flux (from the spectro-photometric measurement). Recalling Eq. 3.24, this definition can be rewritten as

$$\left|\mu(\vec{B})\right| = \left|\frac{\int I(\vec{\theta}) e^{-\mathrm{i}k\vec{\theta}\,\vec{B}} \mathrm{d}\vec{\theta}}{I_0}\right| = \left|\frac{F_{\mathrm{cor}}}{F_{\mathrm{tot}}}\right| \tag{4.1}$$

where $|\mu(\vec{B})|$ is the quantity measured by the interferometer. However, in the observational process, this acquired magnitude – called instrumental visibility – still contains atmospheric

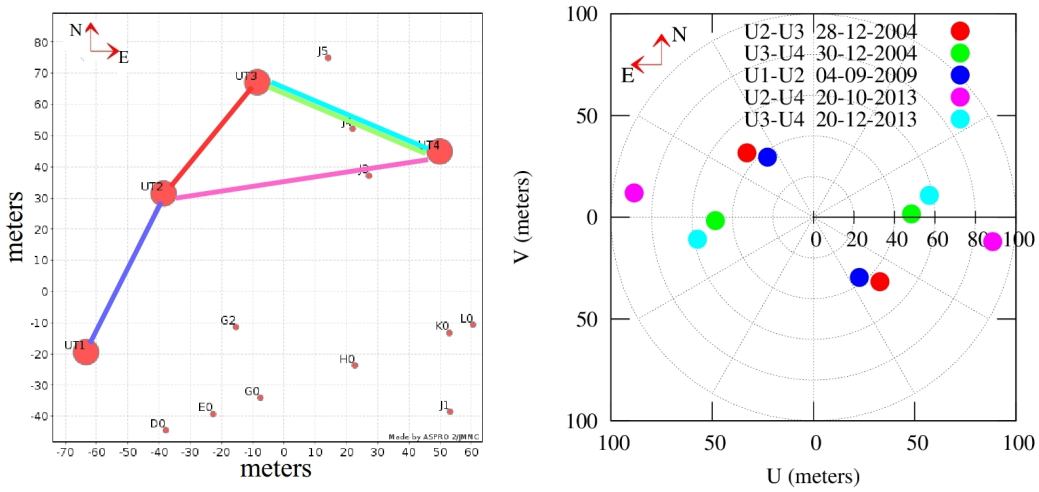

Figure 4.4: *Left*: VLTI baseline configuration with the UTs used for the 5 observing runs of V892 Tau. The red dots depict the UTs and ATs stations. This plot has been made with the ASPRO software [Bourgès et al., 2013], and corresponds to the view of the observatory from the sky (geographic north-east). *Right*: uv-plane coverage achieved with the baselines in the left, plotted with their respective colors. Table 4.4 provides more details of this coverage. In the figure, unlike the observatory view from the left panel, north is pointing up and east is pointing left.

and instrumental correlation losses. In order to correct these effects, in the same region of the sky and following the same observational sequence, the observation of a source with known diameter and visibility[2] must be accomplished immediately after the science target. Therefore, the total calibrated visibility $V_{\rm cal}$ is obtained only after the correction of the form

$$V_{\rm cal}(\vec{B}) = \frac{|\mu_{\rm instr_{science}}(\vec{B})|}{|\mu_{\rm instr_{calibrator}}(\vec{B})|}. \tag{4.2}$$

The total time intended by ESO for MIDI observations under such sequence is 60 minutes, including science target and calibrator. The delivered products of MIDI observations are:

- an image of the source with a default filter at 8.7 μm
- a spectrum in the N-band between 8–13 μm
- spectrally resolved visibilities at the same spectral window
- differential phases in the N-band, and
- correlated fluxes in the N-band

4.2.2 Dataset of V892 Tau

The MIDI interferometric observations of V892 Tau cover a 9-year timescale. The observations with the UTs were split into 5 runs: two in December 2004, one in September 2009 and two in October and December 2013. Each run used the HIGH-SENS mode (total flux measured just after the fringe acquisition) with the PRISM in low spectral resolution ($\lambda/\Delta\lambda = 30$).

[2]This is the reason why, commonly, the calibrators are bright point sources with a visibility of 1.

Table 4.4: Journal of observations of Elias 1 and its photometric and interferometric calibrators. The columns "Diameter" and "F10" (flux at 10 μm) are the correspondent parameters of the calibrators used during the reduction process.

	Object	Date [dd-mm-yyyy]	UT [hh:mm]	Baseline	PBL [m]	PBLA [°]	Airmass
science	V892 Tau	28-12-2004	05:02	U2-U3	45.62	46.09	2.29
		30-12-2004	04:08	U3-U4	48.46	91.97	1.92
		04-09-2009	09:43	U1-U2	37.24	37.49	1.67
		20-10-2013	07:25	U2-U4	89.37	82.32	1.67
		20-12-2013	03:26	U3-U4	58.28	100.67	1.67

	Object	Date [dd-mm-yyyy]	UT [hh:mm]	Baseline	PBL [m]	PBLA [°]	Airmass	Diameter [mas]	F10 [Jy]
calibrators	HD25604[1]	28-12-2004	00:33	U2-U3	28.62		1.66	1.88	6.44
	HD37160[1]		02:33		36.68		1.28	2.02	8.40
	HD37160[2]		02:58		38.65		1.24	2.02	8.40
	HD25604[2]		04:34		45.96		1.85	1.88	6.44
	HD37160[3]		05:32		46.30		1.35	2.02	8.40
	HD37160[4]		06:49		46.32		1.77	2.02	8.40
	HD98292		07:45		42.12		1.44	3.03	16.01
	HD102461		08:38		44.35		1.24	2.96	13.25
	HD49161	30-12-2004	02:53	U3-U4	59.83		1.38	2.70	9.80
	HD37160[1]		03:29		61.77		1.21	2.02	8.40
	HD37160[2]		06:32		38.74		1.68	2.02	8.40
	HD102461		07:29		54.14		1.34	2.96	13.25
	HD122451		09:11		52.18		1.46	0.93	9.74
	HD37160	04-09-2009	09:03	U1-U2	41.32	11.50	1.50	2.02	8.40
	HD25604	20-10-2013	07:10	U2-U4	89.39	82.20	1.46	1.88	6.44
	HD37160		07:44		86.77	84.10	1.22	2.02	8.40
	HIP22957		08:01		89.43	82.00	1.28	2.49	11.90
	HD69142		08:33		82.12	55.80	1.21	2.07	8.38
	HIP22957	20-12-2013	01:02	U3-U4	57.29	117.90	1.72	2.49	11.90
	HIP24197		01:53		60.50	114.90	1.57	2.69	10.31
	HD25604		02:55		60.00	104.20	1.46	1.88	6.44
	HD37160		03:40		62.44	108.80	1.23	2.02	8.40

At 10 μm the longest baseline – 89 m on 20-10-2013 – offers an angular resolution of $\lambda/B \approx 20$ mas (≈3 AU at 140 pc, the distance to the source), while the shortest one – 37 m on 04-09-2009 – provides an angular resolution of $\lambda/B \approx 60$ mas (≈8 AU). A detailed journal of observations is given in Table 4.4.

The observing runs included the observation of several interferometric and photometric calibrators before and after the science target, except in 2009 due to poor weather conditions. These calibrators are spatially unresolved bright sources that enable the calibration of the interferometric transfer function and the total flux spectrum according to the observational sequence exposed above. The uv-coverage achieved when combining the five observing runs is shown in Fig. 4.4.

The produced interferometric measurements are stored in binary Flexible Image Transport System (FITS) binary tables to be further used in the reduction process. Each raw data file contains a header and a binary table with information about the observing run, the

instrument configuration and the observatory.

4.2.3 Data reduction and delivered products

The MIDI data reduction was performed with the version 2.0 of the package MIA+EWS[3]. This package runs in the Interactive Data Language (IDL), and has been developed and maintained by Sterrewacht Leiden.

Once each detector in each of the two telescopes has received a two-dimensional signal in accordance with Eq. 3.23, recalled as follows

$$I(\vec{\theta}) = I_0 \left(1 + |\mu(\vec{B})| \cos(\phi(\vec{B}) + k\, \vec{\theta}\, \vec{B})\right)$$

each channel is multiplied by a mask which is centred on the spectrum of the source and acts as spatial weighting functions. These masks suppress the noise signal on the detector frames above and below the spectrum. Then, the weighted detector signals are collapsed in the direction perpendicular to the dispersion direction, which in the case of the PRISM used for the observations of V892 Tau corresponds to 41 because the subarray on the detector has a size of 171×41 pixels. The result for each aperture is the retrieval of two one-dimensional signals corresponding to two opposite interferograms of the form

$$I_1 = S_1 + I_0 \left(1 + V(B_\lambda) \cos(\phi + k\, d)\right)$$

$$I_2 = S_2 + I_0 \left(1 - V(B_\lambda) \cos(\phi + k\, d)\right)$$

where, for simplicity, the visibility amplitude $|\mu(\vec{B})|$ has been denoted as $V(B_\lambda)$ and the product of the components $\vec{\theta}\, \vec{B}$ has been denoted with d. d is the delay term composed by the sum of the known instrumental delay and the unknown atmospheric delay, $d = d_{\rm ins} + d_{\rm atm}$. One can mention also the terms S_1 and S_2 which are introduced to account for the large background signal due to sky emission and warm optical elements.

The next step supposes the subtraction of the interferograms from each other to remove a large part of the background. Therefore

$$\begin{aligned} I &= I_1 - I_2 \\ &= S_1 + I_0 \left(1 + V(B_\lambda) \cos(\phi + k\, d)\right) - S_2 - I_0 \left(1 - V(B_\lambda) \cos(\phi + k\, d)\right) \\ &= S_1 - S_2 + 2 I_0 V(B_\lambda) \cos(\phi + k\, d) \end{aligned} \tag{4.3}$$

where the difference $S_1 - S_2$ is the residual background that is suppressed by subtracting the average of the entire spectrum over the multiple obtained frames. The remaining expression is thus the interferometric signal[4]

$$I_{\rm int} = 2 I_0 V(B_\lambda) \cos(\phi + k\, d). \tag{4.4}$$

Because the MIDI Interactive Analysis (MIA) and Expert WorkStation (EWS) routines as independent data reduction tools use different methods to extract the information of this interferogram, they are independently reviewed below.

[3]The software package is publicly available at `www.home.strw.leidenuniv.nl/~jaffe/ews/`

[4]This equation reviews the ideal case when no inequalities exist in the beams. Normally, an additional correcting factor is applied during the reduction process.

MIA

MIA performs an incoherent method to determine the fringe amplitude, namely, the power spectrum analysis. With this purpose, each fringe scan of the interferometric signal (Eq. 4.4) is Fourier transformed from the delay space d to the frequency space k' as follows

$$\begin{aligned} F(k') &= \int I_{\rm int}(d) e^{-{\rm i}k'd} {\rm d}d \\ &= \int 2I_0 V(B_\lambda)\, \cos(\phi + k\, d) e^{-{\rm i}k'd} {\rm d}d \end{aligned} \tag{4.5}$$

where, now, the cosine can be expressed in terms of the Euler's formula, resulting

$$\begin{aligned} F(k') &= I_0 V(B_\lambda) \int \left(e^{{\rm i}(\phi + k\, d)} + e^{-{\rm i}(\phi + k\, d)} \right) e^{-{\rm i}k'd} {\rm d}d \\ &= I_0 V(B_\lambda) \int \left(e^{{\rm i}d(k-k')} e^{{\rm i}\phi} + e^{-{\rm i}d(k+k')} e^{-{\rm i}\phi} \right) {\rm d}d \\ &= I_0 V(B_\lambda) \left[\delta\left(k - k'\right) e^{{\rm i}\phi} - \delta\left(k + k'\right) e^{-{\rm i}\phi} \right]. \end{aligned} \tag{4.6}$$

Consequently the power spectrum is defined as

$$P(k') = \left| F(k') \right|^2 = I_0 V(B_\lambda) \left[\delta(k - k') - \delta(k + k') \right]. \tag{4.7}$$

This power spectrum has two peaks at $\pm k'$, whose shape and intensity depend on the wavelength and OPD variation. With this information, the power inside the correct frequency interval, accounting for atmospheric effects in the OPD, is integrated. Therefore this method calculates the raw correlated flux $F_{\rm cor} = I_0 V(B_\lambda)$. When describing the observational sequence with MIDI, it was mentioned that the OPD is centred on the white-light fringe. This is the reason why the power spectrum method performed by MIA does not deliver information about the interferometric phase.

The commands of MIA – between others – to calculate the raw visibility curve of a dataset consisting of fringe measurements and photometric measurements include:

- `midigui` to select the dataset files in the "Gorgonzola" window

- `xmdv` to access the main routine of MIA and create the appropriate masks with which the fringes and photometry are extracted

- `gui` to bring up the main graphical user interface, visualize and save the results

After these same reduction steps have been followed both for science and calibrator, the instrumental visibility has to be determined with the function `instruvisi` and the known diameter of the calibrator. Finally, the routine `calibratedvisi` calculates the calibrated visibility of the science object by dividing the raw visibility of the science object by the obtained instrumental visibility of the calibrator according to Eq. 4.2.

The left panels of Fig. 4.5 show the raw visibility of the science object V892 Tau with very low values (gray line) and the instrumental visibility of all calibrators per date of observation, in accordance with Table 4.4. The right panels illustrate the calibrated visibility per night of observation for each of them. The several calibrators obtained per night allow to monitor the long-term variability of the interferometric transfer function over a given night.

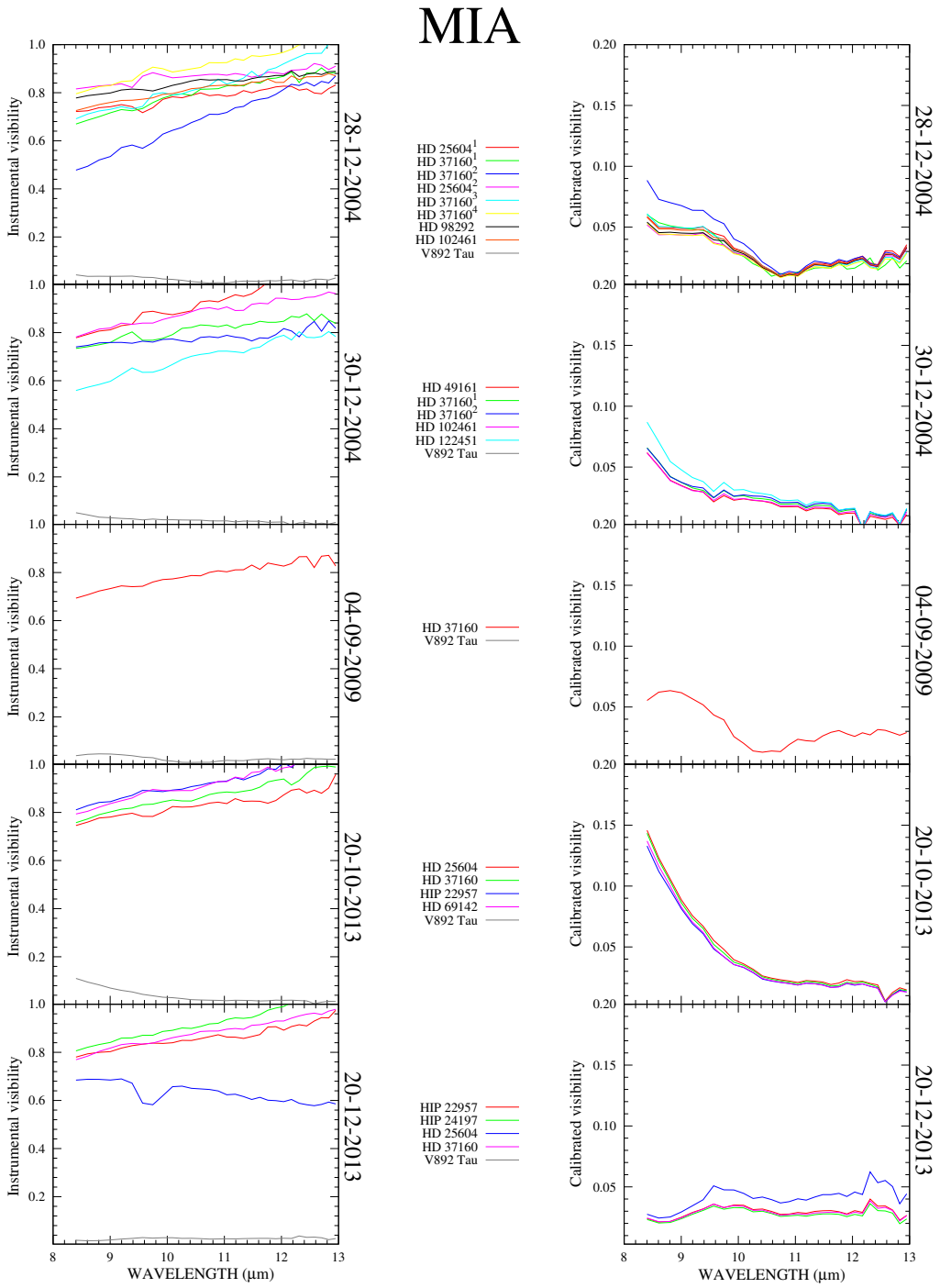

Figure 4.5: Instrumental (left panels) and calibrated (right panels) visibilities obtained with MIA, the incoherent method based on a power spectrum analysis. The raw visibility of the science object V892 Tau is also shown close to be fully resolved in the left panels (gray line). The photometric and interferometric calibrators here plotted are in correspondence with Table 4.4.

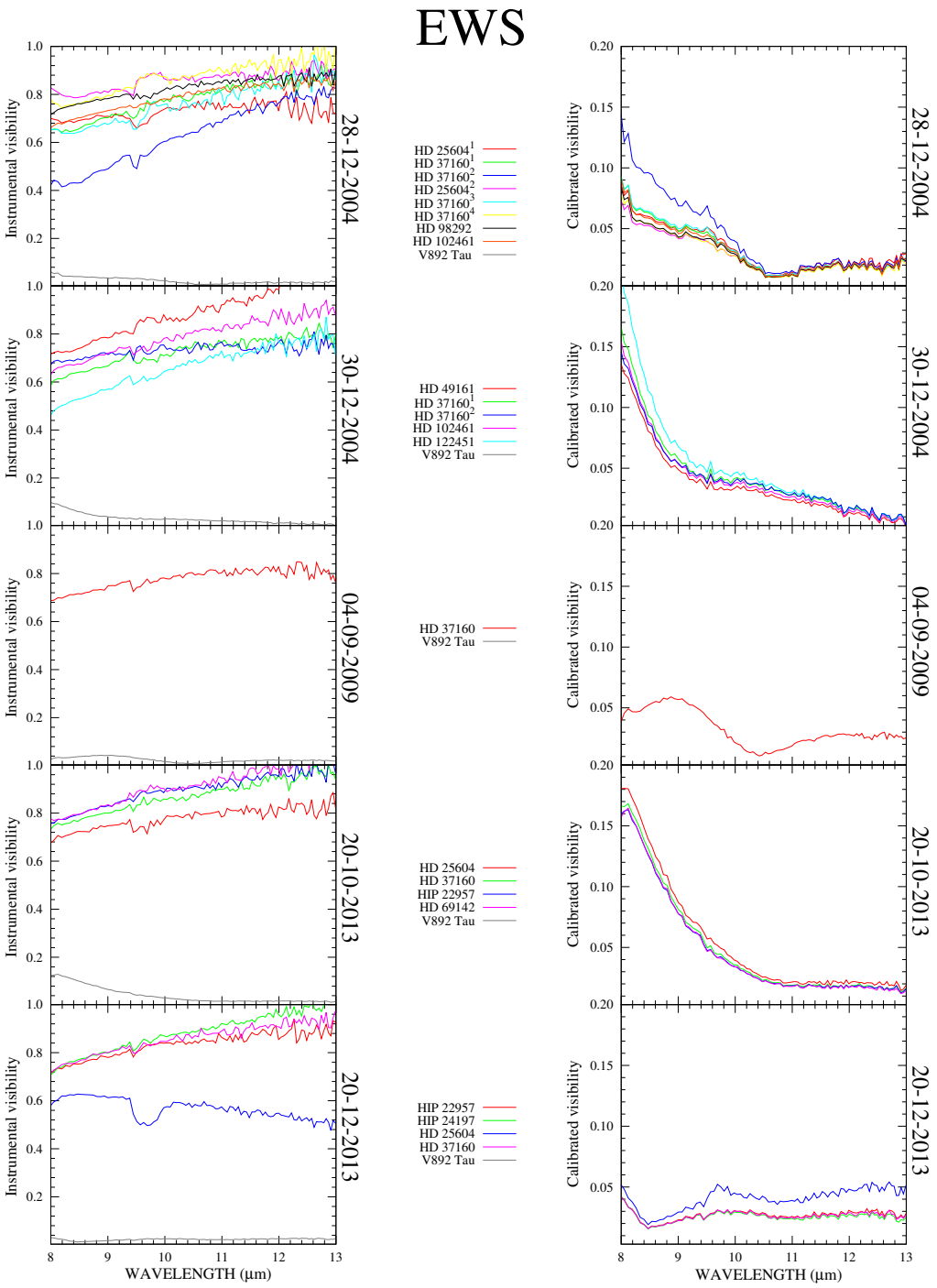

Figure 4.6: Instrumental (left panels) and calibrated (right panels) visibilities obtained with EWS, which performs a coherent analysis of dispersed fringes to estimate the complex visibility. The raw visibility of Elias 1 is traced with a gray line in the left panels. In comparison to Fig. 4.5, these profiles have a higher spectral resolution between 8 and 13 μm (97), although both agree well in shape.

EWS

The MIDI data reduction with EWS supposes a coherent integration of a complex observable using the vector average and the vector alignment within their statistical error to avoid a result of zero. With this purpose the instrumental OPD – or $d_{\rm ins}$ – included in the interferometric signal of Eq. 4.4, is subtracted by multiplying each frame by the complex observable $e^{-{\rm i}\ kd_{\rm ins}}$, as follows

$$\begin{aligned} I_{\rm rot} &= I_{\rm int}\ e^{-{\rm i}\ kd_{\rm ins}} \\ &= 2I_0V(B_\lambda)\ \cos(\phi + k\ d)e^{-{\rm i}\ kd_{\rm ins}} \end{aligned} \tag{4.8}$$

where the cosine again can be expressed in terms of the Euler's formula, and the delay term equals $d = d_{\rm ins} + d_{\rm atm}$. Consequently

$$\begin{aligned} I_{\rm rot} &= I_0V(B_\lambda)\ \left(e^{{\rm i}(\phi+k\ d)} + e^{-{\rm i}(\phi+k\ d)}\right)\ e^{-{\rm i}\ kd_{\rm ins}} \\ &= I_0V(B_\lambda)\ \left(e^{{\rm i}\phi+{\rm i}kd_{\rm atm}} + e^{-{\rm i}\phi-{\rm i}k(d_{\rm atm}+2d_{\rm ins})}\right). \end{aligned} \tag{4.9}$$

Eq. 4.9 is a complex observable called rotation by the group delay. Then, each frame is Fourier transformed from the frequency domain k to the delay domain d'

$$\begin{aligned} F(d') &= \int I_{\rm rot}\ e^{-{\rm i}kd'}{\rm d}k \\ &= \int I_0V(B_\lambda)\ \left(e^{{\rm i}\phi+{\rm i}kd_{\rm atm}} + e^{-{\rm i}\phi-{\rm i}k(d_{\rm atm}+2d_{\rm ins})}\right)e^{-{\rm i}kd'}{\rm d}k. \end{aligned} \tag{4.10}$$

The function $F(d')$ is called delay function, and it can be easily calculated by considering an infinitely broadband and constant visibility, following

$$\begin{aligned} F(d') &= I_0V(B_\lambda)\int \left(e^{{\rm i}\phi+{\rm i}kd_{\rm atm}} + e^{-{\rm i}\phi-{\rm i}k(d_{\rm atm}+2d_{\rm ins})}\right)e^{-{\rm i}kd'}{\rm d}k \\ &= I_0V(B_\lambda)\int \left(e^{{\rm i}k(d_{\rm atm}-d')}e^{{\rm i}\phi} + e^{-{\rm i}k(d_{\rm atm}+2d_{\rm ins}+d')}e^{-{\rm i}\phi}\right){\rm d}k \\ &= I_0V(B_\lambda)\left[\delta\left(d_{\rm atm}-d'\right)e^{{\rm i}\phi} - \delta\left(d_{\rm atm}+2d_{\rm ins}+d'\right)e^{-{\rm i}\phi}\right]. \end{aligned} \tag{4.11}$$

Although it was considered that the source brightness and the visibility amplitude are constant, the peaks of this delay function are shaped by the product $I_0V(B_\lambda)$. Thus, Eq. 4.11 can be more generally expressed in terms of its Fourier transform as

$$F(d') = \mathfrak{F}\left[I_0(k)\ V(k)\right](d')\left[\left(d_{\rm atm}-d'\right)e^{{\rm i}\phi} - \left(d_{\rm atm}+2d_{\rm ins}+d'\right)e^{-{\rm i}\phi}\right]. \tag{4.12}$$

The positions of the two peaks corresponding to the group delay are at $\pm d'$. The first of them varies slowly with the changes in the optical delay $d_{\rm atm}$, the second, on the contrary, oscillates rapidly due to the modulation of the instrumental delay with the piezo mirrors. Once the value of d' is known, the value of the factor $\cos(\phi + k\ d)$ is revealed, and the correlated flux $F_{\rm cor} = I_0V(B_\lambda)$ can be estimated. Also the differential phase ϕ can be extracted. In order to obtain the normalized visibility $V(B_\lambda)$, the total intensity of the source I_0 has to be determined, being thus fruitful the spectro-photometric measurement of the source.

The reduction process of MIDI data with EWS begins with the pipeline `midigui` to select the dataset files. Posteriorly a `tag` which identifies all the outputs has to be given.

Finally the `midipipe` command produces the uncalibrated results. The same process has to be followed for science and calibrators. The data reduction with this tool concludes with the calibration between science and calibrator through the pipeline `midiCalibrate`, where the flux at 10 μm of the calibrator and its diameter have to be given (columns "F10" and "Diameter" of Table 4.4). This information is taken from a database created by R. van Boekel based on infrared templates created by Cohen et al. [1999]. As for the MIA reduction, the left panels of Fig. 4.6 show the EWS raw visibility of the science object V892 Tau (gray line) and the instrumental visibility of all calibrators per date of observation. The right panels illustrate the individual calibrated visibility per night of observation.

Error estimation

One of the biggest defects during the MIDI data reduction is the unreliable error determination for the delivered products. On the one hand, MIA does not provide any error estimation. The only possibility to estimate uncertainties in the measurements and reduction is to calibrate the science target with several calibrators observed under the same instrument mode and account for the scatter that they produce. On the other hand, EWS derives error values due to the large amount (few thousands) of individual frames taken during the fringe tracking and the photometry steps. Therefore, the errors given by EWS are a root mean square deviation, and cannot be taken as absolute errors because systematic errors can be neglected [e.g. Tristram, 2007]. The commonly adopted order of these error estimates is 5–15% for observations in the mid-IR.

I take advantage of the results and outputs produced by EWS for the further analysis in this investigation. The datasets consist of calibrated visibilities, differential phases and photometric measurements in the N-band. Although the MIA products have less default spectral channels between 8 and 13 μm (MIA has 30 and EWS has 97), a comparison between the two methods shows consistency of the reduction and calibration. This is clearly seen from Figs. 4.5 and 4.6. Contrasting these two reduction processes is especially valuable to disregard "suspicious reductions" with any of the two algorithms. For instance, an instrumental visibility rather different than for the rest of calibrators is observed on 28-12-2004 (HD37160[2]) and 20-10-2013 (HD25604). This effect appears both for MIA and EWS, and therefore it can be accepted as an inherent effect of the observations (possibly due to clouds on one or both apertures). In spite of their peculiarity, this calibrated data has been included because the runs were acquired close in time with the science target, and may trace a long-term variability in the interferometric transfer function.

Because the observing runs of V892 Tau included the observations of at least 4 calibrators (excepting the run on 04-09-2009), it was carried out an error estimation based on both, the standard deviation of the different calibrated measurements over a given night ($\sigma_{\rm cal}$) which represents a long-term variability of the interferometric transfer function, and on the computation provided by EWS ($\sigma_{\rm EWS}$) which traces short-term statistical errors. Therefore, the total error estimation ($\sigma_{\rm total}$) per wavelength channel is defined by the expression

$$\sigma_{\rm total} = \sqrt{\sigma^2_{\rm EWS} + \sigma^2_{\rm cal}}. \tag{4.13}$$

The EWS products of mid-IR visibilities, differential phases and fluxes (correlated and total) with their respective error-bars are vertically presented in Fig. 4.7. In the figure each run is horizontally organized with an independent color. These delivered products are further used in my research.

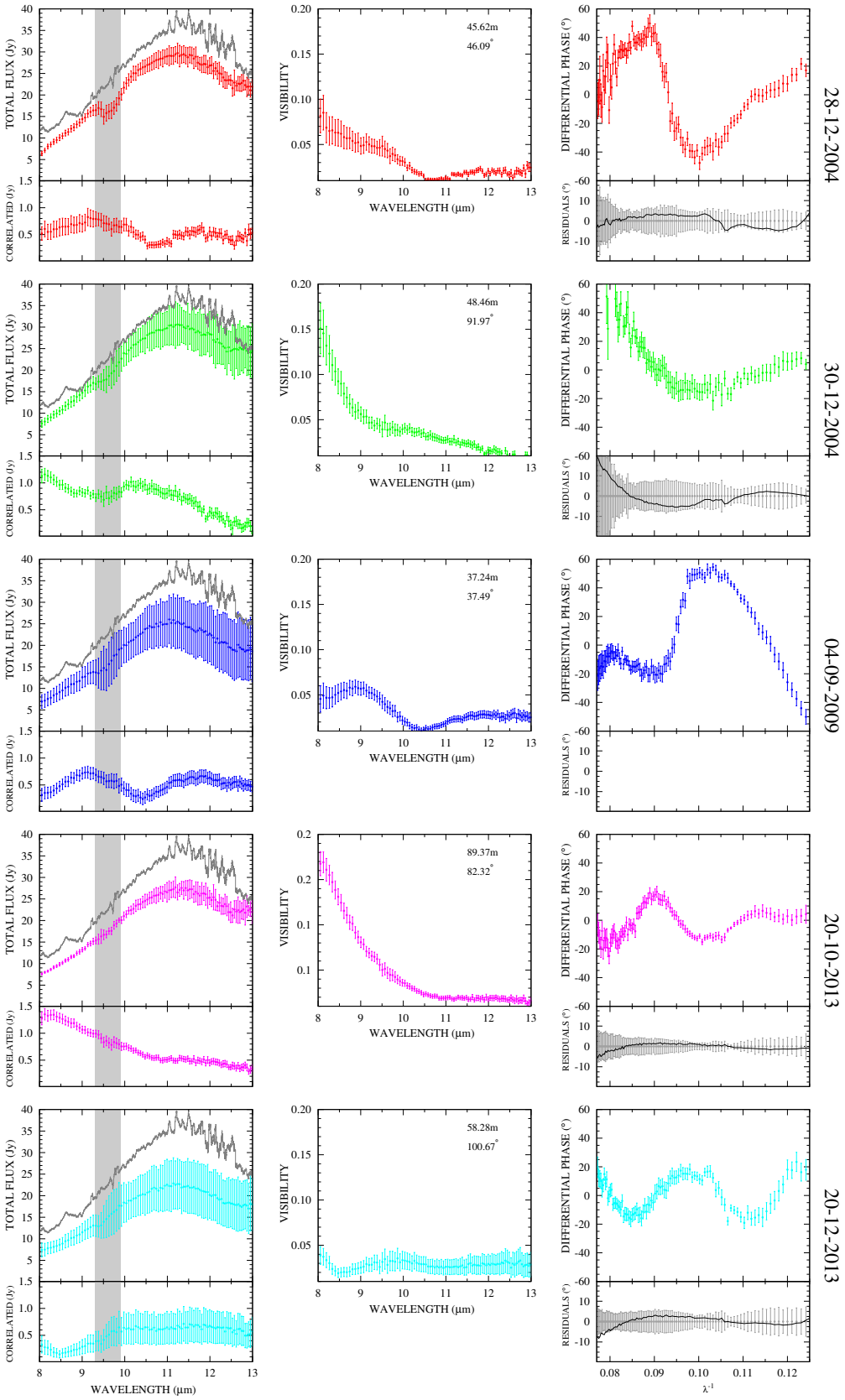

Figure 4.7: EWS products used for this study. The vertical panels containing the total and calibrated flux, the visibilities, and the differential phases with their residuals as a function of spatial frequency are horizontally organized per observing run.

4.2.4 Observational analysis of MIDI data

The delivered products shown in Fig. 4.7 motivate a first description of their characteristics:

- **The averaged MIDI total flux** for each observing run is shown in the left panels of Fig. 4.7 with the label "TOTAL FLUX". For comparison, also the ISO SWS spectrum[5] presented before in Fig. 4.2 is overplotted with a gray line. The spectra exhibit the broad silicate feature typically found in young disks. Both, ISO and MIDI fluxes, agree well in shape and reach values of ~ 25 Jy at 10 μm. However, only the ISO spectrum presents the PAHs feature at 8.6 μm due to its spectral resolution of $\sim$1500. The gray band between 9.3 and 9.9 μm in the figure denotes the ozone band where a drop in flux is seen. The uncertainty of the absolute photometric calibration is of the order of 10–15%, similar to the uncertainty reported by Ratzka et al. [2007] for the young star TW Hya. A possible origin of this effect is the significant background emission variability and the hard absolute calibration of MIDI total flux measurements. In addition, the residual fluctuations of the beams' position on the detector may imply a flux underestimation because the mask used to isolate and extract the target light on the detector might have missed some flux [e.g. Chesneau, 2007]. Also, an extra glance to the five runs suggests that the flux measurements vary from date to date in a range of 5 Jy. For instance, the 2013 data seems to have recorded less flux in comparison to the previous days. At 10 μm such variation supposes a magnitude variability of $\sim$0.3 mag. Even though the background emission and calibration have some influence, the intrinsic mid-IR variability of the object within few months due to non-axisymmetric changes in its circumstellar environment can be a major factor. Based on multi-epoch observations, such mid-IR variability has been identified in other HAeBe stars such as SV Cep, with a flux variation of about $\pm$20% [Prusti and Natta, 2002].

- In the lower part of the same left panels of Fig. 4.7 **the averaged MIDI correlated flux** measurements are traced. They represent the flux contribution from the unresolved inner regions close to the central star. They are responsible for shaping the visibility curves and adopt values between 0.1 and 1.5 Jy.

- **The mid-IR visibilities**, as seen from the middle panels of Fig. 4.7, correspond to a source close to being fully resolved in the five observed epochs. The visibility curves result from dividing the correlated flux by the total flux of the left panels. The data shows variations at shorter wavelengths ranging between $\sim$ 0.05 and 0.2, and a more general trend showing a constant plateau beyond 10 μm. In particular, the higher visibilities at 8 μm (in the case of 30-12-2004 and 20-10-2013) mean that the interferometer rather resolves the disk at 13 μm than at shorter wavelengths. Similar trends in the N-band with a steeper drop between 8–10 μm and flat signatures longward have been found [Leinert et al., 2004] and modelled [van Boekel et al., 2005] in a larger sample of HAeBe objects hosting disks.

- **The differential or chromatic phases** per observing run with MIDI are displayed in the right panels of Fig. 4.7. The data is especially relevant for this study since they bear information about possible brightness asymmetries in the system. Indeed, the interferometric phases exhibit deviations from zero when flux contributions from opposite sides of the system fail to cancel each other completely [Panić et al., 2014]. The MIDI data presents deviations as large as $\sim$60°, much larger than the $\sim$10° phase

[5] Publicly available in the NASA archive

signal produced by longitudinal dispersion effects due to the atmospheric water vapour [e.g. Tubbs et al., 2004, Matter et al., 2010].

I tested the influence of the atmosphere following the analysis by Panić et al. [2014]. Namely, I used the observations of the calibrators acquired at different airmasses immediately before and after the science target to cross-calibrate and compare the phase difference. The resulting phase difference is traced with a black line in the lower part of the left panels of Fig. 4.7 (except for the third run where the observation of only one calibrator is insufficient to make this comparison). This phase difference which estimates the atmospheric contribution appears to be lower – or of the same order – than the MIDI error-bars. This fact leads me to conclude that the large variations seen in the MIDI differential phases are intrinsic to the V892 Tau system.

4.3 Modelling of data

As seen from Chapter 3, the normalized visibility given for various source morphologies can be used to build visibility building blocks of more complex astronomical sources. Therefore, in order to simultaneously model the MIDI interferometric measurements and the SED of V892 Tau, I adopt a visibility block consisting of a binary system and uniform disks with temperature-gradient dependence. This permits to evaluate the spatial distribution at AU-scale regions of dusty structures detected in the mid-IR with the 2×2 arcsec field-of-view of MIDI. Furthermore, I coupled this semi-physical temperature-gradient disk model with the Modelling and Analysis Generic Interface for eXternal numerical codes (MAGIX). Its χ^2-minimization and Monte Carlo based algorithms allow me to refine the results of the analysed scenarios.

4.3.1 Investigated scenarios of components forming V892 Tau

In addition to testing a configuration consisting of the previously reported binary stars with near-equal brightness [Smith et al., 2005] and the large circumbinary disk which surrounds them detected through mid-IR observations [Monnier et al., 2008], in this work I investigate the possibility of dust survival within the circumbinary disk. In such case, I review the possible existence of thermal emission originating from a circumstellar disk around one of the stellar components, or from a disk-like source unattached to the stars. Therefore, the three scenarios that I define are the following (Figs. 4.8–4.10):

1) *A model consisting of a binary system with a geometrically flat circumbinary disk*

2) *A model consisting of a binary system with a geometrically flat circumbinary disk and a circumstellar disk around one stellar component*

3) *A model consisting of a binary system with a geometrically flat circumbinary disk and a dusty disk-like component in the circumbinary cavity*

4.3.2 Temperature-gradient model

A temperature-gradient analysis is ideal to be applied to the high-resolution mid-IR data because of the restricted available data both in wavelength coverage (8–13 μm) and in observing runs (five dates). Taking the concepts and modelling approach defined in the

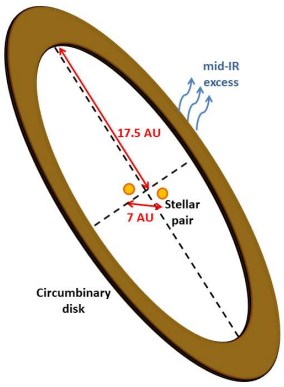

Figure 4.8: Illustration of the model studied in subsection 4.3.6. The stellar pair is only surrounded by the large circumbinary disk, which is the source of the mid-IR emission observed in the SED.

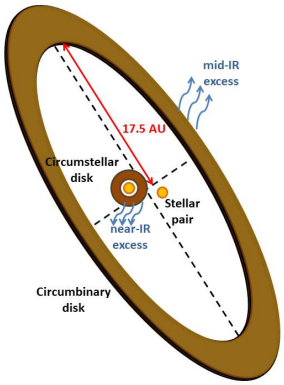

Figure 4.9: Scheme of the components considered in subsection 4.3.7. In addition to the stellar pair and the circumbinary disk, a circumstellar component around one star produces near-IR emission and deviates the photocenter of the system. Such phenomenon would manifest in the N-band observations with MIDI.

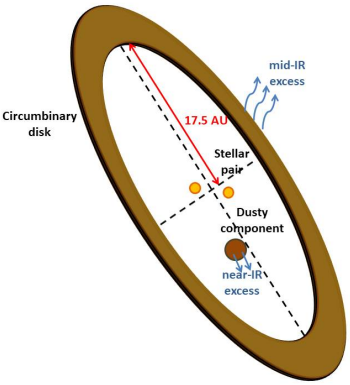

Figure 4.10: Sketch of the model of subsection 4.3.8 consisting of a stellar pair, a circumbinary disk and a hot disk-like component inside the large cavity. The additional dusty component produces near-IR emission and sets an asymmetry in the system which affect the MIDI visibilities and differential phases.

previous chapter, the unnormalized complex visibility function of a binary system consisting of two unresolved objects can be derived from Eq. 3.45, becoming

$$V_{\mathrm{bin},\lambda}(u,v) = F_{\mathrm{s1}}(\lambda)e^{-2\pi\mathrm{i}(u\alpha_{\mathrm{s1}}+v\beta_{\mathrm{s1}})} + F_{\mathrm{s2}}(\lambda)e^{-2\pi\mathrm{i}(u\alpha_{\mathrm{s2}}+v\beta_{\mathrm{s2}})} \tag{4.14}$$

where the subscripts $s1$ and $s2$ refer to the two stellar components. F and (α, β) are the flux and the angular coordinates in the sky plane of a given component, respectively, and (u, v) are the coordinates in the uv-plane that define the projected baseline.

I model the circumbinary emission as a geometrically flat temperature-gradient disk that has temperature and surface density radial profiles given by Eq. 3.33, as follows

$$\begin{aligned} T_{r_{\mathrm{cb}}} &= T_{\mathrm{in_{cb}}} \left(\frac{r_{\mathrm{cb}}}{R_{\mathrm{in_{cb}}}}\right)^{-q_{\mathrm{cb}}} \\ \Sigma_{r_{\mathrm{cb}}} &= \Sigma_{\mathrm{in_{cb}}} \left(\frac{r_{\mathrm{cb}}}{R_{\mathrm{in_{cb}}}}\right)^{-p_{\mathrm{cb}}} \end{aligned} \tag{4.15}$$

where r_{cb} is the distance to the centre of the system, and $T_{\mathrm{in_{cb}}}$ and $\Sigma_{\mathrm{in_{cb}}}$ are respectively the temperature and surface density at the inner radius of the circumbinary disk $R_{\mathrm{in_{cb}}}$. q_{cb} is the temperature power-law exponent and p_{cb} is the surface density power-law exponent. Such a temperature-gradient model splits the disk into n infinitesimal ringlets emitting like a blackbody. Each ringlet is located at a distance $r_{\mathrm{cb}}(n)$ from the center of the system and its blackbody emission is weighted similarly to the emissivity factor of Eq. 2.39

$$\epsilon_{\mathrm{cb}_\tau} = 1 - e^{\tau_{\lambda,r_{\mathrm{cb}}}/\cos i_{\mathrm{cb}}} \tag{4.16}$$

where the vertical optical depth $\tau_{\lambda,r_{\mathrm{cb}}}$ is a function of the dust opacity according to the expression of Eq. 2.24

$$\tau_{\lambda,r_{\mathrm{cb}}} = \kappa_\lambda \Sigma_{r_{\mathrm{cb}}}. \tag{4.17}$$

As discussed in the previous chapter, the different opacity laws have distinct impact on the SED modelling. Thus, I performed a visual comparison and a narrow-band χ^2-minimization to determine which dust composition of the circumbinary disk alone better shapes the silicate bump of the MIDI spectrum. The best χ^2-results were obtained by adopting the dust opacity computed by Pollack et al. [1994] and Semenov et al. [2003] shown in Figs. 2.8 and 3.15. This dust opacity is based on a mix of olivine, orthopyroxene, organics, water ice, troilite and metallic iron grains (Fig. 4.11). The decision on the adopted composition is, nevertheless, a mere step to improve the χ^2-fit to the observed data, being a detailed analysis of the dust composition around Elias 1 out of the scope of this work.

By recalling the expression to calculate the total flux produced by an inclined disk in Eq. 3.36 and the visibility building block for an individual ring in Eq. 3.52, the total flux and the visibility amplitude of the circumbinary disk can be respectively expressed as

$$F_{\mathrm{cb},i}(\lambda) = \frac{\cos i}{d^2} \int_{R_{\mathrm{in_{cb}}}}^{R_{\mathrm{out_{cb}}}} 2\pi r_{\mathrm{cb}} B_\lambda(T_{r_{\mathrm{cb}}}) \epsilon_{\mathrm{cb}_\tau} A_{\mathrm{V}}(\lambda) \mathrm{d}r \tag{4.18}$$

and

$$V_{\mathrm{cb},\lambda}(B_{\mathrm{p}}(i,\varphi)) = \frac{1}{F_\lambda(0)} \int_{R_{\mathrm{in_{cb}}}}^{R_{\mathrm{out_{cb}}}} 2\pi r_{\mathrm{cb}} B_\lambda(T_{r_{\mathrm{cb}}}) \epsilon_{\mathrm{cb}_\tau} J_0\left(\frac{2\pi}{\lambda} B_{\mathrm{p}}(i,\varphi)\frac{r_{\mathrm{cb}}}{d}\right) \mathrm{d}r \tag{4.19}$$

where

$$B_{\mathrm{p}}(i,\varphi) = \sqrt{B_{u,\varphi}^2 + B_{v,\varphi}^2 \cos^2 i} \tag{4.20}$$

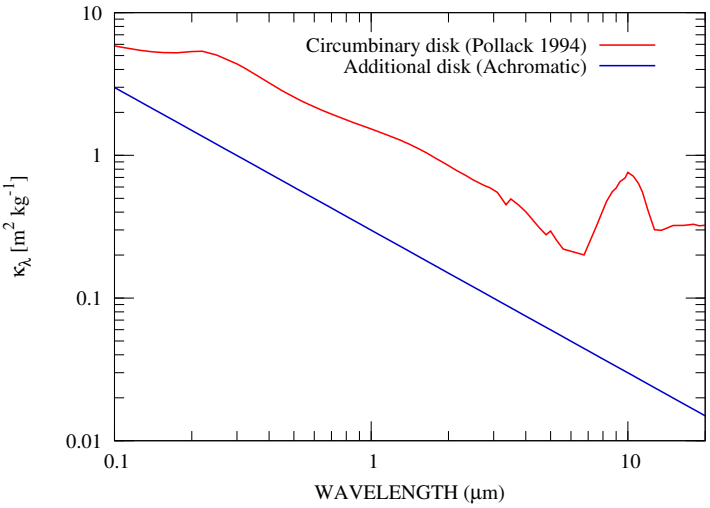

Figure 4.11: Dust opacity law implemented in the model of the circumbinary disk tested in scenarios 1), 2) and 3) (red line), and the uniform disk-like additional component of models 2) and 3) (blue line). The first composition is a mix of olivine, orthopyroxene, organics, water ice, troilite and metallic iron grains [Pollack et al., 1994], whereas the second law has an achromatic nature according to Eq. 3.38. The peak featured at 10 μm corresponds to the silicate band present in the spectrum of V892 Tau.

is the length of the projected baseline expressed in the reference frame under a rotation φ and inclination i. This "frame reconstruction" makes possible to apply the standard visibility equations for circular symmetric objects [Berger and Segransan, 2007]. In turn, this projected baseline is written in terms of its rotated components

$$\begin{aligned} B_{u,\varphi} =& B_u \cos\varphi + B_v \sin\varphi \\ B_{v,\varphi} =& - B_u \cos\varphi + B_v \sin\varphi. \end{aligned} \tag{4.21}$$

In addition to the stellar pair and the large circumbinary disk, the proposed scenarios 2) and 3) contemplate the presence of an additional near-IR source. Scenario 2) incorporates a disk surrounding one of the stellar components, and scenario 3) inserts a uniform disk-like dusty body located inside the cavity of the circumbinary disk. I represent this new component as a uniform disk that can be treated similarly to the model of the large circumbinary disk. Namely, in accordance with Eqs. 4.18 and 4.19, this new component would have a total flux $F_{\mathrm{new},i_{\mathrm{new}}}(\lambda)$ and a visibility $V_{\mathrm{new},\lambda}(u,v)$, where the subindex "new", instead of "cb" for the circumbinary disk, would be denoted as "cs" for the case 2) of the circumstellar disk, and as "dc" for the case 3) of the freely floating dusty component.

To date, very few works [e.g. Ratzka et al., 2009, Panić et al., 2014] have focused on the information provided by the interferometric differential phases to study brightness asymmetries. This is understandable, in part, because of the irrelevant information that they provide for observations of axisymmetric objects with close-to-zero phases [Tristram, 2007]. The observational data produced by EWS reveals that the MIDI differential phases are largely modulated, with values of up to $\pm 50^{\circ}$ (Fig. 4.7). Hence, a relevant aspect of my investigation is the inclusion of the phases in the modelling of the system V892 Tau. The differential phases contain information about the nature and morphology of the presumable additional near-IR source that causes a deviation of the photocenter. The signal detected by MIDI contains a phase term that is modelled following the procedure presented in the previous

chapter. Namely, the source phase $\phi_{\rm s}(\lambda)$, as a function of the wave number $k = 2\pi/\lambda$, can be written as the polynomial expression

$$\phi_{\rm s}(k) = \psi_0 + \psi_1 k + \psi_c(k) \tag{4.22}$$

where the two first terms representing the atmospheric and instrumental contribution can be extracted by fitting a linear function, and the higher order terms belong to the intrinsic source phase. Subsequently, I retrieve the differential phases out of the complex visibilities resulting from the three studied models (Eqs. 4.34, 4.40 and 4.45) according to

$$\phi_{\rm s}(k) = \tan^{-1}\left(\frac{{\rm Im}(V_{{\rm model},\lambda}(u,v))}{{\rm Re}(V_{{\rm model},\lambda}(u,v))}\right). \tag{4.23}$$

Afterwards, the atmospheric and instrumental imprint is removed through a linear fit in the frequency domain followed by the subtraction of the average phase over the N-band.

4.3.3 Definition of fixed parameters

A first step to model the experimental data, interferometric and spectro-photometric, is to establish a set of fixed parameters based on the literature and reports on V892 Tau as a convenient approach to optimize computational and analytical efforts.

First, I adopt a distance to the system $d = 140$ pc as it has been determined by surveys of the Taurus cloud [e.g. Elias, 1978]. Then, the parameters concerning the binary stellar components can be also established:

• *Effective temperature* $T_{\rm eff}$: Reports on the spectral type and visual extinction reviewed in the introductory part of this chapter encompass a range A6–B9. According to the Stefan-Boltzmann law of Eq. 2.33, a small variation in spectral type of the object, and therefore in its effective temperature or radius, carries an influence proportional to a power of 4 in the photospheric flux, admitting temperatures between 8000–12000 K. Thus, this parameter provokes an overestimation, or underestimation, of the stellar photospheric flux and, consequently, erroneous models of also other components in the system (e.g. circumbinary or circumstellar disks). For this reason, the values adopted by Monnier et al. [2008] to reproduce the flat SED of V892 Tau with a very bright and extinguished stellar pair (400 $L_\odot$) plus a circumbinary warm (450 K) inner wall at 18 AU have to be taken with caution because, although this barely simulates the spectral energy distribution (Fig. 4.3), a significant contribution from a near-IR source may be hidden. With the pink line of Fig. 4.12 I present a comparison of this temperature-luminosity value with evolutionary tracks for PMS stars by Palla and Stahler [1993].

Instead, in the same figure a more concurring determination of the stellar luminosity is traced with blue lines. These values correspond to a spectral type B8.5V–A0Ve with an effective temperature of 11000 K given by the more recent report by Mooley et al. [2013] on which this investigation relies. Moreover, isochrone calculators [Siess et al., 2000] reveal that the corresponding stellar luminosity for such value is around 60 $L_\odot$, the mass is 2.75 $M_\odot$, and its age some 4–5 Myr. I can conclude from the report on the binarity and spectroscopy of the object that the stellar pair has a near-equal brightness, and hence the luminosity of the object reaches 120 $L_\odot$. This is in agreement with the work on the properties of PMS objects in the Taurus molecular cloud by Rebull et al. [2010], where a luminosity of 100 $L_\odot$ for V892 Tau was derived, and also with the values used by Güdel et al. [2007] accounting for an effective temperature of 10500 K. The assumption of an equal-brightness pair remains valid in the N-band due to the minor stellar contribution ($< 5\%$) in this spectral range. With

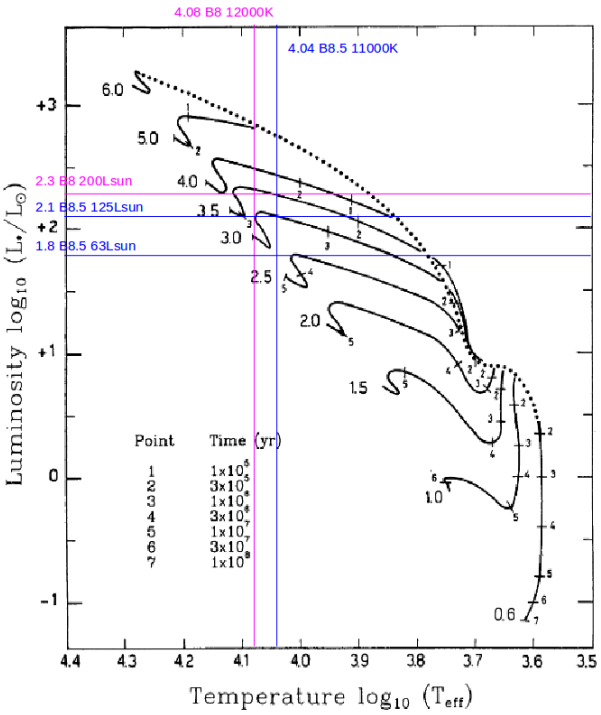

Figure 4.12: Evolutionary tracks for PMS objects from their birthline (dotted curve) until the ZAMS by Palla and Stahler [1993], reproduced from Fig. 2.3. The pink line depicts that the high luminosity of 200 $L\odot$ for each star considered by Monnier et al. [2008] indeed represents a B8 class with $T_{\rm eff} = 12000$ K. From the track, however, this fact disagrees with the system mass of 5.5 $M_\odot$ in their report, and alters the orbital solution. On the contrary, the newest report by Mooley et al. [2013], on which my work relies, shows with blue lines that in order to match the orbital solution and system mass, a luminosity of about 60 $L_\odot$ and 2.75 $M_\odot$ for each component is required. This analysis is corroborated with isochrone calculators, from which an age of some 4–5 Myr is deduced for the system, unlike a younger age of 1.5 Myr for the 2008 work. These stellar parameters are established for the following study and the corresponding photospheric flux can be seen in the SED of Fig. 4.14. [Credit: adapted from Palla and Stahler [1993]. Reproduced with permission ©AAS.]

this in mind, the lack of infrared emission in this Class II object becomes more evident than in the estimate by Monnier et al. [2008] of 400 $L_\odot$ (see Fig. 4.3).

• *Stellar radius $R_\star$ and coefficient of total visual extinction A_V*: After the total luminosity and effective temperature of the stars have been deduced, a visualization and numerical analysis with the support of the χ^2-optimizer MAGIX allows me to determine the optimal radius and visual extinction to fit the SED slope of Elias 1 at the shortest wavelengths. The best obtained result indicates a stellar radius of 2.1 $R_\odot$ for each star and an extinction law with a coefficient $A_V = 7.5$ (Fig. 4.14).

• *Position at the time of observations ($\alpha_{\rm bin}$,$\beta_{\rm bin}$)*: Following the orbital solution by Monnier et al. [2008] presented in Fig. 4.13, the angular coordinates on the plane of the sky of the stellar components at the time of MIDI observations are fixed. These coordinates are free-parameters only in a test of model 1), where a slightly shifted pair in relation to the center of the circumbinary disk may provoke an asymmetry that attempts to simulate the MIDI differential phases.

Based on the results on the large circumbinary emission, some of its parameters can also

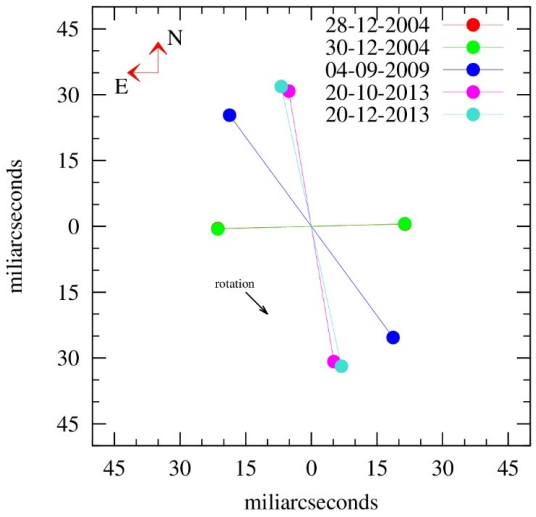

	Epoch	ρ [mas]	$\theta[^\circ]$
MIDI data	2004.9897	42.77	91.36
	2004.9958	42.71	91.58
	2009.6760	62.98	216.40
	2013.8014	62.51	9.48
	2013.9676	65.20	12.19
Smith et al. [2005]	1996.75	49.99	234.50
&	2003.76	59.95	58.87
Monnier et al. [2008]	2004.67	46.63	80.64

Figure 4.13: Distance ρ and position angle θ between the components of the binary system on the basis of the orbital solution determined by Monnier et al. [2008] (Table 4.2). In the figure, the position of the components with respect to their barycentre at the time of MIDI observing runs is plotted. Due to its proximity in epoch the first and second runs practically overlap. The angle is defined in the north-east direction. The values in the table are given for the 5 dates of MIDI data and the 3 previous observations by Smith et al. [2005] and Monnier et al. [2008].

be settled down:

• *Inclination* $i_{\rm cb}$: Under the assumption of long-term invariability of the disk, a value of 60° is assumed from the 2008 report.

• *Position angle* $\varphi_{\rm cb}$: For the same reason, the position angle of the circumbinary disk in the north-east direction has a value of 50°, as represented by the sketches of the disk.

• *Surface density power-law exponent* $p_{\rm cb}$: This parameter defined in Eq. 2.32 is set to 1, a value generally representative of the dust surface density profile in the outer regions of disks [e.g. Andrews et al., 2010].

• *Outer radius* $R_{\rm out_{cb}}$: The outer radius was restrained to a value of 100 AU typical found in Herbig and T Tauri objects [e.g. Vicente and Alves, 2005, Andrews and Williams, 2007b].

For the sake of reducing the number of free-parameters in the analysis and facilitating the interpretation of the nature of the near-IR source introduced in models 2) and 3) (either circumstellar or free-floating in the circumbinary cavity), two of its parameters are also fixed:

• *Temperature power-law exponent* $q_{\rm cs,dc}$: The additional component is assumed to be an achromatic blackbody, consequently its uniform energy distribution means $q_{\rm cs,dc} = 0$. The subindexes "cs" and "dc" are valid for the respective models 2) or 3).

• *Surface density power-law exponent* $p_{\rm cs,dc}$: Because of the same justification, a value of 0 for $p_{\rm cs,dc}$ also inserts a radial independence of the surface density.

Table 4.5 summarizes the fixed parametrization implemented in the modelling of spatial configurations 1), 2) and 3).

4.3.4 The spectral energy distribution of V892 Tau

To be modelled, the reduced interferometric dataset between 8–13 μm consists of three files: visibilities, differential phases and spectrum, where each data file contains 97 spectral

Table 4.5: Fixed parameters considered in the modelling of MIDI and SED measurements. The parametrization of the stellar pair and the circumbinary disk is used in all explored models, while the parameters fixed for the model with the circumstellar disk or dusty component have the corresponding subindexes "cs" and "dc".

Parameter	Value	Parameter	Value
d [pc]	140	$\varphi_{\rm cb}$ [°]	50
$T_\star$ [K]	2×11000	$p_{\rm cb}$	1
$R_\star$ [$R_\odot$]	2×2.1	$R_{\rm out_{cb}}$ [AU]	100
$A_{\rm v}$	7.5		
$L_\star$ [$L_\odot$]	2×60	$q_{\rm cs,dc}$	0
i [°]	60	$p_{\rm cs,dc}$	0

Note: The coordinates of the stellar pair ($\alpha_{\rm bin}$,$\beta_{\rm bin}$) given by the orbital solution [Fig. 4.13 Monnier et al., 2008] are also fixed parameters. However, they are free during the test of model 1) that probes a brightness asymmetric system.

channels. However, the implementation of the temperature-gradient modelling of V892 Tau produces flux measurements along the whole SED, being the N-band spectrum insufficient to gather information about the total flux distribution of the components.

For this reason, I have used additional spectro-photometric data from the literature[6] to build a composite spectrum between 2 and 20 μm – the range at which the stars and infrared sources influence the mid-IR data – with the same amount of spectral channels (97). This composite file allows to equalize the weight of the SED points during the fitting process, with also a 10% error-bar introduced to be comparable to the uncertainties quantified for the mid-IR data.

I have created the spectro-photometric composite spectrum by interpolating the measurements listed in Table 4.6 and plotted with blue dots in the SED of Fig. 4.14, which shows also the stellar flux contribution according to the fixed parameters of the stars.

4.3.5 Numerical χ^2-optimizer MAGIX

MAGIX[7] [Möller et al., 2013] is a model optimizer developed at the I. Physikalisches Institut of the University of Cologne that works in conjunction with external numerical models – and not necessarily only astrophysical – to explore the parameter space and find a set of parameter values that provide the best fits (the least χ^2-value) to the observational/experimental data. It provides diverse algorithms with the goal of global optimization, i.e. the finding of global optima (also usually referred as global minima) of an objective function. MAGIX provides also error estimations, and it is possible to use some of its algorithms in combination to refine the finding. Indeed, although the uttermost results of this investigation are based on extended minimizations with the Markov chain Monte Carlo (MCMC) algorithm due to its accurate analysis of the whole parameter space, more moderate minimizations with a chain algorithm consisting of Genetic algorithm (GA) and MCMC were also performed, for instance, for quantifying the expected inadequate reproduction of the observational data with the model of an axisymmetric system with a circumbinary disk alone.

[6]Measurements available at `http://vizier.u-strasbg.fr/vizier/sed/`
[7]Website: `https://magix.astro.uni-koeln.de`

Table 4.6: Spectro-photometric measurements taken from the literature to create a composite spectrum included in the model fitting. These values are graphically represented in the plot of Fig. 4.14 with blue dots.

Photometric system	Filter	Wavelength [μm]	SED flux [Jy]
Johnson	B	0.44	1×10^{-3}
Johnson	V	0.55	3×10^{-3}
Johnson	R	0.69	1.73×10^{-2}
POSS-II	I	0.79	4.86×10^{-2}
2MASS	J	1.24	5.22×10^{-1}
2MASS	H	1.65	1.66
2MASS	K	2.16	3.27
WISE	W1	3.35	2.70
WISE	W2	4.6	4.89
ISO SWS		2.45–20	Fig. 4.2
MIDI	N	8–13	Spectrum of this work

Genetic algorithm

The GA is a heuristic search and optimization technique motivated by the natural Darwininan principle of evolution through genetic selection [e.g. McCall, 2005, Herrera et al., 2005, Malhotra et al., 2011]. A GA develops a highly abstract version of evolutionary processes to create solutions to a given problem. With this purpose the algorithm operates on a population of artificial chromosomes, which are strings in a finite alphabet (usually binary). Each chromosome is a solution to a problem and therefore has a fitness, which is a real number measuring how good the solution is to the particular problem. A genetic algorithm follow a structure as outlined below and represented in the attached diagram:

1. *Initialization*: The first step is to generate a random population of chromosomes, that is, possible solutions for the problem. Although the greater the number of initial chromosomes, the larger the exploration of the parameter space, a value of 100 chromosomes with MAGIX was used since no significant variation would be seen in the χ^2-value determined after the given number of iterations is completed.

2. *Fitness assignment*: The second step is to compute the fitness value of each chromosome in the population. A χ^2-value is the quantity used to assign the fitness of the function. These raw fitness scores are used to convert them into a more usable range of values, called expectation values.

3. *Selection*: Then, parent chromosomes from a population are selected according to their fitness values to create an "elite". The better the fitness, the greater the chance to be selected.

4. *Crossover*: These parents form new offspring, or children, through a crossover probability. If no crossover is performed, then the children are the exact copy of their parents.

5. *Mutation*: In addition to crossover, new children are produced by making random changes to a single parent, called mutation.

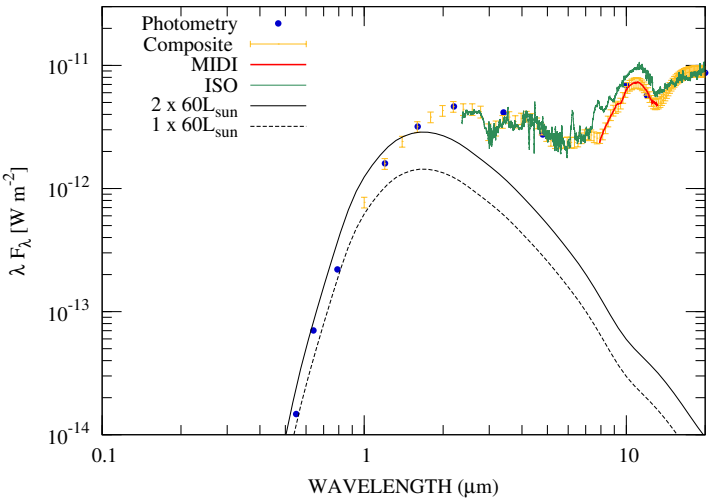

Figure 4.14: SED of V892 Tau. The blue dots correspond to the photometric measurements in the literature listed in Table 4.6. The N-band MIDI averaged spectrum is traced with red, and the ISO SWS with green from 2.45 μm on. The yellow error-bars correspond to the composite spectrum used for the model fitting. The total stellar flux for the two stars of the system is traced with the black line, and the contribution of only one of them is shown with the dashed line. This stellar photospheric flux is invariable in the model fitting applied in next sections.

6. *Replacement*: A current population is replaced with the children to form the next generation.

7. *Test*: If the end condition is satisfied, the algorithm stops and returns the best solution in the current population.

8. *Loop*: On the contrary, if the searched criteria is not fulfilled, the algorithm repeats step 2. In the control file of MAGIX this value was set to 100 since a greater number would just result in larger computational cost with insignificant variation in the χ^2-determination. The χ^2-value used as criteria was set to a small value to avoid stopping before the number of given iterations was completed.

The advantages of the GA over other global optimization algorithms is that it is capable of finding and analysing multiple minima without specific knowledge about the problem under study, it has a rapid convergence and thus reduces computational costs. The setting parameters under which the genetic algorithm carried out its analysis included: number of chromosomes, number of iterations and the stopping value given by a χ^2-limit. Fig. 4.15 summarizes the structure of the genetic algorithm, and the values used during this minimization routine are indicated in its attached table.

Markov chain Monte Carlo

After the first algorithm in the chain has performed its χ^2-minimization, the determined best site in the parameter space is explored by the MCMC method. The purpose of the algorithm MCMC is approximating the result based on sampling and defining probabilities[8]. Let us

[8]Publicly available resources extensively explain this numerical algorithm. The description here presented is taken and summarized from the MAGIX manual at `https://magix.astro.uni-koeln.de/sites/magix/files/files/MAGIX_Manual.pdf`

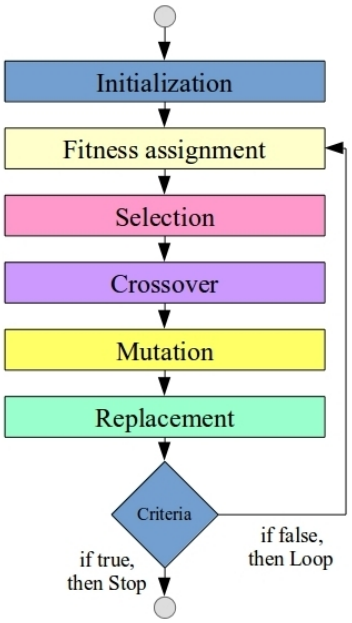

Number of chromosomes	Number of iterations	Criteria χ^2
$10 \times N_{\text{free}}$	100	$< 10^{-5}$

Figure 4.15: State diagram for the genetic algorithm. The attached table indicates its setting parameters managed by the MAGIX control file.

assume that M samples θ_i are drawn from the posterior probability density

$$P(\theta, a|D) = \frac{1}{Z} P(\theta, a) P(D|\theta, a) \tag{4.24}$$

where the prior distribution $P(\theta, a)$ and the likelihood function $P(D|\theta, a)$ can be computed for any particular value (θ_i, a_i). The normalizing factor $Z = P(D)$ is independent of θ and a once the form of a generative model has been chosen, meaning that it is possible to sample from $P(\theta, a|D)$ without computing Z. After the samples produced by MCMC are created, the marginalized constraints on θ can be approximated by the histograms of the samples projected into the parameter subspace spanned by θ. Therefore the expectation value of a function of the model parameter $f(\theta)$ is

$$\langle f(\theta) \rangle = \int P(D|\theta) f(\theta) \mathrm{d}\theta \approx \frac{1}{M} \sum_{i=1}^{M} f(\theta_i). \tag{4.25}$$

The generation of samples θ_i is simpler for cases where the $P(\theta, a|D)$ is a specific analytic distribution, such as a Gaussian. However, for a non-normal distribution, such as the case of a parametric temperature-gradient model, it may be a non-trivial task. In this algorithm the sets of samples are generated randomly (random walkers) over time along the entire parameter space. This means that each point in a Markov chain $X(t_i) = [\theta_i, a_i]$ depends only on the location of the previous step $X(t_i - 1)$.

The MCMC algorithm in MAGIX implements the "stretch move" method. This method consists of an ensemble of K walkers, $S = X_k$, which are simultaneously evolving. The proposal distribution for one walker k is based on the current position of the $K - 1$ walkers in the complementary ensemble $S_{[k]} = X_j, \forall_j \neq k$. To update the position of a walker at position X_k, a walker X_j is randomly sampled from the remaining walkers $S_{[k]}$ and a new position is proposed

$$X_k(t) \rightarrow Y = X_j + Z[X_k(t) - X_j] \tag{4.26}$$

Table 4.7: Setting parameters used for the minimization and error estimation with the MCMC algorithm. These parameters are set up in the control file of MAGIX.

Number of samplers	Error estimation accuracy	Number of iterations burn-in phase	Number of iterations	Criteria χ^2
1000	2σ	100	1000	$< 10^{-5}$

where Z is a random variable drawn from a distribution $g(Z = z)$. If $g(z^{-1}) = z\, g(z)$, the proposal in the equation above is symmetric. Then, the chain satisfies detailed balance if the proposal is accepted with the probability

$$q = \min\left(1, Z^{N-1}\frac{P(Y)}{P(X_k(t))}\right) \tag{4.27}$$

where N is the dimension of the parameter space. The same procedure is repeated for each walker in the ensemble series. The function $g(z)$ takes the form

$$g(z) \propto \begin{cases} \frac{1}{\sqrt{z}} & \text{if } z \in \left[\frac{1}{a}, a\right] \\ 0 & \text{otherwise} \end{cases} \tag{4.28}$$

where a is an adjustable scale parameter. The condition of detailed balance is violated if a parallelization of the stretch move algorithm is implemented. In such case each walker is simultaneously advanced on the state of the ensemble instead of evolving the walkers in series, and the full ensemble is divided into two subsets, $S(0) = X_k, \forall_k = 1, ..., K/2$ and $S(1) = X_k, \forall_k = K/2 + 1, ..., K$ to update all the walkers in $S(0)$ based only on the positions of the walkers in the set $S(1)$. After that, by using the new positions $S(0)$ the set $S(1)$ is updated. In this case, the outcome is a valid step for all the walkers.

One of the advantages of implementing the Markov chain Monte Carlo minimization is that, after finishing the algorithm, the probability distribution and the corresponding highest posterior density (HPD) interval of each free-parameter is calculated.

Likewise the genetic algorithm, the setting parameters of MCMC are also given in the control file of MAGIX, including: the number of samplers used for the error estimation, the accuracy of the error estimation in terms of σ, the number of iterations within the burn-in phase, the maximum number of iterations and the stopping value given by a χ^2-limit. The values of these parameters used in the minimization routine are indicated in Table 4.7. The number of samplers can be any integer number greater than 0. It is important to note that the greater the number of samplers (or walkers), iterations for the burn-in phase and iterations for the calculation, the better accuracy in the determination of the probability space of each parameter. However, this translates to significantly higher computational costs. Therefore, the values here used were set to quantities that permit relatively fast calculations (one week of computational time per calculation), and at the same time show negligible invariance in the obtained results.

As a result of the optimization with MCMC, MAGIX provides two results: the 2σ-probability distribution for each parameter and the χ^2-minima which in an ideal case is located in the mode of the distribution of the first quantity. Nevertheless, the parameter-site results of these two outputs may slightly vary within the 2σ-estimation because of the differences between the probability function and the χ^2-function. These results can be observed from the later corner plots determined for each model in Figs. 4.18, 4.22 and 4.25.

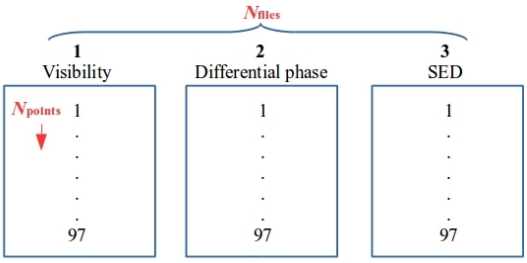

Figure 4.16: Scheme of a dataset per observing run. The SED file is general for all the runs, and the MIDI data (visibilities and phases) expands over five epochs, resulting in a total of $N_{\text{files}} = 11$.

Configuration of datasets

The minimized value supplied by the optimization with MAGIX is expressed according to the expression

$$\chi^2_{\text{total}} = \sum_{i=1}^{N_{\text{points}}} \left[\frac{(y_i^{\text{obs}} - y_i^{\text{fit}})^2}{(\sigma_i^{\text{error}})^2} \right] \tag{4.29}$$

where y_i^{obs} and y_i^{fit} are the experimental and modelled values respectively, and σ_i^{error} represents the error of the *i*-th data point. N_{points} is the number of data points considered, each of which is an independent variable. Ideally, given the random fluctuations of the values y_i^{obs} about their mean values y_i^{fit}, each term of the sum is 1. Hence, the expected calculated value of χ^2_{total} will be equal to N_{points}. In such case one conclude that the data are well described by the model, that is, the hypothesized function.

Nevertheless, since the expected distribution of the sample variables is not a set of independent variables, but rather they are connected by some relations (the number of free-parameters of the model N_{free}), the number of degrees of freedom of the distribution is defined according to the expression

$$\nu = N_{\text{points}} - N_{\text{free}} \tag{4.30}$$

For convenience, however, the goodness of the fit to the experimental data is expressed in terms of the total χ^2_{total}-value normalized per degree of freedom. Therefore, the magnitude offered by MAGIX is divided according to the following expression

$$\frac{\chi^2}{\nu} = \frac{\chi^2_{\text{total}}}{N_{\text{points}} - N_{\text{free}}}. \tag{4.31}$$

Hereafter, this ratio which expresses a reduced χ^2-value is used and referred as simply χ^2.

The dataset per observing run is composed of three files: visibility, differential phase and SED measurements. Each file contains 97 spectral channels (Fig. 4.16). Hence, the sampled number of hypothesized quantities (N_{points}) is taken from the expression

$$N_{\text{points}} = N_{\text{files}} \times 97 \tag{4.32}$$

where N_{files} is the number of files containing visibility, phase and/or SED measurements. The different combination of them out of the 11 available (5 MIDI visibilities, 5 MIDI differential phases and 1 file with photometric measurements), as seen in later tests, allows to inspect variability of V892 Tau over the 9-year observations.

4.3.6 First model: Temperature-gradient model of a binary system with a geometrically flat circumbinary disk

Model 1), based on the description by Monnier et al. [2008], is composed of a stellar pair surrounded by a circumbinary disk (Fig. 4.8). The total flux of this system can be written as the sum of the independent flux of its components – the stars and the circumbinary disk – , where the flux ratio between the stars is $F_{\rm s1}/F_{\rm s2} = 1$. Therefore

$$F_{\rm 1m}(\lambda) = F_{\rm s1}(\lambda) + F_{\rm s2}(\lambda) + F_{{\rm cb},i}(\lambda) = F_{\rm bin}(\lambda) + F_{{\rm cb},i}(\lambda). \tag{4.33}$$

And its normalized complex visibility is defined according to Eq. 3.24 as

$$V_{{\rm 1m},\lambda}(u,v) = \frac{F_{\rm bin}(\lambda)V_{{\rm bin},\lambda}(u,v) + F_{{\rm cb},i}(\lambda)V_{{\rm cb},\lambda}(u,v)}{F_{\rm 1m}(\lambda)}. \tag{4.34}$$

The fixed parameters are the ones of subsection 4.3.3, and the four free-parameters to determine in this model are:

• *Temperature at the inner rim of the circumbinary disk* $T_{\rm in_{cb}}$: This parameter is scanned based on the initial reference that the inner edge of the circumbinary disk is at a distance of $r = 17.5$ AU from the barycenter between the stars. Out of the total stellar luminosity of $L_\star = 120\,{\rm L}_\odot$ (the total power produced by the two equal stars) assumed to be centralized in the barycentre of the system, only a fraction of it strikes the grains, namely

$$Q_{\rm star/dust} = L_\star \left(\frac{\pi R_{\rm dust}^2}{4\pi r^2}\right) \tag{4.35}$$

where $R_{\rm dust}$ is the radius of the spherical grain, and r is the mentioned distance. The dusty grains, however, reflect a fraction α of this energy, known as albedo. In other words, the grains absorb a fraction $1-\alpha$ of the stars' light. Therefore, the power absorbed by a grain can be expressed as

$$Q_+ = (1-\alpha)Q_{\rm star/dust}. \tag{4.36}$$

Here, I consider an albedo of 0, corresponding to a blackbody that absorbs all incident radiation. Although the grain absorbs as only a circular area, it reemits in the infrared range equally in all directions as a sphere. Therefore, its emitted energy per second can be also written according to the Stefan-Boltzmann law as

$$Q_- = 4\pi R_{\rm dust}^2 \sigma T_{\rm dust}^4 \tag{4.37}$$

Then, the temperature at the inner rim of the circumbinary disk $T_{\rm in_{cb}} = T_{\rm dust}$ can be calculated from the "ideal" condition that the emissivity of dust grains is equal to their absorptivity, following

$$\begin{aligned} Q_+ &= \epsilon\, Q_- \\ L_\star \left(\frac{\pi R_{\rm dust}^2}{4\pi r^2}\right) &= \epsilon \left(4\pi R_{\rm dust}^2 \sigma T_{\rm in_{cb}}^4\right) \\ T_{\rm in_{cb}}^4 &= \frac{L_\star}{16\pi r^2 \sigma \epsilon} \\ T_{\rm in_{cb}} &= \frac{1}{2}\left(\frac{L_\star}{\pi r^2 \sigma \epsilon}\right)^{1/4}. \end{aligned} \tag{4.38}$$

Since the actual temperature of the dust grains will depend on their properties, the factor ϵ

which varies between 0 and 1 has been introduced to define the emissivity efficiency – or cooling efficiency – in the infrared range. Replacing the known values into the last equation, this leads to

$$T_{\mathrm{in_{cb}}} = \left(\frac{1}{\epsilon}\right)^{1/4} 220 \text{ K}.$$

This last expression allows to scan temperatures of the dust between 220 and 391 K, respectively corresponding to grains with $\epsilon = 1$ and $\epsilon = 0.1$, in which case heating is more efficient than cooling and the grains can be heated to higher temperatures than that of a blackbody [Dullemond and Monnier, 2010, Matter et al., 2014].

• *Surface density at the inner rim of the circumbinary disk* $\Sigma_{\mathrm{in_{cb}}}$: The investigated interval of this parameter for values less than 0.2 kg m^{-2} is based on the reports in the literature, with densities commonly reported in the order of 10^{-3} kg m^{-2} [e.g. Matter et al., 2014].

• *Temperature power-law exponent* q_{cb}: This parameter is varied between 0.45 and 0.7, respectively associated to flared irradiated disks and standard viscous or flat irradiated disks.

• *Radius of the circumbinary disk from the barycenter of the system to its inner rim* $R_{\mathrm{in_{cb}}}$: Although the determination of the interval in which the temperature is studied makes a first assumption on the work by Monnier et al. [2008], some flexibility for nearby values between 16 and 19 AU is enabled to this parameter in the reduction.

At this point, I remark that the available data taken on different epochs, and consisting of interferometric visibilities, differential phases and flux measurements, gives the possibility to group the datasets in such a way that signs of variability in the properties of V892 Tau along the 9-year baseline can be determined through the fitting process with MAGIX. Therefore, I perform the following χ^2-reduction tests for this model 1):

(i) **SED fit of a symmetric system, and posterior comparison to MIDI data**

The symmetry of V892 Tau in this scenario is given by the fixed respective position of the equal stellar companions and the circumbinary disk around a common center. Here, initially only the best fit to the SED points is searched ($N_{\mathrm{files}} = 1$ in Eq. 4.31), and then the resulting synthetic mid-IR visibilities and phases out of this fit are contrasted with the MIDI ones. This conservative approach therefore does not consider any variability in the structure of Elias 1 along the 9-year timescale and baseline configurations, but instead provides a first inspection to the goodness of a "simplistic" model.

The best fit to the SED measurements is plotted as "SED fit" in the left panels of Fig. 4.17[9], where also the associated χ^2-value is indicated. The total system flux is traced with lines thicker than the circumbinary contribution which peaks at the N-band. The medium and right panels contrast the corresponding synthetic mid-IR visibilities and differential phases, these last ones showing a zero deviation.

(ii) **Combined fit to all datasets considering an asymmetric system**

This MAGIX test associates all available datasets (5 MIDI datasets + SED, which result in a total of $N_{\mathrm{files}} = 11$) in order to determine the best common solution for a system consisting of a circumbinary disk and a stellar pair whose barycentre does not coincide with the center of the disk. The slightly shifted stellar pair creates an asymmetric system.

In addition to the 4 free-parameters defined previously, two additional parameters which define the barycentre coordinates, $(\alpha_{\mathrm{bin}}, \beta_{\mathrm{bin}})$, are also explored in a range of

[9]The figures are organized horizontally per observing run, whereas vertically, from left to right, the SED measurements, the visibility curve, and the differential phases are respectively mapped.

$\pm$35 mas, roughly the estimated binary separation. Therefore, the analysis over this interval enables to locate one of the stars in the center of the system. The results of this global fit of the SED are plotted as "combined fit" in Fig. 4.17. It can be observed that since the test evaluates a common solution, the SED of the left panel remains invariable along the 5 runs. Nevertheless, the different outcomes for the visibilities and phases due to their distinct baseline configuration can be appreciated in the contiguous boxes.

(iii) **Fit per epoch considering an asymmetric system**

The different baseline configurations, the presumed asymmetry of the system and its complexity, suggest an analysis that encompasses temporal variability along the period of observations. The investigation of such phenomenon is addressed through the analysis of independent epochs of MIDI observations. Excepting the first and second observing runs that can be accounted as one single epoch due to their proximity in time – and therefore this epoch consists of 5 files – , the rest of epochs are formed by $N_{\rm files} = 3$ corresponding to visibility, phase and SED measurements. This test maintains the 6 free-parameters used in point (ii), and the results for each date are shown in Fig. 4.17 with their respective epoch label.

As seen from Fig. 4.17, in this first model the inclusion of only the stellar pair and circumbinary disk induces a significant lack of IR excess between 2 and 8 μm in contrast with what is photometrically measured ($\sim$55% at 2 μm, and up to 85% at 5 μm). This is also numerically represented by the largely deviated χ^2-values. Moreover, the most simplistic fitting approach with a centred circumbinary emission results in a zero-differential phase that is incompatible with the MIDI observations. The MAGIX minimization with both "combined" and "fit per epoch" datasets fails to simultaneously reproduce the SED and MIDI data, turning to be satisfactory either for only the visibility and phase (e.g. 28-12-2004), or only to the larger wavelengths of the SED (e.g. 20-12-2013).

It can be noticed that the optimization with "combined" or "fit per epoch", in spite of its strong inaccuracy, converge with the least χ^2-value for most of the observing runs. For this reason, in Fig. 4.18 I expose the corner plots produced by the MCMC minimization with MAGIX for the combined dataset and for the four independent epochs. The corner plots show the one- and two-dimensional projections of the posterior 2σ-probability distribution of all the parameters. The histograms on the diagonal also denote this interval, whose peak value – mode – and $\pm$ error range is written on top. For the cases where the parameter itself contains decimal values (e.g. the parameter $q_{\rm cb}$ on 04-09-2009), the uncertainty range denoted on top may look like "0.00", meaning that the mode lies on the border of the parameter space or that its calculated value may be of a smaller fractional scale. The position in the histograms of the best χ^2-fit parameter is traced with a blue line.

In Fig. 4.19 I summarize the best-fit parameters obtained for the three minimization tests. From these panels it can be derived that the temperature at the inner edge of the circumbinary disk is around 300 K, with a standard deviation of 10% throughout the independent analysis. The parameter $q_{\rm cb}$ presents larger variations over the parameter space, and, consequently, also $\Sigma_{\rm in_{cb}}$ largely fluctuates over the observed epochs. The inner edge of the circumbinary disk shows a rather stable value of $\sim$17.5 AU that is well in agreement with its previous estimations [Monnier et al., 2008, Menu et al., 2015]. The panel with coordinates $(\alpha_{\rm bin}, \beta_{\rm bin})$ of Fig. 4.19, which depicts the variable position of the pair barycentre, also exposes the weakness of this model by showing very large variations in the best-fit location of the barycentre, even for observations close in epoch.

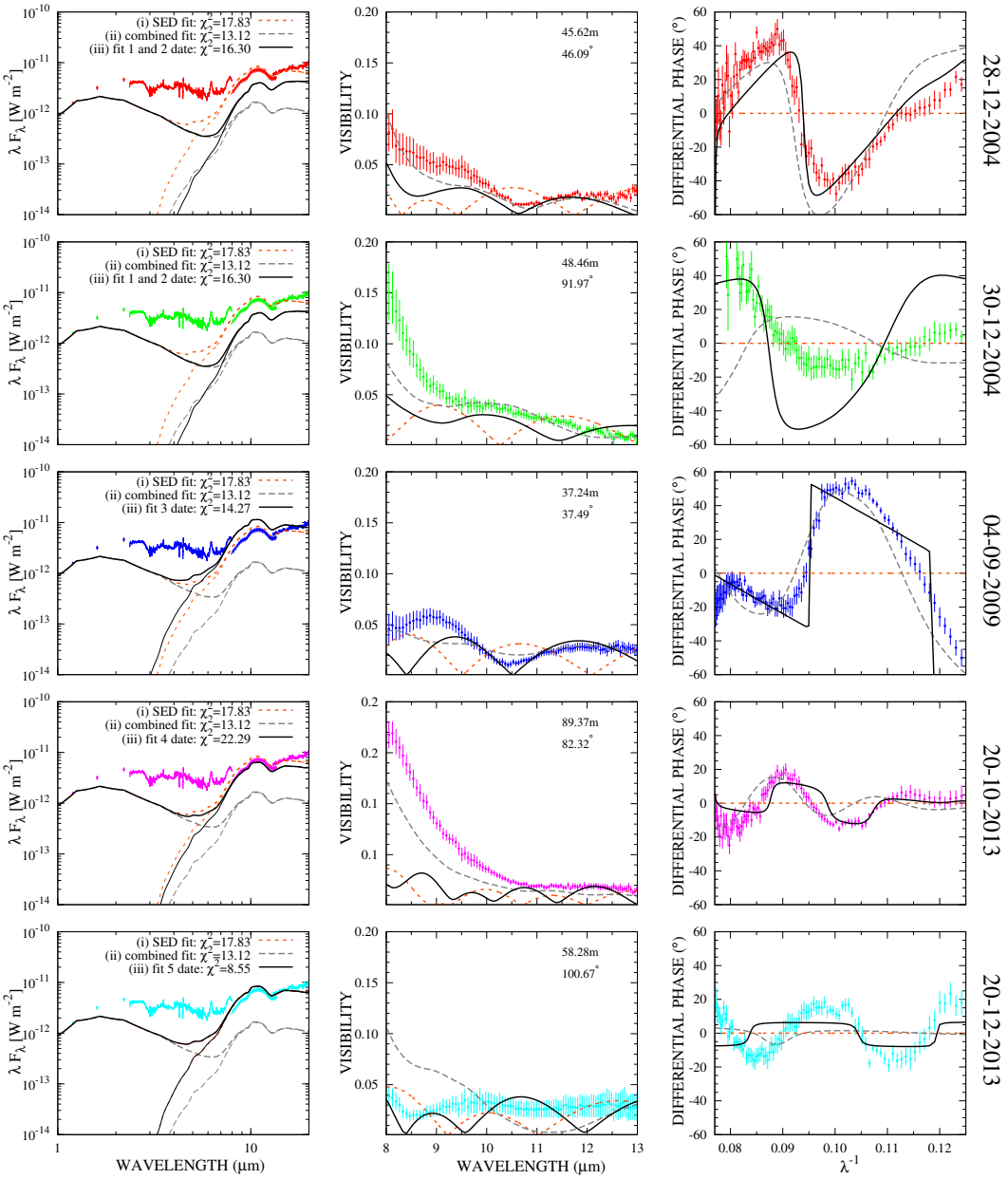

Figure 4.17: Best χ^2-minimization fits for the first model consisting only of stellar pair and circumbinary disk. The three investigated possibilities per date are traced on the SEDs (left panels), MIDI visibilities (middle panels) and MIDI differential phases (right panels). This first model demonstrates that the flux contribution of the circumbinary disk is capable of reproducing well the SED in the N-band (e.g. observations in 2013), however, the observed strong lack of near-IR emission suggests the necessary inclusion of an additional source in the system to compensate the slope at shorter wavelengths.

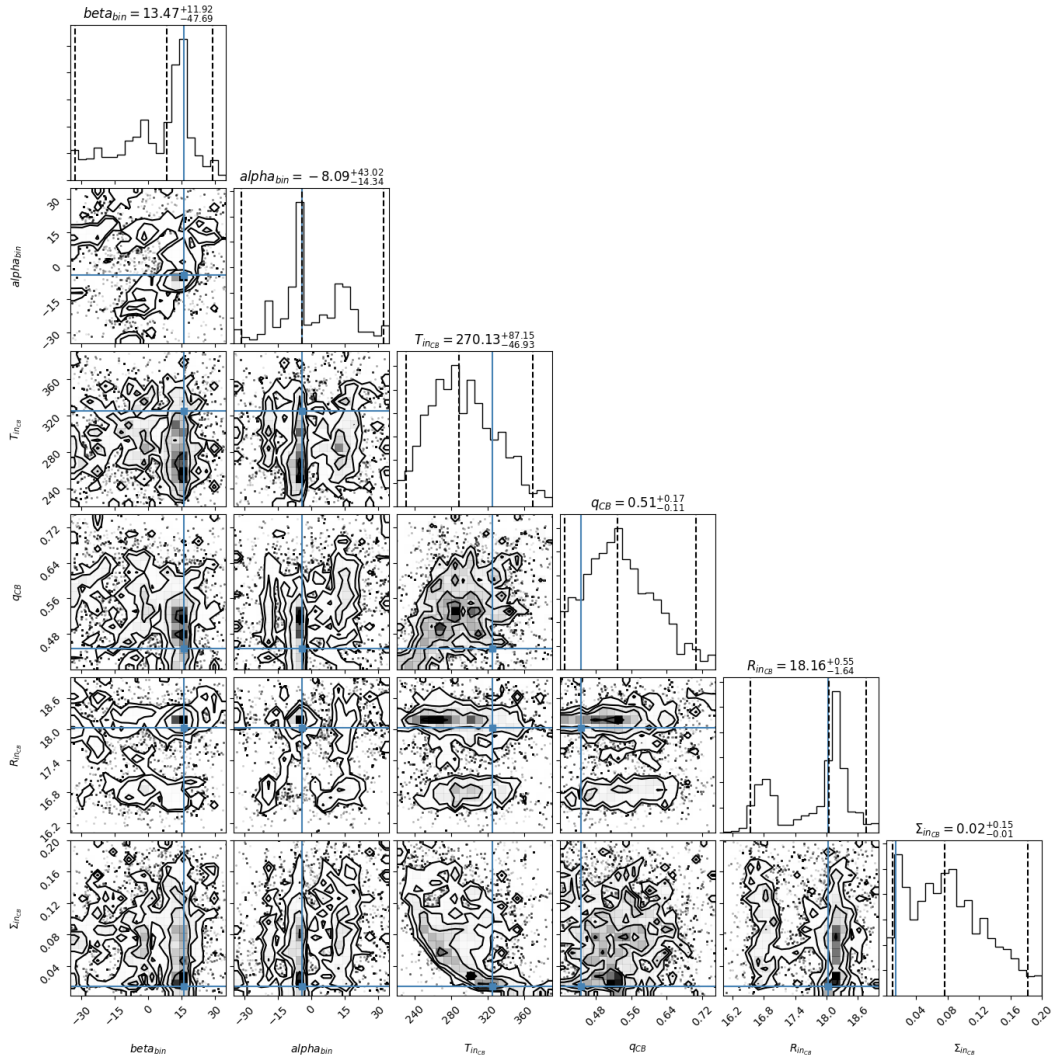

Figure 4.18: MCMC corner plot of the test with all combined datasets using model 1. The plot reunites the one- and two-dimensional projections of the posterior 2σ-probability distributions of the 4 free-parameters, as well as the site of the best χ^2-value traced with blue lines. Ideally, for a case with a normal Gaussian probability distribution, the darkest site and mode corresponding to the peak of the probability function and the site of the χ^2 blue line are expected to coincide. However, the 2σ-contours demonstrate that the parameter space and model are rather complex, and the probability function may differ from the χ^2-function. The best χ^2-values nevertheless lie within the one-dimensional projection of the 2σ-space delimited with dashed lines. Three dashed vertical lines should be seen in every one-dimensional histogram, unless the dashed line of the peak matches the anterior or posterior limit of the 2σ-distribution, or in turn these two confining dashed lines coincide with the edge of the scanned parameter space. The central dashed lines indicates the 50-percentile of the distribution, whereas the anterior and posterior lines delimit the 2σ-range. Therefore, the top values indicate the position of the mode of the probability distribution and the $\pm$ errors as the distance between the mode and the limiting dashed lines.

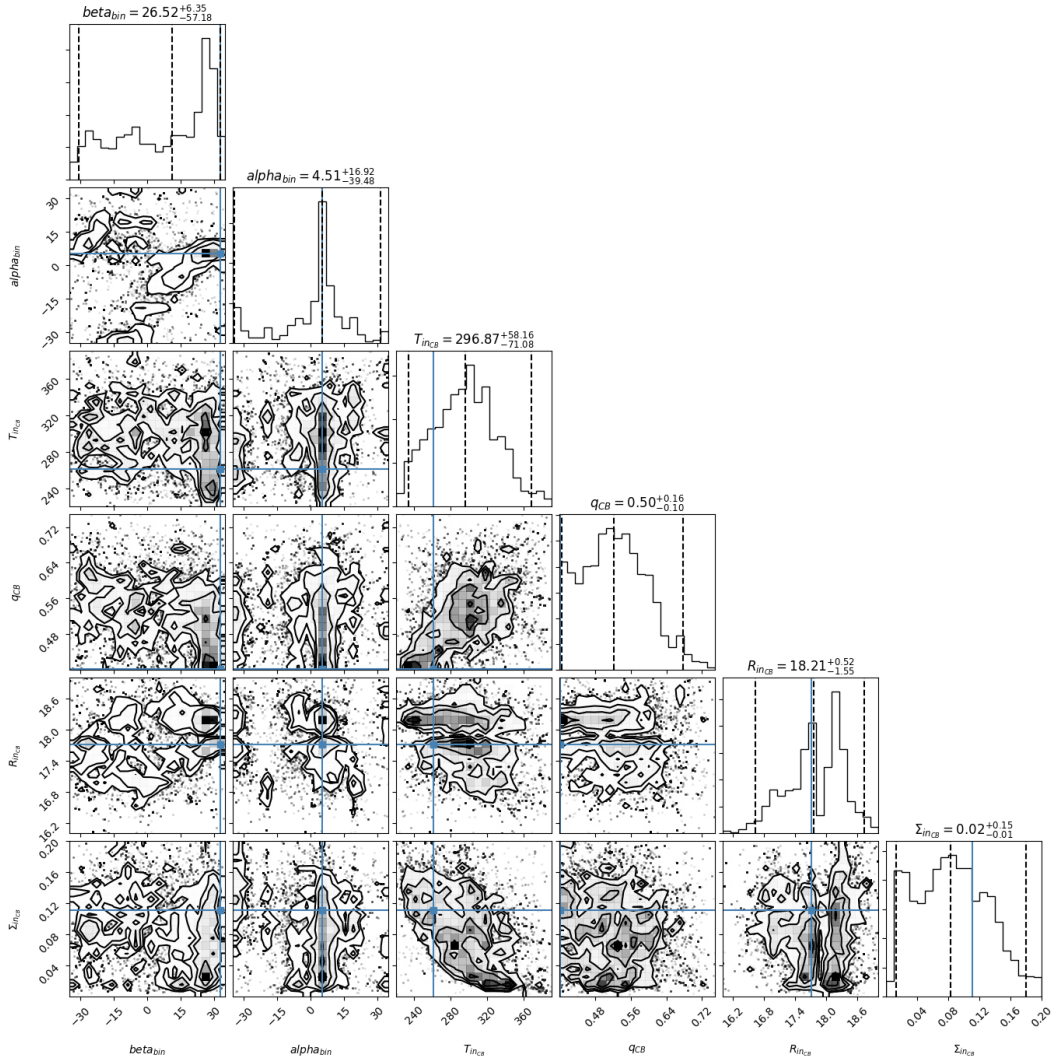

Figure 4.18: Model 1: resulting MCMC corner plot using the dataset of the first epoch alone – 28-12-2004 and 30-12-2004 –. The description of this plot is analogous to the one of the previous figure.

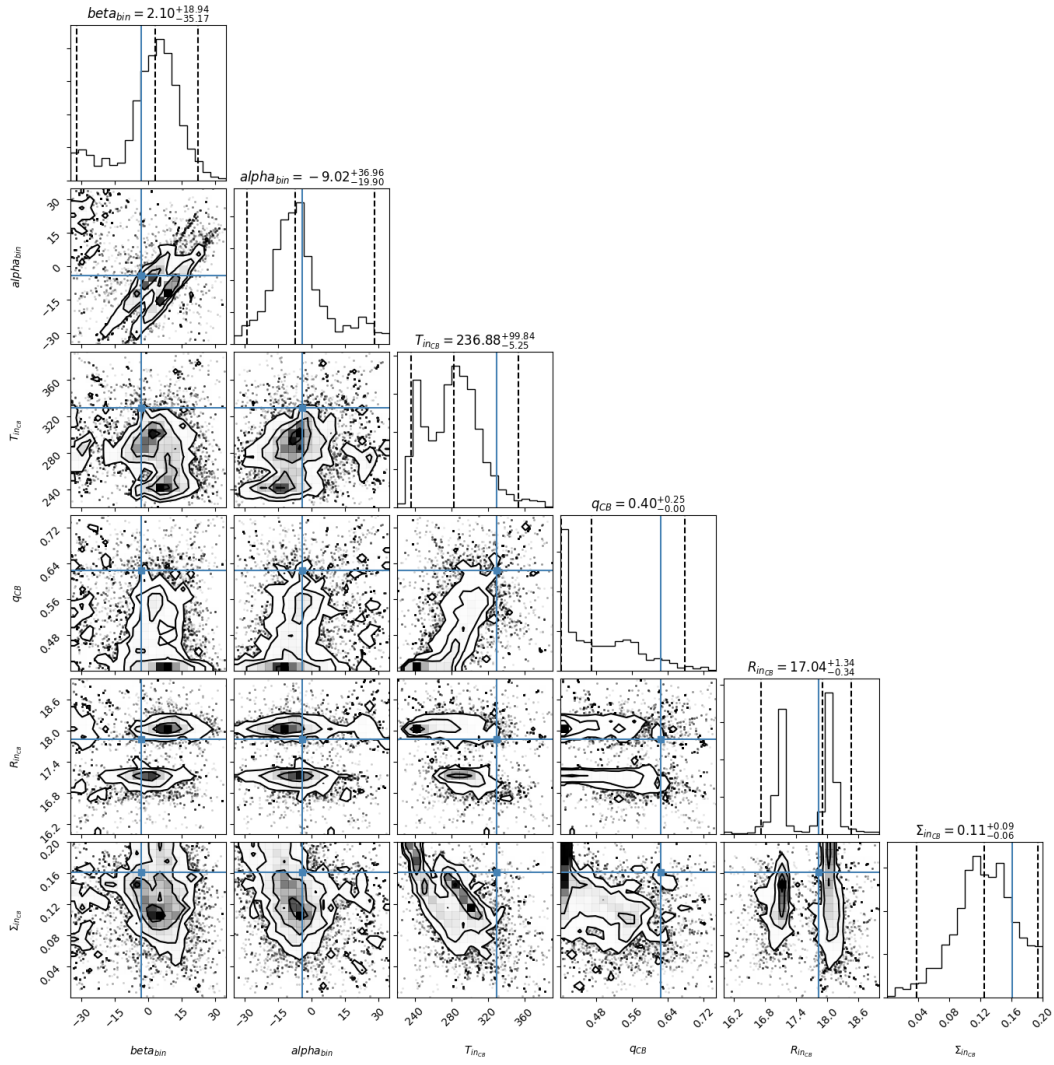

Figure 4.18: Model 1: resulting MCMC corner plot using the dataset of the second epoch alone – 04-09-2009 –.

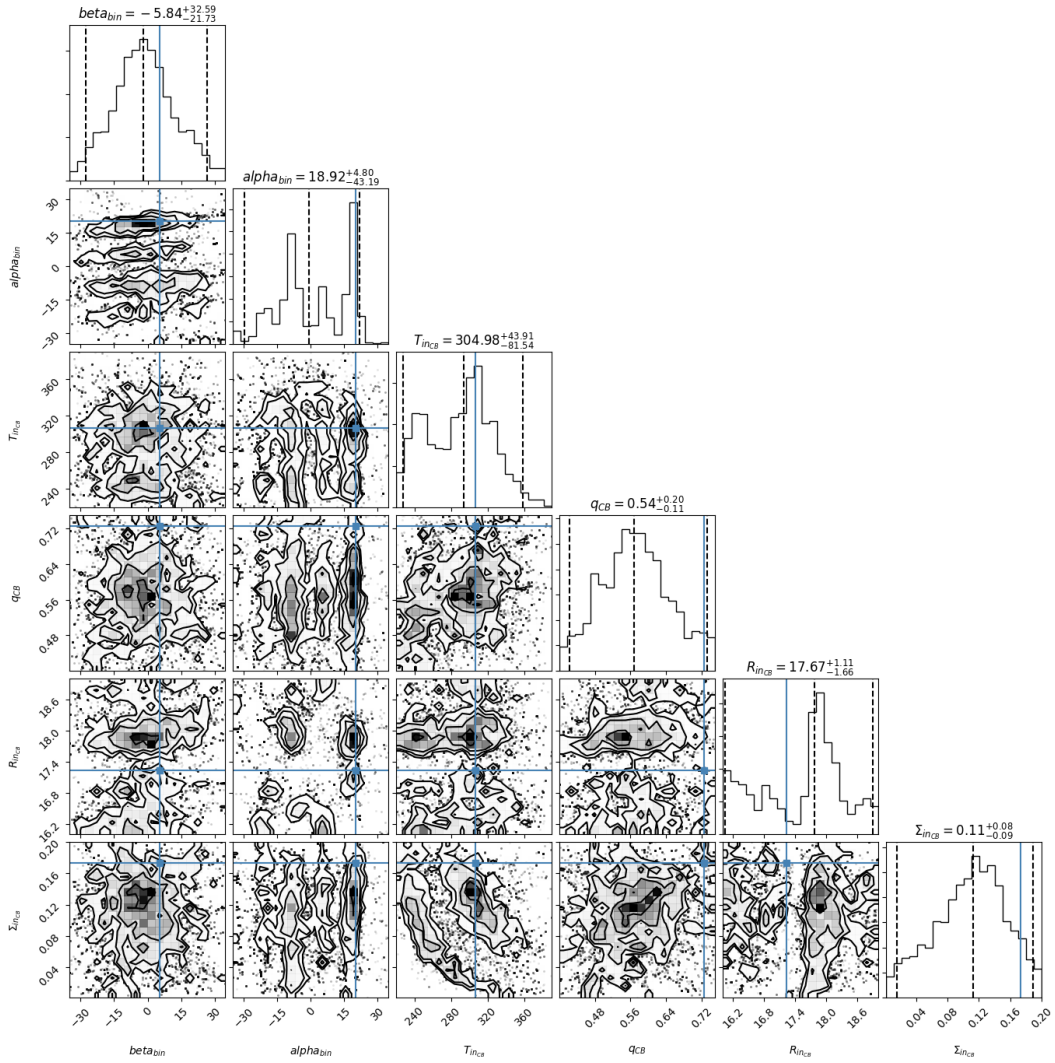

Figure 4.18: Model 1: resulting MCMC corner plot using the dataset of the third epoch alone – 20-10-2013 –.

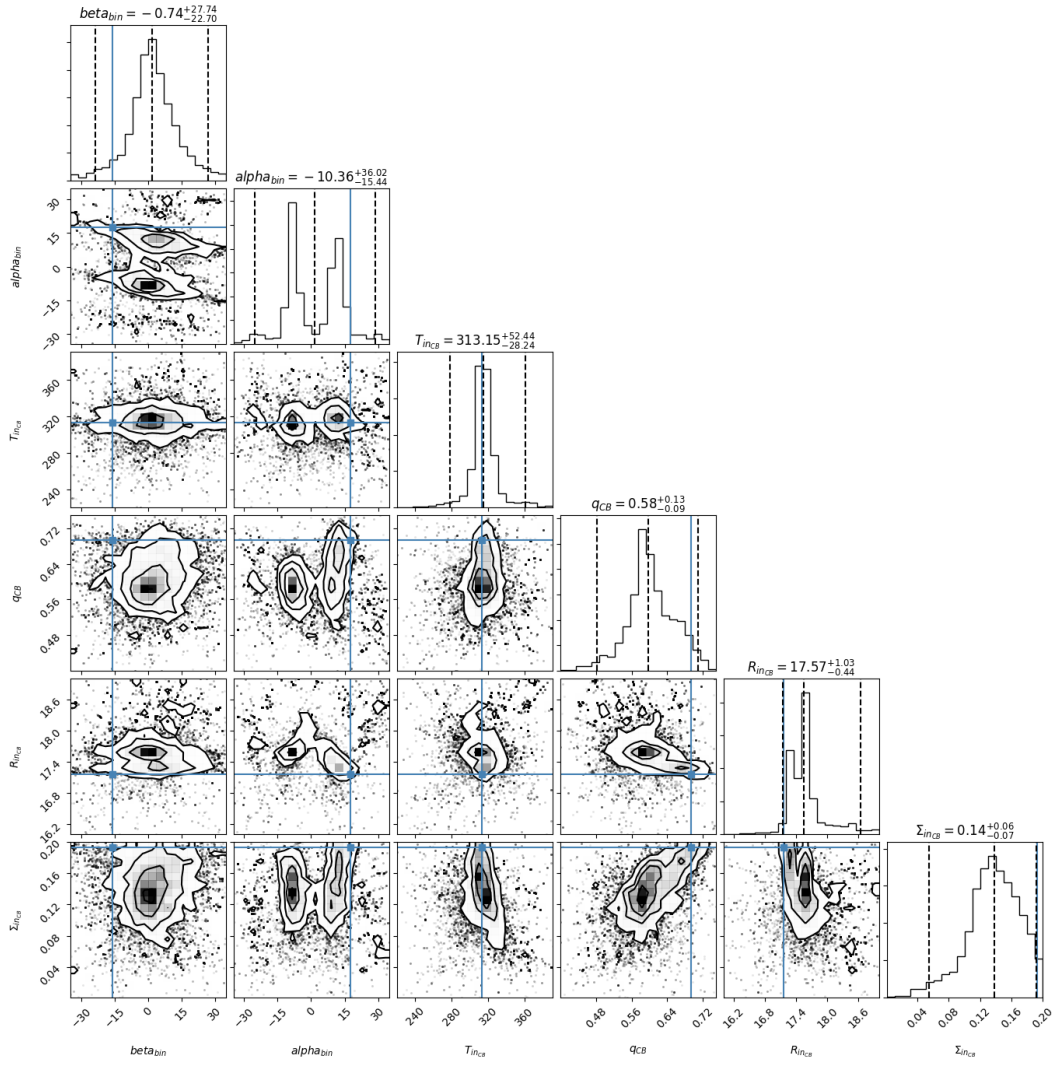

Figure 4.18: Model 1: resulting MCMC corner plot using the dataset of the fourth epoch alone – 20-12-2013 –.

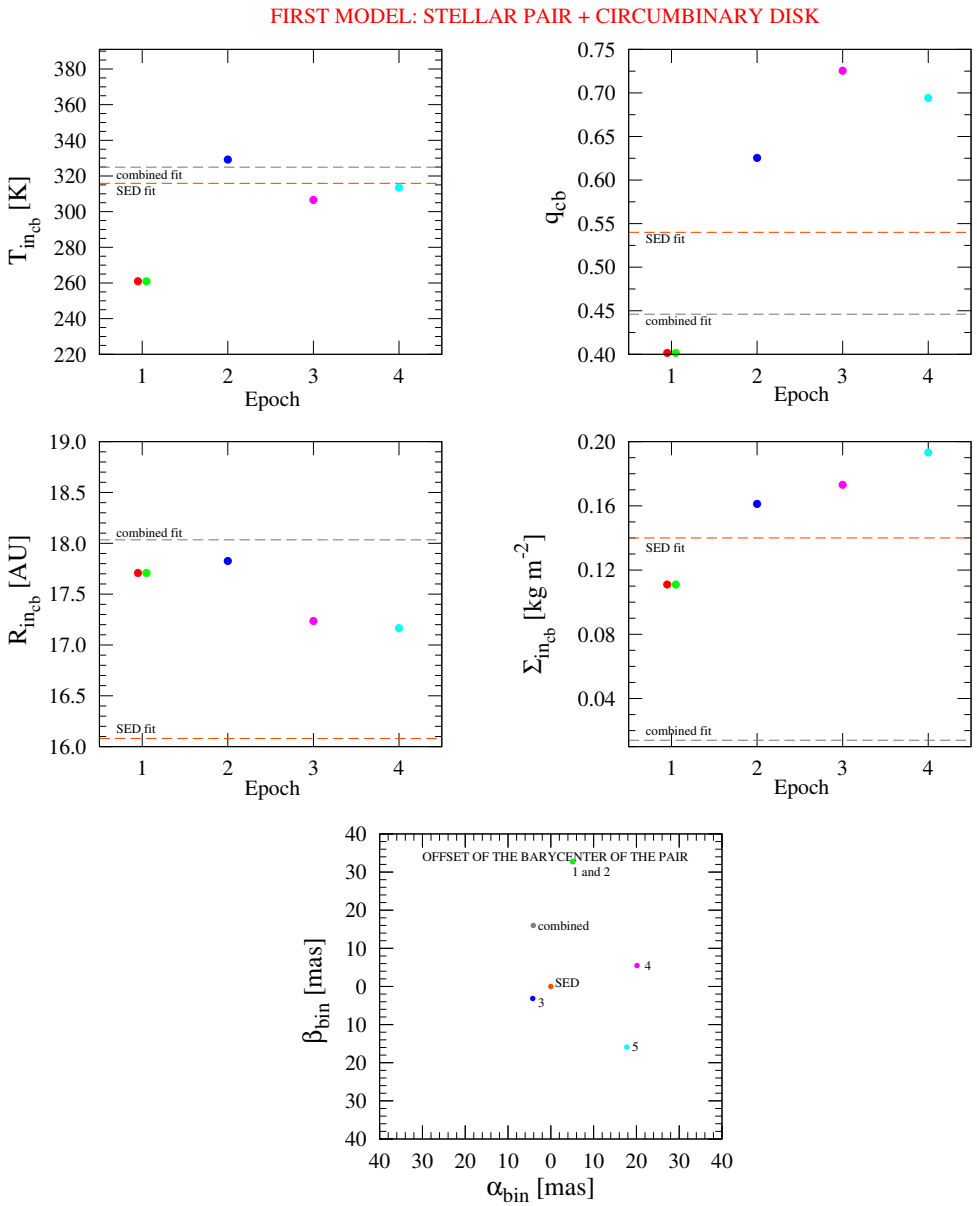

Figure 4.19: Visualization of the obtained parameters for the three tests (SED fit alone, combined fit and independent fit) which produce the best χ^2 fit seen in Fig. 4.17. These values are the same as the ones traced with blue lines in their respective corner plots. The panel with the coordinates of the shifted barycentre $(\alpha_{\rm bin}, \beta_{\rm bin})$ shows the central position of the pair explored for an asymmetric system. In this case, the numerical labels correspond to the datasets of each epoch, for instance, "1 and 2" corresponds to the central position of the stars at the first epoch of observations.

4.3.7 Second model: Temperature-gradient model of a binary system with a geometrically flat circumbinary disk and a circumstellar disk around one stellar component

In model 2), the addition of a uniform circumstellar component bounded to one of the equal-brightness stars is suggested as a solution to account for the near-IR excess in the SED and the non-zero mid-IR differential phases (Fig. 4.9). The total flux of this second model is therefore defined as

$$F_{2\mathrm{m}}(\lambda) = F_{\mathrm{bin}}(\lambda) + F_{\mathrm{cb},i}(\lambda) + F_{\mathrm{cs},i}(\lambda) \tag{4.39}$$

and its normalized complex visibility according to Eq. 3.24 as

$$V_{2\mathrm{m},\lambda}(u,v) = \frac{F_{\mathrm{bin}}(\lambda)V_{\mathrm{bin},\lambda}(u,v) + F_{\mathrm{cb},i}(\lambda)V_{\mathrm{cb},\lambda}(u,v) + F_{\mathrm{cs},i}(\lambda)V_{\mathrm{cs},\lambda}(u,v)}{F_{2\mathrm{m}}(\lambda)}. \tag{4.40}$$

Following Isella and Natta [2005], I assume that the dust component of the disk is truncated by dust evaporation, creating an inner cavity of radius $R_{\mathrm{in_{cs}}}$, or also known as dust sublimation radius R_{sub}. Inside this hole, only optically thin gas exists, being possible to neglect its absorbing effect. The relation between this radius, its temperature and its efficiency factor can be expressed as a function of the angle α between the incident stellar radiation and the disk surface [Muzerolle et al., 2004], as follows

$$T^4_{\mathrm{in_{cs}}} = T^4_{\mathrm{sub}} = \left(2\mu + \frac{1}{\epsilon_{\mathrm{cs}}}\right)\left(\frac{R_\star}{2R_{\mathrm{in_{cs}}}}\right)^2 T^4_\star \tag{4.41}$$

where $\mu = \sin\alpha$ and ϵ_{cs} is the dust emissivity factor. Two bounding cases can be considered out of this equation. First, for the flaring part of the disk where $\mu \ll 1$, the expression adopts a form similar to the case considered for the flared circumbinary disk of Eq. 4.38, namely

$$T^4_{\mathrm{in_{cs}}} = T^4_{\mathrm{sub}} = \frac{1}{\epsilon_{\mathrm{cs}}}\left(\frac{R_\star}{2R_{\mathrm{in_{cs}}}}\right)^2 T^4_\star \tag{4.42}$$

Second, in the case of the circumstellar disk whose inner rim is perpendicularly exposed to the stellar radiation ($\mu \approx 1$), Eq. 4.41 takes the form

$$T^4_{\mathrm{in_{cs}}} = T^4_{\mathrm{sub}} = \left(2 + \frac{1}{\epsilon_{\mathrm{cs}}}\right)\left(\frac{R_\star}{2R_{\mathrm{in_{cs}}}}\right)^2 T^4_\star \tag{4.43}$$

As exposed in previous sections of my work, the temperature T_{sub} at which silicate dust grains evaporate is $\sim$1500 K. However, values differing by some hundred degrees can be found depending on the cooling efficiency of the grains or on the gas density [e.g. Isella and Natta, 2005, Tannirkulam et al., 2007, Kama et al., 2009]. On this basis, I investigate a circumstellar disk with a uniform temperature – radially independent – between 1500–2155 K. The relation between this temperature range and the consequent parametric range of the rest of variables is graphically represented in Fig. 4.20. Subsequently, in addition to the four free-parameters introduced in point (i) of the previous model, this model inserts three free-parameters that describe the geometry and brightness of the uniform circumstellar disk:

• *Inner radius of the circumstellar disk* $R_{\mathrm{in_{cs}}}$: The smallest value that the inner radius adopts is given by the limiting case of blackbody-like dust ($\epsilon_{\mathrm{cs}} = 1$) exposed to stellar radiation at a close-to-zero angle (Eq. 4.42). This limiting value corresponds to 0.26 AU (black dashed line in Fig. 4.20). The greatest value that this parameter can take is as large as 2 AU from the star, close to the limits determined by the binary truncation effects. The explored range of

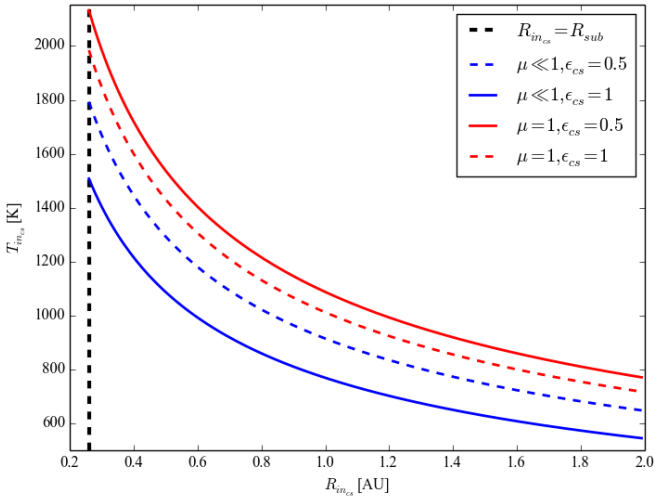

Figure 4.20: Relation between the magnitudes $T_{\mathrm{in_{cs}}}$, $R_{\mathrm{in_{cs}}}$ and ϵ_{cs} of Eq. 4.41 that describe the geometry and luminosity of the proposed circumstellar disk. The parameter space analysed with the optimization routine is confined by the red and blue solid lines.

0.26–2 AU includes also the value of 0.455 AU at which perpendicularly exposed blackbody grains would evaporate according to Eq. 4.43.

• *Extension of the uniform disk between its inner and outer rims* ΔR_{cs}: The minimum width of the disk is given by a nominal value of 0.001 AU. On the contrary, at the outer edge, the maximum extension of the disk is limited by the binary truncation effects that can reach about a third of the separation between the stellar pair [Artymowicz and Lubow, 1994], meaning 2 AU.

• *Achromatic emissivity factor* ϵ_{cs}: Since the lack of near-IR data prevents a deeper analysis on the properties of the dust composing the circumstellar disk, instead of applying a dust opacity law as for the circumbinary structure shown in red in Fig. 4.11, only an achromatic dependence is assumed (blue trace in Fig. 4.11). The range of this parameter is dictated by the equations above to comply with the thermal conditions. Therefore, as seen from Fig. 4.20, the thermal scope starting at the inner radius between the blue and red solid lines corresponds to a range $0.5 \leq \epsilon_{\mathrm{cs}} \leq 1$.

Likewise the tests performed in subsection 4.3.6, I perform the following χ^2-minimization tests with MAGIX:

(i) **Combined fit to all datasets with a circumstellar disk bounded to one star**
In this attempt, I implement the optimizer MAGIX with all MIDI observational files and the 97 SED points ($N_{\mathrm{files}} = 11$ in Eq. 4.31) to find the best-fit combination of values for the 7 free-parameters. As a consequence, the properties of the face-on ($i = 0°$) circumstellar disk remain invariable over the 9 years of observations, excepting its bounded position to one of its host star on the sky plane.

The resulting traces and its χ^2-value are labelled as "combined fit" in the SED (left panels), visibilities (middle panels) and differential phases (right panels) of Fig. 4.21. The values of the 7 free-parameters can be also observed in the panels of Fig. 4.23.

(ii) **Fit per epoch with a circumstellar disk bounded to one star**
As in point (iii) of subsection 4.3.6, here the SED + each MIDI dataset is fitted

independently per epoch, therefore each run consists of $N_{\rm files} = 3$ (excepting the first epoch with grouped dates in December 2004). This test was performed for a circumstellar disk oriented face-on to the observer ($i = 0°$). The corresponding best-fit curves to the experimental data are shown in Fig. 4.21.

The inclusion of an additional component surrounding one stellar component, as demonstrated in Fig. 4.21, clearly improves the fit of the observed infrared flux of V892 Tau. The inadequacy of this model may lie in the rigid location of the uniform disk-like emission that prevents a good fit to the MIDI differential phases, also reflected in still largely deviated χ^2-values. Especially questionable is the result for a "combined fit" of datasets with a value of about 18. The minimization is nonetheless improved for the examination of fits "per epoch", in some cases (e.g. 20-10-2013 or 20-12-2013) showing values less than 5.

In Fig. 4.22 I show the MCMC corner plots produced with MAGIX for both tests executed for this case of a non-inclined circumstellar disk. The figures present the 2σ-probability distribution of all free-parameters and the least χ^2-value denoted with a blue line.

The values of the 7 parameters for each epoch are graphically summarized in Fig. 4.23. The best-fit values of the parameters defining the circumbinary disk show different trends over the independent tests: $T_{\rm in_{cb}}$ has an average of ~ 300 K with a standard deviation of 50 K, $q_{\rm cb}$ lies consistently on the lowest border of the parameter space at 0.4, $R_{\rm in_{cb}}$ averages a value of 17 AU and fluctuates over 1.3 AU, and $\Sigma_{\rm in_{cb}}$ largely varies all over the parametric space. On the other side, although the thickness $\Delta R_{\rm cs}$ of the circumstellar disk seems consistently small, its inner rim $R_{\rm in_{cs}}$ arises at different radii from the star. This means that also the temperature at such radii varies between 760–2150 K. The emissivity, in turn, reflects results that steadily lie on the border of the parametric space at 0.5. Although the last panel of Fig. 4.23 showing the coordinates $(\alpha_{\rm cs}, \beta_{\rm cs})$ does not correspond to a free-parameter, it illustrates the position of the star that hosts this uniform circumstellar disk in accordance with Fig. 4.13.

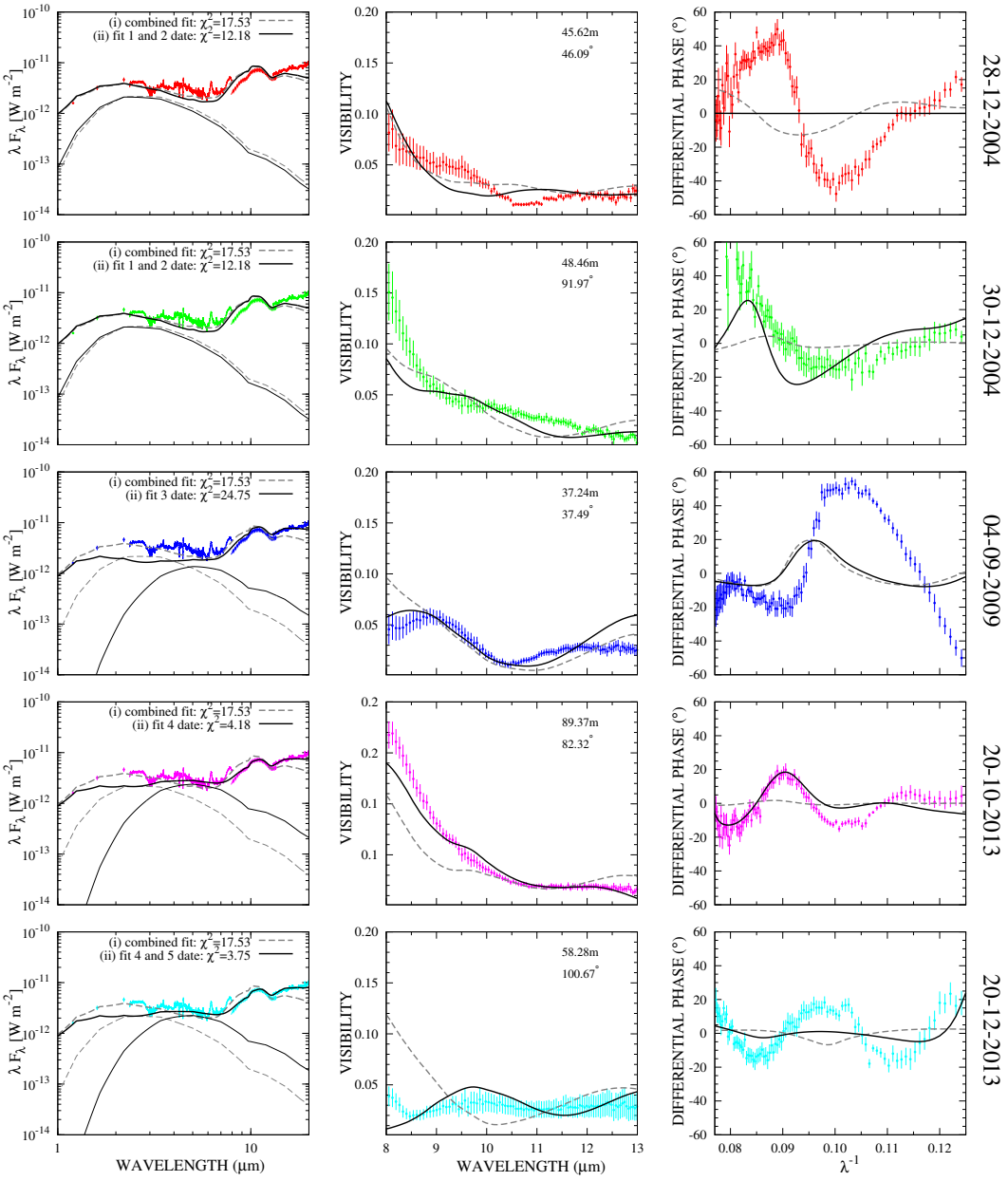

Figure 4.21: Likewise Fig. 4.17, this figure traces the best χ^2-fits for the model consisting of a stellar pair, circumbinary and circumstellar disk. The flux contribution of the circumstellar component better reproduces the near-IR emission observed in the SED. However, its position adhered to one of the stars obstructs a finer fit to the differential phases of the right panels. The dashed lines correspond to the test which combines all datasets, whereas the black solid lines characterize the results of the fits per epoch of observation.

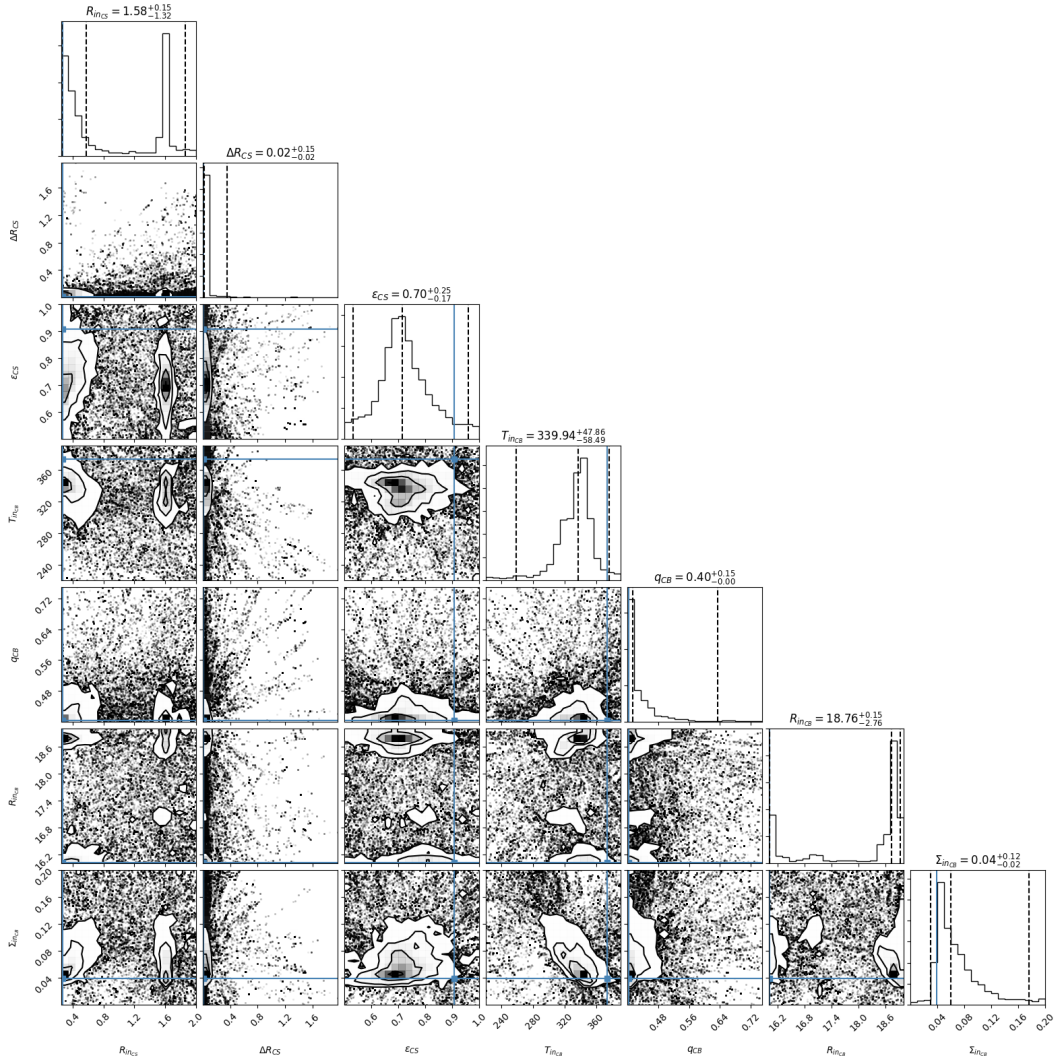

Figure 4.22: MCMC corner plot of the test with grouped datasets using model 2. The plot reunites the one- and two-dimensional projections of the posterior 2σ-probability distributions of the 7 free-parameters, as well as the best χ^2-value traced with blue lines. In analogy with the description of Fig. 4.18, the reader must be aware that the darkest site corresponding to the peak (mode) of the 2σ-probability and the site of the χ^2 blue line may not coincide due to the difference between the probability function and the χ^2-function. The best χ^2-values nevertheless lie within the three dashed vertical lines delineating the one-dimensional projection of the 2σ-space. Three dashed vertical lines should be seen in every one-dimensional histogram, unless the dashed line of the 50-percentile matches the anterior or posterior limit of the 2σ-distribution, or in turn these two confining dashed lines coincide with the edge of the parameter space.

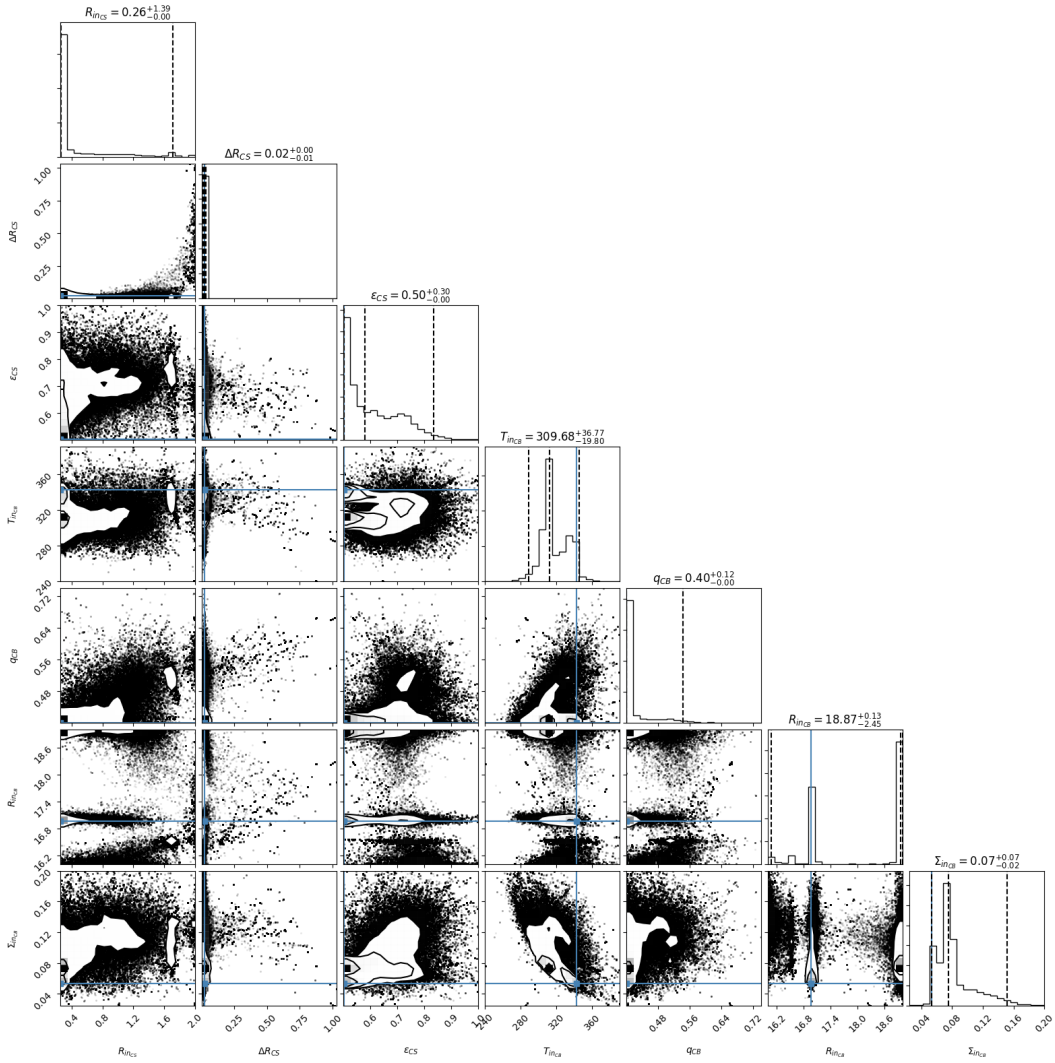

Figure 4.22: Model 2: resulting MCMC corner plot using the dataset of the first epoch alone – 28-12-2004 and 30-12-2004 –.

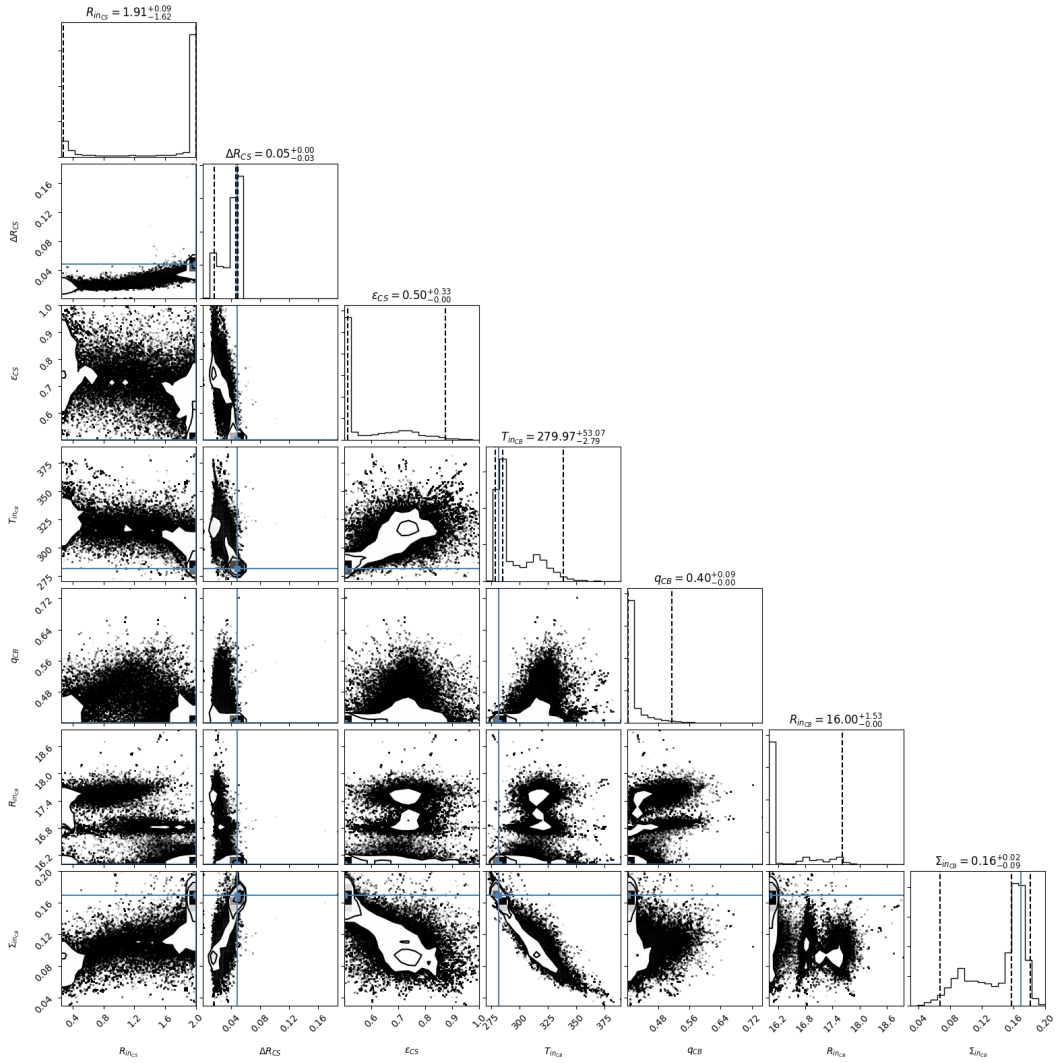

Figure 4.22: Model 2: resulting MCMC corner plot using the dataset of the second epoch alone – 04-09-2009 –.

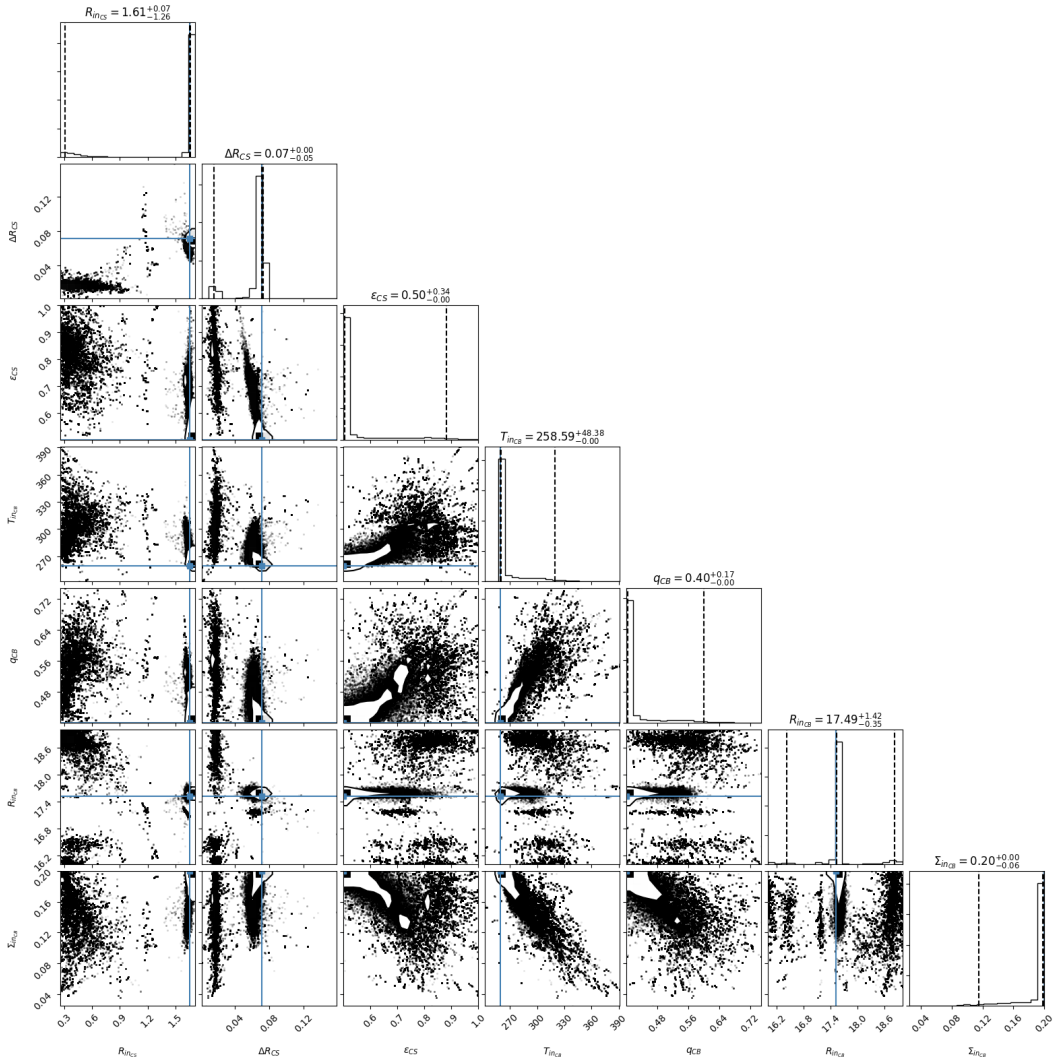

Figure 4.22: Model 2: resulting MCMC corner plot using the dataset of the third epoch alone – 20-10-2013 –.

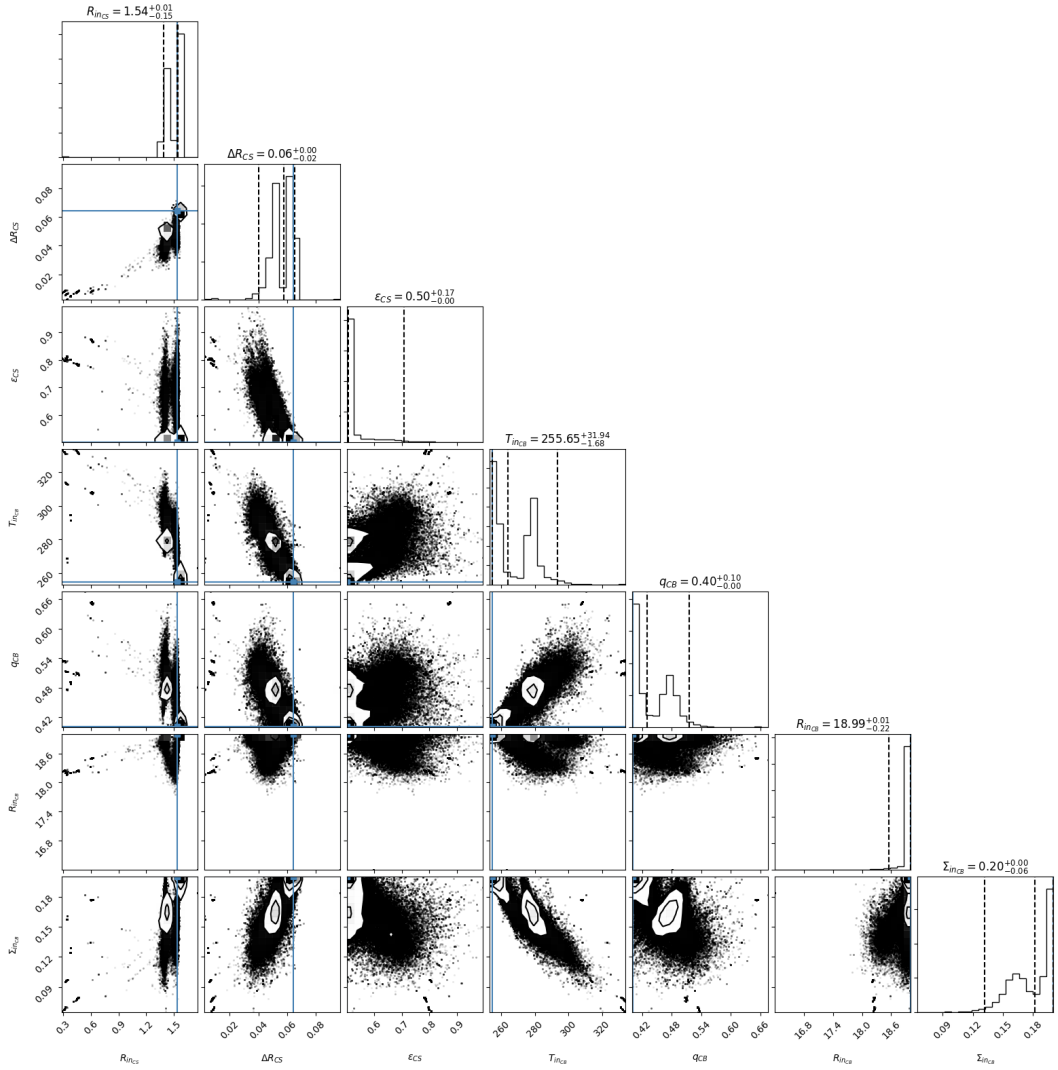

Figure 4.22: Model 2: resulting MCMC corner plot using the dataset of the fourth epoch alone – 20-12-2013 –.

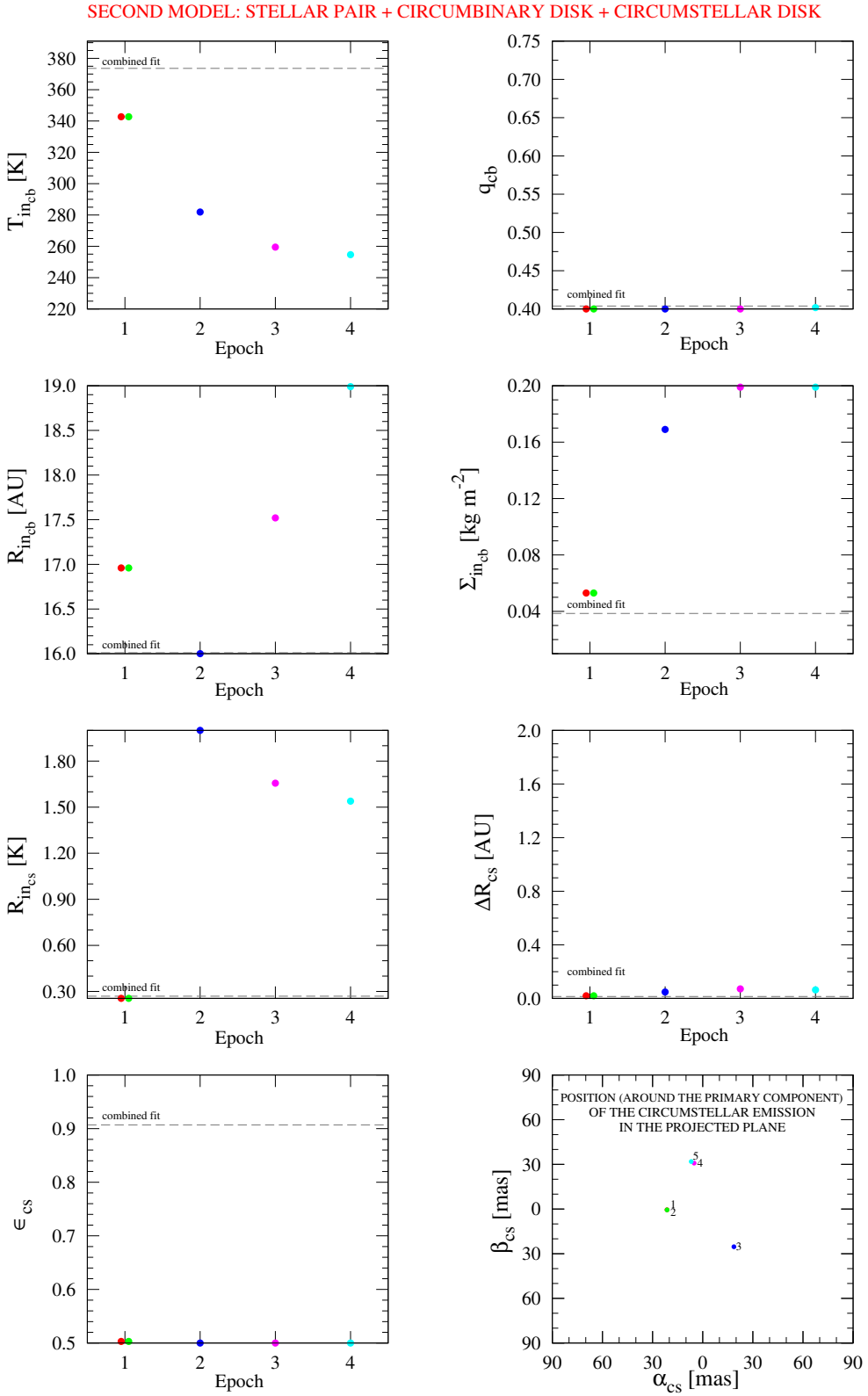

Figure 4.23: Parametric values of the 7 variables which produce the least χ^2-results and, consequently, the finest fits of Fig. 4.21. The values of the combined test are traced with dashed horizontal lines over the entire boxes and labelled as "combined". The optimized values for independent datasets are depicted with dots above their respective epoch. The coordinates $(\alpha_{cs}, \beta_{cs})$ show the fixed position of the star that hosts the disk (similar to Fig. 4.13).

4.3.8 Third model: Temperature-gradient model of a binary system with a geometrically flat circumbinary disk and a dusty disk-like component in the circumbinary cavity

The fact that a circumstellar disk is attached to one stellar component, like in the previous subsection 4.3.7, creates an asymmetry effect but narrows a decent fit to the MIDI differential phases. In this third model I hypothesize the existence of a dusty free-floating component inside the cavity which separates the central pair from the circumbinary disk (Fig. 4.10). The flux of this uniform disk-like emission, $F_{\mathrm{dc},i=0}(\lambda)$, is added up to the total flux of the system

$$F_{3\mathrm{m}}(\lambda) = F_{\mathrm{bin}}(\lambda) + F_{\mathrm{cb},i}(\lambda) + F_{\mathrm{dc},i=0}(\lambda) \tag{4.44}$$

and to the normalized complex visibility

$$V_{3\mathrm{m},\lambda}(u,v) = \frac{F_{\mathrm{bin}}(\lambda)V_{\mathrm{bin},\lambda}(u,v) + F_{\mathrm{cb},i}(\lambda)V_{\mathrm{cb},\lambda}(u,v) + F_{\mathrm{dc},i=0}(\lambda)V_{\mathrm{dc},\lambda}(u,v)}{F_{3\mathrm{m}}(\lambda)}. \tag{4.45}$$

Although an inclination dependence of this disk-like structure is plausible, this investigation aims at confirming the presence of this near-IR source with the least possible number of free-parameters and based on mid-IR observations. Therefore, I adopt simply a face-on configuration. The undetermined location of this emission and the absence of an inner rim due to its independence of a host star make necessary some modifications in comparison to the previous model, and the addition of two additional free-parameters, resulting in a total of 9 variables:

• *Uniform temperature of the dusty disk* T_{dc}: The inserted dusty component, instead of being a ring-like structure around a star, is a uniform disk with homogeneous temperature over its whole extension. This means that a relation between parameters as seen in Eq. 4.41 is unnecessary. The temperature range of this parameter is, nevertheless, investigated in a space between 500–2000 K, suggested by the wavelength range at which the photometric measurements show the peak emission in the near-IR. This interval encompasses the dust sublimation temperature of silicate grains.

• *Outer radius of the disk* $R_{\mathrm{out_{dc}}}$: The size of this emission is given by the radius of the uniform disk scanned over a nominal value of 0.001 and 2 AU. This limit is set based on predictions of the binary truncation effect for the estimated separation between stellar components of V892 Tau.

• *Achromatic emissivity factor* ϵ_{dc}: Similarly to the previous model, only an achromatic dependence is assumed for this free-floating component (blue trace in Fig. 4.11). The parameter ϵ_{cs} is therefore scanned over its entire range, from 0 to 1.

• *Coordinates of the center of the dusty component in the non-projected plane* $(\alpha_{\mathrm{dc}}, \beta_{\mathrm{dc}})$: Since the peak of the SED suggests a hot object with a temperature circa 2000 K and it is presumably formed of dust, I restrict its search to a radius of $\pm$125 mas ($\sim$9 AU) within the circumbinary cavity, where the vicinity to the stellar pair can induce such high dust temperatures. Although this search is carried out for the non-projected plane involving the stars and the circumbinary disk (results of the corner plots), the last panel of Fig. 4.26 displays the position of the additional component on the sky plane (projected plane).

On the basis of this 9 free-parameter model, the following MAGIX χ^2-minimization tests were performed:

(i) **Combined fit to all datasets with a dusty hot component**

As in point (i) of subsection 4.3.7, the SED + the 5 MIDI observing epochs are fitted

altogether ($N_{\rm files} = 11$). This implies that the location of the dusty component, its morphology and the one of the circumbinary disk remain constant along the years of observation. The produced traces and χ^2-value are shown as "combined fit" in the panels of Fig. 4.24 and Fig. 4.26.

(ii) **Fit per epoch with a dusty hot component**

This minimization allows me to test signatures of variability, both in location and morphology of the components, or, in its defect, trends observed over the 9-year span. The 9 free-parameter model was independently fitted to each of the MIDI observing epochs + the SED measurements, containing a dataset of $N_{\rm files} = 3$ (excepting the first epoch that has $N_{\rm files} = 5$) and offering more flexibility to the fitting capacities of the numerical routine. The best fits to the observed visibilities, chromatic phases and SED points are plotted in Fig. 4.24 under the label "fit per epoch". The fluctuation of the calculated parameter values are depicted in Fig. 4.26.

The advantage of this model is the unrestrained location of the dusty component. First, the blackbody emission of this uniform disk-like structure fills the observed near-IR excess and, second, it acceptably modulates the large mid-IR differential phases. This is shown in Fig. 4.24, where systematically lower reduced χ^2-values were obtained. Even when fitting all the epochs simultaneously via the "combined fit" experiment, the reduced χ^2 remains rather low ($\chi^2 = 6.49$) compared to the two previous models. Moreover, the fit to the observed data is improved for all dates when considering independent datasets ("fit per epoch"). This result points to a temporal variability and/or asymmetry in the components forming the system V892 Tau. Because of its finer results – both visually and numerically – I consider this model as the closest and most representative outcome of this investigation. The corresponding corner plots produced by the MCMC algorithm for the combined experiment and each independent dataset per epoch are displayed in Figs. 4.25.

In the eight panels of Fig. 4.26 I illustrate the best-fit values of the 9 free-parameters obtained with the two tested cases. The parameters of the circumbinary disk show different trends. On the one hand, the temperature at the inner rim $T_{\rm in_{cb}}$ and its radius $R_{\rm in_{cb}}$ are congruent over the epochs within a 10% variation. On the other hand, the temperature power-law $q_{\rm cb}$ and the surface density at the inner rim $\Sigma_{\rm in_{cb}}$ include larger fluctuations from epoch to epoch over the parametric space.
The best-fit parameters for the dusty component seem less spread out for the different individual optimizations, being only the fourth epoch (20-12-2013) slightly deviated from the common trend of the rest of observing runs. Indeed, according to this tendency, the uniform temperature of the dusty component is close to the upper limit of the parametric space ($T_{\rm dc} \sim 2000$ K), the compact size of the disk is $R_{\rm out_{dc}} \sim 0.15$ AU, and its emissivity factor is established at $\epsilon_{\rm dc} \sim 0.4$. Especially, both, the independent and combined fits, point to an emission feature in the projected plane represented by the additional dusty component located in the close central region of the stellar pair, in an area with coordinates ($\alpha_{\rm dc} = -1.78 \pm 29$ mas, $\beta_{\rm dc} = 10 \pm 37$ mas). Interestingly, this result agrees with the west lobe detected through image reconstruction by Monnier et al. [2008] (Fig. 4.3).

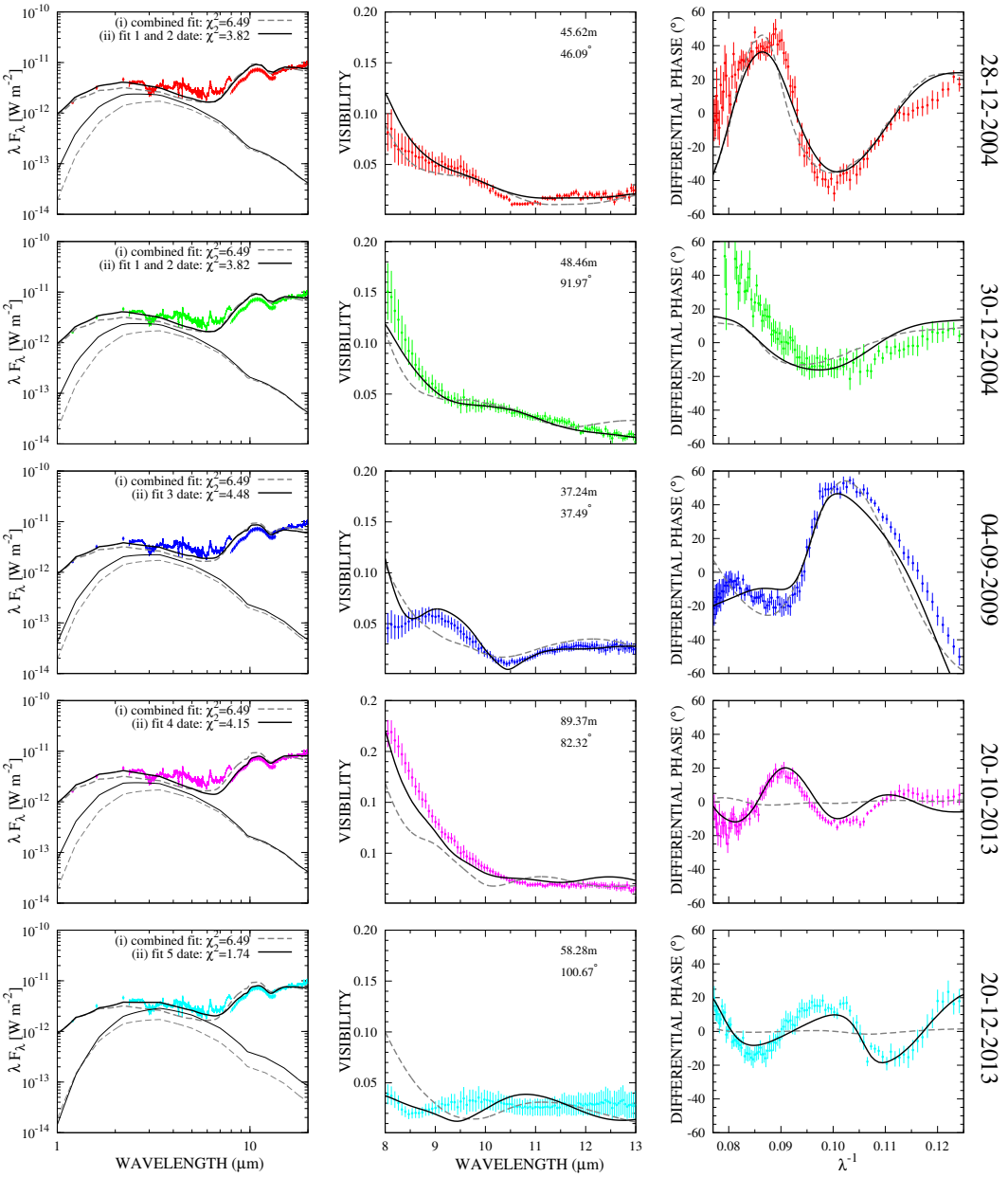

Figure 4.24: Best χ^2-fits for the model consisting of stellar pair, circumbinary disk and dusty component inside the large cavity. The flux contribution provided by the new source of near-IR emission, as well as its location closer to the central stars, satisfactorily simulate the near-IR bump revealed through the SED measurements and the MIDI data. The tests with combined datasets and independent epochs are respectively depicted with gray dashed and solid black lines. For a better visualization, only the curve of the near-IR source is plotted in addition to the total flux of the SEDs.

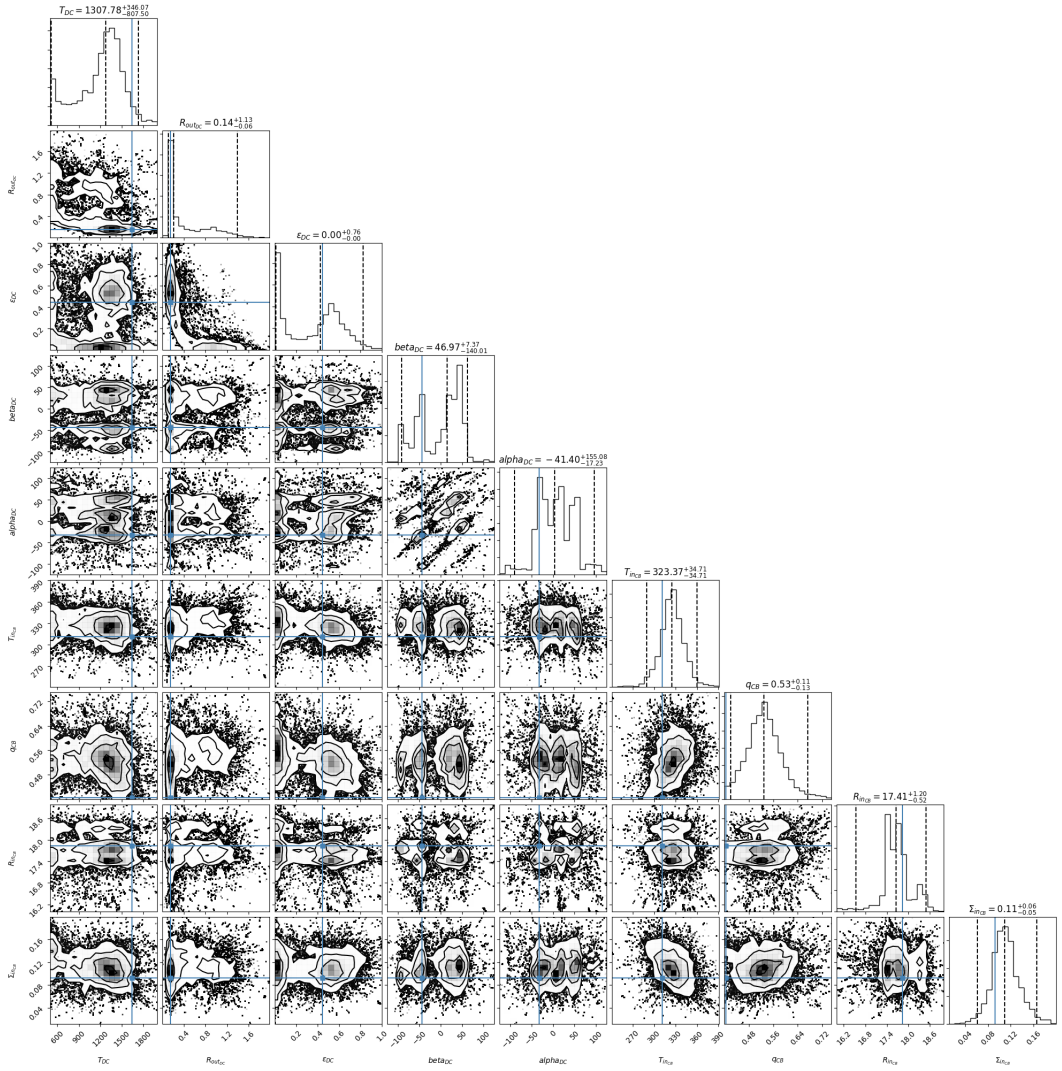

Figure 4.25: MCMC corner plot for the experiment that groups all datasets and SED measurements with the parametric model 3, which consists of a stellar pair, circumbinary disk and additional dusty component nearby the central stars. The plot reunite the one- and two-dimensional projections of the posterior 2σ-probability distributions of the 9 free-parameters, as well as the best χ^2-value traced with blue. In the one-dimensional histograms, three vertical dashed lines delineate respectively the anterior, 50-percentile and posterior borders of the 2σ-probability distribution. If the central dashed line coincides with one of the borders, or in turn the boundaries match the edge of the parameter space, less dashed lines might be apparently noticed. The difference between the probability function and the χ^2-function may cause an imprecise coincidence between the histogram peak (mode) and the blue lines. On the top of each parameter, the mode of the distribution and the 2σ range are indicated. It is important to remark that the best-fit curves of Fig. 4.24 were obtained specifically with the least χ^2-values indicated by the blue line.

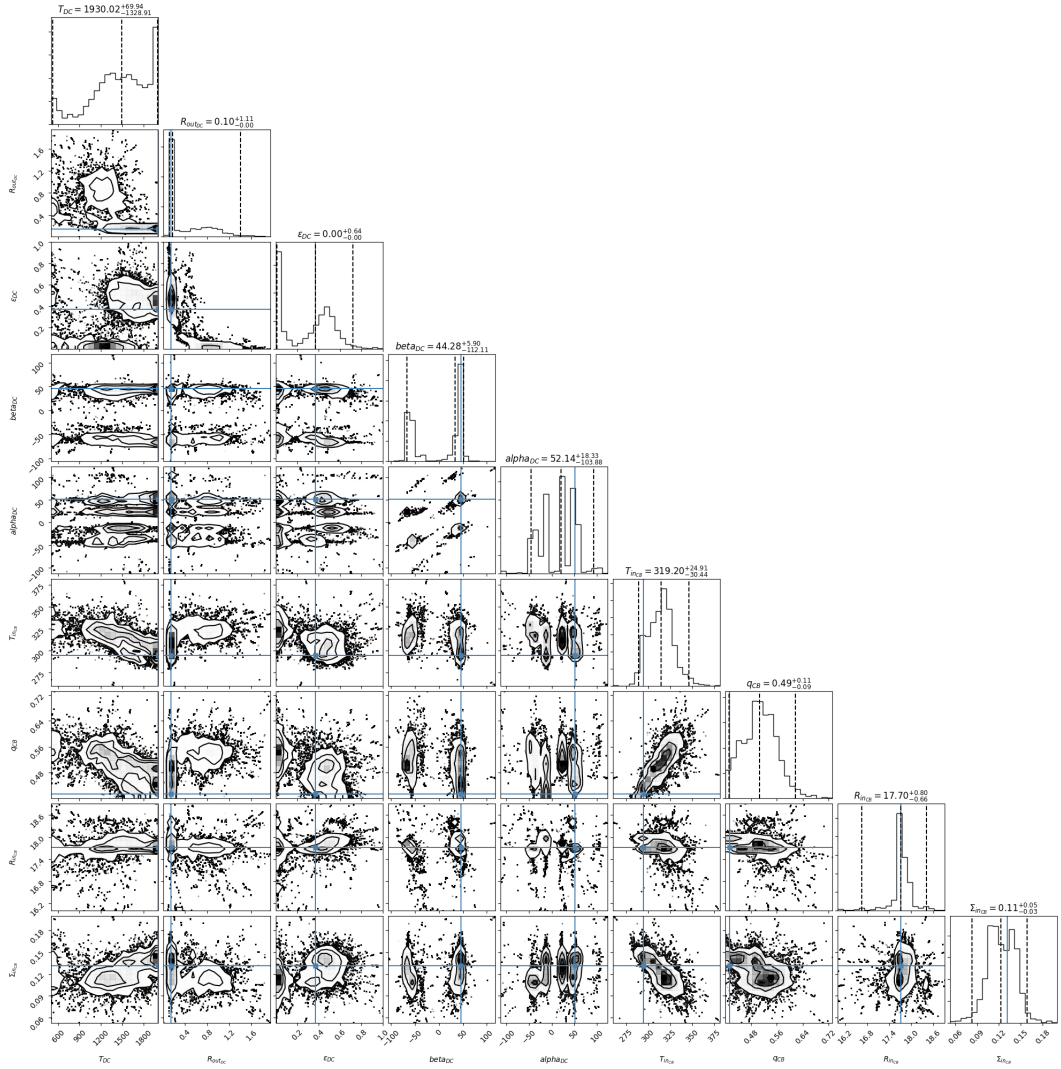

Figure 4.25: Model 3: resulting MCMC corner plot using the dataset of the first epoch alone – 28-12-2004 and 30-12-2004 –.

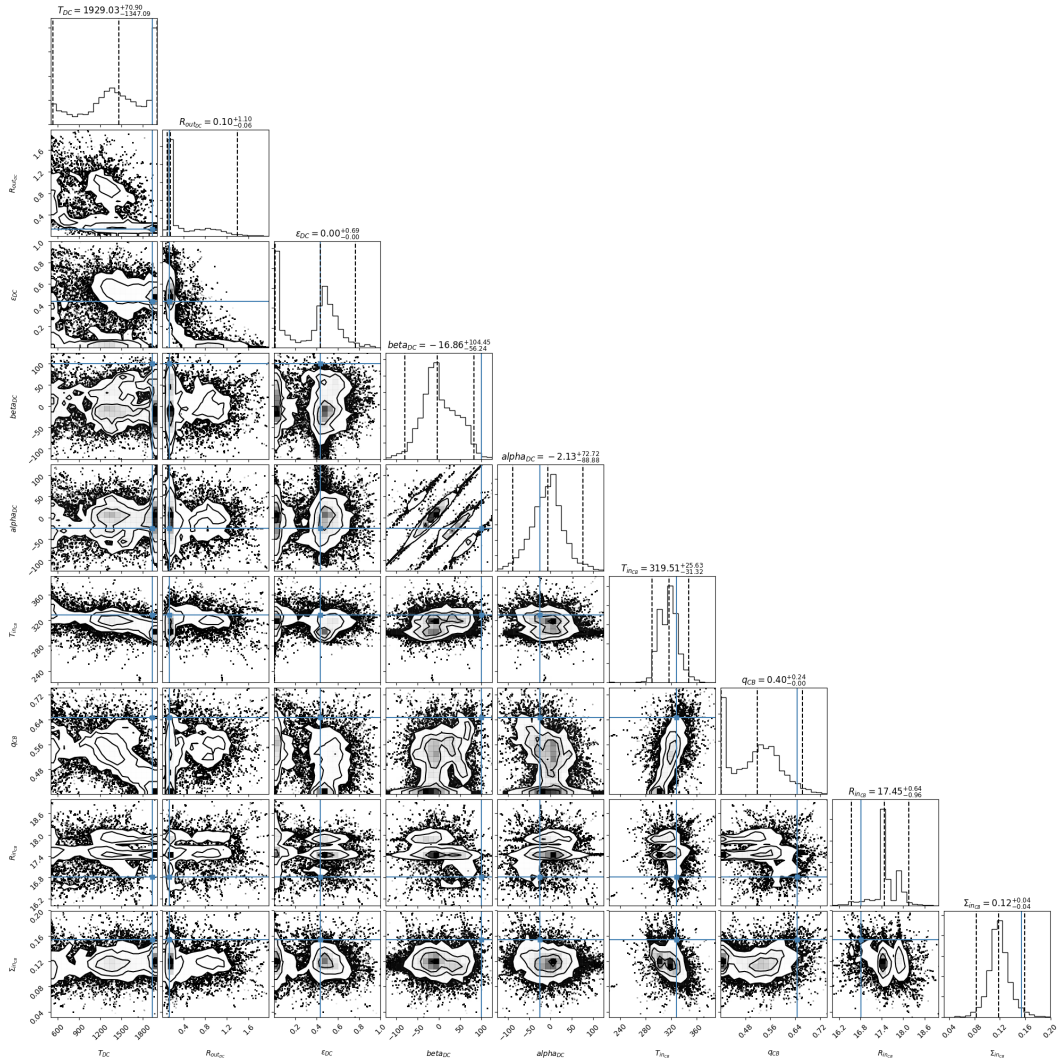

Figure 4.25: Model 3: resulting MCMC corner plot using the dataset of the second epoch alone – 04-09-2009 –.

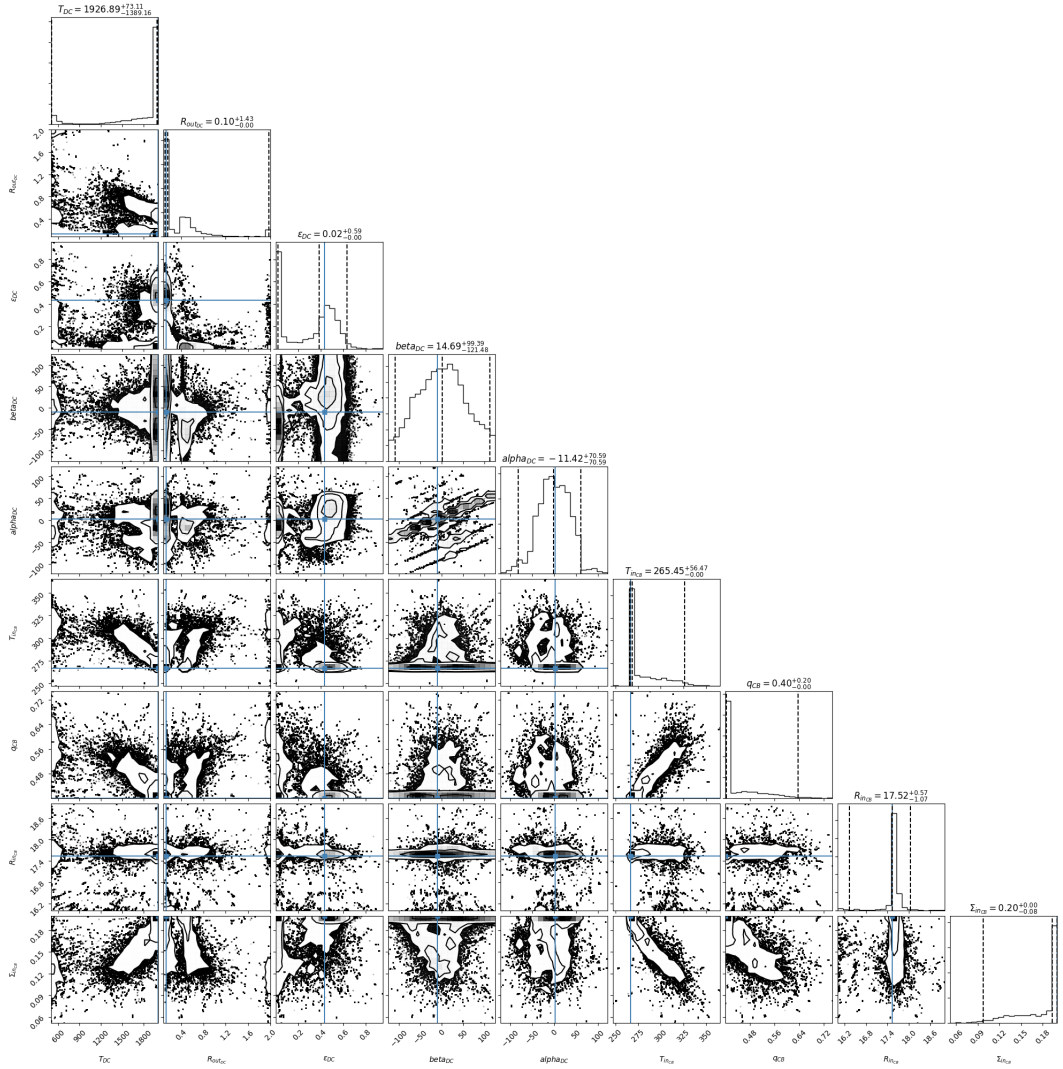

Figure 4.25: Model 3: resulting MCMC corner plot using the dataset of the third epoch alone – 20-10-2013 –.

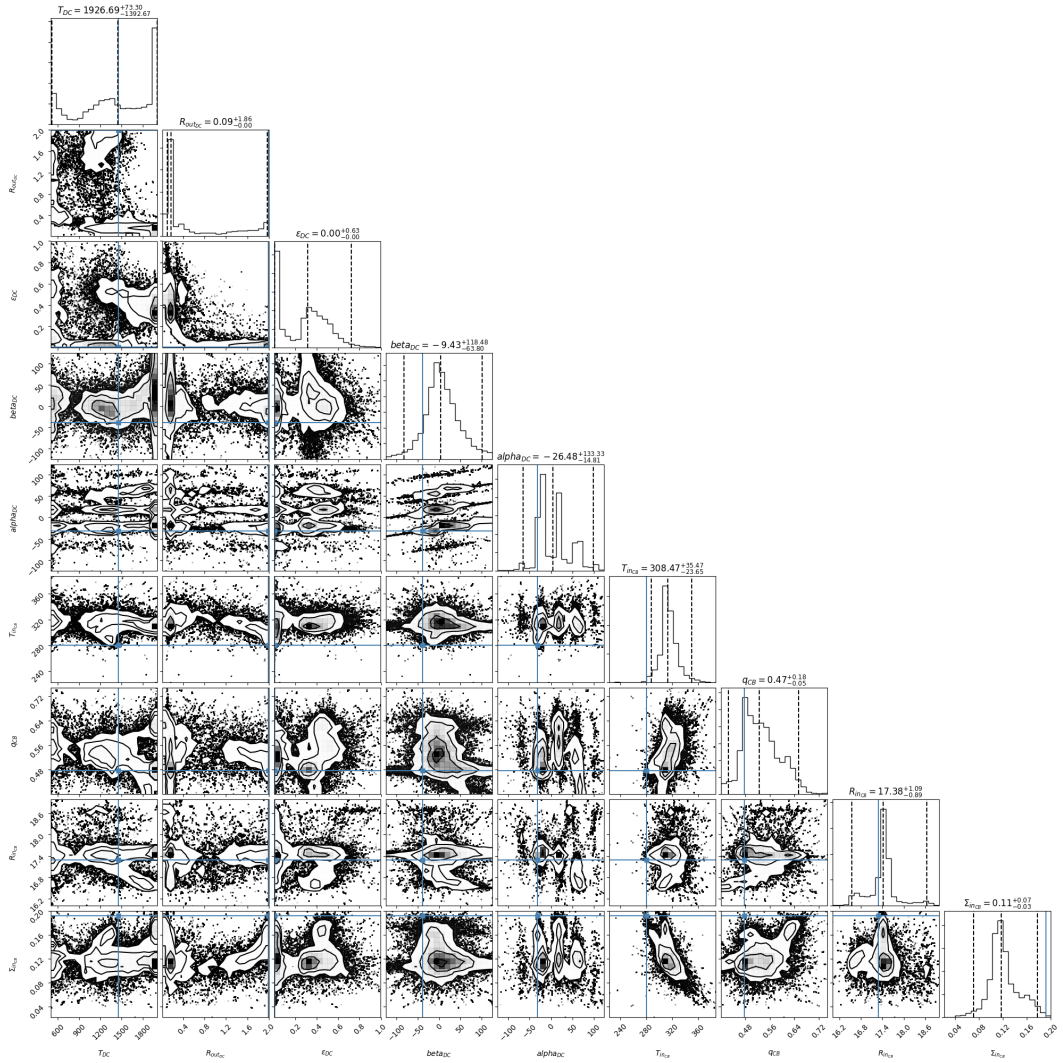

Figure 4.25: Model 3: resulting MCMC corner plot using the dataset of the fourth epoch alone – 20-12-2013 –.

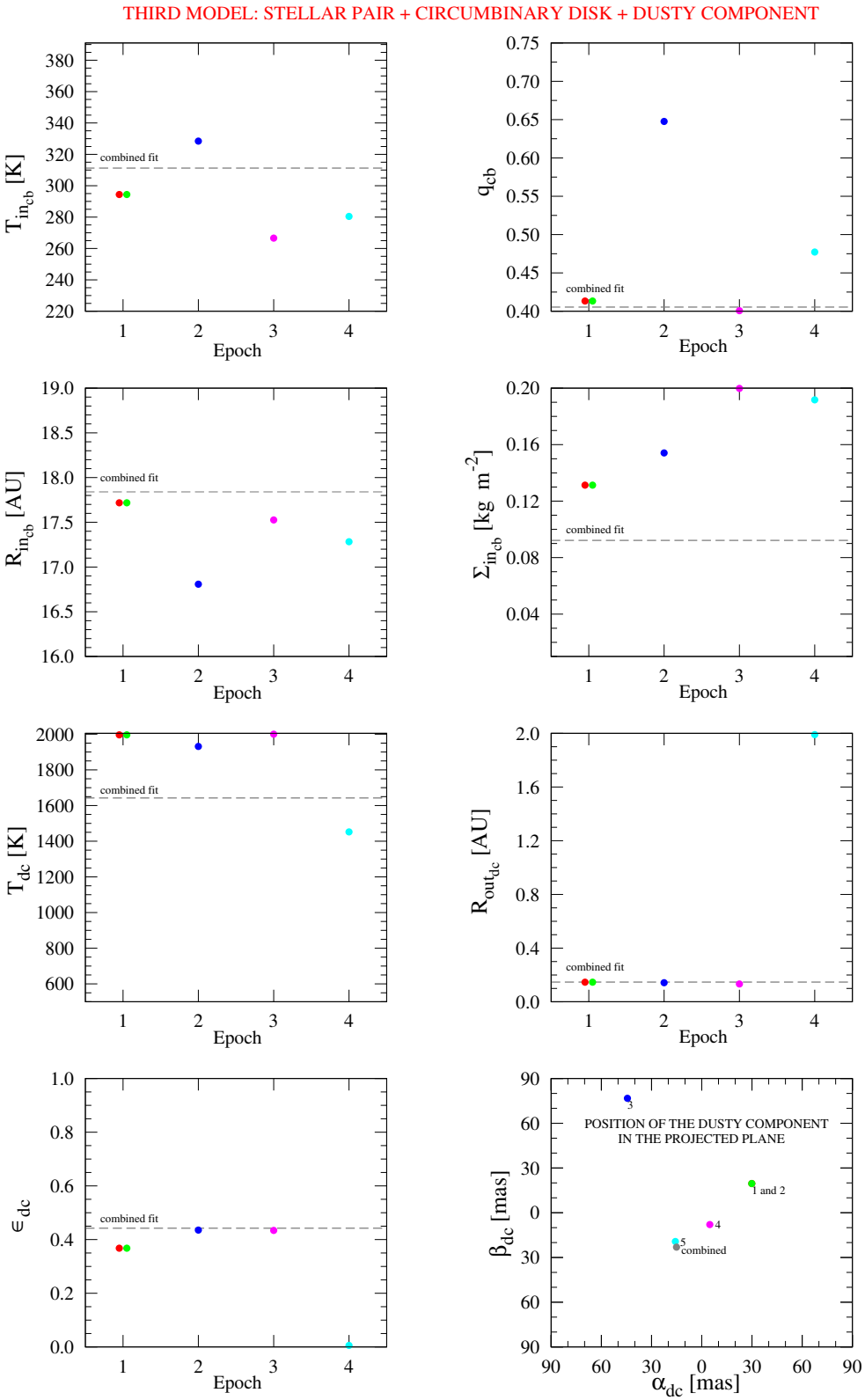

Figure 4.26: Values of the 9 free-parameters obtained for the third model of V892 Tau with the minimizer MAGIX. These parameter vectors produce the finest fits to the experimental data in Fig. 4.24 and consequently the least χ^2-values (also seen with blue lines in the corner plots). The results correspond to the combined and individual experiments, and are respectively labelled. The last panel displaying the coordinates $(\alpha_{\rm dc}, \beta_{\rm dc})$ shows the location of the proposed hot component for each case.

CHAPTER 5

Discussion and Prospects

5.1 On the results of the temperature-gradient modelling

The temperature-gradient modelling and MAGIX reduction favour a configuration of the Herbig Ae/Be object V892 Tau consisting of an equal-brightness stellar pair, an extended circumbinary disk and a small dusty disk-like component located inside the cavity of the circumbinary disk, close to the central stellar pair.

The model fitting confirms that the inner edge of the rather irradiated ($q_{\rm cb} \sim 0.4$) circumbinary disk is located at $R_{\rm in_{cb}} \sim 17.5$ AU from the barycentre of the stellar pair. The derived dust temperature at the inner edge is ~ 300 K, which would translate to a cooling efficiency of $\epsilon = 0.29$ according to Eq. 4.38. The modelled circumbinary disk considers an opacity law that shapes the N-band silicate feature present in the MIDI and ISO spectrum of V892 Tau. Thus, my results disagree with the ones of Monnier et al. [2008] since they found a much higher temperature of 450 K at the inner edge of the disk, and considered a stellar pair producing an excessive photospheric flux with a high luminosity of $400 L_\odot$. I explain their overestimation in terms of, first, the consideration of only a circumbinary disk which emits as an optically thick blackbody, and second, the negligence of an additional near-IR emitting component in their study, whose absence obligates to increase both the temperature of the circumbinary component and the luminosity of the stars to reward the spectro-photometric measurements.

Indeed, the best result of this examination reveals that a uniform disk-like structure with a tentative size of $R_{\rm out_{dc}} \sim 0.15$ AU is preferentially located within an area of ± 30 mas (~ 4 AU) west of the center. This component can produce enough infrared emission to reproduce well the observed infrared excess at 2 μm (45%), 5 μm (60%), and at 8 μm (10%). Moreover, the dusty component would have a temperature of $T_{\rm dc} \sim 2000$ K and an emissivity of $\epsilon_{\rm dc} \sim 0.4$. The inclusion of this additional source allows to reproduce the variable visibilities at the short edge of the N-band and the bumpy differential phases.

In spite of these results, I am aware that the limitations of modelling mid-IR interferometric data based on visibility building blocks of axisymmetric objects hardly allows to conclude on the exact nature of the near-IR source. However, based on the advantage of multi-epoch interferometric observation in the mid-IR, my investigation reports on the necessary existence of an additional hot dusty component in the central environment of the binary to reproduce the near-IR excess observed in the SED of V892 Tau, as reflected

Table 5.1: Summary of the best normalized χ^2-values per observing run obtained for the experiment "fit per epoch" with the third model.

Epoch	28-12-2004 30-12-2004	04-09-2009	20-10-2013	20-12-2013
$\chi^2 \equiv \chi^2/\nu$	3.82	4.48	4.15	1.74

in subsections 4.3.7 and 4.3.8. Nevertheless, in the panels showing the best parameter values some trends and correlations over time can be established. I contemplate that the variable MIDI visibilities and non-zero phases could be explained almost equally well by non-axisymmetric starlight scattered off the circumstellar component/s in the pair or by a free-floating (sub)stellar companion, making it difficult to discriminate between the exposed "circumstellar disk" and "dusty component" configurations. Similar degeneracy has been reported with closure-phase observations of other protoplanetary disks [e.g. Cieza et al., 2013, Olofsson et al., 2013, Di Folco et al., 2014].

Interpretation of the best χ^2-values

At first sight, the synthetic visibilities, differential phases and SED of the third model with a binary system, a circumbinary disk and an additional hot free-floating component adequately fit the mid-IR experimental data and the broadband SED, with some small deviation especially at the shortest wavelengths of the N-band. The independent fit of this model also numerically shows the least χ^2-values (summarized in Table 5.1) that can be used for a further test of their goodness per observing date.

In theory, the χ^2-distribution is an asymmetric distribution whose minimum value is 0, but has no maximum value as it approaches the horizontal axis. The shape of this distribution depends on the degrees of freedom. Its mean is the degree of freedom ($\mu = \nu$) and the standard deviation is twice the degree of freedom ($\sigma^2 = 2\nu$). Then, for a given significance level α (commonly the 5%) and from an appropriate table or graph[1], the value $\chi^2_{\nu,\alpha} \equiv \chi^2_{\nu,\alpha}$ can be determined. This value is subsequently compared to the measured $\chi^2 \equiv \chi^2/\nu$ to establish the level of confidence of the model.

As seen from subsection 4.3.5, the degree of freedom for the particular "fit per epoch" case with three datafiles of the best model of V892 Tau can be quantified as

$$\nu = N_{\text{files}} \times N_{\text{points}} - N_{\text{free}} = 3 \times 97 - 9 = 282$$

and consequently $\mu = 282$ and $\sigma^2 = 564$.

The larger the degrees of freedom, the more spread out and approximate to a normal the χ^2-distribution. In other words, the approximation is much better at much larger ν. At such high value of ν, any significance α of the literature shows that the values of χ^2 of Table 5.1 are much less than any $\chi^2_{\nu,\alpha}$. Then, this drives me to conclude that: (i) either the model is valid but that a statistically improbable excursion of χ^2 has occurred, (ii) the values of σ_i^{error} in Eq. 4.29 have been overestimated, or (iii) the data is fraudulent or "too good to be true". A too small value of χ^2 is not indicative of a poor model. On the contrary, the closer to the mean value of 1 the better. Hence, the numerical minimization can be positively validated.

From this test, it may arise the question whether the rest of models that also show a small χ^2-value in comparison to their degrees of freedom are valid. However, at this point,

[1]Multiple samples of χ^2-distribution tables are available on the internet, for instance at `https://www.medcalc.org/manual/chi-square-table.php`, or `http://math.arizona.edu/~piegorsch/571A/TR194.pdf`

intuition and visual judgement of the fits serve as an indicator to corroborate the results. For instance, I conclude that the "fit per epoch" of all observing runs in Fig. 4.24 is better than the other tests because it has a χ^2-value closer to 1 and, visually, it clearly shows a finer reproduction of the observational data. Moreover, the optimization and error estimation via the MCMC method reinforce the adopted results because they determine a 2σ-probability range for each parameter, within which the best χ^2-value is contained and mostly matches the mode of the distribution.

Temperature of the additional dusty component

The arguments mentioned above concerning the limitations of the modelling also impede to make conclusive statements on the disk size and shape of the introduced hot component. On the contrary, the derived value of $\sim$2000 K for the effective temperature can be further discussed since it has direct impact on the geometrical and chemical properties of the dust grains forming this source.

Independently on the exact location and shape of a dusty structure close to the central stars, the sublimation front and temperature contributes to define the physical conditions in the dusty planet-forming region. It has been confirmed [e.g. Natta et al., 2001, Tuthill et al., 2001, Isella and Natta, 2005] that near-infrared excesses seen as a bump in the 2–8 μm SED region of Herbig Ae/Be are compatible with the size of a frontally illuminated, and therefore hotter, rim. The size of this rim is correlated with the luminosity of the central stars and consistent with the dust sublimation radius of silicate grains at a temperature of 1500 K. However, for a significant sample of objects, the advantages of spectrally-resolved interferometry has further revealed the presence of an additional hot component emitting from within the sublimation radius [e.g. Kraus et al., 2008a,b, Tannirkulam et al., 2008, Eisner et al., 2009].

Alternative interpretations proposed to explain the near-IR excess between 2–8 μm and the existence of hotter emission within the sublimation radius are: an extended (spherical) dusty envelope [e.g. Vinković et al., 2006], disk winds [e.g. Bans and Königl, 2012], magnetically lifted grains [e.g. Ke et al., 2012], supported disk atmosphere [e.g. Turner et al., 2014] and dependence on grain size of cooling efficiency and dust settling [e.g. Tannirkulam et al., 2007]. Moreover, recently, a statistical study on the milliarcsecond morphology of the near-IR emission around 51 HAeBe objects found that dust at the inner rim of the disks has a sublimation temperature of 1800 K, corresponding to carbon instead of silicates, and justifying dust survival in more hostile environments [Lazareff et al., 2017].

In conclusion, I believe that the found effective temperature for the introduced additional component of V892 Tau of $\sim$2000 K is plausible, and can be validated by some of the frameworks mentioned above. This value, indeed, may point to a circumstellar environment consisting of a mixture of silicate and graphite. Such composition has been previously used to probe the circumstellar environment of Herbig Ae stars [e.g. Il'In and Krivov, 1994, Ragland et al., 2012]. Also, the relatively high temperature suggested for the dusty component cannot be simply compared to the canonical value of 1500 K typically used in other works. One reason is that the dust sublimation temperature depends as well on the gas partial pressure as highlighted by Kama et al. [2009], where they show that the dust sublimation temperature can rise to up to 2000 K with increasing gas pressure.

Only dedicated near-IR direct imaging and spectrally-resolved interferometry observations will allow to discriminate the different scenarios.

Asymmetry and morphology of the additional dusty component

In addition to the large circumbinary disk surrounding the stellar pair of V892 Tau, the best-fit result of this work proposes a small disk-like dusty object in the vicinity of the central stars to produce a non-zero interferometric phase signal.

The detection of such asymmetrical brightness distribution has been possible also for other – although single – objects with transition disks. For instance, aperture masking observations in the near-IR have revealed a (proto)planet surrounded by dusty material within the gap of the transition disk around of LkCa 15, at about 15 AU from the main component [Kraus and Ireland, 2012]. Similarly, Naos-Conica (NACO) observations of T Chamaeleontis in the L'- and K-band reported a substellar companion separated $\sim$7 AU, which was detected in the L'-band but unseen in the K-band. This redness is attributed to its youth and amount of dust around it [Huélamo et al., 2011]. Later, however, interferometric, photometric and imaging observations allowed Olofsson et al. [2013] to conclude that the near-IR excess of T Cha is explained by two concentric dusty circumstellar disks separated by a gap, and that the phase signals may arise from the asymmetry generated by forward scattering by dust grains in the upper layers of the outer disk. Near-IR scattered light imaging observations have also shown that the spatial distribution of dust of protoplanetary disks may display spiral arms [e.g. Benisty et al., 2015, Dong et al., 2018]. Although two-arm spiral arms are more common in disks surrounding HAeBe, asymmetric cases like the one-arm spiral disk around V1247 Ori have been observed. Such asymmetry can be induced by the presence of an unseen companion and/or ongoing planet-forming processes [Ohta et al., 2016].

In the particular case of V892 Tau, the asymmetric mid-IR emission of the large transition disk was already reported by Monnier et al. [2008], and their interferometric data was better fitted by a "skewed asymmetric ring model" (Fig. 4.3). These authors attributed such emission to the dynamical interaction between the eccentric binary and the surrounding disk via resonances or disk warping. Although such brightness distribution indeed may generate a modulation in the phase, I deduce that the separation between the circumbinary disk and the stars is too large to heat the grains up to the temperatures needed to simulate the near-IR excess of the SED. Nonetheless, if the emission were indeed originating from the $\sim$18 AU circumbinary disk, a possible explanation to account for an asymmetric centroid of light and very red color ($\mathrm{K} - \mathrm{N}$), meaning detectable in the N-band and imperceptible in previous near-IR observations [e.g. Smith et al., 2005, Monnier et al., 2008], would be that a (sub)stellar companion were highly obscured along the line of sight by the dust of the large disk. The natural scenario that my investigation explores is that the unseen companion, modelled by a small disk-like source, is under the radiative influence of the luminous central stars. Hence, the range of search encompasses only the circumbinary cavity in a non-projected space of $\pm$125 mas with respect to the barycentre ($\sim$35 AU in diameter). In such a scenario, the non-detection by previous high-angular resolution observations would be justified if the newly proposed near-IR source were too close to the stars.

In binary PMS objects with disks, asymmetries may have different grounds due to their complex density structures. Supposedly, two inner circumstellar disks located inside the Roche lobes, rotating around the individual stars, and a circumbinary disk outside the L2 and L3 Lagrangian points may coexist [Fig. 2.17; Lubow and Artymowicz, 1997]. In addition, streamers from the CB feed up the CS, otherwise they would not survive. In the framework of intermediate-separation PMS binaries, there are only two well known systems where such a complex structure has been directly imaged: GG Tau A with a separation of components of 36 AU [Guilloteau et al., 1999, Dutrey et al., 2014] and UY Aur with a separation of $\sim$100 AU [Hartigan and Kenyon, 2003, Tang et al., 2014]. High-resolution numerical simulations have allowed Günther and Kley [2002] to show that these two stellar

systems, due to a mass ratio different from unity, still after many orbital periods show an asymmetric configuration. Near-IR scattered light and CO observations show that UY Aur is highly inhomogeneous [Dutrey et al., 2016]. Furthermore, it has been shown that the T Tauri binary object CS Cha (separation ca. 4 AU and circumbinary cavity size of about 38 AU) experiences mid-IR variability due to mass variation and illumination of optically thin dust, which in addition to the optically thick inner edge of the circumbinary disk, is present in the circumbinary inner hole and especially in the two streams connecting the saddle points and the two inner CS disks [Nagel et al., 2012].

To conclude on whether the asymmetry and the near-IR excess detected in V892 Tau emerge from inhomogeneous dust overdensities around the individual stars or along streamers is beyond the bounds of this investigation. According to the simulations by Günther and Kley [2002], equal-mass binaries on a circular orbit are expected to reach a quasi-stationary symmetry with respect to the line connecting the stars. From the initial assumptions on the stellar pair adopted in my research, the same picture would be expected for Elias 1. On the other hand, shocks from the CB disk to the outer rim of an hypothetical CS disk (or the other way around) may be quite bright and produce strong thermal radiation, especially in the X-ray band [e.g. Shi and Krolik, 2016, and references therein]. Consequently, if existing, these shocks may also decipher the X-ray activity reported in V892 Tau.

To my knowledge, on the side of HAeBe objects, only the binary HD142527 [Biller et al., 2012], with a separation of 13 AU, may posses a large circumbinary cavity, a circumstellar disk and/or an unseen planetary companion. For this reason, based on multi-epoch mid-IR interferometric observations, this report on the detection of a hot component in the central neighbourhood of V892 Tau brings new insight in the field, and offers a benchmark for advancing theoretical hydrodynamical simulations of dynamically disrupted circumbinary environments. Near-IR high-angular resolution observations with interferometry and imaging are compelled to unambiguously determine the nature of the near-IR excess in the circumbinary cavity of V892 Tau.

5.2 V892 Tau in the era of second generation instruments

Allocated NACO and GRAVITY observations

A step forward has been taken in this project by proposing the acquisition of high-resolution near-IR data of V892 Tau in the oncoming ESO observing period. For the first time, V892 Tau will be observed in the near-IR with the imaging instrument NACO [Lenzen et al., 2003] and the interferometric instrument GRAVITY [Gravity Collaboration et al., 2017a]. This allocated time will serve to probe the circumbinary cavity and determine the morphology and precise location of the hot source detected by this mid-IR interferometric investigation.

According to the SED modelled in this study (Fig. 4.24), the detected near-IR component provides $\sim$30% of the total luminosity in H-band (1.75 μm) and $\sim$50% in K-band (2.24 μm). Therefore, the object to be resolved by the new observations would correspond to magnitudes of $\mathrm{H} = 8.5$ and $\mathrm{K} = 7$. For comparison, the magnitudes of the system V892 Tau in the different filters are: $\mathrm{V} = 14.7$, $\mathrm{H} = 7$, $\mathrm{K} = 5.8$. Moreover, from the orbital solution of the binary system, I predict a separation between stars of $\rho \sim 45$ mas at the time of the planned acquisitions.

The combined observations with the two instruments will allow to explore different spatial scales within the inner circumbinary edge (Fig. 5.1) and discriminate between the here proposed second and third model:

1. On the one hand, if the near-IR excess source is not bound to any stellar component

but instead rather separated from the barycentre by more than 60 mas (∼8 AU), the NACO diffraction-limit resolution in K-band will detect it with a good signal-to-noise ratio (SNR∼1200). Although H-band data will be simultaneously recorded and allow to refine the binary orbit, the observing run is intended in K-band because at this range the data contains little contamination from the circumbinary disk, and at the same time the stellar contribution is also less than in the H-band.

NACO is assisted by the NAOS adaptive optics system which is equipped with one infrared (IR-WFS, 0.8–2.5 μm) and one visible wavefront sensor (VIS-WFS, 0.45–1 μm). In the case of the proposed observations of V892 Tau, the IR-WFS will be implemented with the science star itself as reference star, allowing to achieve a Strehl ratio on target of ∼35%. The dichroic configuration will be N90C10, which means that 90% of the light will be used for the NAOS WFS, and only 10% transmitted to the CONICA camera.

The high-resolution capacity of NACO for around two decades has been probed to be fundamental in the characterization of the dusty environment around YSOs, such as in the case of TY CrA [Chauvin et al., 2003], GG Tau A [Di Folco et al., 2014], HD100546 [Stolker et al., 2016b] or HH250 [Comerón et al., 2018].

2. On the other hand, if the source of near-IR excess emission is of circumstellar nature, it will be detected and characterized with GRAVITY. The interferometric field-of-view of the VLTI is limited to the Airy disk of each individual aperture, i.e. 250 mas for the ATs and 60 mas for the UTs in K-band. The proposed observations with the UTs will reach a high-angular resolution of ∼2 mas (sub-AU resolution) for a baseline of 100 m, allowing to detect the innermost structures associated to the stars. One snapshot with GRAVITY produces six baselines (four UTs), making possible safe modelling with little degeneracy associated to the central pair. The offered visibilities are expected to vary between 0.2 and 1 depending on whether the near-IR emission is bounded or not to any of the stars.

   The observations will benefit from the single-field mode of GRAVITY, consisting of splitting 50–50% the source light for the fringe tracking channel (FT) and the science channel (SC). The FT is performed at a frequency of approximately one kHz to correct for the atmospheric and instrumental piston, i.e. the residual OPD between the combined beams, by modulating piezo mounted mirrors within the instrument. The FT spectrometer always operates at low spectral resolution ($\Delta\lambda/\lambda \sim 20$), but the planned observations will be obtained at high resolution ($\Delta\lambda/\lambda \sim 4000$), allowing to resolve spectral features within the K-window, such as the Brγ line (2.166 μm), the He I line (2.057 μm) or the CO bandheads between 2.3–2.4 μm.

   The GRAVITY interferometric visibilities, differential phases, closure phases and high-resolution spectrum will allow to constrain not only the hot dusty object's structure, but also the gas distribution due to the spectro-interferometric information. Each of the spectral lines mentioned above are associated to different processes and regions of the system. For instance, the CO bandheads may trace warm (>1000 K) neutral gas which usually spatially extends and comes from the region between the stars, corresponding, for example, to gas streams between inner circumstellar disks. The Brγ, on the contrary, traces hot (>10000 K) ionised gas and may reveal both mass accretion and ejection processes. The spectral lines make it possible to determine whether they are associated to the primary star, secondary star, or the extended environment. A further comparison with the phase and visibility signals permits to indicate where each of the

lines originate in the system and determine the source of brightness asymmetry [e.g. Gravity Collaboration et al., 2017b, Kraus et al., 2017a].

The future with MATISSE

The upcoming second generation instrument MATISSE for the VLTI [Lopez et al., 2014] will allow to continue the exploration of V892 Tau with a spectral resolution 30–5000, and a spatial resolution 5–10 mas. The four-beam combination will be possible in the L- (3–4 μm), M- (4.5–5 μm) and N-band (8–13 μm), offering six baselines simultaneously and including the analysis of closure phases in the mid-IR.

In the particular context of V892 Tau, MATISSE will provide a better uv-coverage than existing 2-beam combiners, and the possibility of applying image reconstruction techniques to reveal the details of the circumbinary disk over a wider wavelength range. This is expected to improve the results obtained with MIDI in this investigation and the previous report by Monnier et al. [2008]. If the mid-IR brightness asymmetry observed in the circumbinary disk is unrelated to the hot near-IR source here discussed, it can be caused by an embedded protoplanet or signatures of planet formation, such as spiral arms, or dust overdensities pointing to the evolutionary status of grains. The feasibility of MATISSE to detect forming protoplanets around PMS at intermediate distances, and even at a low flux ratio between the hosting star and the embedded source, has already been probed by Brunngräber and Wolf [2018] and will be one of the promising areas of exploitation of this state-of-the-art instrument.

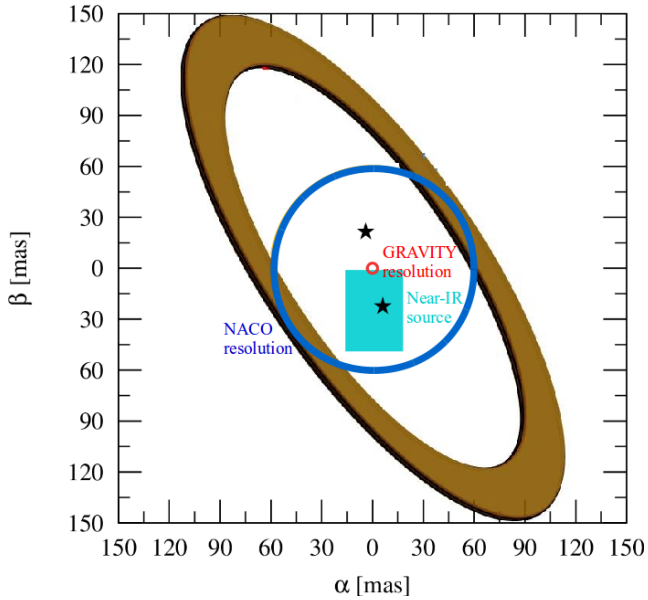

Figure 5.1: Sketch of the expected sky view at the time of the new granted observations, end of 2018. The separation between the stars will be ∼45 mas. The turquoise area depicts the 1σ-area where the proposed dusty component would be located according to my best-fit measurements. The red and blue circles show the diffraction-limit resolution of GRAVITY and NACO, which will complement each other to explore the entire cavity.

5.3 On the new Gaia high-precision parallax measurements of V892 Tau

Gaia[2] is a space observatory of the European Space Agency launched in December 2013 with the purpose of charting a three-dimensional map of the Milky Way and providing high-accuracy astrometry measurements for more than a billion stars in and beyond our Galaxy. The range of observations of Gaia covers the visible G-band (central wavelength at 550 nm), and its limiting magnitude encompasses $3 \lesssim \mathrm{G} \lesssim 20$.

At the time of this interferometric analysis of V892 Tau, the second intermediate Gaia data release DR2 [Gaia Collaboration et al., 2018] was published, containing precise positions, proper motions and parallaxes for more than 1.3 billion objects [Luri et al., 2018]. This updated information revealed that the Herbig object V892 Tau of my investigation has a parallax of 8.52 ± 0.12 mas, which translates to a distance of 117.5 ± 2.7 pc. This means that the science target is located $\sim$16% closer in comparison to the distance of 140 pc credited in previous works [e.g. Elias, 1978, Smith et al., 2005, Monnier et al., 2008] and this research.

Aware that the assumption of a closer object may modify the obtained results, I carried out several tests to monitor the possible variations to this work. I considered only the best-fit case of a binary system surrounded by a circumbinary disk and an additional free-floating disk-like structure inside the gap, and performed a χ^2-minimization modelling with MAGIX just as the method here adopted, but with a fixing distance of 117 pc instead of the "old" measurement. The number of free-parameters and the parameter range were identically maintained. Out of these examinations, the above presented results are reinforced due to the following conclusions:

1. The parameters describing the circumbinary disk remain stable within the 10% fluctuation previously established ($T_{\mathrm{in_{cb}}} \sim 300$, $q_{\mathrm{cb}} \sim 0.4$, $R_{\mathrm{in_{cb}}} \sim 17.5$ AU and $\Sigma_{\mathrm{in_{cb}}} \sim 0.1$ kg m^{-2}).

2. Although the value of the emissivity factor and the radius of the new hot component hardly vary in comparison to the above reported ($\epsilon_{\mathrm{dc}} \sim 0.4$ and $R_{\mathrm{out_{dc}}} \sim 0.15$ AU), for some of the tests its temperature decreases up to $\sim$500 K. I explain such quantity in terms of Eq. 3.36 and the inverse relation of the flux to the distance of the object. In order to keep the same flux contribution of the disk, capable of reproducing the SED in near-IR wavelengths, but at a shorter distance, it is also necessary to reduce the temperature alleged in the Planck function of the numerator. Obviously, a lower temperature brings to discussion the geometry and composition of the dust particles forming the disk. Whereas higher temperatures in the range of $\sim$1800–2000 K can be reached by a layout of carbon-evolved grains, lower temperatures contemplate the existence of silicate grains due to their lowest evaporation temperature. Nevertheless, I acknowledge that the study of the mineralogy of the source detected through MIDI observations lies beyond the outlook of my thesis. I commit such scrutiny to the soon-to-come high-angular resolution data planned with modern instruments and other techniques and facilities.

3. The freshly determined coordinates in the projected plane still preferentially situate the hot dusty component in the southern region of the central stellar pair. However, in comparison to the reported area ($\alpha_{\mathrm{dc}} = -1.78 \pm 29$ mas, $\beta_{\mathrm{dc}} = 10 \pm 37$ mas), from test-to-test the updated values depict a more spread possible site where the detected near-IR source may lie. As debated in section 5.1, the precise morphology

[2]Website: `http://sci.esa.int/gaia/`

and location of the detected hot emission has to be probed with dedicated near-IR interferometry and imaging techniques. This investigation in the mid-IR limits itself to the detection and report on the existence of an additional component inside the circumbinary cavity of V892 Tau, as it is restricted by only N-band measurements and modelling of interferometric data based on axisymmetric morphologies.

4. The performed tests do not improve the χ^2-values summarized in my investigation. Nonetheless, from the deliberation on the validity of χ^2-fitting presented in section 5.1, they can be well contemplated as adequate. However, the closer proximity to $\chi^2 = 1$ of the here accepted models endorses the preceding analysis.

5.4 Mid-IR study of the T Tauri object AS 209

AS 209, also known as V1121 Oph, is a single T Tauri object located at a distance $d = 130$ pc in the Ophiuchus star-forming region, with an age of 0.5–1 Myr [Natta et al., 2006]. This source has a stellar mass $M_\star = 0.9$ $M_\odot$, a spectral type K5 and luminosity of $L_\star = 1.5$ $L_\odot$ [Tazzari et al., 2016].

The protoplanetary disk around AS209 has been recently resolved with high-angular resolution ALMA 1.3 mm dust continuum observations [Fedele et al., 2018]. They have shown that a main central core is surrounded by two prominent rings of radii 75 AU and 130 AU (Fig. 5.2). The rings are separated by two gaps with different widths and depths at 62 AU and 103 AU. Supposedly, the inner gap is filled with millimetre grains while the outer gap is largely devoid of dust. The origin of the outer gap is attributed to the presence of a giant planet of $\sim$0.7 $M_{\rm Saturn}$ at 95 AU from the star[3]. Although the same planet may explain the opening of the inner gap by dynamical interactions with the disk, alternative scenarios point to the presence of another less massive planet in the inner region of the system.

The initial steps to investigate the central mid-IR emission of AS209 have been taken by reducing and calibrating MIDI interferometric data obtained during two observing runs in 2014 (Table 5.2). The instrumental and calibrated mid-IR visibilities obtained with EWS are plotted in Fig. 5.3. One snapshot of the science source was acquired on the first run, and two on the second run. The calibration of each of them with all the available calibrators registered on one night allows to monitor the long-term variability of the interferometric transfer function over the given night.

Table 5.2: Journal of observations of AS209 and its photometric and interferometric calibrator HD151011. The flux at 10 μm and the diameter of the calibrator used for the calibration preocess is 11.5272 Jy and 2.77 mas, respectively.

Date [dd-mm-yyyy]	Object	UT [hh:mm]	Baseline	PBL [m]	PBLA [°]
16-04-2014	HD151011	09:07	U3-U4	59.20	118.55
	HD151011	09:43	U3-U4	56.20	123.30
	AS209	09:57	U3-U4	53.82	122.60
18-06-2014	HD151011	03:53	U1-U3	102.26	33.50
	AS209	04:14	U1-U3	102.07	35.25
	AS209	04:26	U1-U3	102.29	36.15
	HD151011	04:39	U1-U3	102.27	37.40

[3] $1\ M_{\rm Saturn} = 95.16\ M_\oplus = 5.683 \times 10^{26}$ kg

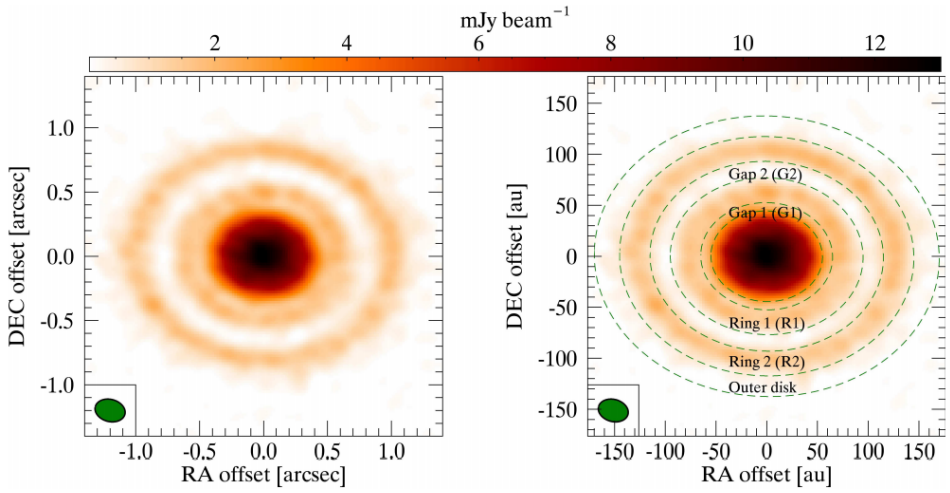

Figure 5.2: Image of AS209 at the 1.3 mm dust continuum with ALMA. The right picture remarks the two concentrical rings and the two cavities between them. [Credit: Fedele et al. [2018]. Reproduced with permission ©ESO.]

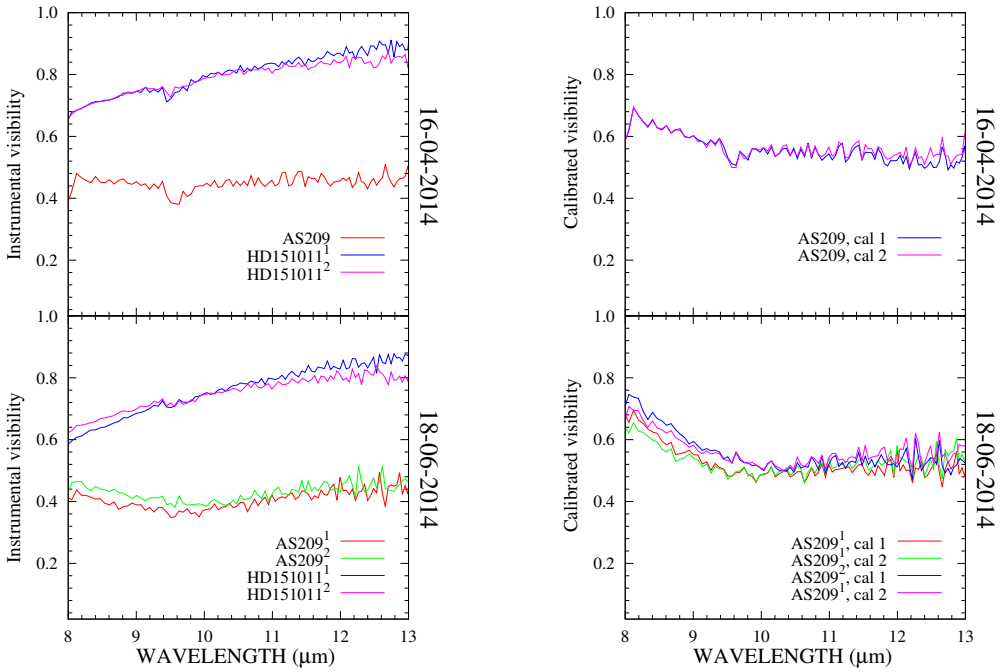

Figure 5.3: N-band instrumental (left) and calibrated (right) visibilities of AS209 obtained with EWS. The science source and its calibrator are plotted in correspondence with Table 5.2.

The analysis of the available data with the same temperature-gradient method developed for the analysis of V892 Tau will allow me to complement the (sub)millimetre observations and compare the properties (e.g. elongation and inclination) of the inner mid-IR and outer sub-mm disk regions. Moreover, this oncoming investigation will study in detail the inner dust geometry and properties (radial temperature, density and brightness profile, dust composition, grain size) along with the dust migration at work in the first few AUs of the disk. This region is precisely the planet-forming region that the ALMA measurements have failed to assess, and where the grounds for the inner gap opening are still intriguing.

Since the temperature range (100–1000 K) is similar to the one studied in V892 Tau, the semi-physical temperature-gradient model used for this investigation can be applied with confidence. Furthermore, the multicomponent structure of V892 Tau makes possible to adapt the existing numerical routine to cases such as the one of AS209. Then, these preliminary results of the geometric and temperature-gradient modelling can be used for more complex radiative transfer approximations [e.g. with RADMC-3D; Dullemond and Dominik, 2004b].

Glossary

ALMA Atacama Large Millimetre/submillimetre Array. 41, 51, 58, 143, 144, 158

AMBER Astronomical Multi-BEam combineR. 53, 55, 58, 69

AO adaptive optics. 57, 153

ATs Auxiliary Telescopes. 52, 53, 55, 58, 82, 140, 154

CB circumbinary. 33–35, 78, 138, 139, 151, 154

CIAO Coudé Infrared Adaptive Optics. 52, 55

CS circumstellar. 33–35, 138, 139

DSS Digitized Sky Survey. 73, 74, 154

ESO European Southern Observatory. 51, 82, 139

EWS Expert WorkStation. 84, 87–90, 95, 143, 144, 154, 158

FINITO Fringe-tracking Instrument of NIce and TOrino. 52, 53, 55, 58

GA Genetic algorithm. 99–101

GMCs giant molecular clouds. 5, 6, 8, 149

HAeBe Herbig Ae/Be stars. 15, 17, 19, 26, 27, 35, 38, 73, 75–79, 91, 137–139, 150

IMF initial mass function. 14, 15

IRAC Infrared Array Camera. 73, 74, 154

ISO Infrared Space Observatory. 20, 77, 91, 101, 135, 154, 155

MACAO Multi Application Curvature Adaptive Optics. 52, 54, 57, 80, 152, 153

MAGIX Modelling and Analysis Generic Interface for eXternal numerical codes. 92, 97, 99–104, 106, 107, 116, 117, 125, 133, 135, 142, 155, 158, 159

MATISSE Multi-AperTure mid-Infrared SpectroScopic Experiment. 55, 141

MCMC Markov chain Monte Carlo. 99, 101–103, 117, 126, 128, 137, 158, 159

MIA MIDI Interactive Analysis. 84–86, 89, 154

MIDI MID-infrared Interferometric instrument. 53–56, 58, 59, 70, 71, 76, 77, 80–82, 84, 85, 88, 89, 91–95, 97–99, 101, 104, 106–108, 116, 117, 125–127, 135, 136, 141–143, 152, 155–157, 159

MS main sequence. 17, 76

NACO Naos-Conica. 138–140

NASA National Aeronautics and Space Administration. 20, 91

OPD optical path difference. 47–50, 54, 56, 58, 81, 85, 88, 140, 152

PAHs Polycyclic Aromatic Hydrocarbons. 37, 76, 77, 79, 91, 154

PIONIER Precision Integrated-Optics Near-infrared Imaging ExpeRiment. 52, 55, 59

PMS pre-main sequence. 11, 15, 17, 18, 20, 26, 27, 31, 33, 37, 40, 76, 96, 97, 138, 141, 150, 155

SED spectral energy distribution. 12, 14, 15, 20, 25, 26, 29–31, 60–62, 64, 65, 73, 78, 92–94, 96, 97, 99, 101, 104, 106–108, 115, 116, 125–127, 135–139, 142, 151, 153–157, 159

SPHERE Spectro-Polarimetric High-contrast Exoplanet REsearch instrument. 38, 40

STRAP System for Tip/tilt Removal with Avalanche Photodiodes. 52, 80

SWS short wavelength spectrometer. 77, 91, 101, 154, 155

TTS T Tauri stars. 15, 17, 26, 27, 31, 35, 38, 39, 60, 73, 74, 76, 151, 154

UTs Unit Telescopes. 51–53, 55, 56, 58, 82, 140, 154

VLTI Very Large Telescope Interferometer. 51–59, 81, 140, 141, 152, 153, 159

YSOs Young stellar objects. 12, 14, 15, 18, 19, 23, 24, 27, 38, 51, 60, 61, 140, 150

ZAMS zero age main sequence. 11, 12, 97, 149, 155

List of Figures

List of Tables

Bibliography

B. Acke, J. Bouwman, A. Juhász, T. Henning, M. E. van den Ancker, G. Meeus, A. G. G. M. Tielens, and L. B. F. M. Waters. Spitzer's View on Aromatic and Aliphatic Hydrocarbon Emission in Herbig Ae Stars. *ApJ*, 718:558–574, July 2010. doi:10.1088/0004-637X/718/1/558.

F. C. Adams and F. H. Shu. Ambipolar Diffusion In Molecular Cloud Cores and the Gravomagneto Catastrophe. *ApJ*, 671:497–517, Dec. 2007. doi:10.1086/522925.

R. L. Akeson, M. R. Swain, and M. M. Colavita. Differential phase technique with the Keck Interferometer. In P. Léna and A. Quirrenbach, editors, *Interferometry in Optical Astronomy*, volume 4006 of *SPIE*, pages 321–327, July 2000. doi:10.1117/12.390222.

S. H. P. Alencar, C. H. F. Melo, C. P. Dullemond, J. Andersen, C. Batalha, L. P. R. Vaz, and R. D. Mathieu. The pre-main sequence spectroscopic binary AK Scorpii revisited. *A&A*, 409:1037–1053, Oct. 2003. doi:10.1051/0004-6361:20031229.

Y. Alibert, C. Mordasini, W. Benz, and C. Winisdoerffer. Models of giant planet formation with migration and disc evolution. *A&A*, 434:343–353, Apr. 2005. doi:10.1051/0004-6361:20042032.

P. R. Allen. Star Formation via the Little Guy: A Bayesian Study of Ultracool Dwarf Imaging Surveys for Companions. *ApJ*, 668:492–506, Oct. 2007. doi:10.1086/521207.

P. Andre and T. Montmerle. From T Tauri stars to protostars: Circumstellar material and young stellar objects in the rho Ophiuchi cloud. *ApJ*, 420:837–862, Jan. 1994. doi:10.1086/173608.

P. Andre, D. Ward-Thompson, and M. Barsony. Submillimeter continuum observations of Rho Ophiuchi A - The candidate protostar VLA 1623 and prestellar clumps. *ApJ*, 406: 122–141, Mar. 1993. doi:10.1086/172425.

P. André, F. Motte, A. Bacmann, and A. Belloche. The Initial Conditions of Star Formation: Observations of Prestellar Cores and Young Protostars. In T. Nakamoto, editor, *Star Formation 1999*, pages 145–152, Dec. 1999.

P. Andre, D. Ward-Thompson, and M. Barsony. From Prestellar Cores to Protostars: the Initial Conditions of Star Formation. *Protostars and Planets IV*, page 59, May 2000.

S. M. Andrews and J. P. Williams. Circumstellar Dust Disks in Taurus-Auriga: The Submillimeter Perspective. *ApJ*, 631:1134–1160, Oct. 2005. doi:10.1086/432712.

S. M. Andrews and J. P. Williams. A Submillimeter View of Circumstellar Dust Disks in ρ Ophiuchi. *ApJ*, 671:1800–1812, Dec. 2007a. doi:10.1086/522885.

S. M. Andrews and J. P. Williams. High-Resolution Submillimeter Constraints on Circumstellar Disk Structure. *ApJ*, 659:705–728, Apr. 2007b. doi:10.1086/511741.

S. M. Andrews, D. J. Wilner, A. M. Hughes, C. Qi, and C. P. Dullemond. Protoplanetary Disk Structures in Ophiuchus. *ApJ*, 700:1502–1523, Aug. 2009. doi:10.1088/0004-637X/700/2/1502.

S. M. Andrews, D. J. Wilner, A. M. Hughes, C. Qi, and C. P. Dullemond. Protoplanetary Disk Structures in Ophiuchus. II. Extension to Fainter Sources. *ApJ*, 723:1241–1254, Nov. 2010. doi:10.1088/0004-637X/723/2/1241.

S. M. Andrews, K. A. Rosenfeld, A. L. Kraus, and D. J. Wilner. The Mass Dependence between Protoplanetary Disks and their Stellar Hosts. *ApJ*, 771:129, July 2013. doi:10.1088/0004-637X/771/2/129.

F. Anthonioz, F. Ménard, C. Pinte, J.-B. Le Bouquin, M. Benisty, W.-F. Thi, O. Absil, G. Duchêne, J.-C. Augereau, J.-P. Berger, S. Casassus, G. Duvert, B. Lazareff, F. Malbet, R. Millan-Gabet, M. R. Schreiber, W. Traub, and G. Zins. The VLTI/PIONIER near-infrared interferometric survey of southern T Tauri stars. I. First results. *A&A*, 574:A41, Jan. 2015. doi:10.1051/0004-6361/201424520.

P. J. Armitage. *Astrophysics of Planet Formation*. 2010.

P. Artymowicz and S. H. Lubow. Dynamics of binary-disk interaction. 1: Resonances and disk gap sizes. *ApJ*, 421:651–667, Feb. 1994. doi:10.1086/173679.

P. Artymowicz and S. H. Lubow. Mass Flow through Gaps in Circumbinary Disks. *ApJL*, 467:L77, Aug. 1996. doi:10.1086/310200.

P. Artymowicz, C. J. Clarke, S. H. Lubow, and J. E. Pringle. The effect of an external disk on the orbital elements of a central binary. *ApJL*, 370:L35–L38, Mar. 1991. doi:10.1086/185971.

H. Avenhaus, S. P. Quanz, H. M. Schmid, M. R. Meyer, A. Garufi, S. Wolf, and C. Dominik. Structures in the Protoplanetary Disk of HD142527 Seen in Polarized Scattered Light. *ApJ*, 781:87, Feb. 2014. doi:10.1088/0004-637X/781/2/87.

H. Avenhaus, S. P. Quanz, A. Garufi, S. Perez, S. Casassus, C. Pinte, G. H.-M. Bertrang, C. Caceres, M. Benisty, and C. Dominik. Disks around T Tauri Stars with SPHERE (DARTTS-S). I. SPHERE/IRDIS Polarimetric Imaging of Eight Prominent T Tauri Disks. *ApJ*, 863:44, Aug. 2018. doi:10.3847/1538-4357/aab846.

X.-N. Bai. Towards a Global Evolutionary Model of Protoplanetary Disks. *ApJ*, 821:80, Apr. 2016. doi:10.3847/0004-637X/821/2/80.

X.-N. Bai and J. M. Stone. Wind-driven Accretion in Protoplanetary Disks. I. Suppression of the Magnetorotational Instability and Launching of the Magnetocentrifugal Wind. *ApJ*, 769:76, May 2013. doi:10.1088/0004-637X/769/1/76.

D. Baines, R. D. Oudmaijer, J. M. Porter, and M. Pozzo. On the binarity of Herbig Ae/Be stars. *MNRAS*, 367:737–753, Apr. 2006. doi:10.1111/j.1365-2966.2006.10006.x.

S. A. Balbus and J. F. Hawley. Instability, turbulence, and enhanced transport in accretion disks. *Reviews of Modern Physics*, 70:1–53, Jan. 1998. doi:10.1103/RevModPhys.70.1.

C. Baldovin-Saavedra, M. Audard, A. Carmona, M. Güdel, K. Briggs, L. M. Rebull, S. L. Skinner, and B. Ercolano. On the origin of [Ne II] emission in young stars: mid-infrared and optical observations with the Very Large Telescope. *A&A*, 543:A30, July 2012. doi:10.1051/0004-6361/201118329.

J. Ballesteros-Paredes, R. S. Klessen, M.-M. Mac Low, and E. Vazquez-Semadeni. Molecular Cloud Turbulence and Star Formation. *Protostars and Planets V*, pages 63–80, 2007.

A. Bans and A. Königl. A Disk-wind Model for the Near-infrared Excess Emission in Protostars. *ApJ*, 758:100, Oct. 2012. doi:10.1088/0004-637X/758/2/100.

I. Baraffe and G. Chabrier. Effect of episodic accretion on the structure and the lithium depletion of low-mass stars and planet-hosting stars. *A&A*, 521:A44, Oct. 2010. doi:10.1051/0004-6361/201014979.

F. Baron. Image Reconstruction in Optical Interferometry: An Up-to-Date Overview. In H. M. J. Boffin, G. Hussain, J.-P. Berger, and L. Schmidtobreick, editors, *Astronomy at High Angular Resolution*, volume 439 of *Astrophysics and Space Science Library*, page 75, 2016. doi:10.1007/978-3-319-39739-9_5.

S. Basu and T. C. Mouschovias. Magnetic braking, ambipolar diffusion, and the formation of cloud cores and protostars. 1: Axisymmetric solutions. *ApJ*, 432:720–741, Sept. 1994. doi:10.1086/174611.

M. R. Bate. Predicting the properties of binary stellar systems: the evolution of accreting protobinary systems. *MNRAS*, 314:33–53, May 2000. doi:10.1046/j.1365-8711.2000.03333.x.

M. R. Bate. Stellar, brown dwarf and multiple star properties from a radiation hydrodynamical simulation of star cluster formation. *MNRAS*, 419:3115–3146, Feb. 2012. doi:10.1111/j.1365-2966.2011.19955.x.

M. R. Bate, I. A. Bonnell, and V. Bromm. The formation mechanism of brown dwarfs. *MNRAS*, 332:L65–L68, May 2002a. doi:10.1046/j.1365-8711.2002.05539.x.

M. R. Bate, I. A. Bonnell, and V. Bromm. The formation of close binary systems by dynamical interactions and orbital decay. *MNRAS*, 336:705–713, Nov. 2002b. doi:10.1046/j.1365-8711.2002.05775.x.

M. R. Bate, G. I. Ogilvie, S. H. Lubow, and J. E. Pringle. The excitation, propagation and dissipation of waves in accretion discs: the non-linear axisymmetric case. *MNRAS*, 332: 575–600, May 2002c. doi:10.1046/j.1365-8711.2002.05289.x.

M. R. Bate, I. A. Bonnell, and V. Bromm. The formation of a star cluster: predicting the properties of stars and brown dwarfs. *MNRAS*, 339:577–599, Mar. 2003. doi:10.1046/j.1365-8711.2003.06210.x.

A. H. Batten. *Binary and multiple systems of stars*. 1973.

S. V. W. Beckwith, A. I. Sargent, R. S. Chini, and R. Guesten. A survey for circumstellar disks around young stellar objects. *AJ*, 99:924–945, Mar. 1990. doi:10.1086/115385.

V. J. S. Béjar, B. Gauza, R. Rebolo, C. Álvarez, M. R. Zapatero Osorio, and L. Labadie. Mid-IR characterization of substellar companions with CanariCam. In *European Physical Journal Web of Conferences*, volume 101 of *European Physical Journal Web of Conferences*, page 06005, Sept. 2015. doi:10.1051/epjconf/201510106005.

A. Belloche, P. André, D. Despois, and S. Blinder. Molecular line study of the very young protostar IRAM 04191 in Taurus: infall, rotation, and outflow. *A&A*, 393:927–947, Oct. 2002. doi:10.1051/0004-6361:20021054.

M. Benisty, A. Juhasz, A. Boccaletti, H. Avenhaus, J. Milli, C. Thalmann, C. Dominik, P. Pinilla, E. Buenzli, A. Pohl, J.-L. Beuzit, T. Birnstiel, J. de Boer, M. Bonnefoy, G. Chauvin, V. Christiaens, A. Garufi, C. Grady, T. Henning, N. Huelamo, A. Isella, M. Langlois, F. Ménard, D. Mouillet, J. Olofsson, E. Pantin, C. Pinte, and L. Pueyo. Asymmetric features in the protoplanetary disk MWC 758. *A&A*, 578:L6, June 2015. doi:10.1051/0004-6361/201526011.

J. P. Berger and D. Segransan. An introduction to visibility modeling. *New AR*, 51:576–582, Oct. 2007. doi:10.1016/j.newar.2007.06.003.

F. Berrilli, G. Corciulo, G. Ingrosso, D. Lorenzetti, B. Nisini, and F. Strafella. Infrared emission from dust structures surrounding Herbig Ae/Be stars. *ApJ*, 398:254–272, Oct. 1992. doi:10.1086/171853.

G. H.-M. Bertrang, H. Avenhaus, S. Casassus, M. Montesinos, F. Kirchschlager, S. Perez, L. Cieza, and S. Wolf. HD 169142 in the eyes of ZIMPOL/SPHERE. *MNRAS*, 474: 5105–5113, Mar. 2018. doi:10.1093/mnras/stx3052.

J.-L. Beuzit, D. Mouillet, B. R. Oppenheimer, and J. D. Monnier. Direct Detection of Exoplanets. *Protostars and Planets V*, pages 717–732, 2007.

J.-L. Beuzit, M. Feldt, K. Dohlen, D. Mouillet, P. Puget, F. Wildi, L. Abe, J. Antichi, A. Baruffolo, P. Baudoz, A. Boccaletti, M. Carbillet, J. Charton, R. Claudi, M. Downing, C. Fabron, P. Feautrier, E. Fedrigo, T. Fusco, J.-L. Gach, R. Gratton, T. Henning, N. Hubin, F. Joos, M. Kasper, M. Langlois, R. Lenzen, C. Moutou, A. Pavlov, C. Petit, J. Pragt, P. Rabou, F. Rigal, R. Roelfsema, G. Rousset, M. Saisse, H.-M. Schmid, E. Stadler, C. Thalmann, M. Turatto, S. Udry, F. Vakili, and R. Waters. SPHERE: a 'Planet Finder' instrument for the VLT. In *Ground-based and Airborne Instrumentation for Astronomy II*, volume 7014 of *SPIE*, page 701418, July 2008. doi:10.1117/12.790120.

B. Biller, S. Lacour, A. Juhász, M. Benisty, G. Chauvin, J. Olofsson, J.-U. Pott, A. Müller, A. Sicilia-Aguilar, M. Bonnefoy, P. Tuthill, P. Thebault, T. Henning, and A. Crida. A Likely Close-in Low-mass Stellar Companion to the Transitional Disk Star HD 142527. *ApJL*, 753:L38, July 2012. doi:10.1088/2041-8205/753/2/L38.

L. Blitz and J. P. Williams. Molecular Clouds. In C. J. Lada and N. D. Kylafis, editors, *NATO Advanced Science Institutes (ASI) Series C*, volume 540 of *NATO Advanced Science Institutes (ASI) Series C*, page 3, 1999.

J. M. Blondin. Tidally-driven transport in accretion disks in close binary systems. *New Astron*, 5:53–68, Mar. 2000. doi:10.1016/S1384-1076(00)00006-3.

P. Bodenheimer. Angular Momentum Evolution of Young Stars and Disks. *ARAA*, 33: 199–238, 1995. doi:10.1146/annurev.aa.33.090195.001215.

P. Bodenheimer, A. Burkert, R. I. Klein, and A. P. Boss. Multiple Fragmentation of Protostars. *Protostars and Planets IV*, page 675, May 2000.

C. Boersma, E. Peeters, N. L. Martín-Hernández, G. van der Wolk, A. P. Verhoeff, A. G. G. M. Tielens, L. B. F. M. Waters, and J. W. Pel. A spatial study of the mid-IR emission features in four Herbig Ae/Be stars. *A&A*, 502:175–187, July 2009. doi:10.1051/0004-6361/200911820.

H. M. J. Boffin. Spiral Waves in Accretion Discs - Theory. In H. M. J. Boffin, D. Steeghs, and J. Cuypers, editors, *Astrotomography, Indirect Imaging Methods in Observational Astronomy*, volume 573 of *Lecture Notes in Physics, Berlin Springer Verlag*, page 69, 2001.

M. Bonavita and S. Desidera. The frequency of planets in multiple systems. *A&A*, 468: 721–729, June 2007. doi:10.1051/0004-6361:20066671.

I. Bonnell and P. Bastien. A binary origin for FU Orionis stars. *ApJL*, 401:L31–L34, Dec. 1992. doi:10.1086/186663.

I. A. Bonnell. A New Binary Formation Mechanism. *MNRAS*, 269, Aug. 1994. doi:10.1093/mnras/269.3.837.

I. A. Bonnell and M. R. Bate. The Formation of Close Binary Systems. *MNRAS*, 271, Dec. 1994. doi:10.1093/mnras/271.4.999.

L. Bourgès, G. Mella, S. Lafrasse, and G. Duvert. ASPRO 2: Astronomical Software to PRepare Observations. Astrophysics Source Code Library, Oct. 2013.

J. Bouvier and P. Corporon. Herbig Ae/Be Visual Binaries. In H. Zinnecker and R. Mathieu, editors, *The Formation of Binary Stars*, volume 200 of *IAU Symposium*, page 155, 2001.

C. Braiding. *Star Formation and the Hall Effect*. PhD thesis, PhD Thesis, 2011, Oct. 2011.

E. Bressert, N. Bastian, R. Gutermuth, S. T. Megeath, L. Allen, N. J. Evans, II, L. M. Rebull, J. Hatchell, D. Johnstone, T. L. Bourke, L. A. Cieza, P. M. Harvey, B. Merin, T. P. Ray, and N. F. H. Tothill. The spatial distribution of star formation in the solar neighbourhood: do all stars form in dense clusters? *MNRAS*, 409:L54–L58, Nov. 2010. doi:10.1111/j.1745-3933.2010.00946.x.

R. Brunngräber and S. Wolf. Constraints on observing brightness asymmetries in protoplanetary disks at solar system scale. *A&A*, 611:A90, Apr. 2018. doi:10.1051/0004-6361/201731907.

R. Brunngräber, S. Wolf, T. Ratzka, and F. Ober. DR Tauri: Temporal variability of the brightness distribution in the potential planet-forming region. *A&A*, 585:A100, Jan. 2016. doi:10.1051/0004-6361/201526691.

J. A. Cardelli, G. C. Clayton, and J. S. Mathis. The relationship between infrared, optical, and ultraviolet extinction. *ApJ*, 345:245–256, Oct. 1989. doi:10.1086/167900.

A. Carmona, C. Pinte, W. F. Thi, M. Benisty, F. Ménard, C. Grady, I. Kamp, P. Woitke, J. Olofsson, A. Roberge, S. Brittain, G. Duchêne, G. Meeus, C. Martin-Zaïdi, B. Dent, J. B. Le Bouquin, and J. P. Berger. Constraining the structure of the transition disk HD 135344B (SAO 206462) by simultaneous modeling of multiwavelength gas and dust observations. *A&A*, 567:A51, July 2014. doi:10.1051/0004-6361/201322534.

S. Casassus, G. van der Plas, S. P. M, W. R. F. Dent, E. Fomalont, J. Hagelberg, A. Hales, A. Jordán, D. Mawet, F. Ménard, A. Wootten, D. Wilner, A. M. Hughes, M. R. Schreiber, J. H. Girard, B. Ercolano, H. Canovas, P. E. Román, and V. Salinas. Flows of gas through a protoplanetary gap. *Nature*, 493:191–194, Jan. 2013. doi:10.1038/nature11769.

S. Chandrasekhar and E. Fermi. Problems of Gravitational Stability in the Presence of a Magnetic Field. *ApJ*, 118:116, July 1953. doi:10.1086/145732.

G. Chauvin, A.-M. Lagrange, H. Beust, T. Fusco, D. Mouillet, F. Lacombe, P. Pujet, G. Rousset, E. Gendron, J.-M. Conan, D. Bauduin, D. Rouan, W. Brandner, R. Lenzen, N. Hubin, and M. Hartung. VLT/NACO adaptive optics imaging of the TY CrA system. A fourth stellar component candidate detected. *A&A*, 406:L51–L54, July 2003. doi:10.1051/0004-6361:20030554.

C. H. Chen, B. A. Sargent, C. Bohac, K. H. Kim, E. Leibensperger, M. Jura, J. Najita, W. J. Forrest, D. M. Watson, G. C. Sloan, and L. D. Keller. Spitzer IRS Spectroscopy of IRAS-discovered Debris Disks. *ApJS*, 166:351–377, Sept. 2006. doi:10.1086/505751.

O. Chesneau. MIDI: Obtaining and analysing interferometric data in the mid-infrared. *New AR*, 51:666–681, Oct. 2007. doi:10.1016/j.newar.2007.06.009.

E. I. Chiang and P. Goldreich. Spectral Energy Distributions of T Tauri Stars with Passive Circumstellar Disks. *ApJ*, 490:368–376, Nov. 1997. doi:10.1086/304869.

R. Chini, V. H. Hoffmeister, A. Nasseri, O. Stahl, and H. Zinnecker. A spectroscopic survey on the multiplicity of high-mass stars. *MNRAS*, 424:1925–1929, Aug. 2012. doi:10.1111/j.1365-2966.2012.21317.x.

L. A. Cieza, D. L. Padgett, L. E. Allen, C. E. McCabe, T. Y. Brooke, S. J. Carey, N. L. Chapman, M. Fukagawa, T. L. Huard, A. Noriga-Crespo, D. E. Peterson, and L. M. Rebull. Primordial Circumstellar Disks in Binary Systems: Evidence for Reduced Lifetimes. *ApJL*, 696:L84–L88, May 2009. doi:10.1088/0004-637X/696/1/L84.

L. A. Cieza, M. R. Schreiber, G. A. Romero, M. D. Mora, B. Merin, J. J. Swift, M. Orellana, J. P. Williams, P. M. Harvey, and N. J. Evans, II. The Nature of Transition Circumstellar Disks. I. The Ophiuchus Molecular Cloud. *ApJ*, 712:925-941, Apr. 2010. doi:10.1088/0004-637X/712/2/925.

L. A. Cieza, S. Lacour, M. R. Schreiber, S. Casassus, A. Jordán, G. S. Mathews, H. Cánovas, F. Ménard, A. L. Kraus, S. Pérez, P. Tuthill, and M. J. Ireland. Sparse Aperture Masking Observations of the FL Cha Pre-transitional Disk. *ApJL*, 762:L12, Jan. 2013. doi:10.1088/2041-8205/762/1/L12.

M. Cohen and L. V. Kuhi. Observational studies of pre-main-sequence evolution. *ApJS*, 41: 743–843, Dec. 1979. doi:10.1086/190641.

M. Cohen, R. G. Walker, B. Carter, P. Hammersley, M. Kidger, and K. Noguchi. Spectral Irradiance Calibration in the Infrared. X. A Self-Consistent Radiometric All-Sky Network of Absolutely Calibrated Stellar Spectra. *AJ*, 117:1864–1889, Apr. 1999. doi:10.1086/300813.

F. Comerón, B. Reipurth, H.-W. Yen, and M. S. Connelley. Binary energy source of the HH 250 outflow and its circumstellar environment. *A&A*, 612:A73, Apr. 2018. doi:10.1051/0004-6361/201730917.

B. Commerçon, P. Hennebelle, E. Audit, G. Chabrier, and R. Teyssier. Protostellar collapse: radiative and magnetic feedbacks on small-scale fragmentation. *A&A*, 510:L3, Feb. 2010. doi:10.1051/0004-6361/200913597.

C. R. Cowley, F. Castelli, and S. Hubrig. The Herbig Ae SB2 system HD 104237. *MNRAS*, 431:3485–3493, June 2013. doi:10.1093/mnras/stt430.

G. Csépány, M. van den Ancker, P. Ábrahám, R. Köhler, W. Brandner, F. Hormuth, and H. Hiss. Multi-epoch observations with high spatial resolution of multiple T Tauri systems. *A&A*, 603:A74, July 2017. doi:10.1051/0004-6361/201527494.

T. Currie, S. J. Kenyon, Z. Balog, G. Rieke, A. Bragg, and B. Bromley. The Rise and Fall of Debris Disks: MIPS Observations of h and χ Persei and the Evolution of Mid-IR Emission from Planet Formation. *ApJ*, 672:558-574, Jan. 2008. doi:10.1086/523698.

S. Daemgen, M. G. Petr-Gotzens, S. Correia, P. S. Teixeira, W. Brandner, W. Kley, and H. Zinnecker. Protoplanetary disk evolution and stellar parameters of T Tauri binaries in Chamaeleon I. *A&A*, 554:A43, June 2013. doi:10.1051/0004-6361/201321220.

P. D'Alessio, N. Calvet, L. Hartmann, R. Franco-Hernández, and H. Servín. Effects of Dust Growth and Settling in T Tauri Disks. *ApJ*, 638:314–335, Feb. 2006. doi:10.1086/498861.

R. J. De Rosa, J. Patience, P. A. Wilson, A. Schneider, S. J. Wiktorowicz, A. Vigan, C. Marois, I. Song, B. Macintosh, J. R. Graham, R. Doyon, M. S. Bessell, S. Thomas, and O. Lai. The VAST Survey - III. The multiplicity of A-type stars within 75 pc. *MNRAS*, 437: 1216–1240, Jan. 2014. doi:10.1093/mnras/stt1932.

E. Di Folco, A. Dutrey, J.-B. Le Bouquin, S. Lacour, J.-P. Berger, R. Köhler, S. Guilloteau, V. Piétu, J. Bary, T. Beck, H. Beust, and E. Pantin. GG Tauri: the fifth element. *A&A*, 565: L2, May 2014. doi:10.1051/0004-6361/201423675.

R. Dong. The Effects of Self-shadowing by a Puffed-up Inner Rim in Scattered Light Images of Protoplanetary Disks. *ApJ*, 810:6, Sept. 2015. doi:10.1088/0004-637X/810/1/6.

R. Dong, J. R. Najita, and S. Brittain. Spiral Arms in Disks: Planets or Gravitational Instability? *ArXiv e-prints*, June 2018.

G. Duchêne. Binary fraction in low-mass star forming regions: a reexamination of the possible excesses and implications. *A&A*, 341:547–552, Jan. 1999.

G. Duchêne. Planet Formation in Binary Systems: A Separation-Dependent Mechanism? *ApJL*, 709:L114–L118, Feb. 2010. doi:10.1088/2041-8205/709/2/L114.

G. Duchêne. Herbig AeBe stars: multiplicity and consequences. *Ap&SS*, 355:291–301, Feb. 2015. doi:10.1007/s10509-014-2173-7.

G. Duchêne and A. Kraus. Stellar Multiplicity. *ARAA*, 51:269–310, Aug. 2013. doi:10.1146/annurev-astro-081710-102602.

C. P. Dullemond and C. Dominik. The effect of dust settling on the appearance of protoplanetary disks. *A&A*, 421:1075–1086, July 2004a. doi:10.1051/0004-6361:20040284.

C. P. Dullemond and C. Dominik. Flaring vs. self-shadowed disks: The SEDs of Herbig Ae/Be stars. *A&A*, 417:159–168, Apr. 2004b. doi:10.1051/0004-6361:20031768.

C. P. Dullemond and C. Dominik. Dust coagulation in protoplanetary disks: A rapid depletion of small grains. *A&A*, 434:971–986, May 2005. doi:10.1051/0004-6361:20042080.

C. P. Dullemond and J. D. Monnier. The Inner Regions of Protoplanetary Disks. *ARAA*, 48: 205–239, Sept. 2010. doi:10.1146/annurev-astro-081309-130932.

C. P. Dullemond, C. Dominik, and A. Natta. Passive Irradiated Circumstellar Disks with an Inner Hole. *ApJ*, 560:957–969, Oct. 2001. doi:10.1086/323057.

C. P. Dullemond, A. Juhasz, A. Pohl, F. Sereshti, R. Shetty, T. Peters, B. Commercon, and M. Flock. RADMC-3D: A multi-purpose radiative transfer tool. Astrophysics Source Code Library, Feb. 2012.

A. Duquennoy and M. Mayor. Multiplicity among solar-type stars in the solar neighbourhood. II - Distribution of the orbital elements in an unbiased sample. *A&A*, 248:485–524, Aug. 1991.

A. Dutrey, S. Guilloteau, G. Duvert, L. Prato, M. Simon, K. Schuster, and F. Menard. Dust and gas distribution around T Tauri stars in Taurus-Auriga. I. Interferometric 2.7mm continuum and ˆ13ˆCO J=1-0 observations. *A&A*, 309:493–504, May 1996.

A. Dutrey, E. di Folco, S. Guilloteau, Y. Boehler, J. Bary, T. Beck, H. Beust, E. Chapillon, F. Gueth, J.-M. Huré, A. Pierens, V. Piétu, M. Simon, and Y.-W. Tang. Possible planet formation in the young, low-mass, multiple stellar system GG Tau A. *Nature*, 514: 600–602, Oct. 2014. doi:10.1038/nature13822.

A. Dutrey, E. Di Folco, T. Beck, and S. Guilloteau. GG Tau: the ringworld and beyond. Mass accretion and planetary formation in young multiple stellar systems. *A&ARv*, 24:5, Jan. 2016. doi:10.1007/s00159-015-0091-5.

J. A. Eisner, E. I. Chiang, B. F. Lane, and R. L. Akeson. Spectrally Dispersed K-Band Interferometric Observations of Herbig Ae/Be Sources: Inner Disk Temperature Profiles. *ApJ*, 657:347–358, Mar. 2007a. doi:10.1086/510833.

J. A. Eisner, L. A. Hillenbrand, R. J. White, J. S. Bloom, R. L. Akeson, and C. H. Blake. Near-Infrared Interferometric, Spectroscopic, and Photometric Monitoring of T Tauri Inner Disks. *ApJ*, 669:1072–1084, Nov. 2007b. doi:10.1086/521874.

J. A. Eisner, J. R. Graham, R. L. Akeson, and J. Najita. Spatially Resolved Spectroscopy of Sub-AU-Sized Regions of T Tauri and Herbig Ae/Be Disks. *ApJ*, 692:309–323, Feb. 2009. doi:10.1088/0004-637X/692/1/309.

J. H. Elias. A study of the Taurus dark cloud complex. *ApJ*, 224:857–872, Sept. 1978. doi:10.1086/156436.

B. G. Elmegreen. Formation of interstellar clouds and structure. In E. H. Levy and J. I. Lunine, editors, *Protostars and Planets III*, pages 97–124, 1993.

B. Ercolano and I. Pascucci. The dispersal of planet-forming discs: theory confronts observations. *Royal Society Open Science*, 4:170114, Apr. 2017. doi:10.1098/rsos.170114.

N. Evans, N. Calvet, L. Cieza, J. Forbrich, L. Hillenbrand, C. Lada, B. Merín, S. Strom, and D. Watson. The Diskionary: A Glossary of Terms Commonly Used for Disks and Related Objects, First Edition. *ArXiv e-prints*, Jan. 2009.

N. J. Evans, II. Physical Conditions in Regions of Star Formation. *ARAA*, 37:311–362, 1999. doi:10.1146/annurev.astro.37.1.311.

D. M. Faes, A. C. Carciofi, T. Rivinius, S. Štefl, D. Baade, and A. Domiciano de Souza. Differential interferometric phases at high spectral resolution as a sensitive physical diagnostic of circumstellar disks. *A&A*, 555:A76, July 2013. doi:10.1051/0004-6361/201321313.

J. R. Fairlamb, R. D. Oudmaijer, I. Mendigutía, J. D. Ilee, and M. E. van den Ancker. A spectroscopic survey of Herbig Ae/Be stars with X-shooter - I. Stellar parameters and accretion rates. *MNRAS*, 453:976–1001, Oct. 2015. doi:10.1093/mnras/stv1576.

M. Fang, R. van Boekel, J. Bouwman, T. Henning, W. A. Lawson, and A. Sicilia-Aguilar. Young stars in ϵ Chamaleontis and their disks: disk evolution in sparse associations. *A&A*, 549:A15, Jan. 2013. doi:10.1051/0004-6361/201118528.

D. Fedele, M. Carney, M. R. Hogerheijde, C. Walsh, A. Miotello, P. Klaassen, S. Bruderer, T. Henning, and E. F. van Dishoeck. ALMA unveils rings and gaps in the protoplanetary system ¡ASTROBJ¿HD 169142¡/ASTROBJ¿: signatures of two giant protoplanets. *A&A*, 600:A72, Apr. 2017. doi:10.1051/0004-6361/201629860.

D. Fedele, M. Tazzari, R. Booth, L. Testi, C. J. Clarke, I. Pascucci, A. Kospal, D. Semenov, S. Bruderer, T. Henning, and R. Teague. ALMA continuum observations of the protoplanetary disk AS 209. Evidence of multiple gaps opened by a single planet. *A&A*, 610:A24, Feb. 2018. doi:10.1051/0004-6361/201731978.

G. B. Field. Conditions in collapsing clouds. In T. Gehrels and M. S. Matthews, editors, *IAU Colloq. 52: Protostars and Planets*, pages 243–264, 1978.

D. A. Fischer and G. W. Marcy. Multiplicity among M dwarfs. *ApJ*, 396:178–194, Sept. 1992. doi:10.1086/171708.

M. Fukagawa, M. Hayashi, M. Tamura, Y. Itoh, S. S. Hayashi, Y. Oasa, T. Takeuchi, J.-i. Morino, K. Murakawa, S. Oya, T. Yamashita, H. Suto, S. Mayama, T. Naoi, M. Ishii, T.-S. Pyo, T. Nishikawa, N. Takato, T. Usuda, H. Ando, M. Iye, S. M. Miyama, and N. Kaifu. Spiral Structure in the Circumstellar Disk around AB Aurigae. *ApJL*, 605:L53–L56, Apr. 2004. doi:10.1086/420699.

M. Fukagawa, M. Tamura, Y. Itoh, T. Kudo, Y. Imaeda, Y. Oasa, S. S. Hayashi, and M. Hayashi. Near-Infrared Images of Protoplanetary Disk Surrounding HD 142527. *ApJL*, 636:L153–L156, Jan. 2006. doi:10.1086/500128.

Y. Fukui, T. Iwata, A. Mizuno, J. Bally, and A. P. Lane. Molecular outflows. In E. H. Levy and J. I. Lunine, editors, *Protostars and Planets III*, pages 603–639, 1993.

E. Furlan, L. Hartmann, N. Calvet, P. D'Alessio, R. Franco-Hernández, W. J. Forrest, D. M. Watson, K. I. Uchida, B. Sargent, J. D. Green, L. D. Keller, and T. L. Herter. A Survey and Analysis of Spitzer Infrared Spectrograph Spectra of T Tauri Stars in Taurus. *ApJS*, 165:568–605, Aug. 2006. doi:10.1086/505468.

E. Furlan, D. M. Watson, M. K. McClure, P. Manoj, C. Espaillat, P. D'Alessio, N. Calvet, K. H. Kim, B. A. Sargent, W. J. Forrest, and L. Hartmann. Disk Evolution in the Three Nearby Star-forming Regions of Taurus, Chamaeleon, and Ophiuchus. *ApJ*, 703:1964–1983, Oct. 2009. doi:10.1088/0004-637X/703/2/1964.

Gaia Collaboration, A. G. A. Brown, A. Vallenari, T. Prusti, J. H. J. de Bruijne, C. Babusiaux, and C. A. L. Bailer-Jones. Gaia Data Release 2. Summary of the contents and survey properties. *ArXiv e-prints*, Apr. 2018.

C. F. Gammie. Nonlinear Outcome of Gravitational Instability in Cooling, Gaseous Disks. *ApJ*, 553:174–183, May 2001. doi:10.1086/320631.

V. C. Geers, J.-C. Augereau, K. M. Pontoppidan, C. P. Dullemond, R. Visser, J. E. Kessler-Silacci, N. J. Evans, II, E. F. van Dishoeck, G. A. Blake, A. C. A. Boogert, J. M. Brown, F. Lahuis, and B. Merín. C2D Spitzer-IRS spectra of disks around T Tauri stars. II. PAH emission features. *A&A*, 459:545–556, Nov. 2006. doi:10.1051/0004-6361:20064830.

G. Giardino, F. Favata, G. Micela, and F. Reale. A large X-ray flare from the Herbig Ae star V892 Tau. *A&A*, 413:669–679, Jan. 2004. doi:10.1051/0004-6361:20034151.

A. Glindemann. *Principles of Stellar Interferometry*. 2011. doi:10.1007/978-3-642-15028-9.

A. Glindemann, J. Algomedo, R. Amestica, P. Ballester, B. Bauvir, E. Bugueño, S. Correia, F. Delgado, F. Delplancke, F. Derie, P. Duhoux, E. di Folco, A. Gennai, B. Gilli, P. Giordano, P. Gitton, S. Guisard, N. Housen, A. Huxley, P. Kervella, M. Kiekebusch, B. Koehler, S. Lévêque, A. Longinotti, S. Ménardi, S. Morel, F. Paresce, T. Phan Duc, A. Richichi, M. Schöller, M. Tarenghi, A. Wallander, M. Wittkowski, and R. Wilhelm. The VLTI and Its Subsystems. In *GENIE - DARWIN Workshop - Hunting for Planets*, volume 522 of *ESA Special Publication*, page 5.1, Mar. 2003.

A. I. Gómez de Castro, R. O. P. Loyd, K. France, A. Sytov, and D. Bisikalo. Protoplanetary Disk Shadowing by Gas Infalling onto the Young Star AK Sco. *ApJL*, 818:L17, Feb. 2016. doi:10.3847/2041-8205/818/1/L17.

K. D. Gordon, G. C. Clayton, K. A. Misselt, A. U. Landolt, and M. J. Wolff. A Quantitative Comparison of the Small Magellanic Cloud, Large Magellanic Cloud, and Milky Way Ultraviolet to Near-Infrared Extinction Curves. *ApJ*, 594:279–293, Sept. 2003. doi:10.1086/376774.

U. Gorti, C. P. Dullemond, and D. Hollenbach. Time Evolution of Viscous Circumstellar Disks due to Photoevaporation by Far-Ultraviolet, Extreme-Ultraviolet, and X-ray Radiation from the Central Star. *ApJ*, 705:1237–1251, Nov. 2009. doi:10.1088/0004-637X/705/2/1237.

M. Goto, T. Henning, A. Kouchi, H. Takami, Y. Hayano, T. Usuda, N. Takato, H. Terada, S. Oya, C. Jäger, and A. C. Andersen. Spatially Resolved 3 μm Spectroscopy of Elias 1: Origin of Diamonds in Protoplanetary Disks. *ApJ*, 693:610–616, Mar. 2009. doi:10.1088/0004-637X/693/1/610.

Gravity Collaboration, R. Abuter, M. Accardo, A. Amorim, N. Anugu, G. Ávila, N. Azouaoui, M. Benisty, J. P. Berger, N. Blind, H. Bonnet, P. Bourget, W. Brandner, R. Brast, A. Buron, L. Burtscher, F. Cassaing, F. Chapron, É. Choquet, Y. Clénet, C. Collin, V. Coudé Du Foresto, W. de Wit, P. T. de Zeeuw, C. Deen, F. Delplancke-Ströbele, R. Dembet, F. Derie, J. Dexter, G. Duvert, M. Ebert, A. Eckart, F. Eisenhauer, M. Esselborn, P. Fédou, G. Finger, P. Garcia, C. E. Garcia Dabo, R. Garcia Lopez, E. Gendron, R. Genzel, S. Gillessen, F. Gonte, P. Gordo, M. Grould, U. Grözinger, S. Guieu, P. Haguenauer, O. Hans, X. Haubois, M. Haug, F. Haussmann, T. Henning, S. Hippler, M. Horrobin,

A. Huber, Z. Hubert, N. Hubin, C. A. Hummel, G. Jakob, A. Janssen, L. Jochum, L. Jocou, A. Kaufer, S. Kellner, S. Kendrew, L. Kern, P. Kervella, M. Kiekebusch, R. Klein, Y. Kok, J. Kolb, M. Kulas, S. Lacour, V. Lapeyrère, B. Lazareff, J.-B. Le Bouquin, P. Lèna, R. Lenzen, S. Lévêque, M. Lippa, Y. Magnard, L. Mehrgan, M. Mellein, A. Mérand, J. Moreno-Ventas, T. Moulin, E. Müller, F. Müller, U. Neumann, S. Oberti, T. Ott, L. Pallanca, J. Panduro, L. Pasquini, T. Paumard, I. Percheron, K. Perraut, G. Perrin, A. Pflüger, O. Pfuhl, T. Phan Duc, P. M. Plewa, D. Popovic, S. Rabien, A. Ramírez, J. Ramos, C. Rau, M. Riquelme, R.-R. Rohloff, G. Rousset, J. Sanchez-Bermudez, S. Scheithauer, M. Schöller, N. Schuhler, J. Spyromilio, C. Straubmeier, E. Sturm, M. Suarez, K. R. W. Tristram, N. Ventura, F. Vincent, I. Waisberg, I. Wank, J. Weber, E. Wieprecht, M. Wiest, E. Wiezorrek, M. Wittkowski, J. Woillez, B. Wolff, S. Yazici, D. Ziegler, and G. Zins. First light for GRAVITY: Phase referencing optical interferometry for the Very Large Telescope Interferometer. *A&A*, 602:A94, June 2017a. doi:10.1051/0004-6361/201730838.

Gravity Collaboration, R. Garcia Lopez, K. Perraut, A. Caratti O Garatti, B. Lazareff, J. Sanchez-Bermudez, M. Benisty, C. Dougados, L. Labadie, W. Brandner, P. J. V. Garcia, T. Henning, T. P. Ray, R. Abuter, A. Amorim, N. Anugu, J. P. Berger, H. Bonnet, A. Buron, P. Caselli, Y. Clénet, V. Coudé Du Foresto, W. de Wit, C. Deen, F. Delplancke-Ströbele, J. Dexter, A. Eckart, F. Eisenhauer, C. E. Garcia Dabo, E. Gendron, R. Genzel, S. Gillessen, X. Haubois, M. Haug, F. Haussmann, S. Hippler, Z. Hubert, C. A. Hummel, M. Horrobin, L. Jocou, S. Kellner, P. Kervella, M. Kulas, J. Kolb, S. Lacour, J.-B. Le Bouquin, P. Léna, M. Lippa, A. Mérand, E. Müller, T. Ott, J. Panduro, T. Paumard, G. Perrin, O. Pfuhl, A. Ramirez, C. Rau, R.-R. Rohloff, G. Rousset, S. Scheithauer, M. Schöller, C. Straubmeier, E. Sturm, W. F. Thi, E. van Dishoeck, F. Vincent, I. Waisberg, I. Wank, E. Wieprecht, M. Wiest, E. Wiezorrek, J. Woillez, S. Yazici, and G. Zins. The wind and the magnetospheric accretion onto the T Tauri star S Coronae Australis at sub-au resolution. *A&A*, 608:A78, Dec. 2017b. doi:10.1051/0004-6361/201731058.

T. Greene. Protostars. *American Scientist*, 89:316, Aug. 2001. doi:10.1511/2001.4.316.

M. Güdel, K. R. Briggs, K. Arzner, M. Audard, J. Bouvier, E. D. Feigelson, E. Franciosini, A. Glauser, N. Grosso, G. Micela, J.-L. Monin, T. Montmerle, D. L. Padgett, F. Palla, I. Pillitteri, L. Rebull, L. Scelsi, B. Silva, S. L. Skinner, B. Stelzer, and A. Telleschi. The XMM-Newton extended survey of the Taurus molecular cloud (XEST). *A&A*, 468: 353–377, June 2007. doi:10.1051/0004-6361:20065724.

O. Guillois, G. Ledoux, and C. Reynaud. Diamond Infrared Emission Bands in Circumstellar Media. *ApJL*, 521:L133–L36, Aug. 1999. doi:10.1086/312199.

S. Guilloteau and A. Dutrey. Physical parameters of the Keplerian protoplanetary disk of DM Tauri. *A&A*, 339:467–476, Nov. 1998.

S. Guilloteau, A. Dutrey, and M. Simon. GG Tauri: the ring world. *A&A*, 348:570–578, Aug. 1999.

S. Guilloteau, A. Dutrey, V. Piétu, and Y. Boehler. A dual-frequency sub-arcsecond study of proto-planetary disks at mm wavelengths: first evidence for radial variations of the dust properties. *A&A*, 529:A105, May 2011. doi:10.1051/0004-6361/201015209.

R. Günther and W. Kley. Circumbinary disk evolution. *A&A*, 387:550–559, May 2002. doi:10.1051/0004-6361:20020407.

K. E. Haisch, Jr., E. A. Lada, and C. J. Lada. Disk Frequencies and Lifetimes in Young Clusters. *ApJL*, 553:L153–L156, June 2001. doi:10.1086/320685.

M. Hamidouche. Aperture Synthesis Imaging of V892 Tau and PV Cep: Disk Evolution. *ApJ*, 722:204–211, Oct. 2010. doi:10.1088/0004-637X/722/1/204.

C. Haniff. An introduction to the theory of interferometry. *New AR*, 51:565–575, Oct. 2007a. doi:10.1016/j.newar.2007.06.002.

C. Haniff. Ground-based optical interferometry: A practical primer. *New AR*, 51:583–596, Oct. 2007b. doi:10.1016/j.newar.2007.06.004.

P. Hartigan and S. J. Kenyon. A Spectroscopic Survey of Subarcsecond Binaries in the Taurus-Auriga Dark Cloud with the Hubble Space Telescope. *ApJ*, 583:334–357, Jan. 2003. doi:10.1086/345293.

L. Hartmann. Episodic Phenomena In Early Stellar Evolution. In C. J. Lada and N. D. Kylafis, editors, *NATO Advanced Science Institutes (ASI) Series C*, volume 342 of *NATO Advanced Science Institutes (ASI) Series C*, page 623, 1991.

L. Hartmann. *Accretion Processes in Star Formation*. June 1998.

L. Hartmann. On Age Spreads in Star-forming Regions. *AJ*, 121:1030–1039, Feb. 2001. doi:10.1086/318770.

T. J. Haworth, S. Facchini, C. J. Clarke, and L. I. Cleeves. First evidence of external disc photoevaporation in a low mass star forming region: the case of IM Lup. *MNRAS*, 468: L108–L112, June 2017. doi:10.1093/mnrasl/slx037.

C. Hayashi and T. Nakano. Thermal and Dynamical Properties of a Protostar and Its Contraction to the Stage of Quasi-Static Equilibrium. *Progress of Theoretical Physics*, 34: 754–775, Nov. 1965. doi:10.1143/PTP.34.754.

C. Hayashi, R. Hōshi, and D. Sugimoto. Evolution of the Stars. *Progress of Theoretical Physics Supplement*, 22:1–183, 1962. doi:10.1143/PTPS.22.1.

T. Henning, V. B. Il'In, N. A. Krivova, B. Michel, and N. V. Voshchinnikov. WWW database of optical constants for astronomy. *A&As*, 136:405–406, Apr. 1999. doi:10.1051/aas:1999222.

G. H. Herbig. The Spectra of Be- and Ae-Type Stars Associated with Nebulosity. *ApJS*, 4: 337, Mar. 1960. doi:10.1086/190050.

J. Hernández, N. Calvet, C. Briceño, L. Hartmann, and P. Berlind. Spectral Analysis and Classification of Herbig Ae/Be Stars. *AJ*, 127:1682–1701, Mar. 2004. doi:10.1086/381908.

F. Herrera, M. Lozano, and A. Sánchez. Hybrid crossover operators for real-coded genetic algorithms: an experimental study. *Soft Computing*, 9(4):280–298, Apr 2005. ISSN 1433-7479. doi:10.1007/s00500-004-0380-9. URL `https://doi.org/10.1007/s00500-004-0380-9`.

L. A. Hillenbrand, S. E. Strom, F. J. Vrba, and J. Keene. Herbig Ae/Be stars - Intermediate-mass stars surrounded by massive circumstellar accretion disks. *ApJ*, 397:613–643, Oct. 1992. doi:10.1086/171819.

D. Hollenbach, D. Johnstone, S. Lizano, and F. Shu. Photoevaporation of disks around massive stars and application to ultracompact H II regions. *ApJ*, 428:654–669, June 1994. doi:10.1086/174276.

N. Huélamo, S. Lacour, P. Tuthill, M. Ireland, A. Kraus, and G. Chauvin. A companion candidate in the gap of the T Chamaeleontis transitional disk. *A&A*, 528:L7, Apr. 2011. doi:10.1051/0004-6361/201016395.

V. B. Il'In and A. V. Krivov. Dynamics of small grains near Herbig AE stars. In P. S. The, M. R. Perez, and E. P. J. van den Heuvel, editors, *The Nature and Evolutionary Status of Herbig Ae/Be Stars*, volume 62 of *Astronomical Society of the Pacific Conference Series*, page 177, 1994.

A. Isella and A. Natta. The shape of the inner rim in proto-planetary disks. *A&A*, 438: 899–907, Aug. 2005. doi:10.1051/0004-6361:20052773.

A. Isella, L. Testi, A. Natta, R. Neri, D. Wilner, and C. Qi. Millimeter imaging of HD 163296: probing the disk structure and kinematics. *A&A*, 469:213–222, July 2007. doi:10.1051/0004-6361:20077385.

A. Isella, J. M. Carpenter, and A. I. Sargent. Investigating Planet Formation in Circumstellar Disks: CARMA Observations of Ry Tau and Dg Tau. *ApJ*, 714:1746–1761, May 2010. doi:10.1088/0004-637X/714/2/1746.

A. Johansen, H. Klahr, and T. Henning. Gravoturbulent Formation of Planetesimals. *ApJ*, 636:1121–1134, Jan. 2006. doi:10.1086/498078.

J. K. Jørgensen, T. L. Bourke, P. C. Myers, J. Di Francesco, E. F. van Dishoeck, C.-F. Lee, N. Ohashi, F. L. Schöier, S. Takakuwa, D. J. Wilner, and Q. Zhang. PROSAC: A Submillimeter Array Survey of Low-Mass Protostars. I. Overview of Program: Envelopes, Disks, Outflows, and Hot Cores. *ApJ*, 659:479–498, Apr. 2007. doi:10.1086/512230.

A. H. Joy. T Tauri Variable Stars. *ApJ*, 102:168, Sept. 1945. doi:10.1086/144749.

A. Juhász, T. Prusti, P. Ábrahám, and C. P. Dullemond. Long-term infrared variability of the UX Ori-type star SV Cep. *MNRAS*, 374:1242–1252, Feb. 2007. doi:10.1111/j.1365-2966.2006.11208.x.

M. Kama, M. Min, and C. Dominik. The inner rim structures of protoplanetary discs. *A&A*, 506:1199–1213, Nov. 2009. doi:10.1051/0004-6361/200912068.

I. Kamp and C. P. Dullemond. The Gas Temperature in the Surface Layers of Protoplanetary Disks. *ApJ*, 615:991–999, Nov. 2004. doi:10.1086/424703.

R. Kandori, K. Dobashi, H. Uehara, F. Sato, and K. Yanagisawa. Grain Growth in the Dark Cloud L1251. *AJ*, 126:1888–1895, Oct. 2003. doi:10.1086/377521.

T. T. Ke, H. Huang, and D. N. C. Lin. Rapid Mid-infrared Variability in Protostellar Disks. *ApJ*, 745:60, Jan. 2012. doi:10.1088/0004-637X/745/1/60.

L. D. Keller, G. C. Sloan, W. J. Forrest, S. Ayala, P. D'Alessio, S. Shah, N. Calvet, J. Najita, A. Li, L. Hartmann, B. Sargent, D. M. Watson, and C. H. Chen. PAH Emission from Herbig Ae/Be Stars. *ApJ*, 684:411-429, Sept. 2008. doi:10.1086/589818.

S. J. Kenyon and L. Hartmann. Spectral energy distributions of T Tauri stars - Disk flaring and limits on accretion. *ApJ*, 323:714–733, Dec. 1987. doi:10.1086/165866.

S. J. Kenyon and L. Hartmann. Pre-Main-Sequence Evolution in the Taurus-Auriga Molecular Cloud. *ApJS*, 101:117, Nov. 1995. doi:10.1086/192235.

R. Kippenhahn, A. Weigert, and A. Weiss. *Stellar Structure and Evolution*. 2012. doi:10.1007/978-3-642-30304-3.

Y. Kitamura, M. Momose, S. Yokogawa, R. Kawabe, M. Tamura, and S. Ida. Investigation of the Physical Properties of Protoplanetary Disks around T Tauri Stars by a 1 Arcsecond Imaging Survey: Evolution and Diversity of the Disks in Their Accretion Stage. *ApJ*, 581: 357–380, Dec. 2002. doi:10.1086/344223.

H. Klahr and P. Bodenheimer. Formation of Giant Planets by Concurrent Accretion of Solids and Gas inside an Anticyclonic Vortex. *ApJ*, 639:432–440, Mar. 2006. doi:10.1086/498928.

W. Kley and A. Burkert. Disks and Planets in Binary Systems (Invited Review). In G. Garzón, C. Eiroa, D. de Winter, and T. J. Mahoney, editors, *Disks, Planetesimals, and Planets*, volume 219 of *Astronomical Society of the Pacific Conference Series*, page 189, 2000.

A. Konigl and R. E. Pudritz. Disk Winds and the Accretion-Outflow Connection. *Protostars and Planets IV*, page 759, May 2000.

M. B. N. Kouwenhoven, A. G. A. Brown, H. Zinnecker, L. Kaper, and S. F. Portegies Zwart. The primordial binary population. I. A near-infrared adaptive optics search for close visual companions to A star members of Scorpius OB2. *A&A*, 430:137–154, Jan. 2005. doi:10.1051/0004-6361:20048124.

A. L. Kraus and L. A. Hillenbrand. The Coevality of Young Binary Systems. *ApJ*, 704: 531–547, Oct. 2009. doi:10.1088/0004-637X/704/1/531.

A. L. Kraus and L. A. Hillenbrand. Multiple Star Formation to the Bottom of the Initial Mass Function. *ApJ*, 757:141, Oct. 2012. doi:10.1088/0004-637X/757/2/141.

A. L. Kraus and M. J. Ireland. LkCa 15: A Young Exoplanet Caught at Formation? *ApJ*, 745:5, Jan. 2012. doi:10.1088/0004-637X/745/1/5.

A. L. Kraus, M. J. Ireland, F. Martinache, and L. A. Hillenbrand. Mapping the Shores of the Brown Dwarf Desert. II. Multiple Star Formation in Taurus-Auriga. *ApJ*, 731:8, Apr. 2011. doi:10.1088/0004-637X/731/1/8.

A. L. Kraus, M. J. Ireland, L. A. Hillenbrand, and F. Martinache. The Role of Multiplicity in Disk Evolution and Planet Formation. *ApJ*, 745:19, Jan. 2012. doi:10.1088/0004-637X/745/1/19.

A. L. Kraus, M. J. Ireland, D. Huber, A. W. Mann, and T. J. Dupuy. The Impact of Stellar Multiplicity on Planetary Systems. I. The Ruinous Influence of Close Binary Companions. *AJ*, 152:8, July 2016. doi:10.3847/0004-6256/152/1/8.

S. Kraus. The interferometric view of Herbig Ae/Be stars. *Ap&SS*, 357:97, June 2015. doi:10.1007/s10509-015-2226-6.

S. Kraus, K. H. Hofmann, M. Benisty, J. P. Berger, O. Chesneau, A. Isella, F. Malbet, A. Meilland, N. Nardetto, A. Natta, T. Preibisch, D. Schertl, M. Smith, P. Stee, E. Tatulli, L. Testi, and G. Weigelt. The origin of hydrogen line emission for five Herbig Ae/Be stars spatially resolved by VLTI/AMBER spectro-interferometry. *A&A*, 489:1157–1173, Oct. 2008a. doi:10.1051/0004-6361:200809946.

S. Kraus, T. Preibisch, and K. Ohnaka. Detection of an Inner Gaseous Component in a Herbig Be Star Accretion Disk: Near- and Mid-Infrared Spectrointerferometry and Radiative Transfer modeling of MWC 147. *ApJ*, 676:490–508, Mar. 2008b. doi:10.1086/527427.

S. Kraus, J. Kluska, A. Kreplin, M. Bate, T. J. Harries, K.-H. Hofmann, E. Hone, J. D. Monnier, G. Weigelt, A. Anugu, W. J. de Wit, and M. Wittkowski. A High-mass Protobinary System with Spatially Resolved Circumstellar Accretion Disks and Circumbinary Disk. *ApJL*, 835:L5, Jan. 2017a. doi:10.3847/2041-8213/835/1/L5.

S. Kraus, A. Kreplin, M. Fukugawa, T. Muto, M. L. Sitko, A. K. Young, M. R. Bate, C. Grady, T. T. Harries, J. D. Monnier, M. Willson, and J. Wisniewski. Dust-trapping Vortices and a Potentially Planet-triggered Spiral Wake in the Pre-transitional Disk of V1247 Orionis. *ApJL*, 848:L11, Oct. 2017b. doi:10.3847/2041-8213/aa8edc.

S. Kraus, P. Garcia, and G. Perrin. Maximizing the community exploitation of the VLTI 2nd-generation instruments. *Experimental Astronomy*, Apr. 2018. doi:10.1007/s10686-018-9581-6.

P. Kroupa. The Initial Mass Function of Stars: Evidence for Uniformity in Variable Systems. *Science*, 295:82–91, Jan. 2002. doi:10.1126/science.1067524.

A. Labeyrie, S. G. Lipson, and P. Nisenson. *An Introduction to Optical Stellar Interferometry*. June 2006. doi:10.2277/0521828724.

S. Lacour, B. Biller, A. Cheetham, A. Greenbaum, T. Pearce, S. Marino, P. Tuthill, L. Pueyo, E. E. Mamajek, J. H. Girard, A. Sivaramakrishnan, M. Bonnefoy, I. Baraffe, G. Chauvin, J. Olofsson, A. Juhasz, M. Benisty, J.-U. Pott, A. Sicilia-Aguilar, T. Henning, A. Cardwell, S. Goodsell, J. R. Graham, P. Hibon, P. Ingraham, Q. Konopacky, B. Macintosh, R. Oppenheimer, M. Perrin, F. Rantakyrö, N. Sadakuni, and S. Thomas. An M-dwarf star in the transition disk of Herbig HD 142527. Physical parameters and orbital elements. *A&A*, 590:A90, May 2016. doi:10.1051/0004-6361/201527863.

C. J. Lada and E. A. Lada. Embedded Clusters in Molecular Clouds. *ARAA*, 41:57–115, 2003. doi:10.1146/annurev.astro.41.011802.094844.

E. A. Lada, K. M. Strom, and P. C. Myers. Environments of star formation - Relationship between molecular clouds, dense cores and young stars. In E. H. Levy and J. I. Lunine, editors, *Protostars and Planets III*, pages 245–277, 1993.

R. B. Larson. Numerical calculations of the dynamics of collapsing proto-star. *MNRAS*, 145: 271, 1969. doi:10.1093/mnras/145.3.271.

R. B. Larson. Turbulence and star formation in molecular clouds. *MNRAS*, 194:809–826, Mar. 1981. doi:10.1093/mnras/194.4.809.

R. B. Larson. Cloud fragmentation and stellar masses. *MNRAS*, 214:379–398, June 1985. doi:10.1093/mnras/214.3.379.

R. B. Larson. Bimodal star formation and remnant-dominated galactic models. *MNRAS*, 218:409–428, Feb. 1986. doi:10.1093/mnras/218.3.409.

R. B. Larson. Implications of Binary Properties for Theories of Star Formation. In H. Zinnecker and R. Mathieu, editors, *The Formation of Binary Stars*, volume 200 of *IAU Symposium*, page 93, 2001.

R. B. Larson. The physics of star formation. *Reports on Progress in Physics*, 66:1651–1697, Oct. 2003. doi:10.1088/0034-4885/66/10/R03.

P. R. Lawson, editor. *Principles of Long Baseline Stellar Interferometry*, 2000.

P. R. Lawson, W. D. Cotton, C. A. Hummel, J. D. Monnier, M. Zhao, J. S. Young, H. Thorsteinsson, S. C. Meimon, L. M. Mugnier, G. Le Besnerais, E. M. Thiebaut, and P. G. Tuthill. An interferometry imaging beauty contest. In W. A. Traub, editor, *New Frontiers in Stellar Interferometry*, volume 5491 of *SPIE*, page 886, Oct. 2004. doi:10.1117/12.550710.

B. Lazareff, J.-P. Berger, J. Kluska, J.-B. Le Bouquin, M. Benisty, F. Malbet, C. Koen, C. Pinte, W.-F. Thi, O. Absil, F. Baron, A. Delboulbé, G. Duvert, A. Isella, L. Jocou, A. Juhasz, S. Kraus, R. Lachaume, F. Ménard, R. Millan-Gabet, J. D. Monnier, T. Moulin, K. Perraut, S. Rochat, F. Soulez, M. Tallon, E. Thiébaut, W. Traub, and G. Zins. Structure of Herbig AeBe disks at the milliarcsecond scale . A statistical survey in the H band using PIONIER-VLTI. *A&A*, 599:A85, Mar. 2017. doi:10.1051/0004-6361/201629305.

J.-B. Le Bouquin, J.-P. Berger, B. Lazareff, G. Zins, P. Haguenauer, L. Jocou, P. Kern, R. Millan-Gabet, W. Traub, O. Absil, J.-C. Augereau, M. Benisty, N. Blind, X. Bonfils, P. Bourget, A. Delboulbe, P. Feautrier, M. Germain, P. Gitton, D. Gillier, M. Kiekebusch, J. Kluska, J. Knudstrup, P. Labeye, J.-L. Lizon, J.-L. Monin, Y. Magnard, F. Malbet, D. Maurel, F. Ménard, M. Micallef, L. Michaud, G. Montagnier, S. Morel, T. Moulin, K. Perraut, D. Popovic, P. Rabou, S. Rochat, C. Rojas, F. Roussel, A. Roux, E. Stadler, S. Stefl, E. Tatulli, and N. Ventura. PIONIER: a 4-telescope visitor instrument at VLTI. *A&A*, 535:A67, Nov. 2011. doi:10.1051/0004-6361/201117586.

C. Leinert, U. Graser, F. Przygodda, L. B. F. M. Waters, G. Perrin, W. Jaffe, B. Lopez, E. J. Bakker, A. Böhm, O. Chesneau, W. D. Cotton, S. Damstra, J. de Jong, A. W. Glazenborg-Kluttig, B. Grimm, H. Hanenburg, W. Laun, R. Lenzen, S. Ligori, R. J. Mathar, J. Meisner, S. Morel, W. Morr, U. Neumann, J.-W. Pel, P. Schuller, R.-R. Rohloff, B. Stecklum, C. Storz, O. von der Lühe, and K. Wagner. MIDI - the 10 \mum instrument on the VLTI. *Ap&SS*, 286:73–83, 2003a. doi:10.1023/A:1026158127732.

C. Leinert, U. Graser, A. Richichi, M. Schöller, L. F. B. M. Waters, G. Perrin, W. Jaffe, B. Lopez, A. Glazenborg-Kluttig, F. Przygodda, S. Morel, P. Biereichel, N. Haddad, N. Housen, and A. Wallander. MIDI combines light from the VLTI: the start of 10 μm interferometry at ESO. *The Messenger*, 112:13–18, June 2003b.

C. Leinert, R. van Boekel, L. B. F. M. Waters, O. Chesneau, F. Malbet, R. Köhler, W. Jaffe, T. Ratzka, A. Dutrey, T. Preibisch, U. Graser, E. Bakker, G. Chagnon, W. D. Cotton, C. Dominik, C. P. Dullemond, A. W. Glazenborg-Kluttig, A. Glindemann, T. Henning, K.-H. Hofmann, J. de Jong, R. Lenzen, S. Ligori, B. Lopez, J. Meisner, S. Morel, F. Paresce, J.-W. Pel, I. Percheron, G. Perrin, F. Przygodda, A. Richichi, M. Schöller, P. Schuller, B. Stecklum, M. E. van den Ancker, O. von der Lühe, and G. Weigelt. Mid-infrared sizes

of circumstellar disks around Herbig Ae/Be stars measured with MIDI on the VLTI. *A&A*, 423:537–548, Aug. 2004. doi:10.1051/0004-6361:20047178.

R. Lenzen, M. Hartung, W. Brandner, G. Finger, N. N. Hubin, F. Lacombe, A.-M. Lagrange, M. D. Lehnert, A. F. M. Moorwood, and D. Mouillet. NAOS-CONICA first on sky results in a variety of observing modes. In M. Iye and A. F. M. Moorwood, editors, *Instrument Design and Performance for Optical/Infrared Ground-based Telescopes*, volume 4841 of *SPIE*, pages 944–952, Mar. 2003. doi:10.1117/12.460044.

A. Li. On the Absorption and Emission Properties of Interstellar Grains. In C. C. Popescu and R. J. Tuffs, editors, *The Spectral Energy Distributions of Gas-Rich Galaxies: Confronting Models with Data*, volume 761 of *American Institute of Physics Conference Series*, pages 123–133, Apr. 2005. doi:10.1063/1.1913922.

D. Li, C. M. Telesco, H. Zhang, C. M. Wright, E. Pantin, P. J. Barnes, and C. Packham. Mid-infrared polarization of Herbig Ae/Be discs. *MNRAS*, 473:1427–1437, Jan. 2018. doi:10.1093/mnras/stx2228.

W. M. Liu, P. M. Hinz, M. R. Meyer, E. E. Mamajek, W. F. Hoffmann, G. Brusa, D. Miller, and M. A. Kenworthy. Observations of Herbig Ae Disks with Nulling Interferometry. *ApJ*, 658:1164–1172, Apr. 2007. doi:10.1086/511779.

D. Lommen, S. T. Maddison, C. M. Wright, E. F. van Dishoeck, D. J. Wilner, and T. L. Bourke. Large grains in discs around young stars: ATCA observations of WW Chamaeleontis, RU Lupi, and CS Chamaeleontis. *A&A*, 495:869–879, Mar. 2009. doi:10.1051/0004-6361:200810999.

B. Lopez and R. G. Petrov. Direct Detection of Hot Extrasolar Planets Using Differential Interferometry. In J. Bergeron and A. Renzini, editors, *From Extrasolar Planets to Cosmology: The VLT Opening Symposium*, page 565, 2000. doi:10.1007/10720961_82.

B. Lopez, S. Lagarde, W. Jaffe, R. Petrov, M. Schöller, P. Antonelli, U. Beckmann, P. Berio, F. Bettonvil, A. Glindemann, J.-C. Gonzalez, U. Graser, K.-H. Hofmann, F. Millour, S. Robbe-Dubois, L. Venema, S. Wolf, T. Henning, T. Lanz, G. Weigelt, T. Agocs, C. Bailet, Y. Bresson, P. Bristow, M. Dugué, M. Heininger, G. Kroes, W. Laun, M. Lehmitz, U. Neumann, J.-C. Augereau, G. Avila, J. Behrend, G. van Belle, J.-P. Berger, R. van Boekel, S. Bonhomme, P. Bourget, R. Brast, J.-M. Clausse, C. Connot, R. Conzelmann, P. Cruzalèbes, G. Csepany, W. Danchi, M. Delbo, F. Delplancke, C. Dominik, A. van Duin, E. Elswijk, Y. Fantei, G. Finger, A. Gabasch, J. Gay, P. Girard, V. Girault, P. Gitton, A. Glazenborg, F. Gonté, F. Guitton, S. Guniat, M. De Haan, P. Haguenauer, H. Hanenburg, M. Hogerheijde, R. ter Horst, J. Hron, Y. Hugues, C. Hummel, J. Idserda, D. Ives, G. Jakob, A. Jasko, P. Jolley, S. Kiraly, R. Köhler, J. Kragt, T. Kroener, S. Kuindersma, L. Labadie, C. Leinert, R. Le Poole, J.-L. Lizon, C. Lucuix, A. Marcotto, F. Martinache, G. Martinot-Lagarde, R. Mathar, A. Matter, N. Mauclert, L. Mehrgan, A. Meilland, K. Meisenheimer, J. Meisner, M. Mellein, S. Menardi, J.-L. Menut, A. Merand, S. Morel, L. Mosoni, R. Navarro, E. Nussbaum, S. Ottogalli, R. Palsa, J. Panduro, E. Pantin, T. Parra, I. Percheron, T. P. Duc, J.-U. Pott, E. Pozna, F. Przygodda, Y. Rabbia, A. Richichi, F. Rigal, R. Roelfsema, G. Rupprecht, D. Schertl, C. Schmidt, N. Schuhler, M. Schuil, A. Spang, J. Stegmeier, L. Thiam, N. Tromp, F. Vakili, M. Vannier, K. Wagner, and J. Woillez. An Overview of the MATISSE Instrument - Science, Concept and Current Status. *The Messenger*, 157:5–12, Sept. 2014.

S. H. Lubow and P. Artymowicz. Young Binary Star/Disk Interactions. In D. T. Wickramasinghe, G. V. Bicknell, and L. Ferrario, editors, *IAU Colloq. 163: Accretion Phenomena and Related Outflows*, volume 121 of *Astronomical Society of the Pacific Conference Series*, page 505, 1997.

S. H. Lubow and P. Artymowicz. Interactions of Young Binaries with Disks. *Protostars and Planets IV*, page 731, May 2000.

K. L. Luhman. The Initial Mass Function of Low-Mass Stars and Brown Dwarfs in Taurus. *ApJ*, 544:1044–1055, Dec. 2000. doi:10.1086/317232.

K. L. Luhman. The Formation and Early Evolution of Low-Mass Stars and Brown Dwarfs. *ARAA*, 50:65–106, Sept. 2012. doi:10.1146/annurev-astro-081811-125528.

K. L. Luhman, J. R. Stauffer, A. A. Muench, G. H. Rieke, E. A. Lada, J. Bouvier, and C. J. Lada. A Census of the Young Cluster IC 348. *ApJ*, 593:1093–1115, Aug. 2003. doi:10.1086/376594.

K. L. Luhman, E. E. Mamajek, S. J. Shukla, and N. P. Loutrel. A Survey for New Members of the Taurus Star-forming Region with the Sloan Digital Sky Survey. *AJ*, 153:46, Jan. 2017. doi:10.3847/1538-3881/153/1/46.

X. Luri, A. G. A. Brown, L. M. Sarro, F. Arenou, C. A. L. Bailer-Jones, A. Castro-Ginard, J. de Bruijne, T. Prusti, C. Babusiaux, and H. E. Delgado. Gaia Data Release 2: using Gaia parallaxes. *ArXiv e-prints*, Apr. 2018.

D. Lynden-Bell and J. E. Pringle. The evolution of viscous discs and the origin of the nebular variables. *MNRAS*, 168:603–637, Sept. 1974. doi:10.1093/mnras/168.3.603.

K. M. Maaskant, M. Min, L. B. F. M. Waters, and A. G. G. M. Tielens. Polycyclic aromatic hydrocarbon ionization as a tracer of gas flows through protoplanetary disk gaps. *A&A*, 563:A78, Mar. 2014. doi:10.1051/0004-6361/201323137.

M.-M. Mac Low and R. S. Klessen. Control of star formation by supersonic turbulence. *Reviews of Modern Physics*, 76:125–194, Jan. 2004. doi:10.1103/RevModPhys.76.125.

M. N. Machida, S.-i. Inutsuka, and T. Matsumoto. Second Core Formation and High-Speed Jets: Resistive Magnetohydrodynamic Nested Grid Simulations. *ApJL*, 647:L151–L154, Aug. 2006. doi:10.1086/507179.

M. N. Machida, S.-i. Inutsuka, and T. Matsumoto. Magnetic Fields and Rotations of Protostars. *ApJ*, 670:1198–1213, Dec. 2007. doi:10.1086/521779.

F. Malbet, R. Lachaume, J.-P. Berger, M. M. Colavita, E. di Folco, J. A. Eisner, B. F. Lane, R. Millan-Gabet, D. Ségransan, and W. A. Traub. New insights on the AU-scale circumstellar structure of FU Orionis. *A&A*, 437:627–636, July 2005. doi:10.1051/0004-6361:20042556.

R. Malhotra, N. Singh, and Y. Singh. Genetic algorithms: Concepts, design for optimization of process controllers. *Computer and Information Science*, 2011.

O. Y. Malkov, E. Oblak, E. A. Snegireva, and J. Torra. A catalogue of eclipsing variables. *A&A*, 446:785–789, Feb. 2006. doi:10.1051/0004-6361:20053137.

E. E. Mamajek. Initial Conditions of Planet Formation: Lifetimes of Primordial Disks. In T. Usuda, M. Tamura, and M. Ishii, editors, *American Institute of Physics Conference Series*, volume 1158 of *American Institute of Physics Conference Series*, pages 3–10, Aug. 2009. doi:10.1063/1.3215910.

H. Masunaga and S.-i. Inutsuka. A Radiation Hydrodynamic Model for Protostellar Collapse. II. The Second Collapse and the Birth of a Protostar. *ApJ*, 531:350–365, Mar. 2000. doi:10.1086/308439.

A. Matter, M. Vannier, S. Morel, B. Lopez, W. Jaffe, S. Lagarde, R. G. Petrov, and C. Leinert. First step to detect an extrasolar planet using simultaneous observations with the VLTI instruments AMBER and MIDI. *A&A*, 515:A69, June 2010. doi:10.1051/0004-6361/200913142.

A. Matter, L. Labadie, A. Kreplin, B. Lopez, S. Wolf, G. Weigelt, S. Ertel, J.-U. Pott, and W. C. Danchi. Evidence of a discontinuous disk structure around the Herbig Ae star HD 139614. *A&A*, 561:A26, Jan. 2014. doi:10.1051/0004-6361/201322042.

A. Matter, L. Labadie, J. C. Augereau, J. Kluska, A. Crida, A. Carmona, J. F. Gonzalez, W. F. Thi, J.-B. Le Bouquin, J. Olofsson, and B. Lopez. Inner disk clearing around the Herbig Ae star HD 139614: Evidence for a planet-induced gap? *A&A*, 586:A11, Feb. 2016. doi:10.1051/0004-6361/201525793.

D. Mawet, É. Choquet, O. Absil, E. Huby, M. Bottom, E. Serabyn, B. Femenia, J. Lebreton, K. Matthews, C. A. Gomez Gonzalez, O. Wertz, B. Carlomagno, V. Christiaens, D. Defrère, C. Delacroix, P. Forsberg, S. Habraken, A. Jolivet, M. Karlsson, J. Milli, C. Pinte, P. Piron, M. Reggiani, J. Surdej, and E. Vargas Catalan. Characterization of the Inner Disk around HD 141569 A from Keck/NIRC2 L-Band Vortex Coronagraphy. *AJ*, 153:44, Jan. 2017. doi:10.3847/1538-3881/153/1/44.

C. McCabe, A. M. Ghez, L. Prato, G. Duchêne, R. S. Fisher, and C. Telesco. Investigating Disk Evolution: A High Spatial Resolution Mid-Infrared Survey of T Tauri Stars. *ApJ*, 636:932–951, Jan. 2006. doi:10.1086/498207.

J. McCall. Genetic algorithms for modelling and optimisation. *Journal of Computational and Applied Mathematics*, 184(1):205 – 222, 2005. ISSN 0377-0427. doi:https://doi.org/10.1016/j.cam.2004.07.034. URL `http://www.sciencedirect.com/science/article/pii/S0377042705000774`. Special Issue on Mathematics Applied to Immunology.

M. J. McCaughrean, K. R. Stapelfeldt, and L. M. Close. High-Resolution Optical and Near-Infrared Imaging of Young Circumstellar Disks. *Protostars and Planets IV*, page 485, May 2000.

M. K. McClure, E. Furlan, P. Manoj, K. L. Luhman, D. M. Watson, W. J. Forrest, C. Espaillat, N. Calvet, P. D'Alessio, B. Sargent, J. J. Tobin, and H.-F. Chiang. The Evolutionary State of the Pre-main Sequence Population in Ophiuchus: A Large Infrared Spectrograph Survey. *ApJS*, 188:75–122, May 2010. doi:10.1088/0067-0049/188/1/75.

M. K. McClure, P. D'Alessio, N. Calvet, C. Espaillat, L. Hartmann, B. Sargent, D. M. Watson, L. Ingleby, and J. Hernández. Curved Walls: Grain Growth, Settling, and Composition Patterns in T Tauri Disk Dust Sublimation Fronts. *ApJ*, 775:114, Oct. 2013. doi:10.1088/0004-637X/775/2/114.

C. F. McKee and E. C. Ostriker. Theory of Star Formation. *ARAA*, 45:565–687, Sept. 2007. doi:10.1146/annurev.astro.45.051806.110602.

G. Meeus, J. Bouwman, C. Dominik, L. B. F. M. Waters, and A. de Koter. The absence of the 10 mu m silicate feature in the isolated Herbig Ae star HD 100453. *A&A*, 392: 1039–1046, Sept. 2002. doi:10.1051/0004-6361:20020952.

J. Menu, R. van Boekel, T. Henning, C. Leinert, C. Waelkens, and L. B. F. M. Waters. The structure of disks around intermediate-mass young stars from mid-infrared interferometry. Evidence for a population of group II disks with gaps. *A&A*, 581:A107, Sept. 2015. doi:10.1051/0004-6361/201525654.

A. Mérand, F. Patru, J.-P. Berger, I. Percheron, and S. Poupar. Fringe tracking performance monitoring: FINITO at VLTI. In *Optical and Infrared Interferometry III*, volume 8445 of *SPIE*, page 84451K, July 2012. doi:10.1117/12.925450.

F. Millour. All you ever wanted to know about optical long baseline stellar interferometry, but were too shy to ask your adviser. *New AR*, 52:177–185, June 2008. doi:10.1016/j.newar.2008.04.012.

F. Millour. Interferometry concepts. In *EAS Publications Series*, volume 69 of *EAS Publications Series*, pages 17–52, Sept. 2014. doi:10.1051/eas/1569003.

M. Min, C. P. Dullemond, C. Dominik, A. de Koter, and J. W. Hovenier. Radiative transfer in very optically thick circumstellar disks. *A&A*, 497:155–166, Apr. 2009. doi:10.1051/0004-6361/200811470.

T. Möller, I. Bernst, D. Panoglou, D. Muders, V. Ossenkopf, M. Röllig, and P. Schilke. Modeling and Analysis Generic Interface for eXternal numerical codes (MAGIX). *A&A*, 549:A21, Jan. 2013. doi:10.1051/0004-6361/201220063.

J. D. Monnier. Phases in interferometry. *New AR*, 51:604–616, Oct. 2007. doi:10.1016/j.newar.2007.06.006.

J. D. Monnier and R. Millan-Gabet. On the Interferometric Sizes of Young Stellar Objects. *ApJ*, 579:694–698, Nov. 2002. doi:10.1086/342917.

J. D. Monnier, A. Tannirkulam, P. G. Tuthill, M. Ireland, R. Cohen, W. C. Danchi, and F. Baron. Discovery of a Circumbinary Disk around Herbig Ae/Be System V892 Tauri. *ApJL*, 681:L97, July 2008. doi:10.1086/590532.

J. D. Monnier, P. G. Tuthill, M. Ireland, R. Cohen, A. Tannirkulam, and M. D. Perrin. Mid-Infrared Size Survey of Young Stellar Objects: Description of Keck Segment-Tilting Experiment and Basic Results. *ApJ*, 700:491–505, July 2009. doi:10.1088/0004-637X/700/1/491.

K. Mooley, L. Hillenbrand, L. Rebull, D. Padgett, and G. Knapp. B- and A-type Stars in the Taurus-Auriga Star-forming Region. *ApJ*, 771:110, July 2013. doi:10.1088/0004-637X/771/2/110.

C. Mordasini, Y. Alibert, and W. Benz. Extrasolar planet population synthesis. I. Method, formation tracks, and mass-distance distribution. *A&A*, 501:1139–1160, July 2009. doi:10.1051/0004-6361/200810301.

T. C. Mouschovias and G. E. Ciolek. Magnetic Fields and Star Formation: A Theory Reaching Adulthood. In C. J. Lada and N. D. Kylafis, editors, *NATO Advanced Science Institutes (ASI) Series C*, volume 540 of *NATO Advanced Science Institutes (ASI) Series C*, page 305, 1999.

G. D. Mulders, C. Dominik, and M. Min. Full two-dimensional radiative transfer modelling of the transitional disk LkCa 15. *A&A*, 512:A11, Mar. 2010. doi:10.1051/0004-6361/200912743.

A. Müller, J.-U. Pott, A. Mérand, R. Abuter, F. Delplancke-Ströbele, T. Henning, R. Köhler, C. Leinert, S. Morel, T. Phan Duc, E. Pozna, A. Ramirez, J. Sahlmann, and C. Schmid. Mid-infrared interferometry with K band fringe-tracking. I. The VLTI MIDI+FSU experiment. *A&A*, 567:A98, July 2014. doi:10.1051/0004-6361/201423933.

J. Muzerolle, P. D'Alessio, N. Calvet, and L. Hartmann. Magnetospheres and Disk Accretion in Herbig Ae/Be Stars. *ApJ*, 617:406–417, Dec. 2004. doi:10.1086/425260.

J. Muzerolle, K. Flaherty, Z. Balog, E. Furlan, P. S. Smith, L. Allen, N. Calvet, P. D'Alessio, S. T. Megeath, A. Muench, G. H. Rieke, and W. H. Sherry. Evidence for Dynamical Changes in a Transitional Protoplanetary Disk with Mid-Infrared Variability. *ApJL*, 704: L15–L19, Oct. 2009. doi:10.1088/0004-637X/704/1/L15.

A. T. Myers, C. F. McKee, A. J. Cunningham, R. I. Klein, and M. R. Krumholz. The Fragmentation of Magnetized, Massive Star-forming Cores with Radiative Feedback. *ApJ*, 766:97, Apr. 2013. doi:10.1088/0004-637X/766/2/97.

P. C. Myers, N. J. Evans, II, and N. Ohashi. Observations of Infall in Star-Forming Regions. *Protostars and Planets IV*, page 217, May 2000.

E. Nagel, C. Espaillat, P. D'Alessio, and N. Calvet. Mid-Infrared Variability of the Binary System CS Cha. *ApJ*, 747:139, Mar. 2012. doi:10.1088/0004-637X/747/2/139.

A. Natta, V. P. Grinin, V. Mannings, and H. Ungerechts. The Evolutionary Status of UX Orionis-Type Stars. *ApJ*, 491:885–890, Dec. 1997. doi:10.1086/305006.

A. Natta, T. Prusti, R. Neri, D. Wooden, V. P. Grinin, and V. Mannings. A reconsideration of disk properties in Herbig Ae stars. *A&A*, 371:186–197, May 2001. doi:10.1051/0004-6361:20010334.

A. Natta, L. Testi, and S. Randich. Accretion in the ρ-Ophiuchi pre-main sequence stars. *A&A*, 452:245–252, June 2006. doi:10.1051/0004-6361:20054706.

C. Norman and J. Silk. Clumpy molecular clouds - A dynamic model self-consistently regulated by T Tauri star formation. *ApJ*, 238:158–174, May 1980. doi:10.1086/157969.

S. S. R. Offner, R. I. Klein, C. F. McKee, and M. R. Krumholz. The Effects of Radiative Transfer on Low-Mass Star Formation. *ApJ*, 703:131–149, Sept. 2009. doi:10.1088/0004-637X/703/1/131.

Y. Ohta, M. Fukagawa, M. L. Sitko, T. Muto, S. Kraus, C. A. Grady, J. P. Wisniewski, J. R. Swearingen, H. Shibai, T. Sumi, J. Hashimoto, T. Kudo, N. Kusakabe, M. Momose, Y. Okamoto, T. Kotani, M. Takami, T. Currie, C. Thalmann, M. Janson, E. Akiyama, K. B. Follette, S. Mayama, L. Abe, W. Brandner, T. D. Brandt, J. C. Carson, S. E. Egner, M. Feldt, M. Goto, O. Guyon, Y. Hayano, M. Hayashi, S. S. Hayashi, T. Henning, K. W.

Hodapp, M. Ishii, M. Iye, R. Kandori, G. R. Knapp, M. Kuzuhara, J. Kwon, T. Matsuo, M. W. McElwain, S. Miyama, J.-I. Morino, A. Moro-Martín, T. Nishimura, T.-S. Pyo, E. Serabyn, T. Suenaga, H. Suto, R. Suzuki, Y. H. Takahashi, H. Takami, N. Takato, H. Terada, D. Tomono, E. L. Turner, T. Usuda, M. Watanabe, T. Yamada, and M. Tamura. Extreme asymmetry in the polarized disk of V1247 Orionis*. *PASJ*, 68:53, Aug. 2016. doi:10.1093/pasj/psw051.

C. Olczak, S. Pfalzner, and R. Spurzem. Encounter-triggered Disk Mass Loss in the Orion Nebula Cluster. *ApJ*, 642:1140–1151, May 2006. doi:10.1086/501044.

I. Oliveira, K. M. Pontoppidan, B. Merín, E. F. van Dishoeck, F. Lahuis, V. C. Geers, J. K. Jørgensen, J. Olofsson, J.-C. Augereau, and J. M. Brown. A Spitzer Survey of Protoplanetary Disk Dust in the Young Serpens Cloud: How do Dust Characteristics Evolve with Time? *ApJ*, 714:778–798, May 2010. doi:10.1088/0004-637X/714/1/778.

J. Olofsson, M. Benisty, J.-B. Le Bouquin, J.-P. Berger, S. Lacour, F. Ménard, T. Henning, A. Crida, L. Burtscher, G. Meeus, T. Ratzka, C. Pinte, J.-C. Augereau, F. Malbet, B. Lazareff, and W. Traub. Sculpting the disk around T Chamaeleontis: an interferometric view. *A&A*, 552:A4, Apr. 2013. doi:10.1051/0004-6361/201220675.

J. E. Owen, B. Ercolano, C. J. Clarke, and R. D. Alexander. Radiation-hydrodynamic models of X-ray and EUV photoevaporating protoplanetary discs. *MNRAS*, 401:1415–1428, Jan. 2010. doi:10.1111/j.1365-2966.2009.15771.x.

F. Palla and S. W. Stahler. The Pre-Main-Sequence Evolution of Intermediate-Mass Stars. *ApJ*, 418:414, Nov. 1993. doi:10.1086/173402.

O. Panić, T. Ratzka, G. D. Mulders, C. Dominik, R. van Boekel, T. Henning, W. Jaffe, and M. Min. Resolving HD 100546 disc in the mid-infrared: Small inner disc and asymmetry near the gap. *A&A*, 562:A101, Feb. 2014. doi:10.1051/0004-6361/201219223.

J. Papaloizou and J. E. Pringle. Tidal torques on accretion discs in close binary systems. *MNRAS*, 181:441–454, Nov. 1977. doi:10.1093/mnras/181.3.441.

J. C. B. Papaloizou, R. P. Nelson, W. Kley, F. S. Masset, and P. Artymowicz. Disk-Planet Interactions During Planet Formation. *Protostars and Planets V*, pages 655–668, 2007.

I. Pascucci and M. Sterzik. Evidence for Disk Photoevaporation Driven by the Central Star. *ApJ*, 702:724–732, Sept. 2009. doi:10.1088/0004-637X/702/1/724.

I. Pascucci, D. Hollenbach, J. Najita, J. Muzerolle, U. Gorti, G. J. Herczeg, L. A. Hillenbrand, J. S. Kim, J. M. Carpenter, M. R. Meyer, E. E. Mamajek, and J. Bouwman. Detection of [Ne II] Emission from Young Circumstellar Disks. *ApJ*, 663:383–393, July 2007. doi:10.1086/518535.

R. G. Petrov, F. Malbet, G. Weigelt, P. Antonelli, U. Beckmann, Y. Bresson, A. Chelli, M. Dugué, G. Duvert, S. Gennari, L. Glück, P. Kern, S. Lagarde, E. Le Coarer, F. Lisi, F. Millour, K. Perraut, P. Puget, F. Rantakyrö, S. Robbe-Dubois, A. Roussel, P. Salinari, E. Tatulli, G. Zins, M. Accardo, B. Acke, K. Agabi, E. Altariba, B. Arezki, E. Aristidi, C. Baffa, J. Behrend, T. Blöcker, S. Bonhomme, S. Busoni, F. Cassaing, J.-M. Clausse, J. Colin, C. Connot, A. Delboulbé, A. Domiciano de Souza, T. Driebe, P. Feautrier, D. Ferruzzi, T. Forveille, E. Fossat, R. Foy, D. Fraix-Burnet, A. Gallardo, E. Giani, C. Gil, A. Glentzlin, M. Heiden, M. Heininger, O. Hernandez Utrera, K.-H. Hofmann, D. Kamm,

M. Kiekebusch, S. Kraus, D. Le Contel, J.-M. Le Contel, T. Lesourd, B. Lopez, M. Lopez, Y. Magnard, A. Marconi, G. Mars, G. Martinot-Lagarde, P. Mathias, P. Mège, J.-L. Monin, D. Mouillet, D. Mourard, E. Nussbaum, K. Ohnaka, J. Pacheco, C. Perrier, Y. Rabbia, S. Rebattu, F. Reynaud, A. Richichi, A. Robini, M. Sacchettini, D. Schertl, M. Schöller, W. Solscheid, A. Spang, P. Stee, P. Stefanini, M. Tallon, I. Tallon-Bosc, D. Tasso, L. Testi, F. Vakili, O. von der Lühe, J.-C. Valtier, M. Vannier, and N. Ventura. AMBER, the near-infrared spectro-interferometric three-telescope VLTI instrument. *A&A*, 464:1–12, Mar. 2007. doi:10.1051/0004-6361:20066496.

R. G. Petrov, F. Millour, S. Lagarde, M. Vannier, S. Rakshit, A. Marconi, and G. weigelt. VLTI/AMBER differential interferometry of the broad-line region of the quasar 3C273. In *Optical and Infrared Interferometry III*, volume 8445 of *SPIE*, page 84450W, July 2012. doi:10.1117/12.926595.

S. Pfalzner, M. Steinhausen, and K. Menten. Short Dissipation Times of Proto-planetary Disks: An Artifact of Selection Effects? *ApJL*, 793:L34, Oct. 2014. doi:10.1088/2041-8205/793/2/L34.

A. Pierens and R. P. Nelson. Migration and gas accretion scenarios for the Kepler 16, 34, and 35 circumbinary planets. *A&A*, 556:A134, Aug. 2013. doi:10.1051/0004-6361/201321777.

V. Piétu, A. Dutrey, and S. Guilloteau. Probing the structure of protoplanetary disks: a comparative study of DM Tau, LkCa 15, and MWC 480. *A&A*, 467:163–178, May 2007. doi:10.1051/0004-6361:20066537.

P. Pinilla, M. Flock, M. d. J. Ovelar, and T. Birnstiel. Can dead zones create structures like a transition disk? *A&A*, 596:A81, Dec. 2016. doi:10.1051/0004-6361/201628441.

P. Pinilla, M. Tazzari, I. Pascucci, A. N. Youdin, A. Garufi, C. F. Manara, L. Testi, G. van der Plas, S. A. Barenfeld, H. Canovas, E. G. Cox, N. P. Hendler, L. M. Pérez, and N. van der Marel. Homogeneous Analysis of the Dust Morphology of Transition Disks Observed with ALMA: Investigating dust trapping and the origin of the cavities. *ArXiv e-prints*, Apr. 2018.

C. Pinte, F. Ménard, J. P. Berger, M. Benisty, and F. Malbet. The Inner Radius of T Tauri Disks Estimated from Near-Infrared Interferometry: The Importance of Scattered Light. *ApJL*, 673:L63, Jan. 2008. doi:10.1086/527378.

M. A. Pogodin, V. P. Malanushenko, O. V. Kozlova, T. N. Tarasova, and G. A. P. Franco. The Herbig B0e star HD 53367: circumstellar activity and evidence of binarity. *A&A*, 452:551–559, June 2006. doi:10.1051/0004-6361:20053704.

J. B. Pollack, D. Hollenbach, S. Beckwith, D. P. Simonelli, T. Roush, and W. Fong. Composition and radiative properties of grains in molecular clouds and accretion disks. *ApJ*, 421: 615–639, Feb. 1994. doi:10.1086/173677.

T. Prusti and A. Natta. Mid Infrared Variability of Herbig Ae/Be Stars. In J. F. Alves and M. J. McCaughrean, editors, *The Origin of Stars and Planets: The VLT View*, page 351, 2002. doi:10.1007/10856518_46.

E. Quataert and E. I. Chiang. Angular Momentum Transport in Particle and Fluid Disks. *ApJ*, 543:432–437, Nov. 2000. doi:10.1086/317098.

E. V. Quintana and J. J. Lissauer. Terrestrial planet formation surrounding close binary stars. *Icar*, 185:1–20, Nov. 2006. doi:10.1016/j.icarus.2006.06.016.

D. Raghavan, H. A. McAlister, T. J. Henry, D. W. Latham, G. W. Marcy, B. D. Mason, D. R. Gies, R. J. White, and T. A. ten Brummelaar. A Survey of Stellar Families: Multiplicity of Solar-type Stars. *ApJS*, 190:1–42, Sept. 2010. doi:10.1088/0067-0049/190/1/1.

S. Ragland, K. Ohnaka, L. Hillenbrand, S. T. Ridgway, M. M. Colavita, R. L. Akeson, W. Cotton, W. C. Danchi, M. Hrynevich, R. Millan-Gabet, and W. A. Traub. First Keck Nulling Observations of a Young Stellar Object: Probing the Circumstellar Environment of the Herbig Ae Star MWC 325. *ApJ*, 746:126, Feb. 2012. doi:10.1088/0004-637X/746/2/126.

T. Ratzka, C. Leinert, T. Henning, J. Bouwman, C. P. Dullemond, and W. Jaffe. High spatial resolution mid-infrared observations of the low-mass young star TW Hydrae. *A&A*, 471: 173–185, Aug. 2007. doi:10.1051/0004-6361:20077357.

T. Ratzka, A. A. Schegerer, C. Leinert, P. Ábrahám, T. Henning, T. M. Herbst, R. Köhler, S. Wolf, and H. Zinnecker. Spatially resolved mid-infrared observations of the triple system T Tauri. *A&A*, 502:623–646, Aug. 2009. doi:10.1051/0004-6361/200811390.

L. M. Rebull, D. L. Padgett, C.-E. McCabe, L. A. Hillenbrand, K. R. Stapelfeldt, A. Noriega-Crespo, S. J. Carey, T. Brooke, T. Huard, S. Terebey, M. Audard, J.-L. Monin, M. Fukagawa, M. Güdel, G. R. Knapp, F. Menard, L. E. Allen, J. R. Angione, C. Baldovin-Saavedra, J. Bouvier, K. Briggs, C. Dougados, N. J. Evans, N. Flagey, S. Guieu, N. Grosso, A. M. Glauser, P. Harvey, D. Hines, W. B. Latter, S. L. Skinner, S. Strom, J. Tromp, and S. Wolf. The Taurus Spitzer Survey: New Candidate Taurus Members Selected Using Sensitive Mid-Infrared Photometry. *ApJS*, 186:259–307, Feb. 2010. doi:10.1088/0067-0049/186/2/259.

M. Reggiani, V. Christiaens, O. Absil, D. Mawet, E. Huby, E. Choquet, C. A. Gomez Gonzalez, G. Ruane, B. Femenia, E. Serabyn, K. Matthews, M. Barraza, B. Carlomagno, D. Defrère, C. Delacroix, S. Habraken, A. Jolivet, M. Karlsson, G. Orban de Xivry, P. Piron, J. Surdej, E. Vargas Catalan, and O. Wertz. Discovery of a point-like source and a third spiral arm in the transition disk around the Herbig Ae star MWC 758. *A&A*, 611: A74, Mar. 2018. doi:10.1051/0004-6361/201732016.

H. Rein. A proposal for community driven and decentralized astronomical databases and the Open Exoplanet Catalogue. *ArXiv e-prints*, Nov. 2012.

B. Reipurth. Herbig-Haro Objects. In C. J. Lada and N. D. Kylafis, editors, *NATO Advanced Science Institutes (ASI) Series C*, volume 342 of *NATO Advanced Science Institutes (ASI) Series C*, page 497, 1991.

B. Reipurth and H. Zinnecker. Visual binaries among pre-main sequence stars. *A&A*, 278: 81–108, Oct. 1993.

B. Reipurth, M. M. Guimarães, M. S. Connelley, and J. Bally. Visual Binaries in the Orion Nebula Cluster. *AJ*, 134:2272–2285, Dec. 2007. doi:10.1086/523596.

L. Ricci, L. Testi, A. Natta, R. Neri, S. Cabrit, and G. J. Herczeg. Dust properties of protoplanetary disks in the Taurus-Auriga star forming region from millimeter wavelengths. *A&A*, 512:A15, Mar. 2010. doi:10.1051/0004-6361/200913403.

J. Rodmann, T. Henning, C. J. Chandler, L. G. Mundy, and D. J. Wilner. Large dust particles in disks around T Tauri stars. *A&A*, 446:211–221, Jan. 2006. doi:10.1051/0004-6361:20054038.

G. P. Rosotti and C. J. Clarke. The evolution of photoevaporating viscous discs in binaries. *MNRAS*, 473:5630–5640, Feb. 2018. doi:10.1093/mnras/stx2769.

H. R. Schmitt, T. A. Pauls, C. Tycner, J. T. Armstrong, J. A. Benson, J. H. Clark, R. B. Hindsley, D. J. Hutter, D. M. Peterson, A. M. Jorgensen, D. Mozurkewich, G. C. Gilbreath, and R. T. Zavala. Using differential phases in optical interferometry. In *Society of Photo-Optical Instrumentation Engineers (SPIE) Conference Series*, volume 6268 of *SPIE*, page 62683B, June 2006. doi:10.1117/12.672396.

J. Schneider, C. Dedieu, P. Le Sidaner, R. Savalle, and I. Zolotukhin. Defining and cataloging exoplanets: the exoplanet.eu database. *A&A*, 532:A79, Aug. 2011. doi:10.1051/0004-6361/201116713.

M. Schöller, M. A. Pogodin, J. A. Cahuasquí, N. A. Drake, S. Hubrig, M. G. Petr-Gotzens, I. S. Savanov, B. Wolff, J. F. González, S. Mysore, I. Ilyin, S. P. Järvinen, and B. Stelzer. Spectroscopic signatures of magnetospheric accretion in Herbig Ae/Be stars. I. The case of HD 101412. *A&A*, 592:A50, July 2016. doi:10.1051/0004-6361/201628361.

P. Scicluna, S. Wolf, T. Ratzka, G. Costigan, R. Launhardt, C. Leinert, F. Ober, C. F. Manara, and L. Testi. Understanding discs in binary YSOs - detailed modelling of VV CrA. *MNRAS*, 458:2476–2491, May 2016. doi:10.1093/mnras/stw460.

D. Ségransan. Observability and UV coverage. *New AR*, 51:597–603, Oct. 2007. doi:10.1016/j.newar.2007.06.005.

D. Semenov, T. Henning, C. Helling, M. Ilgner, and E. Sedlmayr. Rosseland and Planck mean opacities for protoplanetary discs. *A&A*, 410:611–621, Nov. 2003. doi:10.1051/0004-6361:20031279.

J. Y. Seok and A. Li. Dust and Polycyclic Aromatic Hydrocarbon in the Pre-transitional Disk around HD 169142. *ApJ*, 818:2, Feb. 2016. doi:10.3847/0004-637X/818/1/2.

J.-M. Shi and J. H. Krolik. How Bright are the Gaps in Circumbinary Disk Systems? *ApJ*, 832:22, Nov. 2016. doi:10.3847/0004-637X/832/1/22.

F. H. Shu and S. Lizano. The Evolution of Molecular Clouds. In J. M. Moran and P. T. P. Ho, editors, *Interstellar Matter*, page 65, 1988.

F. H. Shu, F. C. Adams, and S. Lizano. Star formation in molecular clouds - Observation and theory. *ARAA*, 25:23–81, 1987. doi:10.1146/annurev.aa.25.090187.000323.

F. H. Shu, J. R. Najita, H. Shang, and Z.-Y. Li. X-Winds Theory and Observations. *Protostars and Planets IV*, pages 789–814, May 2000.

A. Sicilia-Aguilar, L. Hartmann, N. Calvet, S. T. Megeath, J. Muzerolle, L. Allen, P. D'Alessio, B. Merín, J. Stauffer, E. Young, and C. Lada. Disk Evolution in Cep OB2: Results from the Spitzer Space Telescope. *ApJ*, 638:897–919, Feb. 2006. doi:10.1086/498085.

L. Siess, E. Dufour, and M. Forestini. An internet server for pre-main sequence tracks of low- and intermediate-mass stars. *A&A*, 358:593–599, June 2000.

S. L. Skinner, A. Brown, and R. T. Stewart. A high-sensitivity survey of radio continuum emission from Herbig Ae/Be stars. *ApJS*, 87:217–265, July 1993. doi:10.1086/191803.

K. W. Smith, Y. Y. Balega, W. J. Duschl, K.-H. Hofmann, R. Lachaume, T. Preibisch, D. Schertl, and G. Weigelt. Close binary companions of the HAeBe stars LkHα 198, Elias 1, HK Ori and V380 Ori. *A&A*, 431:307–319, Feb. 2005. doi:10.1051/0004-6361:20041135.

P. M. Solomon and D. B. Sanders. Star formation in a galactic context - The location and properties of molecular clouds. In D. C. Black and M. S. Matthews, editors, *Protostars and Planets II*, pages 59–80, 1985.

L. Spitzer. *Physical processes in the interstellar medium*. 1978. doi:10.1002/9783527617722.

S. W. Stahler. The birthline for low-mass stars. *ApJ*, 274:822–829, Nov. 1983. doi:10.1086/161495.

S. W. Stahler and F. Palla. *The Formation of Stars*. 2005.

P. Stee, F. X. de Araujo, F. Vakili, D. Mourard, L. Arnold, D. Bonneau, F. Morand, and I. Tallon-Bosc. γ Cassiopeiae revisited by spectrally resolved interferometry. *A&A*, 300: 219, Aug. 1995.

B. Stelzer, G. Micela, K. Hamaguchi, and J. H. M. M. Schmitt. On the origin of the X-ray emission from Herbig Ae/Be stars. *A&A*, 457:223–235, Oct. 2006. doi:10.1051/0004-6361:20065006.

T. Stolker, C. Dominik, H. Avenhaus, M. Min, J. de Boer, C. Ginski, H. M. Schmid, A. Juhasz, A. Bazzon, L. B. F. M. Waters, A. Garufi, J. C. Augereau, M. Benisty, A. Boccaletti, T. Henning, M. Langlois, A. L. Maire, F. Ménard, M. R. Meyer, C. Pinte, S. P. Quanz, C. Thalmann, J. L. Beuzit, M. Carbillet, A. Costille, K. Dohlen, M. Feldt, D. Gisler, D. Mouillet, A. Pavlov, D. Perret, C. Petit, J. Pragt, S. Rochat, R. Roelfsema, B. Salasnich, C. Soenke, and F. Wildi. Shadows cast on the transition disk of HD 135344B. Multiwavelength VLT/SPHERE polarimetric differential imaging. *A&A*, 595:A113, Nov. 2016a. doi:10.1051/0004-6361/201528039.

T. Stolker, C. Dominik, M. Min, A. Garufi, G. D. Mulders, and H. Avenhaus. Scattered light mapping of protoplanetary disks. *A&A*, 596:A70, Dec. 2016b. doi:10.1051/0004-6361/201629098.

J. M. Stone, C. F. Gammie, S. A. Balbus, and J. F. Hawley. Transport Processes in Protostellar Disks. *Protostars and Planets IV*, page 589, May 2000.

K. M. Strom and S. E. Strom. A multiwavelength study of star formation in the L1495E cloud in Taurus. *ApJ*, 424:237–256, Mar. 1994. doi:10.1086/173886.

Y.-W. Tang, A. Dutrey, S. Guilloteau, V. Piétu, E. Di Folco, T. Beck, P. T. P. Ho, Y. Boehler, F. Gueth, J. Bary, and M. Simon. Circumbinary Ring, Circumstellar Disks, and Accretion in the Binary System UY Aurigae. *ApJ*, 793:10, Sept. 2014. doi:10.1088/0004-637X/793/1/10.

A. Tannirkulam, T. J. Harries, and J. D. Monnier. The Inner Rim of YSO Disks: Effects of Dust Grain Evolution. *ApJ*, 661:374–384, May 2007. doi:10.1086/513265.

A. Tannirkulam, J. D. Monnier, R. Millan-Gabet, T. J. Harries, E. Pedretti, T. A. ten Brummelaar, H. McAlister, N. Turner, J. Sturmann, and L. Sturmann. Strong Near-Infrared Emission Interior to the Dust Sublimation Radius of Young Stellar Objects MWC 275 and AB Aurigae. *ApJ*, 677:L51, Apr. 2008. doi:10.1086/587873.

M. Tazzari, L. Testi, B. Ercolano, A. Natta, A. Isella, C. J. Chandler, L. M. Pérez, S. Andrews, D. J. Wilner, L. Ricci, T. Henning, H. Linz, W. Kwon, S. A. Corder, C. P. Dullemond, J. M. Carpenter, A. I. Sargent, L. Mundy, S. Storm, N. Calvet, J. A. Greaves, J. Lazio, and A. T. Deller. Multiwavelength analysis for interferometric (sub-)mm observations of protoplanetary disks. Radial constraints on the dust properties and the disk structure. *A&A*, 588:A53, Apr. 2016. doi:10.1051/0004-6361/201527423.

C. M. Telesco, D. Ciardi, J. French, C. Ftaclas, K. T. Hanna, D. B. Hon, J. H. Hough, J. Julian, R. Julian, M. Kidger, C. C. Packham, R. K. Pina, F. Varosi, and R. G. Sellar. CanariCam: a multimode mid-infrared camera for the Gran Telescopio CANARIAS. In M. Iye and A. F. M. Moorwood, editors, *Instrument Design and Performance for Optical/Infrared Ground-based Telescopes*, volume 4841 of *SPIE*, pages 913–922, Mar. 2003. doi:10.1117/12.458979.

É. Thiébaut and J. Young. Principles of image reconstruction in optical interferometry: tutorial. *Journal of the Optical Society of America A*, 34:904, June 2017. doi:10.1364/JOSAA.34.000904.

K. Tomisaka. Collapse of Rotating Magnetized Molecular Cloud Cores and Mass Outflows. *ApJ*, 575:306–326, Aug. 2002. doi:10.1086/341133.

R. Topalovic, J. Russell, J. McCombie, T. H. Kerr, and P. J. Sarre. Diamonds and polycyclic aromatic hydrocarbons in the circumstellar environment of the Herbig Ae/Be star Elias 1. *MNRAS*, 372:1299–1303, Nov. 2006. doi:10.1111/j.1365-2966.2006.10945.x.

K. R. W. Tristram. *Mid-infrared interferometry of nearby Active Galactic Nuclei*. PhD thesis, Max-Planck-Institut für Astronomie, Königstuhl 17, 69117 Heidelberg, Germany, July 2007.

R. N. Tubbs, J. A. Meisner, E. J. Bakker, and S. Albrecht. Differential phase delay observations with VLTI-MIDI at N-band. In W. A. Traub, editor, *New Frontiers in Stellar Interferometry*, volume 5491 of *SPIE*, page 588, Oct. 2004. doi:10.1117/12.550315.

N. J. Turner, M. Benisty, C. P. Dullemond, and S. Hirose. Herbig Stars' Near-infrared Excess: An Origin in the Protostellar Disk's Magnetically Supported Atmosphere. *ApJ*, 780:42, Jan. 2014. doi:10.1088/0004-637X/780/1/42.

P. G. Tuthill, J. D. Monnier, and W. C. Danchi. A dusty torus around the luminous young star LkHα101. *Nature*, 409:1012–1014, Feb. 2001. doi:10.1038/35059014.

R. van Boekel, C. P. Dullemond, and C. Dominik. Flaring and self-shadowed disks around Herbig Ae stars: simulations for 10 μm interferometers. *A&A*, 441:563–571, Oct. 2005. doi:10.1051/0004-6361:20042252.

M. E. van den Ancker, D. de Winter, and H. R. E. Tjin A Djie. HIPPARCOS photometry of Herbig Ae/Be stars. *A&A*, 330:145–154, Feb. 1998.

C. Van Kerckhoven, A. G. G. M. Tielens, and C. Waelkens. Nanodiamonds around HD 97048 and Elias 1. *A&A*, 384:568–584, Mar. 2002. doi:10.1051/0004-6361:20011814.

J. Varga, K. É. Gabányi, P. Ábrahám, L. Chen, Á. Kóspál, J. Menu, T. Ratzka, R. van Boekel, C. P. Dullemond, T. Henning, W. Jaffe, A. Juhász, A. Moór, L. Mosoni, and N. Sipos. Mid-infrared interferometric variability of ¡ASTROBJ¿DG Tauri¡/ASTROBJ¿: Implications for the inner-disk structure. *A&A*, 604:A84, Aug. 2017. doi:10.1051/0004-6361/201630287.

J. Varga, P. Ábrahám, L. Chen, T. Ratzka, K. É. Gabányi, Á. Kóspál, A. Matter, R. van Boekel, T. Henning, W. Jaffe, A. Juhász, B. Lopez, J. Menu, A. Moór, L. Mosoni, and N. Sipos. VLTI/MIDI atlas of disks around low- and intermediate-mass young stellar objects. *ArXiv e-prints*, May 2018.

M. Vaňko, M. A.-v. Eiff, T. Pribulla, R. Chini, E. Covino, and R. Neuhäuser. The eclipsing binary TY CrA revisited: what near-IR light curves tell us. *MNRAS*, 431:2230–2239, May 2013. doi:10.1093/mnras/stt321.

S. M. Vicente and J. Alves. Size distribution of circumstellar disks in the Trapezium cluster. *A&A*, 441:195–205, Oct. 2005. doi:10.1051/0004-6361:20053540.

D. Vinković, Ž. Ivezić, T. Jurkić, and M. Elitzur. Near-Infrared and the Inner Regions of Protoplanetary Disks. *ApJ*, 636:348–361, Jan. 2006. doi:10.1086/497895.

M. Vioque, R. D. Oudmaijer, D. Baines, I. Mendigutía, and R. Pérez-Martínez. Gaia DR2 study of Herbig Ae/Be stars. *ArXiv e-prints*, Aug. 2018.

A. E. Visser, J. S. Richer, and C. J. Chandler. Completion of a SCUBA Survey of Lynds Dark Clouds and Implications for Low-mass Star Formation. *AJ*, 124:2756–2789, Nov. 2002. doi:10.1086/344071.

J. Vural, A. Kreplin, S. Kraus, G. Weigelt, T. Driebe, M. Benisty, M. Dugué, F. Massi, J. L. Monin, and M. Vannier. Revealing the inner circumstellar disk of the T Tauri star S Coronae Australis N using the VLTI. *A&A*, 543:A162, July 2012. doi:10.1051/0004-6361/201218892.

J. Vural, S. Kraus, A. Kreplin, G. Weigelt, E. Fossat, F. Massi, K. Perraut, and F. Vakili. Study of the sub-AU disk of the Herbig B[e] star HD 85567 with near-infrared interferometry. *A&A*, 569:A25, Sept. 2014. doi:10.1051/0004-6361/201424214.

K. Wagner, R. Dong, P. Sheehan, D. Apai, M. Kasper, M. McClure, K. M. Morzinski, L. Close, J. Males, P. Hinz, S. P. Quanz, and J. Fung. The Orbit of the Companion to HD 100453A: Binary-driven Spiral Arms in a Protoplanetary Disk. *ApJ*, 854:130, Feb. 2018. doi:10.3847/1538-4357/aaa767.

L. B. F. M. Waters and C. Waelkens. Herbig Ae/Be Stars. *ARAA*, 36:233–266, 1998. doi:10.1146/annurev.astro.36.1.233.

G. Weigelt, R. G. Petrov, O. Chesneau, K. Davidson, A. Domiciano de Souza, T. Driebe, R. Foy, D. Fraix-Burnet, T. Gull, J. D. Hillier, K.-H. Hofmann, S. Kraus, F. Malbet, A. Marconi, P. Mathias, J.-L. Monin, F. Millour, K. Ohnaka, F. Rantakyrö, A. Richichi, D. Schertl, M. Schöller, P. Stee, L. Testi, and M. Wittkowski. VLTI-AMBER observations of Eta Carinae with high spatial resolution and spectral resolutions of 1,500 and 10,000. In *Society of Photo-Optical Instrumentation Engineers (SPIE) Conference Series*, volume 6268 of *SPIE*, page 62682S, June 2006. doi:10.1117/12.671582.

J. P. Williams and L. A. Cieza. Protoplanetary Disks and Their Evolution. *ARAA*, 49:67–117, Sept. 2011. doi:10.1146/annurev-astro-081710-102548.

J. P. Williams and C. McPartland. Measuring Protoplanetary Disk Gas Surface Density Profiles with ALMA. *ApJ*, 830:32, Oct. 2016. doi:10.3847/0004-637X/830/1/32.

J. P. Williams, L. Blitz, and C. F. McKee. The Structure and Evolution of Molecular Clouds: from Clumps to Cores to the IMF. *Protostars and Planets IV*, page 97, May 2000.

D. J. Wilner, P. D'Alessio, N. Calvet, M. J. Claussen, and L. Hartmann. Toward Planetesimals in the Disk around TW Hydrae: 3.5 Centimeter Dust Emission. *ApJL*, 626:L109–L112, June 2005. doi:10.1086/431757.

S. Wolf, F. Malbet, R. Alexander, J.-P. Berger, M. Creech-Eakman, G. Duchêne, A. Dutrey, C. Mordasini, E. Pantin, F. Pont, J.-U. Pott, E. Tatulli, and L. Testi. Circumstellar disks and planets. Science cases for next-generation optical/infrared long-baseline interferometers. *A&ARv*, 20:52, Mar. 2012. doi:10.1007/s00159-012-0052-1.

A. N. Youdin and J. Goodman. Streaming Instabilities in Protoplanetary Disks. *ApJ*, 620: 459–469, Feb. 2005. doi:10.1086/426895.

H. Zinnecker and T. Preibisch. X-ray emission from Herbig Ae/Be stars: A ROSAT survey. *A&A*, 292:152–164, Dec. 1994.

H. Zinnecker and H. W. Yorke. Toward Understanding Massive Star Formation. *ARAA*, 45: 481–563, Sept. 2007. doi:10.1146/annurev.astro.44.051905.092549.

Acknowledgements

I would like to express my gratitude to all the people who have contributed in my work during these years.

In particular, I am thankful to Prof. Dr. Lucas Labadie and Prof. Dr. Gerd Weigelt for offering me the opportunity to be part of the "High-angular Resolution" group of the university and develop my career as astronomer. Also, to Prof. Dr. Astrid Kiendler-Scharr and Prof. Dr. Matthias Sperl for agreeing to be co-referee and chair of my Ph.D. committee.

A meaningful progress with this investigation would have not been possible without the valuable cooperation of Dr. Alexis Matter and Dr. Bruno Lopez from the Observatoire de la Côte d'Azur, to whom I am also very thankful.

The collaborative opportunities offered by the I. Physikalisches Institut of the University of Cologne have also allowed me to participate in projects related to my research and learn from Prof. Dr. Peter Schilke, Dr. Rebekka Grellmann, Dr. Álvaro Sánchez Monge and Dr. Esteban Morales, for whose support I feel greatly grateful.

I acknowledge all joint efforts from the scientific, technical and administrative personnel at the institute, such as Dr. Frank Schlöder and Dr. Thomas Möller, whose computational expertise has significantly assisted my work.

I appreciate the constructive scientific – and not only – discussions and conversations maintained with my colleagues. Particularly, I regard the input acquired from Dr. Jan Tepper, Fabio Eupen, Dr. Nadeen Sabha, Dr. Nicola Baccichet and Moritz Wiegand.

Finally, but above all, I am indebted to my beloved ones and to whom I dedicate this work: Nastya, my mother Lupita, my father Juanito, my brother Sebastián and his precious family (Pía and Pame), Elena and Fedor Korolev, my grandfather Ibal and my appreciated relatives, for their support, patience, care and affection.

In spite of the large distances, I always feel that they are behind and make possible to overcome any struggle.

Erklärung

Ich versichere, dass ich die von mir vorgelegte Dissertation selbständig angefertigt, die benutzten Quellen und Hilfsmittel vollständig angegeben und die Stellen der Arbeit – einschließlich Tabellen, Karten und Abbildungen –, die anderen Werken im Wortlaut oder dem Sinn nach entnommen sind, in jedem Einzelfall als Entlehnung kenntlich gemacht habe; dass diese Dissertation noch keiner anderen Fakultät oder Universität zur Prüfung vorgelegen hat; dass sie – abgesehen von unten angegebenen Teilpublikationen – noch nicht veröffentlicht worden ist sowie, dass ich eine solche Veröffentlichung vor Abschluß des Promotionsverfahrens nicht vornehmen werde. Die Bestimmungen dieser Promotionsordnung sind mir bekannt. Die von mir vorgelegte Dissertation ist von Prof. Dr. Lucas Labadie betreut worden.

Köln, 20.05.2019

Juan Andrés Cahuasquí Llerena *25. Juni, 1989*

cahuasqui@ph1.uni-koeln.de
Zülpicher Str. 77 • Köln, 50937 • NRW • Deutschland

Zusammenfassung

Ich bin in Ambato, einer Stadt in der Mitte der Andenregion Ecuadors, geboren. Weil es mein Traum war Astrophysiker zu werden, bewarb ich mich auf ein Auslandsstipendium, das mich 2008 nach Russland fürhte. Ich habe mein "Spezialist Diplom" (entspricht dem deutschen Master) 2014 an dem Astronomischen Institut der Staatlichen Universität Sankt-Petersburg gemacht.

Seit September 2014 bin ich Doktorand und Forscher in der Gruppe "High-angular Resolution" des I. Physikalischen Instituts der Universität zu Köln, Deutschland. In meiner Arbeit untersuche ich mit Hilfe von Spektroscopie, Photometrie und Long-Baseline Interferometrie junge stellare Objekte mit zirkumstellaren Scheiben, in denen sich Planeten formen können.

Bei der Gelegenheit im Ausland zu leben und zu arbeiten, habe ich, außer meinen nun erweiterten Sprachkenntnissen, gelernt mich in den sehr verschiedenen Kulturen zurecht zu finden und mich mit ihnen zu identifizieren.

Bildung

I. Physikalisches Institut
Universität zu Köln — Köln, Deutschland

Doktorand
Dissertation: "Mid-infrared long-baseline interferometry of young stellar objects: Detection of a hot component inside the circumbinary cavity of V892 Tau" *Sep 2014 – Okt 2018*

Unter der Leitung von Prof. Dr. Lucas Labadie liegt der Schwerpunkt der Arbeit auf der Rückbesinnung auf die wichtigsten Aspekte der Interferometrie und deren Anwendbarkeit zur Erforschung der inneren Region des Herbig-Systems V892 Tau. Dank seiner mehrkomponentigen Struktur ist V892 Tau ein ideales Labor, um die Morphologie der protoplanetaren Scheibe um Binärsysteme zu verstehen und mit den theoretischen Erwartungen zu vergleichen. Multiepochen-MIDI/VLTI-Beobachtungen von V892 Tau werden ausgewertet und analysiert, was zur Erkennung einer neuen Emissionsquelle führte, an Hand derer einige der beobachteten Merkmale erklärt werden konnten.

Astronomisches Institut, Mathematisch-Mechanische Fakultät
Staatliche Universität Sankt-Petersburg — Sankt-Petersburg, Russland

Spezialist Diplom - entspricht dem Master
Diplomarbeit: "Determining the rotation periods and probing the structure of the accretion regions in a sample of magnetic Herbig Ae/Be stars"
– Beste Diplomarbeit Astronomischen Instituts, Promotion 2014 – *Sep 2009 – Aug 2014*

Unter der Leitung von Dr. Mikhail Pogodin und Dr. Natalia Drake umfasst die Arbeit eine hochauflösende spektroskopische Untersuchung von drei Sternen mit identifiziertem Magnetfeld: HD101412, HD104237 und HD190073. Die Analyse der Linien He I (10830 Å) und Paγ enthüllt die Akkretion auf dem Stern durch die magnetischen Linien. Einige abgeleitete Sternparameter werden ebenfalls zum ersten Mal berichtet.

Praktika und Stipendien

OPTICON Fizeau Austauschbesucherprogramm in optischer Interferometrie — Nizza, Frankreich
Mai 2016 – Jun 2016

Praktikum am Hauptsitz der Europäischen Südsternwarte ESO — München, Deutschland
Jun 2013 – Aug 2013

Praktikum an der Astronomichen Bergstation des Pulkovo-Observatoriums — Kislovodsk, Russland
Aug 2012 – Sep 2012

Stipendium für akademisches Studium in russischer Sprache — Sankt-Petersburg, Russland
Dez 2008 – Aug 2014